



Provided by the author(s) and University of Galway in accordance with publisher policies. Please cite the published version when available.

Title	Modelling the Effects of Stenting in the Femoropopliteal Artery
Author(s)	Ní Ghriallais, Ríona
Publication Date	2012-08-31
Item record	http://hdl.handle.net/10379/3497

Downloaded 2024-04-19T15:55:05Z

Some rights reserved. For more information, please see the item record link above.



Modelling the Effects of Stenting in the Femoropopliteal Artery

Ríona Ní Ghriallais

B.Eng, National University of Ireland, Galway, 2008



A thesis submitted to the National University of Ireland as fulfilment of the requirements for the Degree of Doctor of Philosophy

Department of Mechanical and Biomedical Engineering
National University of Ireland, Galway

September 2012

Supervisor of Research: Dr. Mark Bruzzi

Director of Research: Professor Peter Mc Hugh

Abstract

The femoropopliteal artery is a complex and challenging environment for stent placement. It is subject to large deformations due to the impact of physiological loading from surrounding muscles. It is also subject to changing haemodynamic conditions due to its curved and tortuous geometry. Stenting has many significant impacts on the vessel including altering its deformation characteristics due to stiffness changes to portions of the artery, and damage to the vessel wall due to cell denudation and tearing of arterial tissue. Despite extensive investigations of stent-artery interactions using finite element simulations, *in vitro* and *in vivo* experiments, the links between the effects of stenting in terms of local stresses, global deformation characteristic changes and biological responses, and their interdependence has yet to be comprehensively assessed.

The objective of this thesis is to examine the effects of stenting in the femoropopliteal artery by investigating the mechanical and biological effects of stent-artery interactions. Finite element models are used to determine stent-artery interactions local to the stented region as a result of stent deployment and physiological loading. Deformation characteristics of the artery as a result of knee bending and changes to these deformation characteristics as a result of stent placement are also investigated. In addition, an *in vitro* model is used to evaluate stent-artery interactions of curved stented vessels in a cellular and biological context.

The investigations presented in this work highlight the importance of taking both ‘local’ and ‘global’ finite element models simultaneously, allowing thorough assessment of the consequences of stenting in terms of the mechanical effect to vessel tissue. In a biological context, the investigations presented in this work allow the effects of stent placement and vessel curvature on the vascular endothelium to be assessed.

Acknowledgements

Firstly, I would like to express my thanks to my supervisor, Dr. Mark Bruzzi, for his support, guidance and encouragement over the past four years. He has ensured that throughout my studies I have had the best facilities, expertise and support available for which I am most thankful.

I would like to thank Dr. Laoise Mc Namara for her support and direction with the *in vitro* work of this thesis. I would also like to thank the following for their expertise and assistance with the experimental work: Dave Connolly, Dermot Mc Dermott, Ed Killculen, Eoin Ó Cearbhaill, Lisa Hynes, Martin Burke, Matt Haugh, Muriel Voisin, Myles Meehan, Pat Kelly, Sandra Ganly, Valerie Barron. They have been a constant source of advice, help and encouragement, which I greatly appreciate. I would also like to thank Liam Mullins for his advice with my computational queries.

I acknowledge the Irish Research Council for Science and Engineering Technology (IRCSET) and the College of Engineering and Informatics, NUIG who funded this PhD research. I also wish to thank the Irish Centre for High End Computing (ICHEC) for the use of their computational facilities and support.

Thanks to my friends and fellow postgraduate students Cat, Claire, Conleth, Dave, Eamonn, Enda, Emer, Eimear, Evelyn, the Fionas, James, Matt, Meadhbh, Muriel, Nicola, Noel, Paul, Stefaan, Ted, Weaf, Will. They have been a constant source of advice, help and encouragement, which I greatly appreciate.

Na cailíní sa mbaile, Méadbh, Máire Treasa agus Katie, and the past and present ladies of 45, Aoife, Ailbhe, Anita, Ciara, Lisa, Michelle and Trish. I could not have gotten through such busy times without your teas, coffees, dinners and more importantly, support, friendship and pep talks for which I am very grateful.

A special thanks to my family. Firstly my parents for their unconditional love and support, both emotional and financial, without which I would not have achieved this. Cian, Éanna and Rónán, thanks for your patience! Finally, a very special thanks to Ciara for her never ending love and support and for always believing in what I did not.

Contents

Abstract	ii
Acknowledgements	iii
Chapter 1. Introduction	1
1.1 Background	1
1.1.1 Peripheral Arterial Disease	1
1.1.2 Self Expanding Stents	2
1.1.3 Nitinol.....	3
1.1.4 Femoral Artery Anatomy	5
1.1.5 Complications Associated with Stenting in the Femoropopliteal Artery	6
1.2 Thesis Objectives.....	7
1.3 Thesis Structure and Overview	9
1.4 Table and Figures	11
1.5 References	23
Chapter 2. Literature Review	29
2.1 Blood Vessel Structure and Function.....	29
2.2 Mechanical Behaviour of Arterial Tissue.....	31
2.3 Haemodynamic Forces within Arteries	33
2.4 Finite Element Modelling of Stents.....	35
2.5 Physiological Loading and Deformation Characteristics of the Femoropopliteal Artery	38
2.6 Tables and Figures.....	44
2.7 References	53
Chapter 3. Finite Element Theory and Formulations	64
3.1 Continuum Mechanics.....	64
3.1.1 Notation	64
3.1.2 Fundamental Principals and Theoretical Formulations.....	65
3.1.3 Elasticity	67

3.2	Constitutive Modelling of Biological Soft Tissues	74
3.2.1	Isotropic Hyperelasticity	74
3.2.2	Anisotropic Hyperelasticity	77
3.2.3	Polynomial Form (Isotropic).....	80
3.2.4	Mooney Rivlin Form (Isotropic).....	82
3.2.5	Holzapfel-Gasser-Ogden Form (Anisotropic).....	82
3.3	Constitutive Modelling of Superelastic Materials.....	85
3.4	Numerical Implementation.....	88
3.4.1	Implicit Finite Element Solution Method.....	88
3.4.2	Explicit Finite Element Solution Method.....	91
3.5	Figures	95
3.6	References	100
Chapter 4. Local Analysis of Stent-Artery Interactions in the Superficial Femoral Artery		103
4.1	Introduction	103
4.2	Radial Force Accuracy and Modelling Approach.....	107
4.2.1	Materials and Methods.....	108
4.2.2	Results.....	115
4.2.3	Discussions	118
4.3	Stresses in the Stented Superficial Femoral Artery due to Physiological Loading	125
4.3.1	Materials and Methods.....	127
4.3.2	Results.....	132
4.3.3	Discussions	133
4.4	Conclusions	135
4.5	Tables and Figures.....	138
4.6	References	163
Chapter 5. Effects of Knee Flexion on the Femoropopliteal Artery: A Computational Study		170

5.1	Introduction	170
5.2	Materials and Methods	173
5.2.1	Geometry	173
5.2.2	Meshing	173
5.2.3	Material Properties.....	174
5.2.4	Quantification of Deformation.....	178
5.3	Results	182
5.3.1	Axial Length Change	182
5.3.2	Curvature Change	182
5.3.3	Radial Compression.....	182
5.3.4	Axial Twist/Torsion.....	183
5.4	Discussions and Conclusions	184
5.5	Tables and Figures.....	188
5.6	References	200
Chapter 6. Effect of Stenting on the Deformation Characteristics of the Superficial Femoral Artery: A Computational Study		211
6.1	Introduction	211
6.2	Materials and Methods	213
6.2	Results	214
6.2.1	Stent Length Investigation	214
6.2.2	Stent Location Investigation	216
6.2.3	Changes in deformation characteristics for stented vessels	217
6.3	Discussions and Conclusions	219
6.4	Tables and Figures.....	223
6.5	References	246
Chapter 7. Comparison of <i>In Vitro</i> Human Endothelial Cell Response to Self Expanding Stent Deployment in a Straight and Curved Peripheral Artery Simulator.....		248
7.1	Introduction	248

7.2	Materials and Methods	253
7.2.1	Bioreactor Design	253
7.2.2	Fabrication of <i>In Vitro</i> Peripheral Artery Models	254
7.2.3	Experimental Models	254
7.2.4	Controls.....	255
7.2.5	Stent deployment	255
7.2.6	Biomechanical Stimulation	256
7.2.7	Cell Number.....	256
7.2.8	Cell Orientation.....	256
7.2.9	Nitric Oxide Production.....	257
7.2.10	Statistical Analysis.....	257
7.3	Results	258
7.3.1	Cell Number.....	258
7.3.2	Cell Orientation.....	259
7.3.3	Nitric Oxide Production.....	260
7.4	Discussions and Conclusions	262
7.5	Figures	268
7.6	References	277
Chapter 8. Concluding Remarks and Future Perspective		287
8.1	References	294

Chapter 1. Introduction

1.1 Background

1.1.1 Peripheral Arterial Disease

Peripheral arterial disease is the term applied to a pathological state of the peripheral arteries, in which atherosclerosis (narrowing of the blood vessels) causes reduced blood circulation in the arteries of the legs, predominantly the femoral artery. Peripheral arterial disease, unlike myocardial infarction, has a relatively low risk of death but causes substantial disability as affected limbs are at a higher risk of amputation and infection (World Health Organisation, 2012).

Peripheral arterial disease results from atherosclerosis and inflammatory processes that lead to stenosis, thrombus and embolus in the artery, which obstructs blood flow. Atherosclerosis is the build-up of plaque (fatty and cholesterol deposits) on the inner lining of the artery wall. Plaque lesions result in a distorted vessel lumen which reduce blood flow velocity and alters blood flow patterns, further effecting haemodynamic force levels (Kalmár et al., 2002). Once the lesion occludes over 50% of the vessel lumen, the narrowed area is termed a stenosis which impedes the artery and can cause pain to the patient. Rupture of such a plaque results in thrombus formation which may further block the artery and can often occlude blood flow completely leading to ischaemia. In the vessels of the lower extremity, this compromised blood flow can lead to lower limb loss.

Percutaneous transluminal angioplasty (PTA) is a method used for the treatment of atherosclerosis. For many physicians, it is the treatment of choice for cases of stenosis and local arterial occlusion. PTA involves the passing of a balloon catheter to the site of the blockage where the small folded balloon is inflated. This compresses the plaque against the artery wall to expand the narrowed lumen and restore blood flow. This imposed expansion of the vessel can cause plaque rupture and damage to the vessel wall which leads to endothelial cell denudation thereby triggering a thrombotic response at the site of angioplasty. This can result in further lumen loss. Studies have shown that weeks to months after angioplasty procedures,

40% of patients treated will develop ‘restenosis’ requiring repeat procedures (Fleisch et al., 1999, Woods et al., 2004).

In order to reduce restenosis rates, ‘stents’ were designed to combat restenosis rates and improve angioplasty outcomes (Fleisch et al., 1999). Therefore in recent years, PTA is generally followed by stent implantation. This involves a metallic scaffold (stent) which is delivered to the stenosed region following PTA, providing a means of supporting the inside of the artery to maintain the lumen patency, allowing uncompromised blood flow (Holmes Jr et al., 1984). Results of one clinical trial that compared the outcome of patients receiving angioplasty alone to those receiving angioplasty followed by stent implantation showed 40% of ‘angioplasty only’ patients required a repeat procedure. The study also showed a 30% lower restenosis rate in those patients who received a stent after angioplasty highlighting the benefits of stenting (Versaci et al., 1997).

1.1.2 Self Expanding Stents

There are many types of stent available on today’s medical device market for the treatment of arterial disease (Duerig et al., 2000, Duerig et al., 2002, Stoeckel et al., 2002). They are categorized according to their application, mechanism, shape, size and manufacturing process and are either balloon expandable or self-expandable. Balloon expandable bare metal stents are the most traditional stent devices on the market. These stents are crimped onto a balloon catheter which, when inflated, expands the stent to become implanted in the target region. Commonly made from stainless steel or cobalt chromium, these stents rely on plastic deformation to crimp the stents and to expand them to their target diameter (Duerig et al., 2002). In recent years, drug eluting stents have been developed which consist of a bare metal stent covered in anti-inflammatory and anti-proliferative agents that target the local inflammatory response associated with stenting (Woods et al., 2004). Furthermore, biodegradable stents have been developed that provide immediate support to the target lesion upon placement but degrade over time, reducing the stiffness of the stented region and also the long term side effects of stenting which include device fracture and restenosis (Hermawan et al., 2010).

Self-expanding stents are primarily used in the peripheral arteries as they are 10-20 times more flexible than balloon expandable stents (Duerig et al., 1999). These devices, typically larger than coronary stents are made from ‘super elastic, shape memory’ alloys and are capable of returning to their original shape even after extreme levels of deformation (Duerig et al., 2000, Stoeckel et al., 2004). Nitinol is the name given to alloys composing of nickel and titanium, a material commonly used for self expanding stents. Although the properties of Nitinol are strongly temperature dependent, the loading and unloading curves of Nitinol (shown in Figure 1.1 and Figure 1.2) show that large strains can be induced in the material during loading and unloading without a corresponding increase in stress (Morgan, 2004, Stoeckel et al., 2004). It has been shown that Nitinol can undergo elastic deformations of up to 11% strain leading to the commonly used terms for Nitinol of ‘super elastic’ (Duerig et al., 1999, Morgan, 2004). This makes it an ideal material choice for stents, allowing these devices to undergo large deformations during manufacture, deployment and physiological loading without significant permanent deformation. This is not seen in other standard stent materials such as stainless steel and cobalt based alloy stents which in most cases can only elastically deform to 1% strain (Duerig et al., 1999).

1.1.3 Nitinol

Nitinol has its own unique mechanism of deformation and as mentioned is termed as both a ‘super elastic’ and ‘shape memory’ material. Superelasticity is a response of Nitinol to stress induced phase transformation (Stoeckel et al., 2004). Unlike other elastic materials which deform due to the stretching of atomic bonds, Nitinol deforms by changing its crystal structure from Austenite to Martensite in response to an applied stress above a critical level (Duerig et al., 1990, Stoeckel et al., 2004). In response to an applied force, phase transformation allows the material to change its properties and hence its response to stress. However, once the force is removed, the material can revert back to its original austenitic structure, recovering its original undeformed shape.

The shape memory property of Nitinol is a result of thermal induced phase transformation and is utilised for the forming of the stent geometry (Duerig et al., 1990, O'Brien et al., 2011, Stoeckel et al., 2004). Deformation at temperatures above

its 'phase transformation temperature' causes a change in the crystal structure of the material, which upon cooling allows this shape to be 'set'. This critical temperature is dependent on the processing history and alloy composition of the material and is not accompanied by a shape change unless a force is applied. It is possible to plastically deform the material when in the low temperature phase, but the material's original shape can still be recovered by heating above the transformation temperature (Duerig et al., 1990, O'Brien et al., 2011, Stoeckel et al., 2004).

Nitinol self-expanding stent production is a multi-step process (Favier et al., 2006, Morgan, 2004). Initially, the stent geometry is cut from Nitinol tubing, which is then expanded to the nominal stent outer diameter (OD), typically by placing the stent over a cylindrical mandrel. The stent is then shape set by heat treating the stent and mandrel, resulting in a stress-free configuration of the stent at its nominal diameter. This is then crimped to a reduced diameter and loaded into a delivery system. Removal of the delivery system allows the stent to 'deploy' to its stress-free nominal diameter due to its 'super-elastic' properties. Transition temperatures are usually set below 30°C which ensures the stent behaves 'superelastically' once implanted into the body.

Since it was initially proposed as a material for stents by Dotter et al. (1983), self-expandable Nitinol stents have shown improved mechanical performance in comparison to stainless steel stents for peripheral artery applications in terms of chronic outward force and flexibility of the stent (Barth et al., 1996, Duda et al., 2000, Duerig et al., 2002, Müller-Hülsbeck et al., 2010), despite their lower radial force values. In clinical studies, treatment of peripheral arterial disease with self-expandable Nitinol stents has shown promising results in comparison to treatment with angioplasty alone along with long-term patency and device durability (Adlakha et al., 2010, Davies et al., 2010, Henry et al., 1995, Jaff et al., 2010, Schillinger et al., 2006). In summary, advantages of self-expanding stents for use in peripheral arteries include their ability to deform with the deformation characteristic of the artery whilst still delivering radial force support to the artery due to their material properties (Allie et al., 2004, Denison, 2004, Duda et al., 2002, Duerig et al., 1999, Ferreira et al., 2007, Ganguly et al., 2011, O'Brien et al., 2011, Pelton et al., 2008, Simons et al., 2010, Stoeckel et al., 2004). However, stent fracture rates are still commonly in up to

28% of cases due to the complex physiological loads imposed by the artery and surrounding tissue which creates a complex and often misunderstood loading environment (Jonker, 2008).

1.1.4 Femoral Artery Anatomy

The circulatory system of the lower limbs (Figure 1.3 and Figure 1.4) begins with the descending aorta which divides into the two common iliac arteries over the lumbar vertebrae, as can be seen in Figure 1.3. The two common iliac arteries descend inferolaterally eventually dividing into the internal and external iliac arteries. The external iliac runs obliquely downwards, entering the thigh where it becomes the femoral artery. The part of the femoral artery proximal to the iliac artery is commonly termed as the common femoral artery. It is here that the one of the largest and most important branches originates – the deep femoral artery, also termed the profundafemoris. The distal segment of the femoral artery is termed as the superficial femoral artery (SFA). In the distal part of the SFA, the femoral artery has a branch called the descending genicular artery which supplies blood to the knee joint. The femoral artery continues to run inferomedially, entirely encased in the muscles of the thigh, as shown in Figure 1.5. It then becomes the popliteal artery which descends behind whilst twisting around the knee. The portion of the femoral artery from the distal segment of the popliteal artery is commonly termed the femoropopliteal artery.

The femoral artery is entirely encased in the muscles of the thigh from its origin at the iliac artery throughout its length. As it descends from the iliac artery it enters the femoral triangle. The femoral triangle is the term given to describe the region bounded by the inguinal ligament, the medial border of the adductor longus and the sartorius muscles. As the femoral artery descends, it passes ‘through’ the femoral triangle along the pectineus and adductor longus muscles (Figure 1.6). It then enters the adductor canal in the medial part of the mid-thigh where the adductor muscles (longus, magnus and brevis) surround it. It leaves the adductor canal through the adductor hiatus, descending into the popliteal artery, running again between the pectineus and adductor longus muscles. These surrounding muscles interact with the underlying blood vessels during movement of the leg, predominantly during knee flexion and extension. Flexion/extension of the knee is

one of the most common movements of the human body and is required in everyday movements of walking, sitting and stair climbing. The muscles involved in flexion and extension of the knee can be seen in Figure 1.7 and Figure 1.8 and are listed in Table 1.1 (Netter, 2006a, Netter, 2006b). Flexion/extension of the knee results in various deformations of the femoral artery due to the interaction of the artery with its closely surrounding muscles. It is also subject to high *in vivo* loads from these surrounding muscle groups. Together, this deformation and loading leads to compression, bending and torsion of the vessel (Jonker, 2008, Smouse et al., 2005).

1.1.5 Complications Associated with Stenting in the Femoropopliteal Artery

Changes to mechanical properties in the stented portion of the vessel are an inevitable side effect of stenting. It is understood that although stenting has the required effect of supporting the walls of an artery and preventing against re-occlusion of a cleared blockage, it increases the stiffness of the artery. This increase is dependent on device design parameters and may reduce the ability of the artery to twist, shorten and bend as required through a range of body movements.

As described, the femoral artery is subject to high *in vivo* loads due to its surrounding muscle groups and experiences deformation which leads to compression, bending and torsion of the vessel, dramatically changing its shape as seen in angiographic images of the artery (Figure 1.9). Repetitive body movements such as knee flexion result in a cyclic loading environment for the stent. These loads often lead to the fracture of stents placed in regions of extreme load levels (i.e. in the distal SFA and popliteal artery close to the knee joint) (Adlakha et al., 2010, Allie et al., 2004, Nikanorov et al., 2008, Scheinert et al., 2005, Schlager et al., 2005). Extreme deformation and loading of the artery can also lead to kinks in the artery along with arterial wall penetration by fractured stent struts (Figure 1.9) (Cheng et al., 2001, Duerig et al., 2002, Ferreira et al., 2007, Ganguly et al., 2011, Kalmár et al., Scheinert et al., 2005, Smouse et al., 2005). This results in vascular injury, resulting in restenosis and inevitably device failure requiring re-stenting of the artery (Kalmár et al., 2002).

1.2 Thesis Objectives

A large amount of research has been done in the field of stent devices which has focused on understanding the effects of stenting on arteries and stent-artery interactions. Studies on stent fracture rates have concluded that biomechanical forces and loading conditions in the femoral artery are very significant factors in the failure of stents placed there (Cheng et al., 2001, Nikanorov et al., 2008, Scheinert et al., 2005, Schlager et al., 2005, Smouse et al., 2005). The major challenge of stenting in the femoropopliteal artery is developing a device that is capable of withstanding the loading conditions of the artery, induced by the repetitive motion of the knee and hip in every day movements such as walking and sitting. However, part of the challenge faced arises from the fact that the loading conditions of the femoral artery are not well understood, as measuring the dynamic forces of the artery and its deformation characteristics represents a great challenge *in vivo*. Many clinical studies have investigated the deformation characteristics of the artery by analysing angiographic images and three dimensional models based on these images (Figure 1.10) (Cheng et al., 2010, Choi et al., 2009, Klein et al., 2009a, Klein et al., 2009b, Wood et al., 2006). However, deformation characteristics have not been linked to levels of stress and strain within the artery which arises from its surrounding muscles, and furthermore, the effect of stent placement on the global characteristic deformations of the artery has never been assessed. It is apparent from the literature that stent failure is not only due to the fracture of stents as a result of extreme loading conditions but that restenosis, the reoccurrence of blockages in the stented region, generally resulting in re-stenting of the artery, also plays a key role in stent failure (Adlakha et al., 2010, Allie et al., 2004, Cheng et al., 2001, Duerig et al., 2002, Ferreira et al., 2007, Ganguly et al., 2011, Kalmár et al., Nikanorov et al., 2008, Scheinert et al., 2005, Schlager et al., 2005, Smouse et al., 2005). This is caused by the response of the cells of the artery wall to stent placement either during or following stent delivery. Contact with the vessel wall at the time of stenting, along with stresses on the vessel wall from the stent, cause disturbance to the cell lining and can lead to restenosis. It is therefore apparent that stenting of the femoral artery has many consequences:

- The local stresses in the arterial wall may lead to damage to the vessel tissue
- The biomechanical loading conditions that the stented artery is subjected to from the surrounding muscles may lead to fracture of the stent
- The change in global deformation characteristics of the artery due to stiffening of the stented artery portion may also induce local stresses at the end of the stented vessel portion
- The endothelial cells may be damaged due to the altered physiological loading environment

Such consequence of stenting in the femoral artery can only be fully understood by assessing all of these effects and how they interact with each other. This is the subject matter of this thesis, and the following are the key objectives of this work:

1. Identification of interactions between the stent and artery, local to the stented region as a result of stent deployment and physiological loading (Chapter 4).
2. Establishment of deformation characteristics of the artery as a result of knee bending (Chapter 5).
3. Identification of the changes in deformation characteristics of the artery (established in Chapter 5) as a result of stent placement (Chapter 6).
4. Development of a peripheral artery simulator system (bioreactor) to evaluate stent-artery interactions in a cellular context (Chapter 7).

1.3 Thesis Structure and Overview

In this thesis, Chapter 2 and Chapter 3 give an overview of the generalised computational and bioreactor methods conducted in this work.

Chapter 4 focuses on methods of modelling stent-artery interactions using the finite element method. More specifically, the objectives in this chapter are to investigate how different methods of modelling stent-artery interactions can affect the accuracy of the results (Ní Ghriallais et al., 2012). Various different finite element models, each with increasing levels of complexity are used to simulate self expanding stent expansion in the SFA in order to determine what level of simplification will still allow for an accurate representation of stent radial force and resulting stress concentrations on the inner lining of the vessel during self-expanding stent deployment. The results of this study are then used to determine the stress concentrations in the SFA following stent placement. Following stent expansion, *in vivo* physiological loads (appropriate for the SFA) are applied to the stented vessel to quantify the stress concentrations due to stenting in this artery.

In Chapter 5, an anatomically accurate, three dimensional finite element model is developed, capable of capturing the loading conditions and deformation characteristics of the femoral artery during knee flexion. Three dimensional geometries of the muscle, bone, arterial and soft tissues of the leg were constructed from CT scan data and knee flexion of approximately 90° was simulated. Deformation characteristics of length change (axial compression), curvature, radial compression and axial twist are quantified from the model. Femoral artery deformation characteristics are associated with stress and strain levels within the arterial tissue.

In Chapter 6, the finite element model developed in Chapter 5 is used to assess the effect of stenting on the global deformation characteristics of the artery (established in Chapter 5). The model was then adapted to represent ‘stented’ cases. A comparison of the deformation characteristics of the artery are investigated for different stent locations and lengths.

In Chapter 7 an *in vitro* study was developed to investigate stent-artery interactions at a cellular level. A peripheral artery simulator was set up to examine endothelial cell response to combinations of straight, curved stented and unstented peripheral vessel models subjected to 24 hours of stimulation in a peripheral artery bioreactor. Changes in cell number, orientation and nitric oxide production was assessed in straight, curved, non-stented and stented pseudovessels to capture the effects of stenting and curvature on peripheral vessels. This study shows that the response of the vascular endothelium is dependent on both curvature and stenting combined and highlights the necessity of investigating the effects of curvature in combination with stenting to fully understand effects on the endothelial layer.

In Chapter 8, the final chapter of the thesis, the results generated from the four main studies of the thesis are discussed, and conclusions are drawn on the advantage of analysing stent-artery interactions through a number of different models at varying size scales.

1.4 Table and Figures

Muscle	Movement	Origin of Muscle	Insertion of Muscle
Sartorius	Flexion	Anterior superior iliac spine	Medial to tibial tuberosity
Gracilis	Flexion	Pubic bone	Medial to tibial tuberosity
Semitendinosus	Flexion	Ischial tuberosity	Medial to tibial tuberosity
Semimembranosus	Flexion	Ischial tuberosity	Medial to tibial tuberosity
Biceps Femoris	Flexion	Femur	Head of fibula
Rectus Femoris	Extension	Anterior inferior iliac spine	Tibial tuberosity (via patella tendon)
Vastus Lateralis	Extension	Linea aspera of femur, greater trochanter, intertrochanteric line	Patella (via quadriceps tendon), tibial tuberosity (via patella tendon)
Vastus Intermedialis	Extension	Lateral side of femur	Patella (via quadriceps tendon)
Vastus Medialis	Extension	Medial side of femur	Patella (via quadriceps tendon)

Table 1.1 Flexors and extensors of the knee and their origins and insertions (Netter, 2006a, Netter, 2006b).

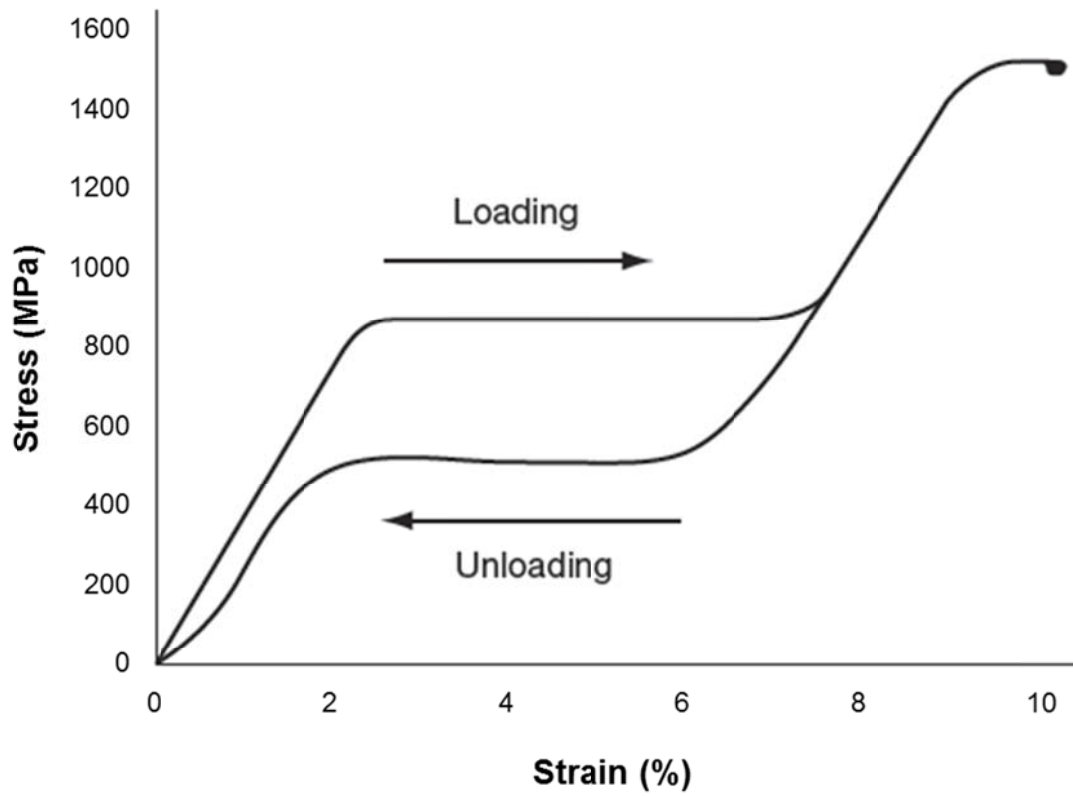


Figure 1.1 Stress strain curve of Nitinol (O'Brien et al., 2011).

Image Removed Due To Copyright

**Figure 1.2 Influence of temperature on tensile properties of Nitinol
(Pelton et al., 2000).**

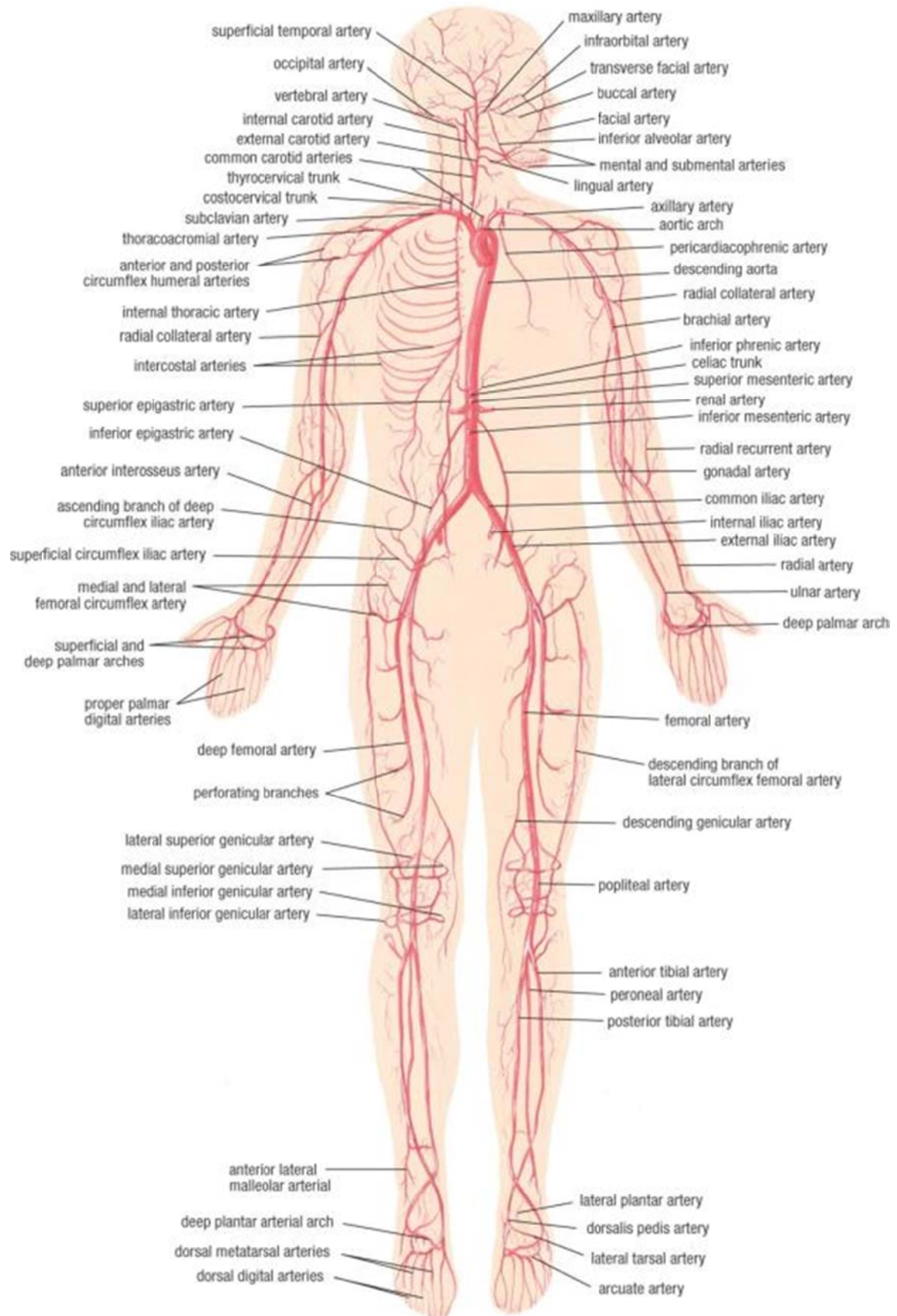


Figure 1.3 Principal arteries of the circulatory system of the human body (Netter, 2006a).

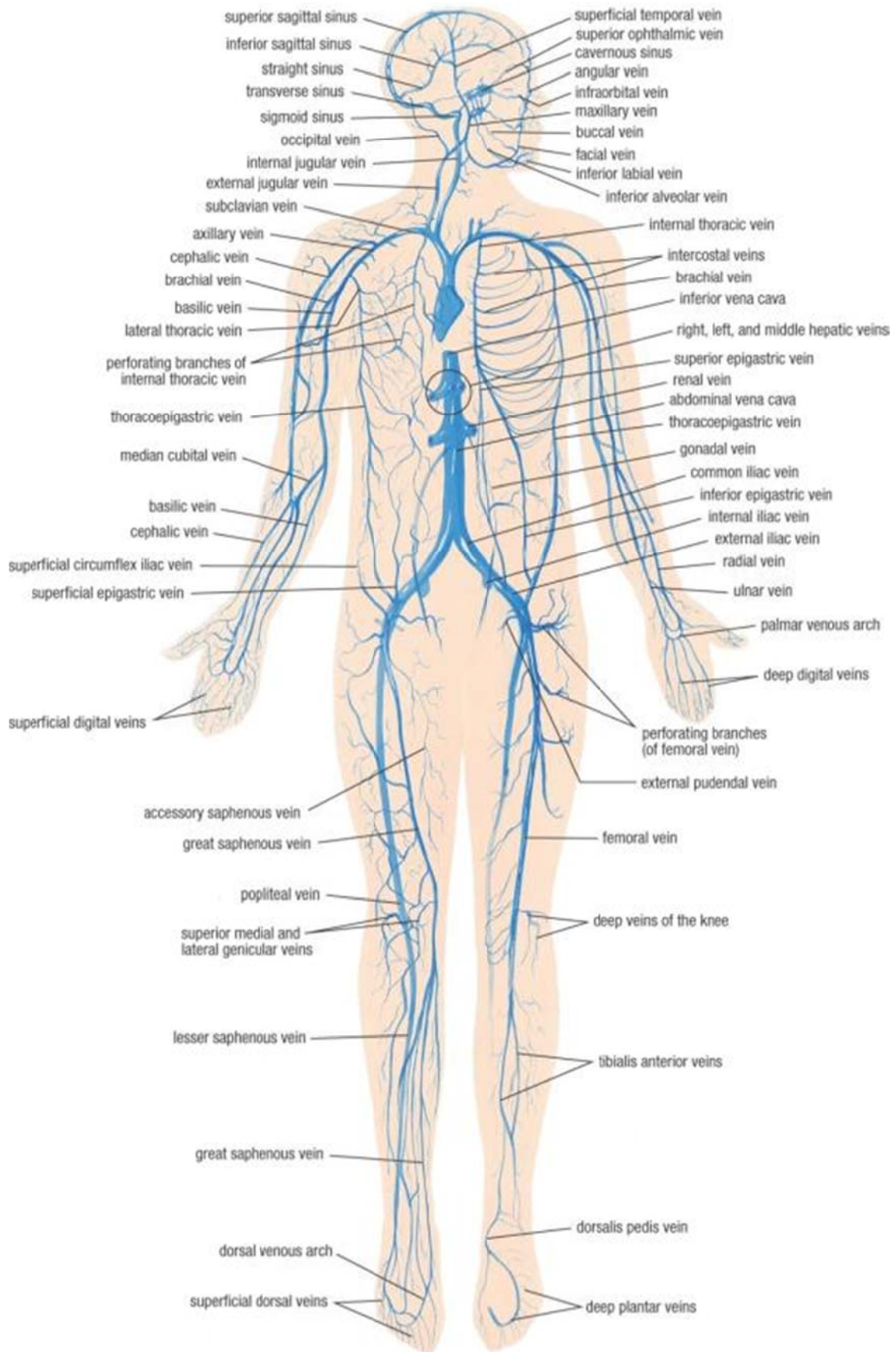


Figure 1.4 Principal veins of the circulatory system of the human body (Netter, 2006a).

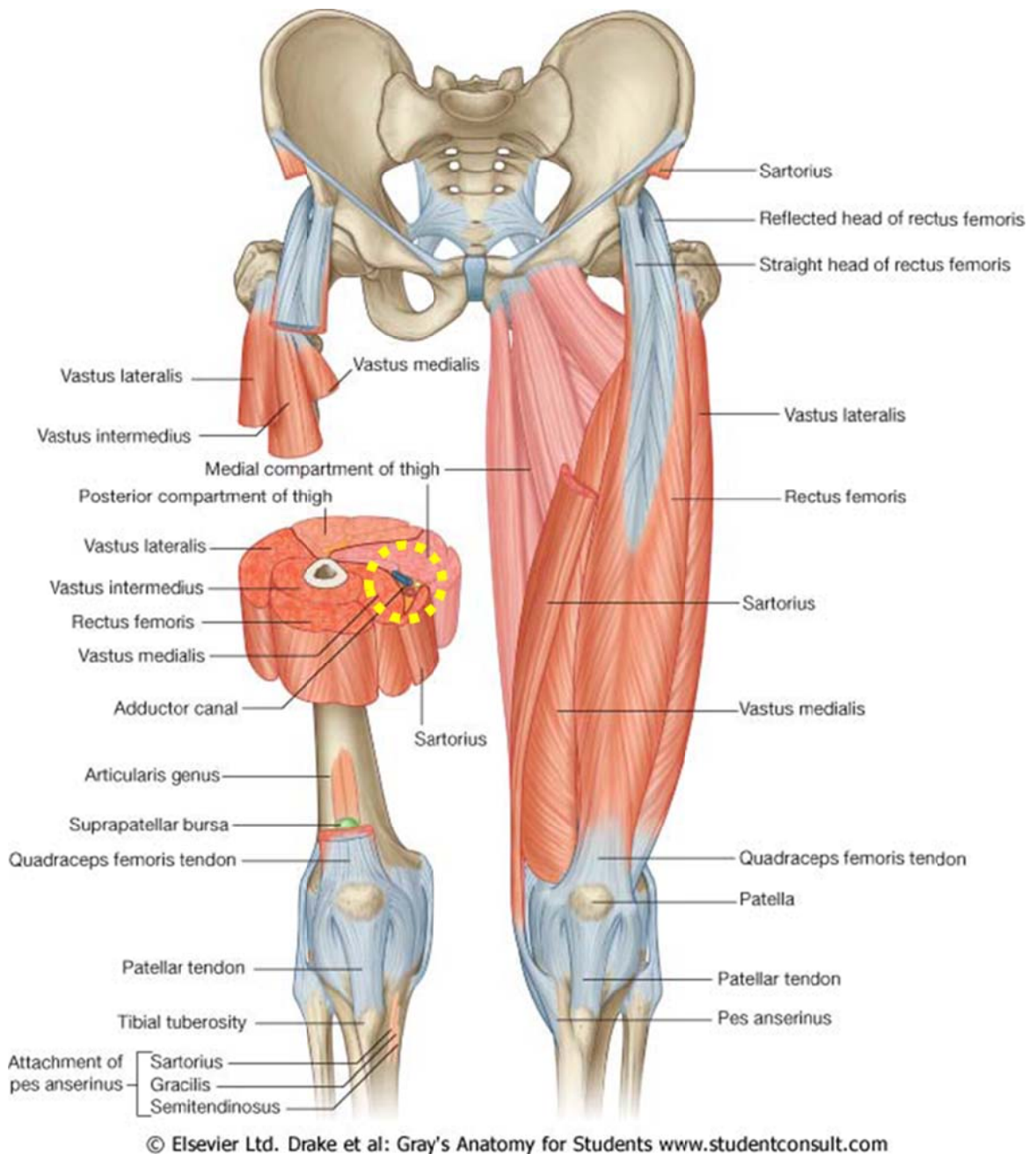


Figure 1.5 Overview of the muscles of the leg showing the femoral artery (center of yellow circle) entirely encased in muscle (Netter, 2006a).

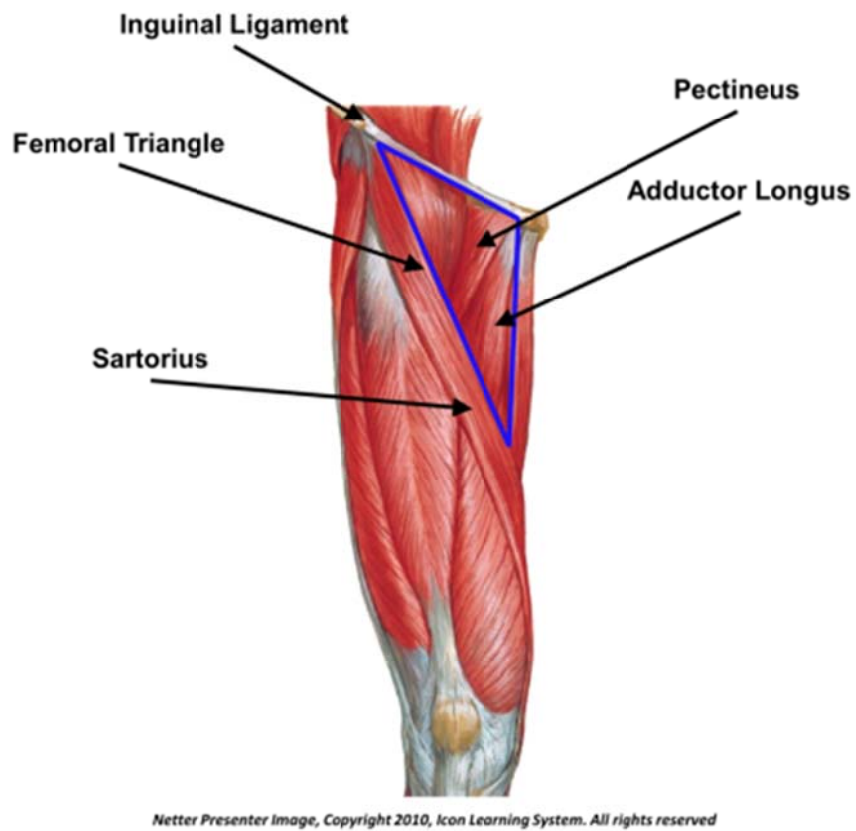


Figure 1.6 The femoral triangle and its limits (Netter, 2006a).

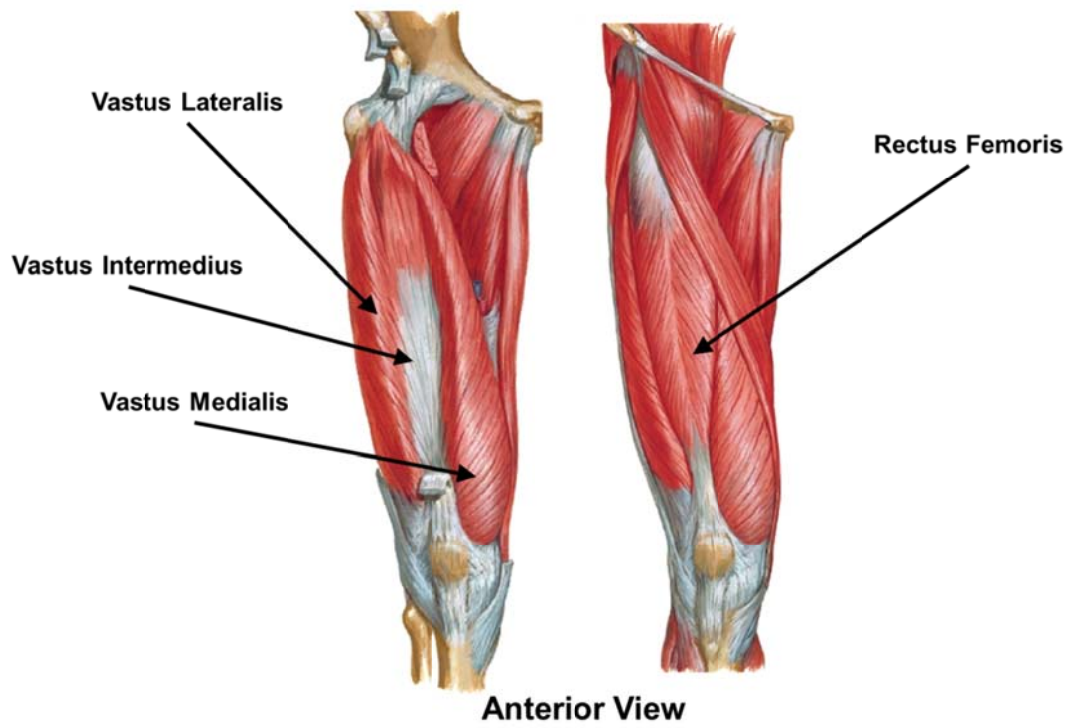


Figure 1.7 Extensors of the knee (Netter, 2006a).

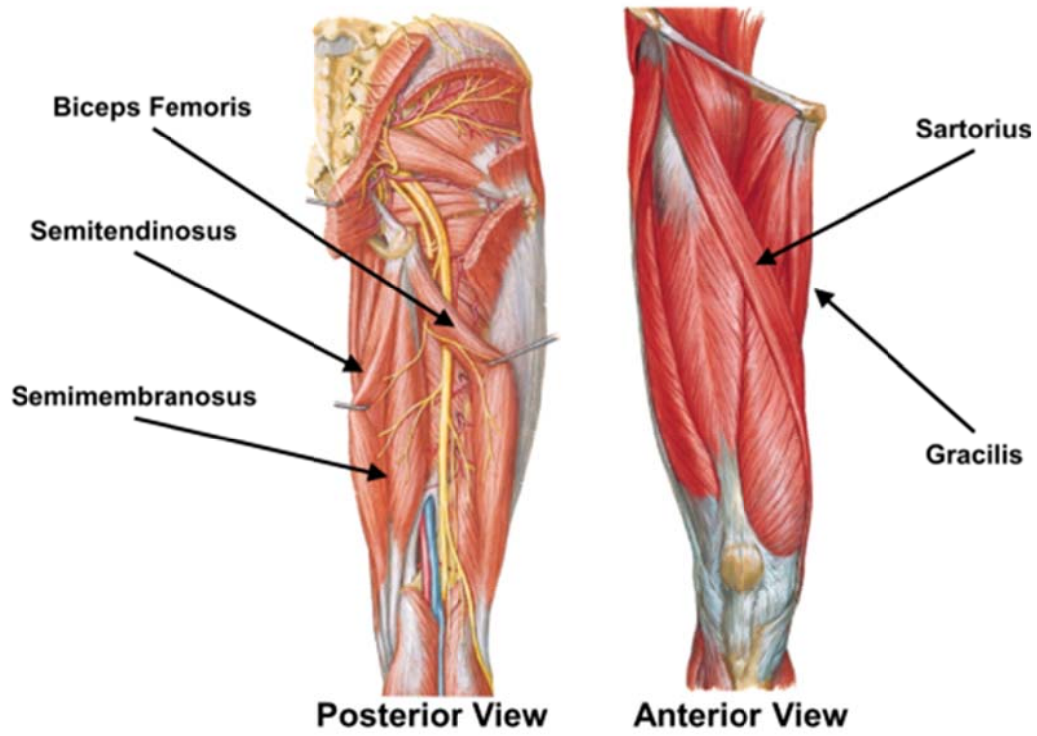


Figure 1.8 Flexors of the knee (Netter, 2006a).

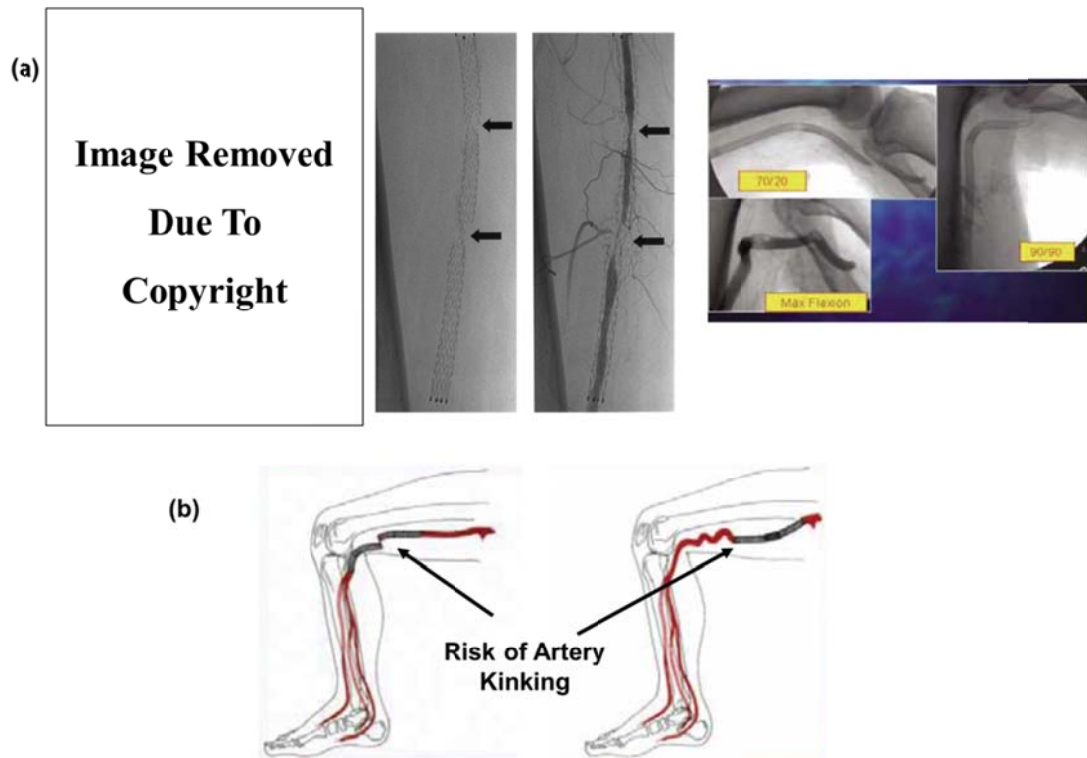


Figure 1.9 The effect of knee flexion on the femoropopliteal artery (a) angiographic images of the stented vessel showing vessel deformation and stent fracture (b) highlighting the regions where stent kinking is likely to occur (Duerig et al., 2002, Scheinert et al., 2005, Smouse et al., 2005).

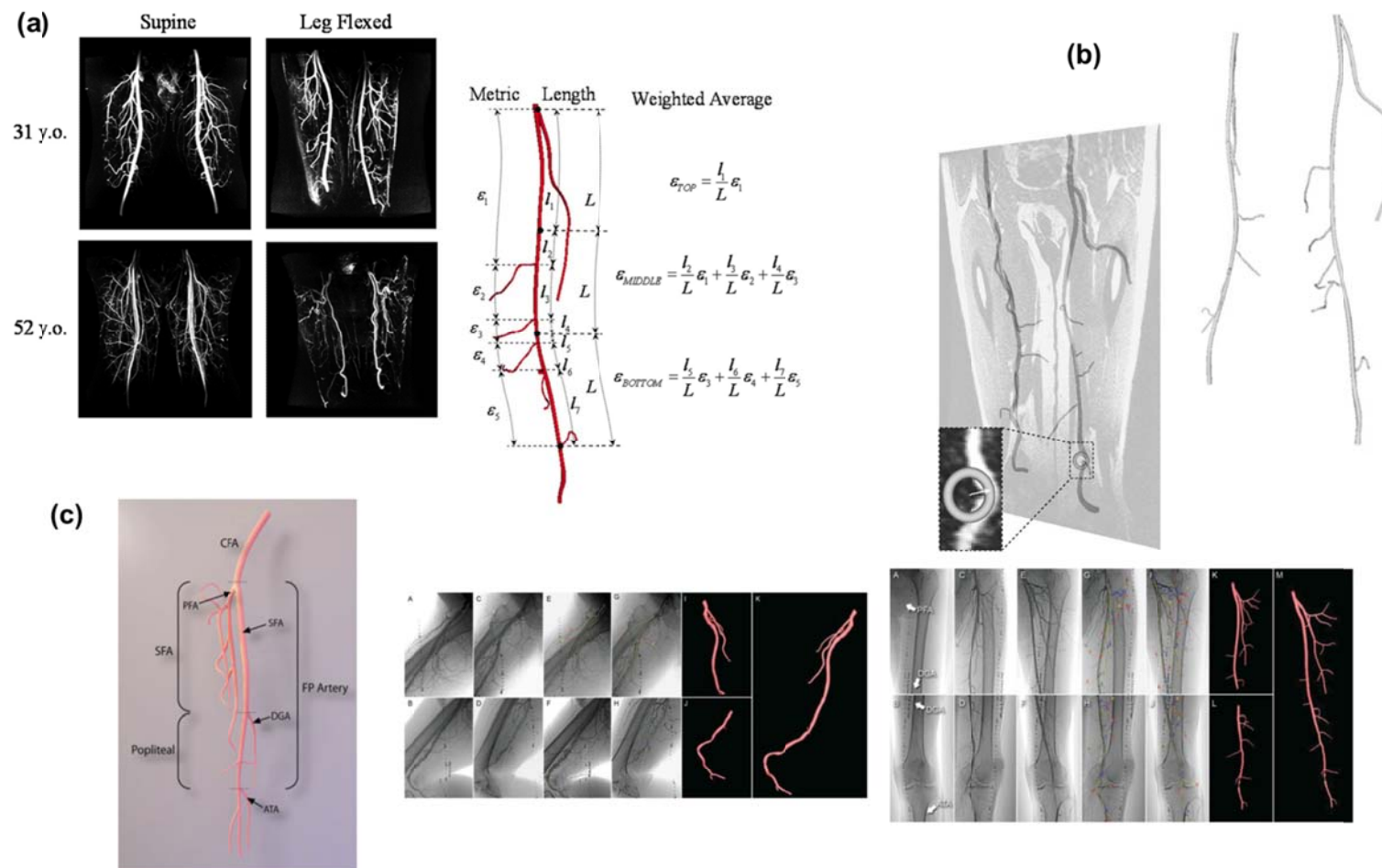


Figure 1.10 Three dimensional models of the femoral artery based on angiographic images (a) Cheng et al. 2010 (b) Choi et al. 2008 (c) Klein et al. 2009b (Cheng et al., 2010, Choi et al., 2009, Klein et al., 2009b).

1.5 References

- Adlakha, S, Sheikh, M, Wu, J, Burket, MW, et al. 2010. Stent Fracture in the Coronary and Peripheral Arteries. *Journal of Interventional Cardiology*. 23: 411-419.
- Allie, DE, Hebert, CJ, and Walker, CM. 2004. Nitinol stent fractures in the SFA. *Endovascular Today*. 3: 22-34.
- Barth, KH, Virmani, R, Froelich, J, Takeda, T, et al. 1996. Paired comparison of vascular wall reactions to Palmaz stents, Strecker tantalum stents, and Wallstents in canine iliac and femoral arteries. *Circulation*. 93: 2161-2169.
- Cheng, CP, Choi, G, Herfkens, RJ, and Taylor, CA. 2010. The effect of aging on deformations of the superficial femoral artery resulting from hip and knee flexion: potential clinical implications. *Journal of Vascular and Interventional Radiology*. 21: 195-202.
- Cheng, SWK, W. Ting, AC, and Wong, J. 2001. Endovascular stenting of superficial femoral artery stenosis and occlusions: results and risk factor analysis. *Cardiovascular Surgery*. 9: 133-140.
- Choi, G, Cheng, CP, Wilson, NM, and Taylor, CA. 2009. Methods for quantifying three-dimensional deformation of arteries due to pulsatile and nonpulsatile forces: implications for the design of stents and stent grafts. *Annals of Biomedical Engineering*. 37: 14-33.
- Davies, MG and Vykoukal, D. 2010. Changing Paradigms in the Management of Peripheral Vascular Disease: The Need for Integration of Knowledge, Imaging, and Therapeutics. *Computational Surgery and Dual Training*. 13.
- Denison, A. Axial and bending fatigue resistance of nitinol stents. in *International Conference on Shape Memory and Superelastic Technologies*. 2004. Baden-Baden, Germany.

- Dotter, CT, Buschmann, R, McKinney, M, and Rösch, J. 1983. Transluminal expandable nitinol coil stent grafting: preliminary report. *Radiology*. 147: 259-260.
- Duda, SH, Pusich, B, Richter, G, Landwehr, P, et al. 2002. Sirolimus-Eluting Stents for the Treatment of Obstructive Superficial Femoral Artery Disease. *Circulation*. 106: 1505-1509.
- Duda, SH, Wiskirchen, J, Tepe, G, Bitzer, M, et al. 2000. Physical Properties of Endovascular Stents: An Experimental Comparison. *Journal of Vascular and Interventional Radiology*. 11: 645-654.
- Duerig, T, Pelton, A, and Stöckel, D. 1999. An overview of nitinol medical applications. *Materials Science and Engineering: A*. 273: 149-160.
- Duerig, T, Tolomeo, D, and Wholey, M. 2000. An overview of superelastic stent design. *Minimally Invasive Therapy & Allied Technologies*. 9: 235-246.
- Duerig, T and Wholey, M. 2002. A comparison of balloon-and self-expanding stents. *Minimally Invasive Therapy & Allied Technologies*. 11: 173-178.
- Duerig, TW, Melton, K, Stockel, D, and Wayman, C, *Engineering aspects of shape memory alloys*, 1990, Butterworth-Heinemann: Oxford.
- Favier, D, Liu, Y, Orgeas, L, Sandel, A, et al. 2006. Influence of thermomechanical processing on the superelastic properties of a Ni-rich Nitinol shape memory alloy. *Materials Science and Engineering*. 429: 130-136.
- Ferreira, M, Lanzioti, L, Monteiro, M, Abuhadba, G, et al. 2007. Superficial femoral artery recanalization with self-expanding nitinol stents: long-term follow-up results. *European Journal of Vascular and Endovascular Surgery*. 34: 702-708.

- Fleisch, M and Meier, B. 1999. Management and outcome of stents in 1998: long-term outcome. *Cardiology in Review*. 7: 215-218.
- Ganguly, A, Simons, J, Schneider, A, Keck, B, et al. 2011. In-vivo imaging of femoral artery Nitinol stents for deformation analysis. *Journal of Vascular and Interventional Radiology*. 22: 244-249.
- Henry, M, Amor, M, Ethevenot, G, Henry, I, et al. 1995. Palmaz stent placement in iliac and femoropopliteal arteries: primary and secondary patency in 310 patients with 2-4-year follow-up. *Radiology*. 197: 167-174.
- Hermawan, H, Dubé, D, and Mantovani, D. 2010. Developments in metallic biodegradable stents. *Acta Biomaterialia*. 6: 1693-1697.
- Holmes Jr, DR, Vlietstra, RE, Smith, HC, Vetrovec, GW, et al. 1984. Restenosis after percutaneous transluminal coronary angioplasty (PTCA): a report from the PTCA Registry of the National Heart, Lung, and Blood Institute. *The American Journal of Cardiology*. 53: C77-C81.
- Jaff, MR and Katzen, BT. 2010. Two-year clinical evaluation of the Zilver vascular stent for symptomatic iliac artery disease. *Journal of Vascular and Interventional Radiology*. 21: 1489-1494.
- Jonker, FS, F. Moll, F. Muhs, B. 2008. Dynamic Forces in the SFA and Popliteal Artery During Knee Flexion. *Endovascular Today*.
- Kalmár, G, Hübner, F, Voelker, W, Hutzenlaub, J, et al. 2002. Radial force and wall apposition of balloon-expandable vascular stents in eccentric stenoses: an in vitro evaluation in a curved vessel model. *Journal of Vascular and Interventional Radiology*. 13: 499-508.
- Klein, AJ, Casserly, IP, Messenger, JC, Carroll, JD, et al. 2009a. In vivo 3D modeling of the femoropopliteal artery in human subjects based on x-ray angiography: Methodology and validation. *Medical physics*. 36: 289-311.

- Klein, AJ, James Chen, S, Messenger, JC, Hansgen, AR, et al. 2009b. Quantitative assessment of the conformational change in the femoropopliteal artery with leg movement. *Catheterization and Cardiovascular Interventions*. 74: 787-798.
- Morgan, N. 2004. Medical shape memory alloy applications—the market and its products. *Materials Science and Engineering: A*. 378: 16-23.
- Müller-Hülsbeck, S, Schäfer, PJ, Charalambous, N, Yagi, H, et al. 2010. Comparison of Second-Generation Stents for Application in the Superficial Femoral Artery: An In Vitro Evaluation Focusing on Stent Design. *Journal of Endovascular Therapy*. 17: 767-776.
- Netter. 2006a. The Netter Presenter. *Journal of Electronic Resources in Medical Libraries*. 3: 75-81.
- Netter, FH, Atlas of Human Anatomy, 2006b, Saunders/Elsevier: Philadelphia.
- Ní Ghriallais, R and Bruzzi, M. 2012. Self-expanding stent modelling and radial force accuracy. *Computer Methods in Biomechanics and Biomedical Engineering*. 1-16.
- Nikanorov, A, Smouse, HB, Osman, K, Bialas, M, et al. 2008. Fracture of self-expanding nitinol stents stressed in vitro under simulated intravascular conditions. *Journal of Vascular Surgery*. 48: 435-440.
- O'Brien, B and Bruzzi, M, 1.104 - Shape Memory Alloys for Use in Medicine, in *Comprehensive Biomaterials*, 2011, Elsevier: Oxford.
- Pelton, AR, Dicello, J, and Miyazaki, S. 2000. Optimisation of processing and properties of medical grade Nitinol wire. *Minimally Invasive Therapy & Allied Technologies*. 9: 107-118.

- Pelton, A, Schroeder, V, Mitchell, M, Gong, XY, et al. 2008. Fatigue and durability of Nitinol stents. *Journal of the Mechanical Behavior of Biomedical Materials*. 1: 153-164.
- Scheinert, D, Scheinert, S, Sax, J, Piorkowski, C, et al. 2005. Prevalence and clinical impact of stent fractures after femoropopliteal stenting. *Journal of the American College of Cardiology*. 45: 312-315.
- Schillinger, M, Sabeti, S, Loewe, C, Dick, P, et al. 2006. Balloon angioplasty versus implantation of nitinol stents in the superficial femoral artery. *New England Journal of Medicine*. 354: 1879-1888.
- Schlager, O, Dick, P, Sabeti, S, Amighi, J, et al. 2005. Long-Segment SFA Stenting—The Dark Sides: In-Stent Restenosis, Clinical Deterioration, and Stent Fractures. *Journal of Endovascular Therapy*. 12: 676-684.
- Simons, J, Dalal, A, and Shockey, D. 2010. Load-Deformation Behavior of Nitinol Stents. *Experimental Mechanics*. 50: 835-843.
- Smouse, B, Nikanorov, A, and LaFlash, D. 2005. Biomechanical forces in the femoropopliteal arterial segment. *Endovascular Today*. 4: 60-66.
- Stoeckel, D, Bonsignore, C, and Duda, S. 2002. A survey of stent designs. *Minimally Invasive Therapy & Allied Technologies*. 11: 137-147.
- Stoeckel, D, Pelton, A, and Duerig, T. 2004. Self-expanding nitinol stents: material and design considerations. *European Radiology*. 14: 292-301.
- Versaci, F, Gaspardone, A, Tomai, F, Crea, F, et al. 1997. A comparison of coronary-artery stenting with angioplasty for isolated stenosis of the proximal left anterior descending coronary artery. *New England Journal of Medicine*. 336: 817-822.
- World Health Organisation. Available from: www.who.int

Wood, NB, Zhao, SZ, Zambanini, A, Jackson, M, et al. 2006. Curvature and tortuosity of the superficial femoral artery: a possible risk factor for peripheral arterial disease. *Journal of Applied Physiology*. 101: 1412-1418.

Woods, TC and Marks, AR. 2004. Drug-eluting stents. *Annu. Rev. Med.* 55: 169-178.

Chapter 2. Literature Review

2.1 Blood Vessel Structure and Function

The circulatory system is composed of distribution vessels which allow the transport of blood which carries oxygen, nutrients, waste products and many other substances around the body (Klabunde, 2005, Marieb et al., 2007). The three main types of blood vessels are arteries, veins and capillaries.

Blood is pumped from the heart through arteries and delivered into tissues and organs of the body. The 'cardiac cycle' is the term given to the stage events that occurs in the process of one heart beat to the next, by which the constant flow of blood around the circulatory system is maintained (Fox, 2002). The two major events involved in the process of the cardiac cycle are diastole and systole in which the heart is relaxed and contracted respectively (Fox, 2002). As the blood is pumped away from the heart, flowing through the body, exchange of substances occurs between the blood and the cells of tissues and organs (Klabunde, 2005, Marieb et al., 2007). This exchange occurs through capillaries. The blood is then returned to the heart through veins.

The three different types of blood vessel each have a unique composite structure (Figure 2.1 and Figure 2.2). Arteries and veins are composed of three layers; the tunica adventitia (outermost layer), the tunica media (middle layer) and the tunica intima (innermost layer) (Klabunde, 2005, Marieb et al., 2007). Each of the three layers has a specific function.

The tunica adventitia, made of fibroblasts and connective tissue provides reinforcement and stability to the vessel. The tunica media, also composed of smooth muscle cells (SMCs) embedded in collagen and elastin aids in the support of the vessel. Collagen and elastin fibres are arranged circumferentially allowing the vessel to dilate and contract. The tunica intima is composed of a single layer of endothelial cells (ECs) and is the single interface between the vessel and blood (Dobrin, 2011, Klabunde, 2005, Marieb et al., 2007).

Mechanical characteristics of blood vessels, established by the composite structure of the vessel wall, involve both its passive (fibrous connective tissues; collagen and elastin) and active components (cells and ground substances) (Dobrin, 1978). Together, these facilitate the vessel function.

2.2 Mechanical Behaviour of Arterial Tissue

The mechanical nature of arteries has been investigated extensively (Bergel, 1961a, Bergel, 1961b, Bergel, 1960, Dobrin, 1978, Dobrin, 2011, Fung, 1967, Fung, 1993, Holzapfel et al., 2005, Humphrey, 1995, Humphrey, 2002, Klabunde, 2004, Lally et al., 2004, Peterson et al., 1960). From the major arteries of the heart to the distributing arteries that deliver blood to the various tissues of the body, their composite structure allows rapid distension and contraction of vessels, assisting the drive and return of blood around the circulatory system (Dobrin, 1978). During the cardiac cycle, systole and diastole result in large dimensional changes of all arteries of the circulatory system as the heart pumps blood. This occurs due to the properties of the vessel wall which allow for the control and regulation of pressure within the arterial system (Dobrin, 1978). *In vivo*, arteries exhibit 8-10% oscillation in external diameter and 15% oscillation in internal diameter with each cardiac cycle (Dobrin, 1978). This is controlled by the release in restraint as the surrounding connective tissues that anchor arteries in place retract. As these connective tissues allows the increase in arterial diameter, it is simultaneously controlled by elastin and medial collagen fibres within the vessel walls which provide stiffness and control as the diameter of the vessel increases (Humphrey, 2002). The distensibility of arteries is dependent on the size and location of the vessel. Arteries are more distensible at small dimensions under low pressure (under 100 mmHg), whereas arteries at large dimensions under high pressure are stiffer (over 100 mmHg) (Dobrin, 1978). In general, arteries increase in stiffness with age and with distance from the heart (Dobrin, 1978).

The arterial wall can be treated as an orthotropic, cylindrical body in which all net strains are orientated along three directions; radial, circumferential and longitudinal as shown in Figure 2.3 (Dobrin, 1978, Humphrey, 1995).

The pulsing action of the blood during the cardiac cycle results in pulsatile pressure that acts radially on the inner surface of the vessel wall as blood is pumped, causing radial distension of the vessel wall (Klabunde, 2004). Pulsatile pressure, traditionally expressed in mmHg, typically ranges in value from 120 to 80 mmHg for systolic and diastolic pressures respectively (Klabunde, 2004). This causes

compressive stresses in the radial direction due to the pressurization from blood on the vessel wall (Dobrin, 1978). Pulsatile pressure is affected by the compliance of the artery wall, determined from its elastin and collagen fibres content (Dobrin, 1978). Stiffer arterial tissue with less elastic and more fibrous content cannot distend to the same proportion as tissue with a higher elastic, lower fibrous content.

Tensile hoop strain acts circumferentially through the vessel wall and results from the radial distension of the vessel as it expands and contracts due to pulsatile pressure (Humphrey, 2002). Tensile hoop strain is dependent on the location of the vessel in the circulatory system (Dobrin, 1978). Typically, arteries undergo 5-10% radial distension during the cardiac cycle (Dobrin, 1978). The thickness of the vessel wall is adapted in order to maintain the tensile hoop strain at the required physiologically level dependent on the location of the vessel segment (Klabunde, 2004). Smooth muscle cells of the medial layer of the artery regulate this adaption process.

Arteries typically exhibit length changes in the order of 1% *in vivo* which result in tensile stress in the longitudinal direction (Dobrin, 1978). Constraints from connective tissues and arterial side branches along with longitudinal forces from pressurization stabilise and anchor the arteries in place, reducing longitudinal vessel movement (Dobrin, 1978). With increased age, the stability of the arteries by these mechanisms is reduced, leading to looser, more tortuous vessels (Dobrin, 1978).

As pressure in the arterial system causes distension of the vessel in all three directions, circumferential, longitudinal and radial properties ensure the vessel does not twist as it enlarges in response to increased blood flow volumes of the pumping cycle, keeping strain in the vessel wall to a minimum despite large deformations (Dobrin, 1978).

2.3 Haemodynamic Forces within Arteries

As discussed, vessel expansion during the cardiac cycle that assists blood flow results in stress and strain of the vessel in three directions; radial, circumferential and longitudinal. The pulsatile flow of blood along the surface of vessel wall also creates a haemodynamic force field in which pulsatile pressure and tensile hoop strain play an integral role in the regulation of many cellular processes that maintain a healthy body. However, the tunica intima, the interface between the vessel and blood, composed of a single layer of endothelial cells, is also constantly exposed to another haemodynamic force; wall shear stress (Figure 2.4) (Barakat et al., 2003, Klabunde, 2004).

Wall shear stress is caused by the frictional shear force acting parallel to the artery wall as blood flows through the vessel, along the intimal surface of the endothelial cells (Barakat et al., 2003, Klabunde, 2004). The governing equation of wall shear stress given below in equation (2.1) defines wall shear stress as dependent on the flow rate and viscosity of the blood and the inner diameter of the vessel (assuming an exactly circular lumen and perfectly parabolic velocity profile) (Cheng et al., 2002). As blood flow rate changes, wall shear stress levels also change, therefore wall shear stress is dependent on local geometries of the vessel i.e. curvatures, branches etc. where flow patterns are changed (Chiu et al., 2011, Krams et al., 2005, Pivkin et al., 2005, Prosi et al., 2004). In healthy physiological conditions, wall shear stress is maintained at a healthy level (5 to 30 dyn/cm²) by smooth muscle cells of the arterial wall (activated by endothelial cell responses) which control vasodilation and decrease/increase the vessel diameter and the amount of soluble and insoluble components of the circulating blood (Girerd et al., 1996).

$$\tau_{mean} = \frac{4\mu Q}{\pi r^3} \quad (2.1)$$

Haemodynamic forces can change due to a number of factors including vessel geometry (bifurcations and branches of the arterial system), changes to the diameter of the blood vessel and deformations of the artery. Changes to haemodynamic conditions have been linked with pathologies of the arterial wall

(Asakura et al., 1990, Caro et al., 1971, Chiu et al., 2011, Chiu et al., 1998, Cines et al., 1998, Deplano et al., 2001, Gimbrone, 1995, Gimbrone et al., 2000, Gnasso et al., 1996, Gnasso et al., 1997, Ishida et al., 1997, Kamiya et al., 1984, Kamiya et al., 1980, Kolpakov et al., 1996, Krams et al., 2005, Moore et al., 1999, Nerem et al., 1998, Pedersen et al., 1997, Pivkin et al., 2005, Prosi et al., 2004, Wood et al., 2006). Vascular pathologies are a direct result of changes to haemodynamic force levels (Caro et al., 1971, Gnasso et al., 1996, Gnasso et al., 1997, Pedersen et al., 1997). Vortices and eddy currents appear around vessel branches and bifurcations and other regions of the vasculature where geometry changes due to vessel deformations. The altered flow conditions in these regions effect haemodynamic force levels which induces vascular pathologies. The mechanisms associated with the development of vascular pathologies from changes in haemodynamic forces is explained in detail in Chapter 7.

2.4 Finite Element Modelling of Stents

Finite element modelling was initially developed and used more than 50 years ago within the aerospace industry (Zienkiewicz et al., 2005). Since then, the advancement of computing facilities has allowed finite element modelling to become an important tools in almost all disciplines of engineering (Zienkiewicz et al., 2005).

Finite element modelling has been used for many years to assess the design and performance of stents and it is now a requirement (by the United States Food and Drug Administration – FDA) for the approval of any stent device, to demonstrate its mechanical integrity. Today, finite element models of stents are an important part of the design process. This has led to countless studies presented in the literature of finite element models of stents which analyse the mechanical performance of stents which address many key issues of stent design including the influence of strut thickness, metal to artery surface area, recoil, foreshortening and dogboning after implantation (Carter et al., 1997, David Chua et al., 2004a, De Beule et al., 2006, Duerig et al., 2002, Kastrati et al., 2000, Migliavacca et al., 2002, Rieu et al., 1999, Stoeckel et al., 2004, Walke et al., 2005, Wang et al., 2006).

In recent years finite element models have been developed that focus extensively on stent-artery interactions. These models simulate contact between the artery wall and stent struts and aim to accurately represent the effects of stenting on arterial tissue. These models, along with models that look at the integrity of stent material, have become increasingly popular in assessing the viability of stent designs (Auricchio et al., 2011, Balossino et al., 2008, Capelli et al., 2009, Conti et al., 2009, David Chua et al., 2004b, Early et al., 2009, Gasser et al., 2007, Gastaldi et al., 2010, Gervaso et al., 2008, Holzapfel et al., 2005, Holzapfel et al., 2002, Lally et al., 2005, Liang et al., 2005, Moore et al., 2002, Mortier et al., 2009, Pericevic et al., 2009, Prendergast et al., 2003, Qiu et al., 2000, Rebelo et al., 2006, Timmins et al., 2008, Walke et al., 2005, Wu et al., 2007a, Wu et al., 2007b, Zunino et al., 2009). In 2005, Mackerle presented a bibliographical review of the finite element models and simulations in the realm of cardiovascular mechanics. This included papers, conference proceedings and theses on a range of specific topics including

cardiovascular soft tissue modelling, material properties and blood flow (Mackerle, 2005).

Whilst there has been a large number of investigations focused on computational modelling of coronary stents, there have been fewer studies of self expanding stents and stenting in the femoral artery. It has been shown by Gong et al. that material models developed to replicate the superelastic behaviour of Nitinol stents can accurately captured the behaviour of Nitinol in finite element models (Gong et al., 2004). It was shown in this study that radial resistive force values and mechanical response of a Nitinol stents evaluated experimentally compared well to those predicted in a finite element model.

Applying similar material models for Nitinol material behaviour, a finite element study by Azaouzi et al. (2012) modelled the deployment of a self expanding stent inside an artery which was then subjected to pulsatile loading. Levels of stress and strain in the stent were established that could potentially be used to make estimates for fatigue levels of such a device. The effect of oversizing (difference between the artery inner diameter and nominal stent diameter) was also considered. Results showed that the strain recovery of the stent depended on the amount of oversizing which will in turn affect fatigue life of the stent. Wu et al. (2007a) developed a model of Nitinol stent deployment in an a curved stenotic carotid vessel. Two stent designs (one of which is composed of a higher number of shorter struts than the other) were compared to investigate the influence of stent design on the interactions of the stent and vessel. Results showed that shorter stent struts resulted in higher radial force levels on the artery tissue. Shorter struts also allowed more conformation of the stent with the tortuous vessel geometry (Tepe et al., 2006).

Early et al. (2009) developed a balloon expandable stent-artery interaction model to simulate bending of a stented peripheral artery. Results showed that high stresses occurred at the proximal and distal ends of the stent. In a later study, Early and Kelly (2011) used finite element modelling to compare stent fatigue failure of both Nitinol self expanding stent and stainless steel balloon expandable stents. Deployment of both stents was simulated in a symmetrically reduced idealised model of a peripheral artery, with boundary conditions applied to simulate bending and compression. The study concluded that both bending and compression may

contribute towards stent fracture due to the high levels of strain amplitude predicted within the stent models. At high levels of bending and compression the strain amplitude of Nitinol stents exceeded fatigue failure threshold values. Higher arterial stresses were predicted after bending of stainless steel stented arteries than Nitinol stented arteries. Compression was shown to be the dominant mechanical factor of stent fatigue in the femoral artery, whilst bending was shown to be the most significant factor in the popliteal artery, due to the different levels of *in vivo* loading that exist in different locations of the femoropopliteal artery. This result highlights the need for location specific stent designs in peripheral arteries and in depth understanding of the load cases that exist there. Stent strut thickness was varied to investigate its effect on arterial stresses after bending with results showing that increasing stent strut thickness caused an increase in arterial stresses following stent deployment and arterial bending in comparison to thinner struts.

2.5 Physiological Loading and Deformation Characteristics of the Femoropopliteal Artery

The inherent properties of arterial and the surrounding tissue prevent buckling of the femoral artery allowing it to maintain its function during a range of physiological movements such as knee and hip flexion. Knee flexion is considered as the physiological movement that causes the most amount of deformation to the femoral artery (Nikanorov et al., 2008, Smouse et al., 2005). As the knee flexes, the straight line distance between the hip and calf decreases, meaning the femoral arterial segment will need to shorten in length to prevent buckling of the artery (Smouse et al., 2005). As the knee bends, the artery follows the movement of the leg, inducing a curved shape in the artery (Wensing et al., 1995). This induced curvature and shortening of the vessel results in deformation and loading of the artery characterised as axial compression, radial compression, bending and torsion (Jonker, 2008). Axial compression occurs when the vessel shortens in length, allowed for by the compression of the elastic and collagenous components of the tunica media of the arterial wall (Wensing et al., 1995). Radial compression occurs as the artery lumen changes shape when subjected to combinations of radial compression and bending. This results in a reduction in its cross sectional area. Reduced cross sectional area has implications on blood flow characteristics causing a change in haemodynamic flow conditions due to alterations in lumen shape. Bending or curvature of the artery primarily occurs close to and behind the knee as a result of the flexed knee configuration. Bending also occurs in the distal SFA in order to allow further shortening of the artery when the artery has axially compressed as much as possible with its inherent elastic properties. Torsion or axial twist of the femoral artery is commonly seen with knee flexion due to the position of the artery as it twists behind the knee in a straight leg configuration.

Many groups have investigated the biomechanical environment of the femoral artery, seeking to understand, categorise and quantify the levels of compression, bending and torsion of the vessel. One of the first studies that assessed femoral artery dynamics was that of Vernon et al. (1987). In this study, the alterations of the popliteal artery axis during knee flexion was assessed through post mortem radiological images of lower limbs. The difference in vessel deformation at

various regions along the length of the artery was examined, with more extreme curvatures observed in the upper part of the artery, and less acute curvatures observed in the lower portion of the artery. It was calculated that if the popliteal artery made a harmonious curve, the arterial axis would shorten 25% at 90° knee flexion. It was postulated that curves in the upper part of the artery compensate for the arterial length excess during knee flexion and that this curvature takes place between two points, the adductor canal hiatus proximally and the origin of the anterior tibial artery distally.

The shortening of the artery with knee flexion was also investigated in a later study in 1995 by Wensing et al. (1995). The group hypothesised that a 'length excess' results in the artery, due to the required shortening of the vessel as the knee bends, and that both longitudinal elasticity of the vessel and arterial tortuosity in the adductor canal compensate for this shortening. To investigate this, the group carried out a study on angiographic images of the extended and flexed knees of healthy patients to investigate how the artery copes with length excess that results from knee bending, and to determine how knee flexion influences three dimensional arterial tortuosity and morphology. Analysis of the images showed a major curve in the artery as it followed the movement of the leg during flexion with small consecutive curves observed in the popliteal region of the artery proximal to the knee joint, close to the adductor canal hiatus. The mean radius of these smaller curves was 63mm, with mean angles of 33.5°. It was concluded that 'excess artery' arises during knee flexion, not absorbed through longitudinal elasticity of the artery leading to a concertina effect in the adductor canal and tortuosity of the vessel. It was proposed that as a loss of arterial elasticity occurs with increased age (Mozersky et al., 1972), this may lead to reduced axial compression, increased tortuosity and acute angles in vessel curvature. It was suggested also that curvature of the parts of the artery that passes through the adductor canal is restricted to the shape and limited space of the canal. From a clinical perspective, it was noted that arterial length excess caused during knee flexion, in combination with different physical properties of stented portions of the vessel may lead to buckling in the transition between stented and non-stented vessel segments, leading to unfavourable haemodynamic conditions. Analysis of images of the deformed artery in the coronal and sagittal planes also lead to the conclusion that the configuration of the artery was non-planar and must be

analysed in more than one view. Following these conclusions, and along with increased reports by physicians of stent fractures in the femoral artery (Scheinert et al., 2005, Smouse et al., 2005) it was recognised that there was little understanding of the morphological changes of the femoral artery (in the SFA and popliteal artery) (Scheinert et al., 2005, Smouse et al., 2005), leading to a succession of investigations that aimed to quantify and characterise these changes.

Smouse et al. (2005) carried out a clinical study to evaluate the SFA by imaging cadavers in various positions of hip and knee flexion to simulate walking, stair climbing and sitting to standing movements. Measurements of all positions were performed on both unstented and Nitinol stented vessels. Stents with varying levels of axial rigidity were placed in the superficial femoral and popliteal portions of the vessel. During both hip flexion and knee bending, axial compression (determined by shortening) and vessel bending were quantified (values reported in Table 2.1). In the unstented vessels, bending was mostly observed behind the knee, becoming more exaggerated as hip and knee flexion increased in magnitude. No significant bending was observed in the straight segment of the SFA region of the vessel. Similar to the theory of Wensing et al. (1995), Smouse et al. (2005) concluded that the elastic and collagenous components of the arterial wall allow for axial compression during movement but that once the segment has axially compressed as much as possible, the straight portion of the artery, above the knee, begins to bend taking a waving conformation allowing further shortening of the vessel length. Regarding stented arteries, it was concluded that whilst stent placement provides the required scaffolding of the artery, opening up blockages and preventing elastic recoil of the vessel, it alters its axial rigidity, reducing the arteries ability to shorten as it innately would. As a result, increased bending ensues to allow the required shortening of the artery to occur as the knee flexes. Severe bending can occur with extreme stent rigidity and long stent lengths. It was observed in the angiographic images that unstented artery portions bend in an exaggerated manner adjacent to stented regions (as seen previously in Figure 1.9), which may contribute to vascular injury of the vessel, resulting in intimal hyperplasia and restenosis. This could also result in stress on the stent, leading to stent buckling and fracture. Furthermore, the musculoskeletal forces that surround the vessel and act on the artery also act on the stent. Stents designed for the femoral artery must therefore be

able to withstand this loading. A small number of groups have made efforts to understand and quantify these load levels by analysing three dimensional models based on magnetic resonance angiographic scans. Cheng et al. (2006) carried out a study to quantify *in vivo* deformations of the SFA during maximum knee and hip flexion by analysing eight healthy adults in the straight leg and flexed knee position. Angiographic volume data produced from magnetic resonance images was used to create three dimensional models of the iliofemoral, profunda femoris and descending genicular arteries of each limb of the patients. Centreline spline paths of the three dimensional volumes were then created to enable mathematical quantification of the path dimensions. Arc lengths of the centreline spline were calculated between the two branch points for each body position and each limb to evaluate length change of the vessel. Quantification of vessel twist was determined by evaluating the angle of separation between the profunda femoris and descending genicular branches of the SFA in both body positions. Results of the study are presented in Table 2.1. The data showed that from straight leg to flexed knee positions, the SFA shortened and twisted significantly highlighting the extreme load cases that occur in the SFA of which devices are subjected to. The group followed this up with a second similar study (Cheng et al., 2010) on older subjects (aged 50-70) to investigate the effects of aging on the deformations of the artery. In this second study, length change and twist were evaluated along with bending of the artery, defined by change in vessel curvature (calculated as the inverse of the radius of the best fit circle to the curved vessel). Results (numerically presented in Table 2.1), showed that the SFA deformed more in the distal region of the vessel, perhaps due to less constraint from surrounding muscle groups in this region. Comparing the deformation results of the older patients of this study with the younger patients of their previous study, Cheng et al. reported that in comparison to younger subjects (where SFAs remained relatively straight with hip and knee flexion), older subjects exhibits substantial curvature and buckling with flexion. This may be due to loss of arterial elasticity with age. In the computational approach detailed in this thesis, vessel deformation was quantified using methods developed by the group following their initial study (Choi et al., 2009).

A similar study to Cheng et al. was carried out by Klein et al. (2009a, 2009b). In their initial study, the group presented methods used to develop three dimensional

models of the entire femoropopliteal artery *in vivo* using angiography. Models were developed by applying three dimensional modelling algorithms to angiographic images of the femoropopliteal arteries of nine patients in the straight leg and bent knee positions. The three dimensional model vessels created were validated by comparing two dimensional views of models with the two dimensional angiographic images of the corresponding patient. The models developed were then used in a further study that quantified changes in length, curvature, tortuosity, twist angle and flexion angle of the artery from the straight to bent knee positions (Figure 2.5). Vessel length was calculated by measuring the centreline arc of the model vessel. Vessel curvatures were measured by the inverse of the radius of the curves, calculated at 0.5 mm intervals along the vessel length. Vessel torsion was defined as the change in position of the vessel in the z-axis. Twist angle was quantified by measuring the angle of separation between the major branch vessels that stem from the femoropopliteal artery. Flexion angles in the vessels were calculated as the difference in the angle measured at flexion points in the artery (the same point in the straight and bent knee positions). Only differences in angle of more than 15° were considered as flexion angles. Their results (numerically presented in Table 2.1), showed that significant changes in length, curvature and twist depended on specific artery location. More modest changes in length and twist occurred in the SFA region of the vessel. Also significant changes were observed in the popliteal artery region of the vessel.

The results of these studies have provided lots of relevant data regarding the highly complex deformation characteristics of the femoral artery which are often responsible for stent failure. Whilst these studies have quantified deformation characteristics, there are currently no investigations that have linked deformation characteristics of the femoral artery to levels of stress and strain within the vascular tissue. Due to this lack of investigation, stent design parameters of stiffness/flexibility, diameter, length, geometry and the altered deformation characteristics of the artery as a result of the location of stent placement cannot be thoroughly investigated before device implantation in a clinical setting. As previously mentioned, the musculoskeletal forces that surround the vessel causing deformation patterns also act on the stent and therefore, stents designed for the

femoral artery must be able to withstand this loading. In order to design such a stent, load levels must be thoroughly understood.

2.6 Tables and Figures

Year	Group	Research	Compression	Bending	Curvature	Torsion
1995	Wensing et al.	Deformations of the unstented femeropopliteal region observed using magnetic resonance angiography of subjects in the sitting position	-	33.5°	63mm	-
2004	Denison	Deformations of the stented femeropopliteal region of cadavers using angiographic assessment	<u>Single stent:</u> 70/20 [†] : 5% 90/90 [†] : 7% <u>Overlapping stents:</u> 90/90 [†] : 10%	<u>Overlapping stents:</u> 70/20 [†] : 48° 90/90 [†] : 69°	-	-
2005	Smouse et al.	Deformations of the unstented superficial femoral and popliteal artery observed using angiography of cadavers in the sitting position	<u>Mid SFA:</u> 70/20 [†] : 5% 90/90 [†] : 10% <u>Distal SFA:</u> 70/20 [†] : 14% 90/90 [†] : 23% <u>Popliteal artery:</u> 70/20 [†] : 9% 90/90 [†] : 14%	<u>SFA:</u> 90/90 [†] : 63°	-	-
2005	Smouse et al.	Deformations of the stented popliteal artery of cadavers in the sitting position observed using angiography	<u>56mm stents:</u> 70/20 [†] : 4% 90/90 [†] : 11% <u>100mm stents:</u> 70/20 [†] : 7% 90/90 [†] : 14%	<u>100mm stents:</u> 90/90 [†] : 69°	-	-

2006	Cheng et al.	Deformations of the unstented femeropopliteal artery observed using magnetic resonance angiography of subjects in the supine position	13±11%	-	-	2.8±1.7°/cm
2008	Nikanorov et al.	Deformations of the unstented superficial femoral artery of cadavers in the using magnetic resonance angiography	<u>Mid SFA:</u> 70/20 [†] : 5±4% 90/90 [†] : 9±5% <u>Distal SFA:</u> 70/20 [†] : 14±5% 90/90 [†] : 23±2% <u>Popliteal artery:</u> 70/20 [†] : 9±5% 90/90 [†] : 14±3%	-	-	-
2008	Nikanorov et al.	Deformations of the stented superficial femoral artery of cadavers in the using magnetic resonance angiography	<u>Mid SFA:</u> 70/20 [†] : 3% 90/90 [†] : 3% <u>Distal SFA:</u> 70/20 [†] : 4% 90/90 [†] : 6% <u>Popliteal artery:</u> 70/20 [†] : 6% 90/90 [†] : 11%	<u>Mid SFA:</u> 70/20 [†] : 3° 90/90 [†] : 4° <u>Distal SFA:</u> 70/20 [†] : 11° 90/90 [†] : 15° <u>Popliteal artery:</u> 70/20 [†] : 33° 90/90 [†] : 54°	-	-

2009	Choi et al.	Deformations of the unstented superficial femoral artery of patients in the straight leg and supine position using magnetic resonance angiography	8.8±4.4%	-	0.039 mm ⁻¹	0.8±0.4°/mm
2010	Cheng et al.	Deformations of the unstented superficial femoral artery of patients in the straight leg and supine position using magnetic resonance angiography	<u>Top SFA:</u> 5.9±3% <u>Mid SFA:</u> 6.7±2.1% <u>Bottom SFA:</u> 8.1±2.0% <u>Top and Middle SFA:</u> 6.3±2.2% <u>Middle and Bottom SFA:</u> 7.4±1.6% <u>Entire SFA:</u> 6.9±1.9%	-	<u>Top SFA:</u> 0.15±0.06cm ⁻¹ <u>Mid SFA:</u> 0.09±0.07cm ⁻¹ <u>Bottom SFA:</u> 0.41±0.22cm ⁻¹ <u>Top and Middle SFA:</u> 0.15±0.06cm ⁻¹ <u>Middle and Bottom SFA:</u> 0.41±0.22cm ⁻¹ <u>Entire SFA:</u> 0.41±0.22cm ⁻¹	<u>Top SFA:</u> 1.3±0.8°/cm <u>Mid SFA:</u> 1.8±1.1°/cm <u>Bottom SFA:</u> 2.1±1.3°/cm <u>Top and Middle SFA:</u> 1.5±1.0°/cm <u>Middle and Bottom SFA:</u> 1.9±1.2°/cm <u>Entire SFA:</u> 1.7±1.1°/cm

†Denotes hip angle/knee angle position of walking (70°/20°) and sitting position (90°/90°)

Table 2.1 Summary of reported physiological deformation levels of the femoral artery.

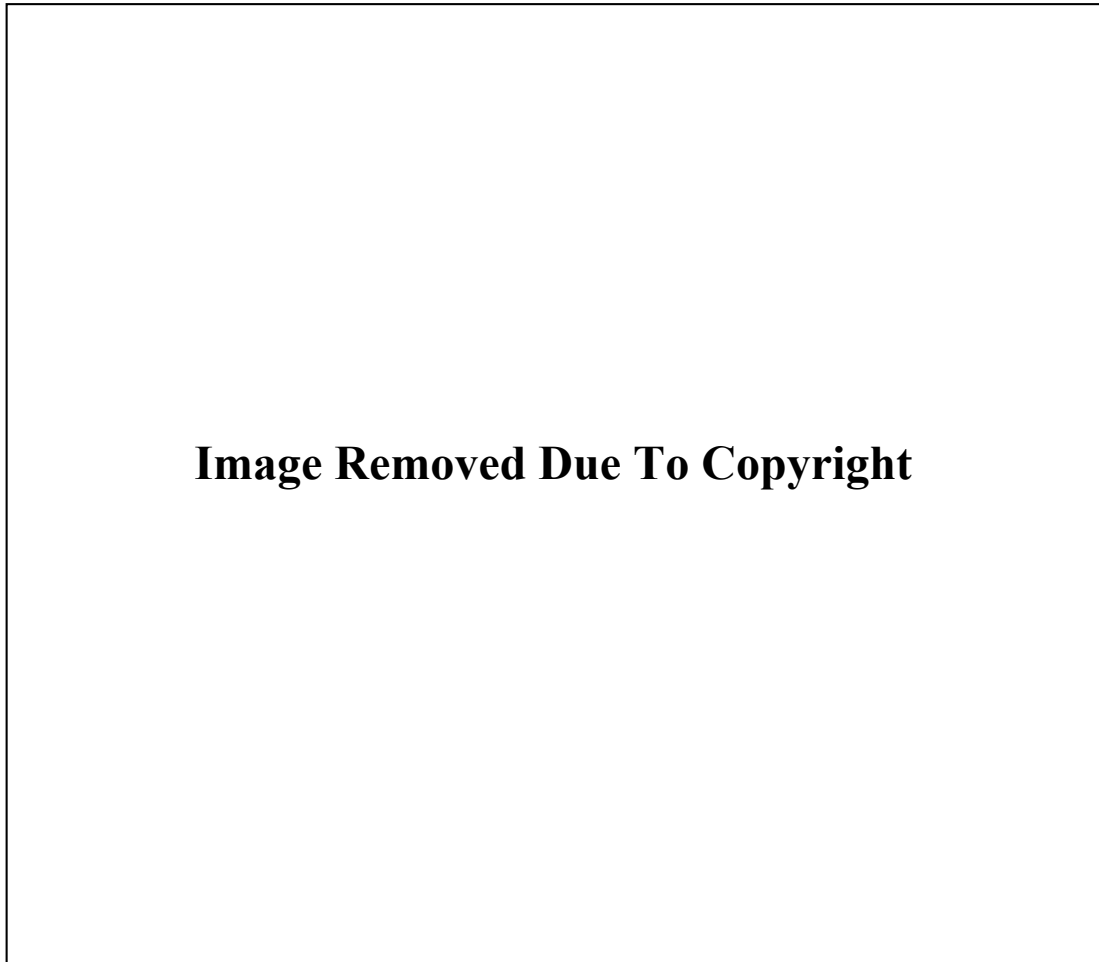


Figure 2.1 Schematic drawings of blood vessels (Pearson(a)).

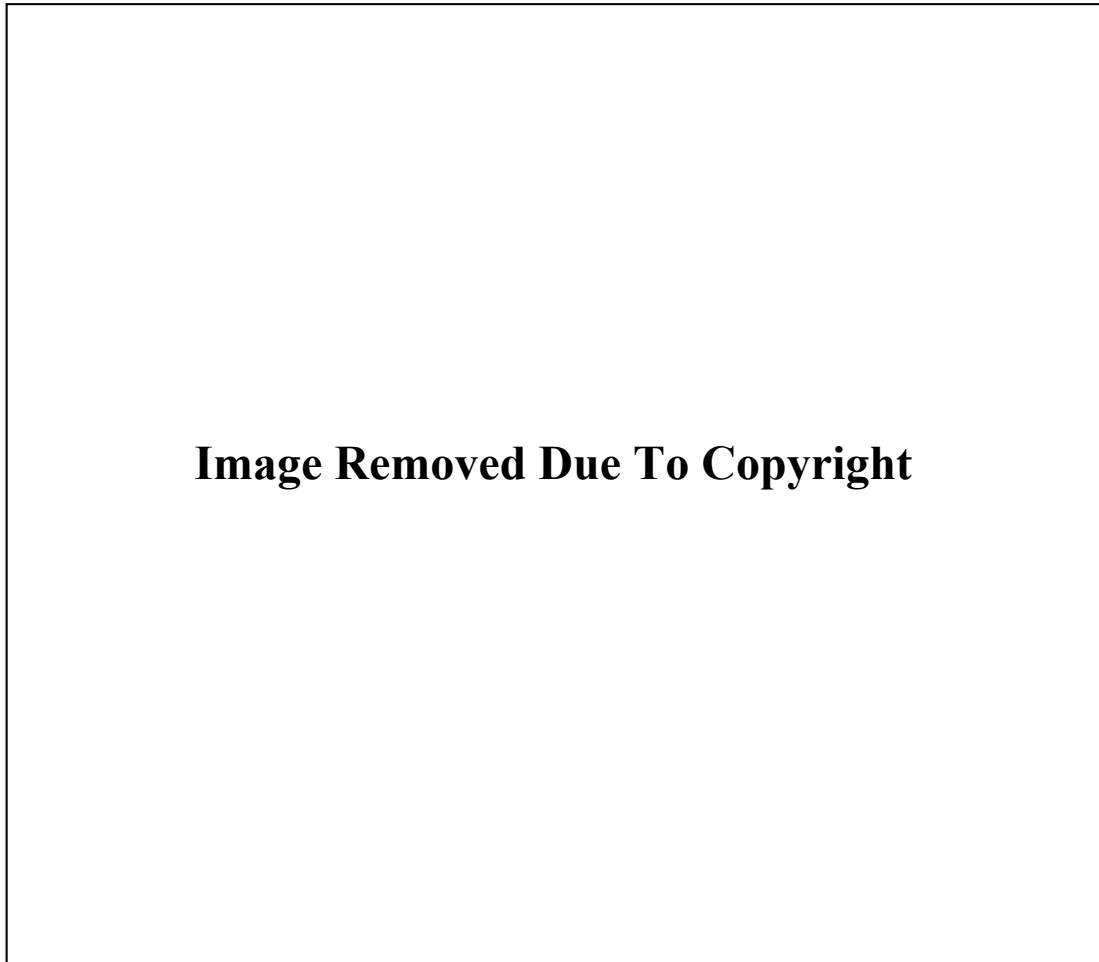


Figure 2.2 Comparison of the structure of an artery and vein (Pearson(b)).

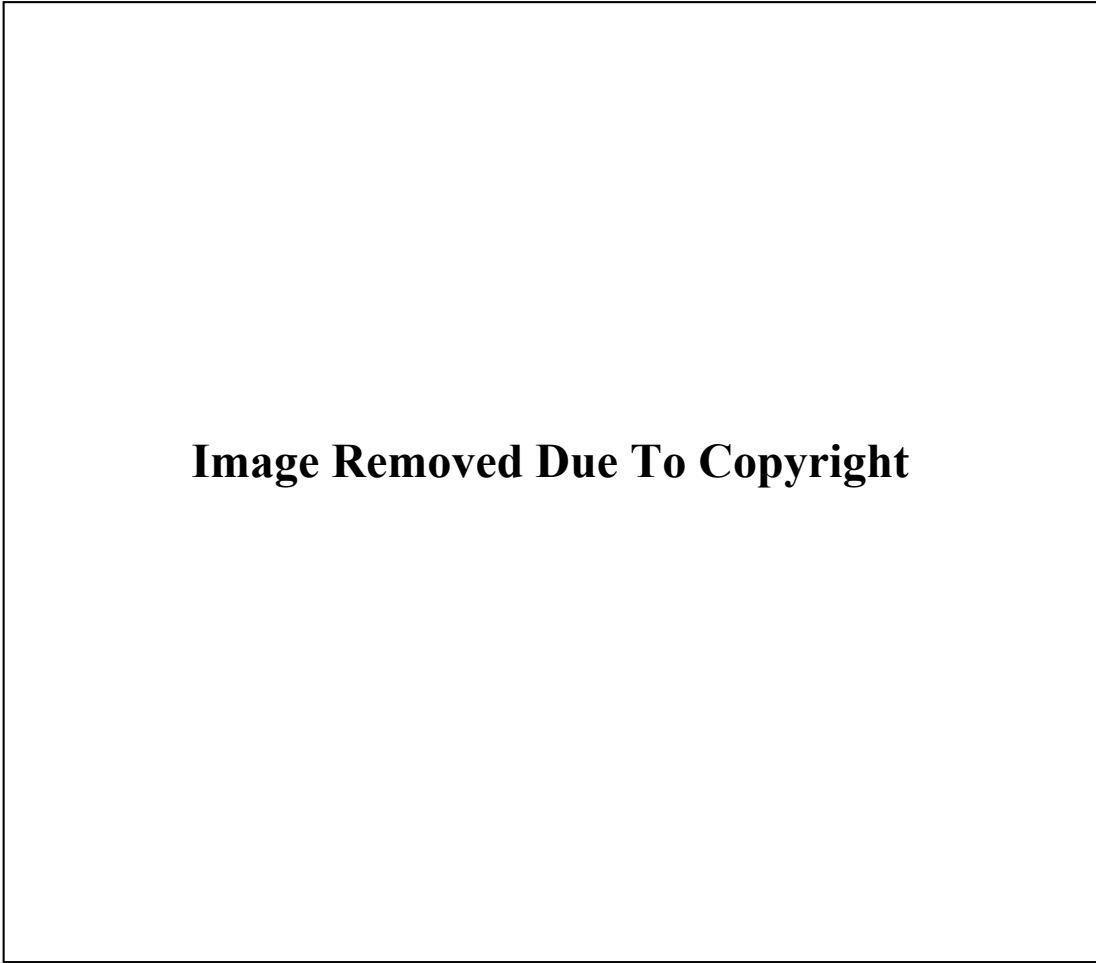


Image Removed Due To Copyright

Figure 2.3 Directions of the stress and strain in an arterial segment. Circumferential (θ) and longitudinal (z) stress/strains are tensile as the vessel distends in these directions with pressure. Radial (r) stress/strains are compressive as the vessel wall narrows with pressure. (Dobrin, 1978).

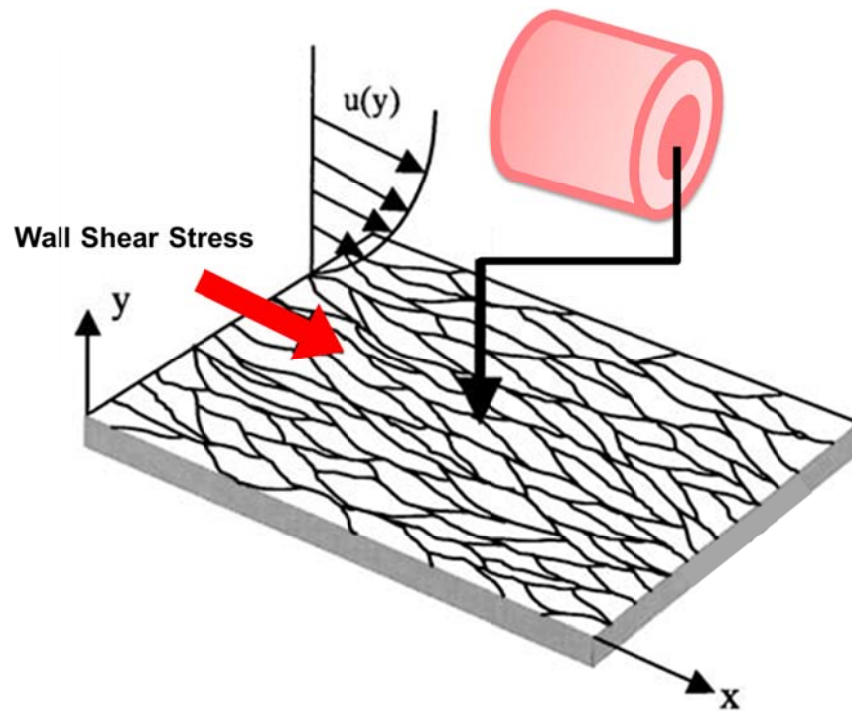


Figure 2.4 Wall shear stress experienced by endothelial cells on the intimal layer of the artery (Barakat et al., 2003).

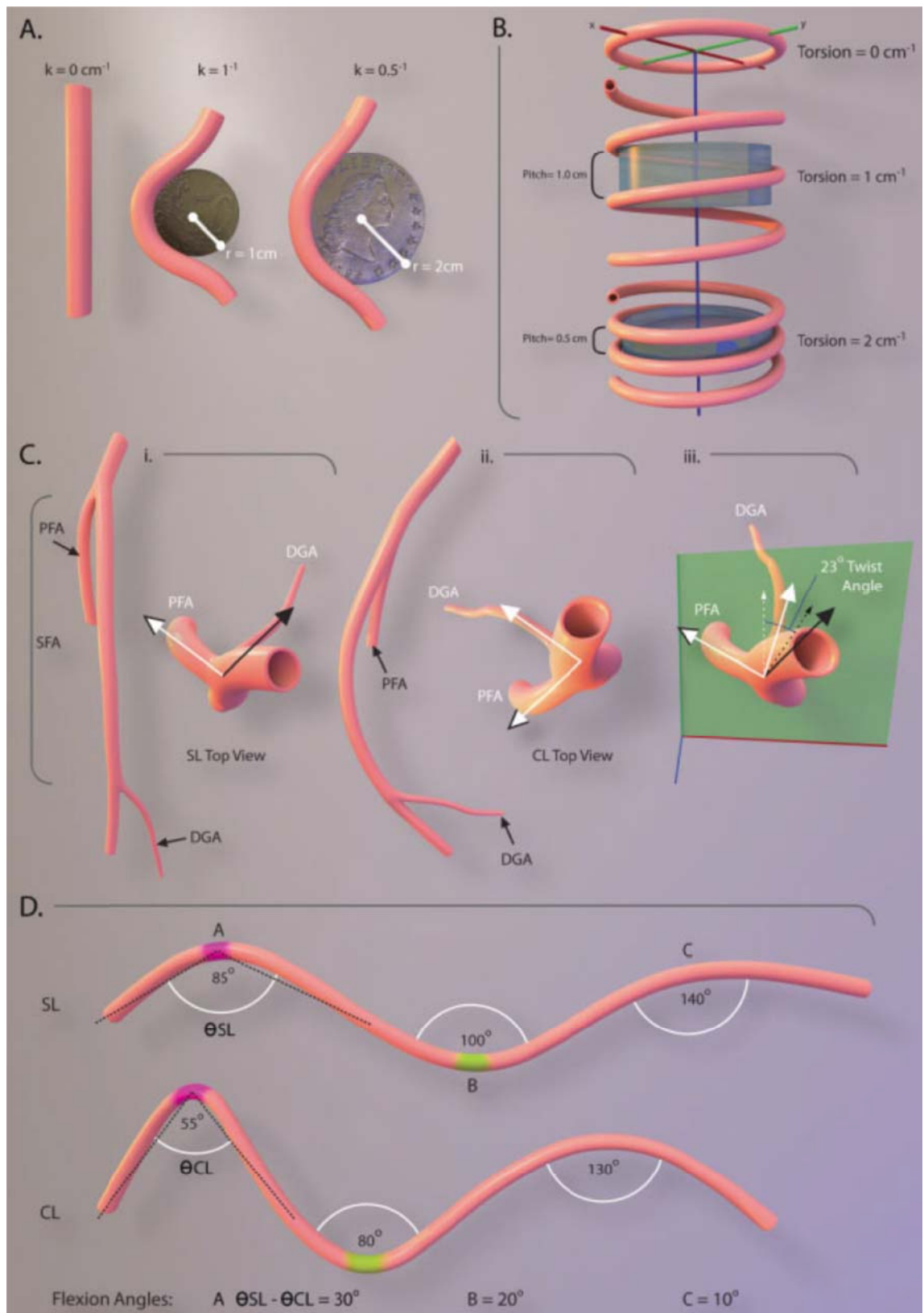


Figure 2.5 Methods of quantitative assessment of arterial deformations of curvature (A), torsion(B), twist angle (C) and flexion angle (D) reproduced from Klein et al. (2009b).

2.7 References

- Asakura, T and Karino, T. 1990. Flow patterns and spatial distribution of atherosclerotic lesions in human coronary arteries. *Circulation Research*. 66: 1045-1066.
- Auricchio, F, Conti, M, De Beule, M, De Santis, G, et al. 2011. Carotid artery stenting simulation: From patient-specific images to finite element analysis. *Medical engineering & physics*. 33: 281-289.
- Azaouzi, M, Makradi, A, and Belouettar, S. 2012. Deployment of a self-expanding stent inside an artery: A finite element analysis. *Materials & Design*. 41: 410-420.
- Balossino, R, Gervaso, F, Migliavacca, F, and Dubini, G. 2008. Effects of different stent designs on local hemodynamics in stented arteries. *Journal of Biomechanics*. 41: 1053-1061.
- Barakat, AI and Lieu, DK. 2003. Differential responsiveness of vascular endothelial cells to different types of fluid mechanical shear stress. *Cell biochemistry and biophysics*. 38: 323-343.
- Bergel, D. 1961a. The dynamic elastic properties of the arterial wall. *The Journal of physiology*. 156: 458-469.
- Bergel, D. 1961b. The static elastic properties of the arterial wall. *The Journal of physiology*. 156: 445-457.
- Bergel, DH. 1960. The visco-elastic properties of the arterial wall.
- Capelli, C, Gervaso, F, Petrini, L, Dubini, G, et al. 2009. Assessment of tissue prolapse after balloon-expandable stenting: influence of stent cell geometry. *Medical engineering & physics*. 31: 441-447.

- Caro, C, Fitz-Gerald, J, and Schroter, R. 1971. Atheroma and arterial wall shear observation, correlation and proposal of a shear dependent mass transfer mechanism for atherogenesis. *Proceedings of the Royal Society of London. Series B. Biological Sciences.* 177: 109-133.
- Carter, A, Scott, D, Bailey, L, Jones, R, et al. 1997. Stent design: in the “ends” it matters. *Circulation.* 96: 1-402.
- Cheng, CP, Choi, G, Herfkens, RJ, and Taylor, CA. 2010. The effect of aging on deformations of the superficial femoral artery resulting from hip and knee flexion: potential clinical implications. *Journal of Vascular and Interventional Radiology.* 21: 195-202.
- Cheng, CP, Parker, D, and Taylor, CA. 2002. Quantification of Wall Shear Stress in Large Blood Vessels Using Lagrangian Interpolation Functions with Cine Phase-Contrast Magnetic Resonance Imaging. *Annals of Biomedical Engineering.* 30: 1020-1032.
- Cheng, CP, Wilson, NM, Hallett, RL, Herfkens, RJ, et al. 2006. In vivo MR angiographic quantification of axial and twisting deformations of the superficial femoral artery resulting from maximum hip and knee flexion. *Journal of Vascular and Interventional Radiology.* 17: 979-987.
- Chiu, J-J and Chien, S. 2011. Effects of Disturbed Flow on Vascular Endothelium: Pathophysiological Basis and Clinical Perspectives. *Physiological Reviews.* 91: 327-387.
- Chiu, JJ, Wang, D, Chien, S, Skalak, R, et al. 1998. Effects of disturbed flow on endothelial cells. *Journal of Biomechanical Engineering.* 120: 2-8.
- Choi, G, Cheng, CP, Wilson, NM, and Taylor, CA. 2009. Methods for quantifying three-dimensional deformation of arteries due to pulsatile and nonpulsatile forces: implications for the design of stents and stent grafts. *Annals of Biomedical Engineering.* 37: 14-33.

- Cines, DB, Pollak, ES, Buck, CA, Loscalzo, J, et al. 1998. Endothelial Cells in Physiology and in the Pathophysiology of Vascular Disorders. *Blood*. 91: 3527-3561.
- Conti, M, Auricchio, F, De Beule, M, and Verheghe, B. Numerical simulation of Nitinol peripheral stents: from laser-cutting to deployment in a patient specific anatomy. in 8th European Symposium on Martensitic Transformations. 2009. Prague, Czech Republic.
- David Chua, S, MacDonald, B, and Hashmi, M. 2004a. Effects of varying slotted tube (stent) geometry on its expansion behaviour using finite element method. *Journal of Materials Processing Technology*. 155: 1764-1771.
- David Chua, S, MacDonald, B, and Hashmi, M. 2004b. Finite element simulation of slotted tube (stent) with the presence of plaque and artery by balloon expansion. *Journal of Materials Processing Technology*. 155: 1772-1779.
- De Beule, M, Mortier, P, Segers, P, Carlier, S, et al. 2006. Finite element simulation of the free expansion of the Cypher stent crimped on a tri-folded balloon. *Journal of Biomechanics*. 39: S297-S297.
- Denison, A. Axial and bending fatigue resistance of nitinol stents. in International Conference on Shape Memory and Superelastic Technologies. 2004. Baden-Baden, Germany.
- Deplano, V, Bertolotti, C, and Boiron, O. 2001. Numerical simulations of unsteady flows in a stenosed coronary bypass graft. *Medical and Biological Engineering and Computing*. 39: 488-499.
- Dobrin, PB. 1978. Mechanical Properties of Arteries. *Physiological Reviews*. 58: 397-460.
- Dobrin, PB, Vascular Mechanics, in *Comprehensive Physiology*, 2011, John Wiley & Sons, Inc.

- Duerig, T and Wholey, M. 2002. A comparison of balloon-and self-expanding stents. *Minimally Invasive Therapy & Allied Technologies*. 11: 173-178.
- Early, M and Kelly, DJ. 2011. The consequences of the mechanical environment of peripheral arteries for nitinol stenting. *Medical and Biological Engineering and Computing*. 49: 1279-1288.
- Early, M, Lally, C, Prendergast, PJ, and Kelly, DJ. 2009. Stresses in peripheral arteries following stent placement: a finite element analysis. *Computer Methods in Biomechanics and Biomedical Engineering*. 12: 25-33.
- Fox, S, *Human Physiology*, 2002, Mc Graw Hill: London.
- Fung, Y. 1967. Elasticity of soft tissues in simple elongation. *American Journal of Physiology*. 213: 1532-1544.
- Fung, Y, *Biomechanics: mechanical properties of living tissues*, 1993, Springer: New York.
- Gasser, TC and Holzapfel, GA. 2007. Modeling plaque fissuring and dissection during balloon angioplasty intervention. *Annals of Biomedical Engineering*. 35: 711-723.
- Gastaldi, D, Morlacchi, S, Nichetti, R, Capelli, C, et al. 2010. Modelling of the provisional side-branch stenting approach for the treatment of atherosclerotic coronary bifurcations: effects of stent positioning. *Biomechanics and Modeling in Mechanobiology*. 9: 551-561.
- Gervaso, F, Capelli, C, Petrini, L, Lattanzio, S, et al. 2008. On the effects of different strategies in modelling balloon-expandable stenting by means of finite element method. *Journal of Biomechanics*. 41: 1206-1212.

- Gimbrone, MA. 1995. Vascular endothelium: an integrator of pathophysiologic stimuli in atherosclerosis. *The American Journal of Cardiology*. 75: 67B-70B.
- Gimbrone, MA, Topper, JN, Nagel, T, Anderson, KR, et al. 2000. Endothelial Dysfunction, Hemodynamic Forces, and Atherogenesis. *Annals of the New York Academy of Sciences*. 902: 230-240.
- Girerd, X, London, G, Boutouyrie, P, Mourad, JJ, et al. 1996. Remodeling of the radial artery in response to a chronic increase in shear stress. *Hypertension*. 27: 799-803.
- Gnasso, A, Carallo, C, Irace, C, Spagnuolo, V, et al. 1996. Association between intima-media thickness and wall shear stress in common carotid arteries in healthy male subjects. *Circulation*. 94: 3257-3262.
- Gnasso, A, Irace, C, Carallo, C, De Franceschi, MS, et al. 1997. In vivo association between low wall shear stress and plaque in subjects with asymmetrical carotid atherosclerosis. *Stroke*. 28: 993-998.
- Gong, XY, Pelton, AR, Duerig, TW, Rebelo, N, et al. Finite element analysis and experimental evaluation of superelastic Nitinol stent. in *International Conference on Shape Memory and Superelastic Technologies*. 2004. Pacific Grove, California, USA.
- Holzapfel, GA, Sommer, G, Gasser, CT, and Regitnig, P. 2005. Determination of layer-specific mechanical properties of human coronary arteries with non atherosclerotic intimal thickening and related constitutive modeling. *American Journal of Physiology - Heart and Circulatory Physiology*. 289: H2048-H2058.
- Holzapfel, GA, Stadler, M, and Schulze-Bauer, CAJ. 2002. A Layer-Specific Three-Dimensional Model for the Simulation of Balloon Angioplasty using

-
- Magnetic Resonance Imaging and Mechanical Testing. *Annals of Biomedical Engineering*. 30: 753-767.
- Humphrey, JD. 1995. Mechanics of the arterial wall: review and directions. *Critical Reviews in Biomedical Engineering*. 23: 1-162.
- Humphrey, JD, *Cardiovascular solid mechanics: cells, tissues, and organs*, 2002, Springer Verlag: New York.
- Ishida, T, Takahashi, M, Corson, MA, and Berk, BC. 1997. Fluid Shear Stress: Mediated Signal Transduction: How Do Endothelial Cells Transduce Mechanical Force into Biological Responses? *Annals of the New York Academy of Sciences*. 811: 12-24.
- Jonker, FS, F. Moll, F. Muhs, B. 2008. Dynamic Forces in the SFA and Popliteal Artery During Knee Flexion. *Endovascular Today*.
- Kamiya, A, Bukhari, R, and Togawa, T. 1984. Adaptive regulation of wall shear stress optimizing vascular tree function. *Bulletin of mathematical biology*. 46: 127-137.
- Kamiya, A and Togawa, T. 1980. Adaptive regulation of wall shear stress to flow change in the canine carotid artery. *American Journal of Physiology-Heart and Circulatory Physiology*. 239: H14-H21.
- Kastrati, A, Dirschinger, J, Boekstegers, P, Elezi, S, et al. 2000. Influence of stent design on 1-year outcome after coronary stent placement: A randomized comparison of five stent types in 1,147 unselected patients. *Catheterization and Cardiovascular Interventions*. 50: 290-297.
- Klabunde, RE, *Cardiovascular physiology concepts*, 2004, Lippincott Williams & Wilkins: Philadelphia.

- Klabunde, RE, Cardiovascular physiology concepts, 2005, Lippincott Williams & Wilkins: Philadelphia.
- Klein, AJ, Casserly, IP, Messenger, JC, Carroll, JD, et al. 2009a. In vivo 3D modeling of the femoropopliteal artery in human subjects based on x-ray angiography: Methodology and validation. *Medical physics*. 36: 289-311.
- Klein, AJ, James Chen, S, Messenger, JC, Hansgen, AR, et al. 2009b. Quantitative assessment of the conformational change in the femoropopliteal artery with leg movement. *Catheterization and Cardiovascular Interventions*. 74: 787-798.
- Kolpakov, V, Polishchuk, R, Bannykh, S, Rekhter, M, et al. 1996. Atherosclerosis-prone branch regions in human aorta: microarchitecture and cell composition of intima. *Atherosclerosis*. 122: 173-189.
- Krams, R, Bambi, G, Guidi, F, Helderman, F, et al. 2005. Effect of vessel curvature on Doppler derived velocity profiles and fluid flow. *Ultrasound in Medicine & Biology*. 31: 663-671.
- Lally, C, Dolan, F, and Prendergast, P. 2005. Cardiovascular stent design and vessel stresses: a finite element analysis. *Journal of Biomechanics*. 38: 1574-1581.
- Lally, C, Reid, A, and Prendergast, P. 2004. Elastic behavior of porcine coronary artery tissue under uniaxial and equibiaxial tension. *Annals of Biomedical Engineering*. 32: 1355-1364.
- Liang, D, Yang, D, Qi, M, and Wang, W. 2005. Finite element analysis of the implantation of a balloon-expandable stent in a stenosed artery. *International Journal of Cardiology*. 104: 314-318.
- Mackerle, J. 2005. Finite element modelling and simulations in cardiovascular mechanics and cardiology: A bibliography 1993–2004. *Computer Methods in Biomechanics and Biomedical Engineering*. 8: 59-81.

- Marieb, EN and Hoehn, K, Human anatomy & physiology, 2007, Pearson Education: London.
- Migliavacca, F, Petrini, L, Colombo, M, Auricchio, F, et al. 2002. Mechanical behavior of coronary stents investigated through the finite element method. *Journal of Biomechanics*. 35: 803-811.
- Moore, J, Steinman, D, Prakash, S, Johnston, K, et al. 1999. A numerical study of blood flow patterns in anatomically realistic and simplified end-to-side anastomoses. *Journal of Biomechanical Engineering*. 121: 265-272.
- Moore, JE and Berry, JL. 2002. Fluid and solid mechanical implications of vascular stenting. *Annals of Biomedical Engineering*. 30: 498-508.
- Mortier, P, De Beule, M, Van Loo, D, Verheghe, B, et al. 2009. Finite element analysis of side branch access during bifurcation stenting. *Medical engineering & physics*. 31: 434-440.
- Mozersky, DJ, Sumnfr, DS, Hokanson, DE, and Strandness JR, DE. 1972. Transcutaneous measurement of the elastic properties of the human femoral artery. *Circulation*. 46: 948-955.
- Nerem, R, Alexander, R, Chappell, D, Medford, R, et al. 1998. The study of the influence of flow on vascular endothelial biology. *The American journal of the medical sciences*. 316: 169-175.
- Nikanorov, A, Smouse, HB, Osman, K, Bialas, M, et al. 2008. Fracture of self-expanding nitinol stents stressed in vitro under simulated intravascular conditions. *Journal of Vascular Surgery*. 48: 435-440.
- Pearson (a) Structure of Blood Vessels. Available from: www.studentconsult.com

- Pearson (b) A Comparison of a Typical Artery and a Typical Vein. Available from: www.studentconsult.com
- Pedersen, E, Kristensen, I, and Yoganathan, A. 1997. Wall shear stress and early atherosclerotic lesions in the abdominal aorta in young adults. *European Journal of Vascular and Endovascular Surgery*. 13: 443-451.
- Pericevic, I, Lally, C, Toner, D, and Kelly, DJ. 2009. The influence of plaque composition on underlying arterial wall stress during stent expansion: the case for lesion-specific stents. *Medical engineering & physics*. 31: 428-433.
- Peterson, LH, Jensen, RE, and Parnell, J. 1960. Mechanical properties of arteries in vivo. *Circulation Research*. 8: 622-639.
- Pivkin, IV, Richardson, PD, Laidlaw, DH, and Karniadakis, GE. 2005. Combined effects of pulsatile flow and dynamic curvature on wall shear stress in a coronary artery bifurcation model. *Journal of Biomechanics*. 38: 1283-1290.
- Prendergast, P, Lally, C, Daly, S, Reid, A, et al. 2003. Analysis of prolapse in cardiovascular stents: a constitutive equation for vascular tissue and finite-element modelling. *Journal of Biomechanical Engineering*. 125: 692-699.
- Prosi, M, Perktold, K, Ding, Z, and Friedman, MH. 2004. Influence of curvature dynamics on pulsatile coronary artery flow in a realistic bifurcation model. *Journal of Biomechanics*. 37: 1767-1775.
- Qiu, Y and Tarbell, JM. 2000. Numerical simulation of pulsatile flow in a compliant curved tube model of a coronary artery. *Journal of Biomechanical Engineering*. 122: 77-85.
- Rebelo, N, Prabhu, S, Feezor, C, and Denison, A. Deployment of a Self-Expanding Stent in an Artery. in *International Conference on Shape Memory and Superelastic Technologies*. 2006. Baden-Baden, Germany.

- Rieu, R, Barragan, P, Masson, C, Fuseri, J, et al. 1999. Radial force of coronary stents: a comparative analysis. *Catheterization and Cardiovascular Interventions*. 46: 380-391.
- Scheinert, D, Scheinert, S, Sax, J, Piorkowski, C, et al. 2005. Prevalence and clinical impact of stent fractures after femoropopliteal stenting. *Journal of the American College of Cardiology*. 45: 312-315.
- Smouse, B, Nikanorov, A, and LaFlash, D. 2005. Biomechanical forces in the femoropopliteal arterial segment. *Endovascular Today*. 4: 60-66.
- Stoeckel, D, Pelton, A, and Duerig, T. 2004. Self-expanding nitinol stents: material and design considerations. *European Radiology*. 14: 292-301.
- Tepe, G, Muschick, P, Laule, M, Reddig, F, et al. 2006. Prevention of carotid artery restenosis after sirolimus-coated stent implantation in pigs. *Stroke*. 37: 492-494.
- Timmins, LH, Meyer, CA, Moreno, MR, and Moore, JE. 2008. Mechanical modeling of stents deployed in tapered arteries. *Annals of Biomedical Engineering*. 36: 2042-2050.
- Vernon, P, Delattre, J, Johnson, E, Palot, J, et al. 1987. Dynamic modifications of the popliteal arterial axis in the sagittal plane during flexion of the knee. *Surgical and Radiologic Anatomy*. 9: 37-41.
- Walke, W, Paszenda, Z, and Filipiak, J. 2005. Experimental and numerical biomechanical analysis of vascular stent. *Journal of Materials Processing Technology*. 164: 1263-1268.
- Wang, WQ, Liang, DK, Yang, DZ, and Qi, M. 2006. Analysis of the transient expansion behavior and design optimization of coronary stents by finite element method. *Journal of Biomechanics*. 39: 21-32.

- Wensing, P, Scholten, F, Buijs, P, Hartkamp, M, et al. 1995. Arterial tortuosity in the femoropopliteal region during knee flexion: a magnetic resonance angiographic study. *Journal of Anatomy*. 187: 133-139.
- Wood, NB, Zhao, SZ, Zambanini, A, Jackson, M, et al. 2006. Curvature and tortuosity of the superficial femoral artery: a possible risk factor for peripheral arterial disease. *Journal of Applied Physiology*. 101: 1412-1418.
- Wu, W, Qi, M, Liu, XP, Yang, DZ, et al. 2007a. Delivery and release of nitinol stent in carotid artery and their interactions: A finite element analysis. *Journal of Biomechanics*. 40: 3034-3040.
- Wu, W, Wang, WQ, Yang, DZ, and Qi, M. 2007b. Stent expansion in curved vessel and their interactions: A finite element analysis. *Journal of Biomechanics*. 40: 2580-2585.
- Zienkiewicz, OC and Taylor, RL, *The finite element method for solid and structural mechanics*, 2005, Butterworth-Heinemann: Oxford.
- Zunino, P, D'Angelo, C, Petrini, L, Vergara, C, et al. 2009. Numerical simulation of drug eluting coronary stents: mechanics, fluid dynamics and drug release. *Computer Methods in Applied Mechanics and Engineering*. 198: 3633-3644.

Chapter 3. Finite Element Theory and Formulations

Numerous constitutive formulations have been developed that allow materials under complex loading conditions to be modelled while accurately capturing their mechanical behaviour using the finite element method. In this thesis, in order to model the mechanical behaviour of Nitinol self expanding stents, the femoral artery, bones and soft tissues of the leg, a number of constitutive formulations are implemented using modules available in the commercial finite element solver Abaqus. Mechanical behaviours are modelled using continuum based constitutive equations which describe the response of a material due to an applied load or specific condition of interest, requiring the principles of continuum mechanics and large deformation kinematics. (Humphrey, 2003). The theoretical formulations employed in this work, directly used in finite element modelling are described in this chapter.

3.1 Continuum Mechanics

3.1.1 Notation

An introduction to the notation used in the current chapter is presented for clarity. As regards notation, capital letters are used for tensors and matrices and small letters are used for vectors. Bold type face font is denoted for vectors, tensors and matrices and their component parts are shown in italics. Tensors and matrices are given capital letters while vectors are given lowercase letters. Index notation is used to illustrate manipulation of these quantities. For index notation a repeated index implies a summation. The coordinate system uses the axes x_1 , x_2 and x_3 or x_i where $i = 1, 2, 3$ (summation over values of the indices from 1 to 3). Index notation summation convention is illustrated below using the dot product (scalar or inner product) of two vectors in 3D (\mathbf{u} , \mathbf{v}), which is the summation of the component parts.

$$\mathbf{u} \cdot \mathbf{v} = u_i v_i = u_1 v_1 + u_2 v_2 + u_3 v_3 \quad (3.1)$$

Second order tensors are represented by nine components in 3D. Each component is denoted by two subscripts that define its location in the tensor. For example, the second order tensor \mathbf{A} in component form is A_{ij} , where the subscripts define the location within the tensor at row i and column j . A fourth order tensor is defined as the linear tensor function of a second order tensor. For example, the linear elastic constitutive law relates the second order stress tensor, $\boldsymbol{\sigma}$, and strain tensor, $\boldsymbol{\varepsilon}$, through the fourth order elastic modulus tensor, \mathbf{C} , as follows:

$$\boldsymbol{\sigma} = \mathbf{C} : \boldsymbol{\varepsilon} \quad (3.2)$$

$$\sigma_{ij} = C_{ijkl} \varepsilon_{kl} \quad (3.3)$$

The product of a fourth order tensor, \mathbf{A} , and a second fourth order tensor, \mathbf{B} , is defined as:

$$(\mathbf{A} : \mathbf{B}) = A_{ijkl} B_{kl} \quad (3.4)$$

3.1.2 Fundamental Principles and Theoretical Formulations

Large deformation kinematics describes the deformation of a body by following its movement from an ‘initial state’ to a ‘deformed state’, typically referred to as the ‘reference configuration’ and ‘current configuration’ of that body respectively. This is represented in Figure 3.1 with position vectors, \mathbf{x} and \mathbf{y} used to define the location of a material point in the reference (position vector \mathbf{x}) and current configurations (position vector \mathbf{y}). The displacement vector (\mathbf{u}) of the material point is represented by:

$$\mathbf{u}(\mathbf{x}, t) = \mathbf{y}(\mathbf{x}, t) - \mathbf{x} \quad (3.5)$$

The velocity vector (\mathbf{v}) is the time derivative of (\mathbf{u}) with respect to time (t):

$$d\mathbf{u} = \mathbf{v}(\mathbf{x}, t) = \frac{d\mathbf{u}}{dt} \quad (3.6)$$

The deformation gradient tensor, \mathbf{F} , relates the distance between two neighbouring material points to that in the reference configuration.

$$d\mathbf{y} = \mathbf{F} \cdot d\mathbf{x} \quad (3.7)$$

$$\mathbf{F} = \frac{\partial \mathbf{y}}{\partial \mathbf{x}} \quad (3.8)$$

The Jacobian (J), the total volume change, is used to quantify volume changes in the deformation of the body, expressed as the determinant of the deformation gradient \mathbf{F} as in equation (3.9).

$$J = \det(\mathbf{F}) \quad (3.9)$$

From the deformation gradient (equation (3.8)), the spatial velocity gradient, \mathbf{L} can be derived as:

$$\mathbf{L} = \frac{\partial \mathbf{v}}{\partial \mathbf{y}} = d\mathbf{F} \cdot \mathbf{F}^{-1} \quad (3.10)$$

The spatial velocity gradient, \mathbf{L} , can be decomposed into a symmetric rate of deformation tensor, \mathbf{D} , and an asymmetric spin tensor, \mathbf{W} . The rate of deformation tensor, \mathbf{D} , is a measure of the strain rate associated with the deformed configuration and is from the spatial velocity gradient, \mathbf{L} , as:

$$\mathbf{D} = \text{sym}(\mathbf{L}) = \frac{1}{2}(\mathbf{L} + \mathbf{L}^T) \quad (3.11)$$

$$\mathbf{W} = \text{asym}(\mathbf{W}) = (\mathbf{L} - \mathbf{L}^T) \quad (3.12)$$

The deformation tensor, \mathbf{D} can be integrated with respect to time to give the logarithmic strain tensor $\boldsymbol{\varepsilon}$, a measure of finite strain, calculated as:

$$\boldsymbol{\varepsilon}(t) = \int_0^t \mathbf{D} dt \quad (3.13)$$

In the present work the Cauchy stress, or true stress, $\boldsymbol{\sigma}$, is the primary measure of stress and is defined as the force per unit area on the current (deformed) configuration.

3.1.3 Elasticity

A continuum constitutive elasticity formulation is required to predict elastic deformation under complex loading and boundary conditions. The common basic assumption of elastic constitutive formulations is that the deformation can be split up into an elastic part that is recoverable (reversible) and a plastic part that is non-recoverable (irreversible) and permanent. Thus, the total deformation gradient, \mathbf{F} , can be defined as follows:

$$\mathbf{F} = \mathbf{F}^{el} \cdot \mathbf{F}^{pl} \quad (3.14)$$

where \mathbf{F}^{el} is the elastic recoverable part of the deformation and \mathbf{F}^{pl} is the plastic non-recoverable part of the deformation. Equation (3.14) can be approximated in terms of the mechanical strain rates in the system:

$$d\boldsymbol{\varepsilon} = d\boldsymbol{\varepsilon}^{el} + d\boldsymbol{\varepsilon}^{pl} \quad (3.15)$$

where $d\boldsymbol{\varepsilon}$ is the total strain rate, $d\boldsymbol{\varepsilon}^{el}$ is the elastic strain rate and, $d\boldsymbol{\varepsilon}^{pl}$ is the plastic strain rate. The total strain tensor, $\boldsymbol{\varepsilon}$, calculated by integrating equation (3.15) with respect to time, consists of the elastic strain, $\boldsymbol{\varepsilon}^{el}$, and the plastic strain, $\boldsymbol{\varepsilon}^{pl}$:

$$\boldsymbol{\varepsilon} = \boldsymbol{\varepsilon}^{el} + \boldsymbol{\varepsilon}^{pl} \quad (3.16)$$

For equations (3.15) and (3.16) to be analogous, the elastic response must always be small, typically less than 1 or 2%. In the elastic region, the relationship between stress and strain is linear and a linear elastic constitutive model can be represented concisely using the generalised Hooke's Law as follows:

$$\boldsymbol{\sigma} = \mathbf{C}^{el} : \boldsymbol{\varepsilon}^{el} \quad (3.17)$$

where $\boldsymbol{\sigma}$ is the stress tensor and \mathbf{C}^{el} is a fourth order tensor of elastic moduli that does not depend on the material deformation. The primary measure of stress used in Abaqus and in this thesis is the Cauchy, or "true" stress, $\boldsymbol{\sigma}$, and is defined as the force per unit area on the current configuration. When a material body is subjected to external forces it deforms. The three dimensional stress state of a material can be represented by the stress tensor, $\boldsymbol{\sigma}$ (i.e. σ_{ij}) as follows:

$$\sigma_{ij} = \begin{bmatrix} \sigma_{11} & \sigma_{12} & \sigma_{13} \\ \sigma_{21} & \sigma_{22} & \sigma_{23} \\ \sigma_{31} & \sigma_{32} & \sigma_{33} \end{bmatrix} \quad (3.18)$$

The stress tensor is symmetric, whereby $\sigma_{ij} = \sigma_{ji}$, therefore only six independent stress components needed to represent a stress state. The eigenvalue problem $\det[\boldsymbol{\sigma} - \lambda \mathbf{I}] = 0$, where $[\mathbf{I}]$ is the 3x3 identity tensor, leads to the characteristic equation:

$$\lambda^3 - I_1(\sigma_{ij})\lambda^2 + I_2(\sigma_{ij})\lambda - I_3(\sigma_{ij}) = 0 \quad (3.19)$$

where the invariants of the stress tensor are:

$$I_1 = \text{trace}(\boldsymbol{\sigma}) = \sigma_{ii} = \sigma_{11} + \sigma_{22} + \sigma_{33} \quad (3.20)$$

$$I_2 = \sigma_{11}\sigma_{22} + \sigma_{22}\sigma_{33} + \sigma_{11}\sigma_{33} - \sigma_{12}^2 - \sigma_{13}^2 - \sigma_{23}^2 \quad (3.21)$$

$$I_3 = \det[\sigma_{ij}] = \sigma_{11}\sigma_{22}\sigma_{33} + 2\sigma_{12}\sigma_{23}\sigma_{31} - \sigma_{33}\sigma_{12}^2 - \sigma_{22}\sigma_{13}^2 - \sigma_{11}\sigma_{23}^2 \quad (3.22)$$

Values of stress invariants are independent of the coordinate system used. The invariants of the stress tensor can also be written in terms of the principal stresses σ_1 , σ_2 and σ_3 as:

$$I_1 = \sigma_1 + \sigma_2 + \sigma_3 \quad (3.23)$$

$$I_2 = \sigma_1\sigma_2 + \sigma_2\sigma_3 + \sigma_3\sigma_1 \quad (3.24)$$

$$I_3 = \sigma_1\sigma_2\sigma_3 \quad (3.25)$$

The associated principal direction for each principal stress, σ_i , can be calculated as:

$$\boldsymbol{\sigma} \cdot \mathbf{n}^i = \sigma_i \mathbf{n}^i \quad (3.26)$$

where \mathbf{n}^i is the unit vector in the i th principal direction. The stress state of a material can be determined if the principal stresses and their directions are known. It is common to express the stress tensor, σ_{ij} , in terms of the deviatoric stress tensor, \mathbf{S} , and the hydrostatic stress (mean stress) tensor, σ_{ij}^0 , as:

$$\begin{aligned} \sigma_{ij} &= S_{ij} + \sigma_{ij}^0 \\ &= S_{ij} + p\delta_{ij} \end{aligned} \quad (3.27)$$

The hydrostatic stress tensor, σ_{ij}^0 , controls the portion of the applied stress that changes the volume where δ_{ij} is the Kronecker tensor and p is the equivalent pressure stress (hydrostatic pressure) defined as:

$$p = \frac{1}{3}\sigma_{ii} = \frac{I_1}{3} = -\frac{1}{3}\text{trace}(\boldsymbol{\sigma}) \quad (3.28)$$

The deviatoric stress tensor, S_{ij} , is the shape changing stress and hence controls the distortion:

$$S_{ij} = \begin{bmatrix} S_{11} & S_{12} & S_{13} \\ S_{21} & S_{22} & S_{23} \\ S_{31} & S_{32} & S_{33} \end{bmatrix} \quad (3.29)$$

and is calculated from:

$$S_{ij} = \sigma_{ij} - p\delta_{ij} \quad (3.30)$$

In terms of the components the stress tensor in equation (3.27) can be written as:

$$\begin{bmatrix} \sigma_{11} & \sigma_{12} & \sigma_{13} \\ \sigma_{21} & \sigma_{22} & \sigma_{23} \\ \sigma_{31} & \sigma_{32} & \sigma_{33} \end{bmatrix} = \begin{bmatrix} S_{11} & S_{12} & S_{13} \\ S_{21} & S_{22} & S_{23} \\ S_{31} & S_{32} & S_{33} \end{bmatrix} + \begin{bmatrix} p & 0 & 0 \\ 0 & p & 0 \\ 0 & 0 & p \end{bmatrix} \quad (3.31)$$

The eigenvalue problem $\det[\mathbf{S} - \lambda\mathbf{I}] = 0$ leads to the characteristic equation:

$$\lambda^3 - I_1(S_{ij})\lambda^2 + I_2(S_{ij})\lambda - I_3(S_{ij}) = 0 \quad (3.32)$$

where the invariants of the deviatoric stress tensor are:

$$J_1 = \text{trace}(S_{ij}) = S_{11} + S_{22} + S_{33} = 0 \quad (3.33)$$

$$J_2 = \frac{1}{2}S_{ij}S_{ij} = S_{12}^2 + S_{13}^2 + S_{23}^2 - S_{11}S_{22} - S_{22}S_{33} - S_{11}S_{33} \quad (3.34)$$

$$J_3 = \det[S_{ij}] \quad (3.35)$$

The invariants of the deviatoric stress tensor can also be written in terms of the principal components as S_1 , S_2 and S_3 as:

$$J_1 = \text{trace}(S_{ij}) = S_1 + S_2 + S_3 = 0 \quad (3.36)$$

$$J_2 = \frac{1}{2}(S_1^2 + S_2^2 + S_3^2) \quad (3.37)$$

$$J_3 = S_1 S_2 S_3 \quad (3.38)$$

The second and third invariants of the deviatoric stress tensor, S_{ij} , are related to the invariants of the stress tensor, σ_{ij} , by the following equations:

$$J_2 = \frac{1}{3}(I_1^2 - 3I_2) \quad (3.39)$$

$$J_3 = \frac{1}{27}(2I_1^3 - 9I_1 I_2 + 27I_3) \quad (3.40)$$

The von Mises equivalent stress (effective stress), q , is commonly used in the elastic analysis of materials and can be defined as:

$$q = \sqrt{\frac{3}{2} S_{ij} S_{ij}} \quad (3.41)$$

The strain tensor, $\boldsymbol{\varepsilon}$, is symmetric whereby $\varepsilon_{ij} = \varepsilon_{ji}$ and can be written as:

$$\boldsymbol{\varepsilon}_{ij} = \begin{bmatrix} \varepsilon_{11} & \varepsilon_{12} & \varepsilon_{13} \\ \varepsilon_{21} & \varepsilon_{22} & \varepsilon_{23} \\ \varepsilon_{31} & \varepsilon_{32} & \varepsilon_{33} \end{bmatrix} \quad (3.42)$$

The eigenvalue problem $\det[\boldsymbol{\varepsilon} - \lambda \mathbf{I}] = 0$ leads to the characteristic equation:

$$\lambda^3 - I_1(\varepsilon_{ij})\lambda^2 + I_2(\varepsilon_{ij})\lambda - I_3(\varepsilon_{ij}) = 0 \quad (3.43)$$

where the invariants of the strain tensor are:

$$I_1 = \text{trace}(\boldsymbol{\varepsilon}) = \varepsilon_{ii} = \varepsilon_{11} + \varepsilon_{22} + \varepsilon_{33} \quad (3.44)$$

$$I_2 = \varepsilon_{12}^2 + \varepsilon_{13}^2 + \varepsilon_{23}^2 - \varepsilon_{11}\varepsilon_{22} - \varepsilon_{22}\varepsilon_{33} - \varepsilon_{11}\varepsilon_{33} \quad (3.45)$$

$$I_3 = \det[\varepsilon_{ij}] \quad (3.46)$$

Similar to the stress tensor, the strain tensor can be written in terms of the deviatoric strain tensor, ε'_{ij} , and the volumetric strain tensor, ε_{ij}^0 , as:

$$\varepsilon_{ij} = \varepsilon'_{ij} + \varepsilon_{ij}^0 \quad (3.47)$$

$$= \varepsilon'_{ij} + \varepsilon_{vol}\delta_{ij} \quad (3.48)$$

where ε_{vol} is the volumetric strain calculated as:

$$\varepsilon_{vol} = \varepsilon_{11} + \varepsilon_{22} + \varepsilon_{33} = \frac{1}{3}\text{trace}(\boldsymbol{\varepsilon}) \quad (3.49)$$

The deviatoric strain tensor can be written as:

$$\varepsilon'_{ij} = \varepsilon_{ij} - \frac{1}{3}\varepsilon_{vol}\delta_{ij} \quad (3.50)$$

In terms of model definition, the elasticity is considered to be isotropic and linear (in terms of finite deformation quantities) and, therefore, the elastic component of the deformation can be defined in terms of two material constants. The bulk modulus, K , and the shear modulus, G can be calculated using the Young's modulus, E , and the Poisson's ratio, ν , as follows:

$$K = \frac{E}{3(1 - 2\nu)} \quad (3.51)$$

$$G = \frac{E}{2(1 + \nu)} \quad (3.52)$$

3.2 Constitutive Modelling of Biological Soft Tissues

Many investigations have focused on gaining further insight into the micro structure of soft biological tissues, in particular muscle and arteries, and developing constitutive equations to describe the gross behaviour that results from the composite structure of both its passive (fibrous connective tissues; collagen and elastin) and active components (cells and ground substances) (Dobrin, 2011, Fung, 1967, Fung, 1993, Holzapfel et al., 2000, Holzapfel, 2006, Holzapfel et al., 2010, Holzapfel et al., 2005, Holzapfel et al., 2004, Humphrey, 1995).

When subjected to small deformations (less than 2–5%), the mechanical behaviour of soft biological tissue can generally be modelled adequately using conventional linear elasticity. However, under large deformations, soft biological tissues exhibits highly nonlinear elastic behaviour due to rearrangements and reorientation of fibre directions with deformation and therefore a linear elastic model does not accurately describe its material behaviour. Simulation of these nonlinear large-strain effects requires advanced constitutive models formulated within the framework of hyperelasticity.

3.2.1 Isotropic Hyperelasticity

Hyperelastic materials are described in terms of a strain energy potential (U), which defines the strain energy stored in the material per unit of reference volume (volume of a body's initial state) as a function of the strain at that point in the material. For this we introduce the deviatoric stretch matrix (the left Cauchy-Green strain tensor) of $\bar{\mathbf{F}}$ as:

$$\bar{\mathbf{B}} = \bar{\mathbf{F}} \cdot \bar{\mathbf{F}}^T \quad (3.53)$$

Using equation (3.53) and equation (3.9), $\bar{\mathbf{F}}$ (the deformation gradient with the volume change eliminated) is defined as:

$$\bar{\mathbf{F}} = J^{-\frac{1}{3}} \mathbf{F} \quad (3.54)$$

The first and second strain invariants (\bar{I}_1 and \bar{I}_2 respectively) of $\bar{\mathbf{B}}$ are then defined as:

$$\bar{I}_1 = \text{trace}(\bar{\mathbf{B}}) \quad (3.55)$$

$$\bar{I}_2 = \frac{1}{2} (\bar{I}_1^2 - \text{trace}(\bar{\mathbf{B}} \cdot \bar{\mathbf{B}})) \quad (3.56)$$

The Cauchy ("true") stress components are defined from the strain energy potential as follows. From the principle of virtual work the internal energy is:

$$\delta W_I = \int_V \boldsymbol{\sigma} : \delta \mathbf{D} dV = \int_{V^0} \mathbf{J} \boldsymbol{\sigma} : \delta \mathbf{D} dV^0 \quad (3.57)$$

where $\boldsymbol{\sigma}$ are the components of the Cauchy ("true") stress, V is the current volume and V^0 is the reference volume. The stress can be decomposed into the equivalent pressure stress:

$$p = -\frac{1}{3} \mathbf{I} : \boldsymbol{\sigma} \quad (3.58)$$

and the deviatoric stress:

$$\mathbf{S} = \boldsymbol{\sigma} + p \mathbf{I} \quad (3.59)$$

The internal energy variation can then be written as:

$$\delta W_I = \int_{V^0} \mathbf{J} (\mathbf{S} : \delta \mathbf{e} - p \delta \varepsilon^{vol}) dV^0 \quad (3.60)$$

For isotropic, compressible materials the strain energy potential, U , is a function of \bar{I}_1 , \bar{I}_2 and J as follows:

$$\delta U = \frac{\partial U}{\partial \bar{I}_1} \delta \bar{I}_1 + \frac{\partial U}{\partial \bar{I}_2} \delta \bar{I}_2 + \frac{\partial U}{\partial J} \delta J \quad (3.61)$$

where $\delta \bar{I}_1$, $\delta \bar{I}_2$ and δJ are as follows:

$$\delta \bar{I}_1 = 2\bar{\mathbf{B}} : \delta \mathbf{e} \quad (3.62)$$

$$\delta \bar{I}_2 = 2(\bar{I}_1 \bar{\mathbf{B}} - \bar{\mathbf{B}} \cdot \bar{\mathbf{B}}) : \delta \mathbf{e} \quad (3.63)$$

$$\delta J = J \delta \varepsilon^{vol} \quad (3.64)$$

Hence, equation (3.61) can be written as:

$$\delta U = 2 \left[\left(\frac{\partial U}{\partial \bar{I}_1} + \bar{I}_1 \frac{\partial U}{\partial \bar{I}_2} \right) \bar{\mathbf{B}} - \frac{\partial U}{\partial \bar{I}_2} \bar{\mathbf{B}} \cdot \bar{\mathbf{B}} \right] : \delta \mathbf{e} + J \frac{\partial U}{\partial J} \delta \varepsilon^{vol} \quad (3.65)$$

Therefore, δW_I , the variation of the strain energy potential (defined as the internal virtual work per reference volume) is:

$$\delta W_I = \int_{V^0} \mathbf{J} (\mathbf{S} : \delta \mathbf{e} - p \delta \varepsilon^{vol}) dV^0 = \int_{V^0} \delta U \delta V^0 \quad (3.66)$$

For a compressible material, where the strain variations are arbitrary, this equation defines the stress components for the material as:

$$\mathbf{S} = \frac{2}{J} DEV \left[\left(\frac{\partial U}{\partial \bar{I}_1} + \bar{I}_1 \frac{\partial U}{\partial \bar{I}_2} \right) \bar{\mathbf{B}} - \frac{\partial U}{\partial \bar{I}_2} \bar{\mathbf{B}} \cdot \bar{\mathbf{B}} \right] \quad (3.67)$$

and

$$p = -\frac{\partial U}{\partial J} \quad (3.68)$$

Two distinct behaviours exist within hyperelastic material behaviour: isotropic and anisotropic. Isotropic materials behave uniformly in all orientations of the material. However due to the presence of preferred directions in their microstructure, some hyperelastic materials are anisotropic and exhibit directionally dependent material behaviour. Due to its composite fibrous structure, arterial tissue exhibits anisotropic hyperelastic material behaviour.

3.2.2 Anisotropic Hyperelasticity

Using the continuum theory of fibre-reinforced composites (Spencer, 1984), the strain energy function can be expressed directly in terms of the invariants of the deformation tensor and fibre directions. For example, for a composite material that consists of an isotropic hyperelastic matrix reinforced with a families of fibres, the directions of the fibres in the reference configuration can be characterized by a set of unit vectors, $\mathbf{A}_\alpha = (\alpha = 1, \dots, N)$. Assuming that the strain energy depends on both the deformation and the fibre directions, the following form is proposed for $\alpha = 1, \dots, N$:

$$U = U(\mathbf{C}, \mathbf{A}_\alpha) \quad (3.69)$$

The strain energy of the material remains unchanged if both the matrix and fibres in the reference configuration undergo a rigid body rotation. Then, following Spencer (1984), the strain energy can be expressed as an isotropic function of an irreducible set of scalar invariants that form the integrity basis of the tensor \mathbf{C} and the vectors \mathbf{A}_α as follows for $\alpha = 1, \dots, N$; $\beta = 1, \dots, \alpha$:

$$U = U(\bar{I}_1, \bar{I}_2, J, \bar{I}_{4(\alpha\beta)}, \bar{I}_{5(\alpha\beta)}, \zeta_{\alpha\beta}) \quad (3.70)$$

\bar{I}_1, \bar{I}_2 are the first and second strain invariants as defined previously in equation (3.55) and equation (3.56), J is the Jacobian as defined previously in

equation (3.9) and $\bar{I}_{4(\alpha\beta)}$ and $\bar{I}_{5(\alpha\beta)}$ are the pseudo-invariants of $\bar{\mathbf{C}}$, \mathbf{A}_α and \mathbf{A}_β , defined as:

$$\bar{I}_{4(\alpha\beta)} = \mathbf{A}_\alpha \cdot \bar{\mathbf{C}} \cdot \mathbf{A}_\beta \quad (3.71)$$

$$\bar{I}_{5(\alpha\beta)} = \mathbf{A}_\alpha \cdot \bar{\mathbf{C}}^2 \cdot \mathbf{A}_\beta \quad (3.72)$$

for $\alpha = 1, \dots, N$; $\beta = 1, \dots, \alpha$. The terms $\zeta_{\alpha\beta}$ are geometric constants (independent of deformation) equal to the cosine of the angle between the directions of any two families of fibres in the reference configuration:

$$\zeta_{\alpha\beta} = \mathbf{A}_\alpha \cdot \mathbf{A}_\beta \quad (3.73)$$

for $\alpha = 1, \dots, N$; $\beta = 1, \dots, \alpha$. From equation (3.70), the variation of U for anisotropic hyperelasticity is given as:

$$\begin{aligned} \delta U = & \frac{\partial U}{\partial \bar{I}_1} \delta \bar{I}_1 + \frac{\partial U}{\partial \bar{I}_2} \delta \bar{I}_2 + \frac{\partial U}{\partial J} \delta J \\ & + \sum_{\alpha=1}^N \sum_{\beta=1}^{\alpha} \left(\frac{\partial U}{\partial \bar{I}_{4(\alpha\beta)}} \delta \bar{I}_{4(\alpha\beta)} + \frac{\partial U}{\partial \bar{I}_{5(\alpha\beta)}} \delta \bar{I}_{5(\alpha\beta)} \right) \end{aligned} \quad (3.74)$$

Using the principle of virtual work (equation (3.66)) the stress components for a compressible material are found as:

$$\begin{aligned} \mathbf{S} = & \frac{2}{J} DEV \left[\left(\frac{\partial U}{\partial \bar{I}_1} + \bar{I}_1 \frac{\partial U}{\partial \bar{I}_2} \right) \bar{\mathbf{B}} - \frac{\partial U}{\partial \bar{I}_2} \bar{\mathbf{B}} \cdot \bar{\mathbf{B}} \right] \\ & + \sum_{\alpha=1}^N \sum_{\beta=1}^{\alpha} \frac{\partial U}{\partial \bar{I}_{4(\alpha\beta)}} DEV(\bar{\mathbf{a}}_\alpha \bar{\mathbf{a}}_\beta + \bar{\mathbf{a}}_\beta \bar{\mathbf{a}}_\alpha) \\ & + \sum_{\alpha=1}^N \sum_{\beta=1}^{\alpha} \frac{\partial U}{\partial \bar{I}_{5(\alpha\beta)}} DEV(\bar{\mathbf{a}}_\alpha \bar{\mathbf{a}}'_\beta + \bar{\mathbf{a}}'_\alpha \bar{\mathbf{a}}_\beta + \bar{\mathbf{a}}_\beta \bar{\mathbf{a}}'_\alpha + \bar{\mathbf{a}}'_\beta \bar{\mathbf{a}}_\alpha) \end{aligned} \quad (3.75)$$

and

$$p = -\frac{\partial U}{\partial J} \quad (3.76)$$

where $\bar{\mathbf{a}}_\alpha = \bar{\mathbf{F}} \cdot \mathbf{A}_\alpha$ and $\bar{\mathbf{a}}'_\alpha = \bar{\mathbf{B}} \cdot \mathbf{A}_\alpha$.

There are several forms of strain energy potentials available in Abaqus to model approximately incompressible *isotropic* elastomers including the Arruda-Boyce, Marlow, Mooney-Rivlin, neo-Hookean, Ogden, polynomial, reduced polynomial, Yeoh and Van der Waals forms. Two particular forms of the strain energy potential are available in Abaqus for incompressible *anisotropic* elastomers namely the generalized Fung form and the Holzapfel-Gasser-Ogden form. Using Abaqus, one can define the mechanical response of a material by choosing a strain energy potential to fit the particular material along with either directly specifying material coefficients or providing experimental test data (allowing Abaqus to automatically determine appropriate values of the coefficients).

It is well established in the literature that non-linear hyperelastic isotropic material models are a good compromise between physical reality and computational efficiency when dealing with human-body soft tissue.

In the work presented in this thesis, three different forms of the strain energy potential are employed; the polynomial form, the Mooney-Rivlin form and the Holzapfel-Gasser-Ogden form. The following section provides a brief description of each form, summarised from section 4.6.1 of the Abaqus Theory Manual (Abaqus, 2011) where a more in depth discussion can be found.

3.2.3 Polynomial Form (Isotropic)

The polynomial strain energy potential is given in equation (3.77) where C_{ij} and D_i are material constants, J^{el} is the elastic volume ratio and N determines the number of terms in the polynomial.

$$U = \sum_{i+j=1}^N C_{ij} (\bar{I}_1 - 3)^i (\bar{I}_2 - 3)^j + \sum_{i=1}^N \frac{1}{D_i} (J^{el} - 1)^{2i} \quad (3.77)$$

\bar{I}_1 and \bar{I}_2 are the first and second strain invariants of the left Cauchy-Green strain tensor, $\bar{\mathbf{B}}$, as defined previously in equation (3.55) and equation (3.56). Material constants C_{ij} and D_i are determined from mechanical tests of the tissue and can be easily related to the elastic material properties of Young's modulus E and Poisson's ration ν as follows:

$$C_{ij} = \frac{E}{4(1 + \nu)} \quad (3.78)$$

$$D_i = \frac{6(1 - 2\nu)}{E} \quad (3.79)$$

J^{el} , the elastic volume ratio which relates J (the Jacobian of the deformation as defined in equation (3.9), also termed the total volume ratio), and the thermal volume ratio, J^{th} as follows:

$$J^{el} = \frac{J}{J^{th}} \quad (3.80)$$

and

$$J^{th} = (1 + \varepsilon_1^{th})(1 + \varepsilon_2^{th})(1 + \varepsilon_3^{th}) \quad (3.81)$$

where ε_i^{th} are the principal thermal expansion strains that are obtained from the temperature and the thermal expansion coefficients.

The D_i value determines the compressibility of the material. If D_i values are zero, the material is taken as fully incompressible. If $D_1 = 0$, all D_i must be zero.

Regardless of the value of N , the initial shear modulus μ_0 , and the bulk modulus k_0 , depend only on the polynomial coefficients of order $N = 1$:

$$\mu_0 = (2C_{10} + C_{01}) \quad (3.82)$$

$$k_0 = \frac{2}{D_1} \quad (3.83)$$

Particular forms of the polynomial model are obtained by setting specific coefficients to zero. Equation (3.77) becomes a ‘reduced’ polynomial strain energy function if all C_{ij} with $j \neq 0$ are set to zero. The reduced polynomial strain energy function is simplified further by setting $N = 1$ where the neo-Hookean form is obtained as per equation (3.84) below. This is the simplest hyperelastic model and often serves as a prototype for elastomeric materials in the absence of accurate material data.

$$U = C_{10}(\bar{I}_1 - 3) + \frac{1}{D_1}(J^{el} - 1)^2 \quad (3.84)$$

In the case of the arterial material model applied in Chapter 4 and Chapter 5 of the work presented in this thesis, equation (3.77) is reduced to a sixth-order reduced polynomial strain energy function as per equation (3.85). This form of the polynomial model is obtained where all C_{ij} with $j \neq 0$ are set to zero and $D_i = 0$. $C_{10} - C_{60}$ are taken from mechanical tests of the tissue found in the literature.

$$\begin{aligned}
U = & C_{10}(\bar{I}_1 - 3) + C_{20}(\bar{I}_1 - 3)^2 + C_{30}(\bar{I}_1 - 3)^3 \\
& + C_{40}(\bar{I}_1 - 3)^4 + C_{50}(\bar{I}_1 - 3)^5 \\
& + C_{60}(\bar{I}_1 - 3)^6
\end{aligned} \tag{3.85}$$

If $N = 1$, only the linear terms in the deviatoric strain energy are retained and the Mooney-Rivlin form is recovered as detailed in the following section.

3.2.4 Mooney Rivlin Form (Isotropic)

The Mooney-Rivlin form is as an extension of the neo-Hookean form. In the Mooney-Rivlin form, as in the neo-Hookean form, $N = 1$. However, it adds a term that depends on the second invariant of the left Cauchy-Green tensor. The Mooney-Rivlin form is represented in equation (3.86). It is generally capable of accounting for large, non-linear elastic deformations. For cases where the nominal strains are small or only moderately large (<100%), the first terms in the polynomial series of equation (3.77) usually provide a sufficiently accurate model. In some cases this form will give a more accurate fit to the experimental data than the neo-Hookean form. In general, however, both models give similar accuracy since they use only linear functions of the invariants. These functions do not allow representation of the “upturn” at higher strain levels in the stress-strain curve.

$$U = C_{10}(\bar{I}_1 - 3) + C_{01}(\bar{I}_2 - 3) + \frac{1}{D_1}(J^{el} - 1)^2 \tag{3.86}$$

3.2.5 Holzapfel-Gasser-Ogden Form (Anisotropic)

This form of the strain energy potential is based on that proposed by Holzapfel, Gasser and Ogden for modelling arterial layers with distributed collagen fibre orientations (Gasser et al., 2006, Holzapfel et al., 2000, Holzapfel, 2006) given in equation (3.87) below.

$$\begin{aligned}
U = C_{10}(\bar{I}_1 - 3) + \frac{1}{D} \left(\frac{(J^{el})^2 - 1}{2} - \ln J^{el} \right) \\
+ \frac{k_1}{2k_2} \sum_{\alpha=1}^N \{ \exp[k_2 \langle \bar{E}_\alpha \rangle^2] - 1 \}
\end{aligned} \tag{3.87}$$

and

$$\bar{E}_\alpha = \kappa(\bar{I}_1 - 3) + (1 - 3\kappa)(\bar{I}_{4(\alpha\alpha)} - 1) \tag{3.88}$$

C_{10} and D are hyperelastic material constants (as defined in equation (3.78) and equation (3.79)), k_1 is a stress like parameter (with dimensions of stress) and k_2 is a dimensionless parameter, all to be determined from mechanical tests of the tissue. κ is the dispersion parameter that characterises the distribution of the collagen fibres and is determined from histological data of the tissue. N is the number of families of fibres ($N \leq 3$). \bar{I}_1 is the first deviatoric strain invariant (previously described in equation (3.55)). J^{el} is the elastic volume ratio as previously described in (3.80). $\bar{I}_{4(\alpha\alpha)}$ is a pseudo-invariant of $\bar{\mathbf{C}}$ and \mathbf{A}_α defined as per equation (3.71).

The model assumes that the directions of the collagen fibres within each family have the same mechanical properties and the same dispersion about a mean preferred direction with rotational symmetry. The level of dispersion in the fibre directions is described by the parameter κ ($0 \leq \kappa \leq 1/3$).

$\rho(\theta)$ is the orientation density function that characterizes the distribution of the fibres. It represents the normalized number of fibres with orientations in the range $(\theta, \theta + d\theta)$ with respect to the mean direction. In this case, κ is defined as per equation (3.89).

$$\kappa = \frac{1}{4} \int_0^\pi \rho(\theta) \sin^3 \theta d\theta \tag{3.89}$$

When $\kappa = 0$, the fibres are have no dispersion and are perfectly aligned. When $\kappa = 1/3$ the fibres are randomly distributed and the material becomes isotropic and the model corresponds to a spherical orientation density function.

\bar{E}_α is a strain like quantity that characterises the deformation of the family of fibres with mean direction A_α . For perfectly aligned fibres ($\kappa = 0$), \bar{E}_α is defined as per equation (3.90) as follows. For randomly distributed fibres ($\kappa = 1/3$), \bar{E}_α is defined as per equation (3.91) as follows:

$$\bar{E}_\alpha = \bar{I}_{4(\alpha\alpha)} - 1 \quad (3.90)$$

$$\bar{E}_\alpha = \bar{I}_1 - 3 \quad (3.91)$$

The first two terms in the expression of the strain energy function represent the distortional and volumetric contributions of the non-collagenous isotropic ground material that makes up arterial tissue. The third term represents the contributions from the various families of collagen fibres, taking into account the effects of dispersion. A basic assumption of the model is that collagen fibres can support only tension, and buckle under compressive loading. Therefore, the anisotropic contribution in the strain energy function appears only when the strain of the fibres is positive or when $\bar{E}_\alpha > 0$.

3.3 Constitutive Modelling of Superelastic Materials

As discussed in Chapter 1, Nitinol is a flexible metal alloy, capable of recovering its original shape through phase transformation following loads that cause large deformations. Nitinol is described as ‘superelastic’ as it is capable of recovering from strains in the order of 8-11% compared to ‘elastic’ strains in typical metals in the order of 0.1%. In the work presented in this thesis, a constitutive model for superelastic material behaviour is employed to model a self expanding Nitinol stent. The following section provides a brief description of the model, summarised from the work of Auricchio and Taylor where a more in depth discussion can be found (Auricchio et al., 1997a, Auricchio et al., 1997b).

The superelastic phase transformation and shape memory transformation temperature curves of Nitinol are shown in Figure 3.2 and Figure 3.3. In the absence of an externally applied load, the material is processed to exist in an austenite phase, at room temperature, which behaves linear elastically. Upon loading, the austenite phase transforms into a martensite phase at a critical stress, allowing large deformations (strains) with a small increase in stress, as seen in the loading portion of the curve in Figure 3.2.

Upon unloading, the transformation is reversible. However, the stresses at which reversible transformation occurs are lower than the stresses required upon loading, as can be seen in the unloading portion of the curve of Figure 3.2. In the case of compression, similar behaviour is observed. In this case, stresses required to produce the transformation of austenite to martensite are higher, while the transformation strains are lower.

Nitinol is a difficult material to characterize numerically. An approximation, capable of modelling the loading part of the model, is hyperelasticity. Whilst other constitutive models have been proposed to address Nitinol’s behaviour, a thorough verification of these models is difficult because the manufacturing requirements of Nitinol are complex. As a result, Nitinol is typically available as relatively thin wires and tubes, for which the testing data available is mostly in the form of uniaxial data. It is moderately straightforward to produce a uniaxial model for Nitinol, but a greater

challenge to produce a model that accurately represents the three-dimensional stress-strain behaviour of Nitinol. Auricchio and Taylor developed a constitutive model to describe the superelastic and shape memory behaviour of these alloys at finite strains. This constitutive model can be implemented through a user material routine (UMAT), developed for and available in Abaqus Standard and Abaqus Explicit (VUMAT) enabling the user to model superelastic materials such as Nitinol in three dimensions. This theory is based on the concept of generalized plasticity and physical principles.

In this material model strain is decomposed into two components: a purely linear elastic component and a transformation component as in equation (3.92).

$$\Delta \boldsymbol{\varepsilon} = \Delta \boldsymbol{\varepsilon}^{el} + \Delta \boldsymbol{\varepsilon}^{tr} \quad (3.92)$$

The austenite to martensite transformation is driven by the resolution of shear forces, and takes place within a range of stress levels, characteristic of the specific composition of the alloy material.

$$\Delta \boldsymbol{\varepsilon}^{tr} = a \Delta \zeta \frac{\partial \mathbf{F}}{\partial \boldsymbol{\sigma}} \quad (3.93)$$

$$F^{Start} \leq F \leq F^{Finish} \quad (3.94)$$

ζ is the fraction of martensite, a is a scalar parameter representing the maximum deformation obtainable by detwinning of the martensite and F is a transformation potential. The same is true for the reverse transformation but at different stress levels. The intensity of the transformation follows the stress in Potential law:

$$\Delta \zeta = F(\sigma, \zeta) \Delta F \quad (3.95)$$

Change in stress direction produces a reorientation of the martensite and changes in temperature results in a linear shift in the stress levels at which the

transformations take place. As there is a volume increase associated with the transformation, it requires less stress to produce the transformation in tension and more in compression. This is modelled with a linear Drucker-Prager approach for the transformation potential:

$$F = \bar{\sigma} - p \tan \beta + CT \quad (3.96)$$

$\bar{\sigma}$ is the Mises equivalent stress, p the pressure stress, T the temperature and C is a material constant. A rule of mixtures is used to implement the change in linear elasticity from the austenite phase into the martensite phase. Whilst computing stresses and strains, the UMAT routine tracks variables specific to the model including the fraction of martensite, transformation strains, and equivalent stresses and strains. These are points in the uniaxial tensile curve into which material points that have a three-dimensional state, specific fractions of martensite, and a specific loading/unloading history are mapped. The UMAT/VUMAT requires the input of material constants, as shown in Figure 3.4 and Figure 3.5. These material constants can be obtained from uniaxial tests in terms of loading, unloading, reverse loading, and temperature effects. However, due to the fact that the specific manufacturing requirements of Nitinol differ depending on the application, individual material constants can vary greatly.

As mentioned above, a more in depth discussion and description of the model, and how it is adapted to a three dimensional case can be found in the work of Auricchio and Taylor (Auricchio et al., 1997a, Auricchio et al., 1997b).

3.4 Numerical Implementation

Finite element simulations are a means of numerically investigating the mechanics of a body by dividing it into a finite number of subdivisions (elements) interconnected at joints (nodes) (Fagan, 1992, Zienkiewicz et al., 2005). The full collection of nodes and elements representing a reference volume or body is known as the finite element mesh. The governing constitutive equations, calculated for each element of the mesh assemble to form a system equation which describes the behaviour of the body as a whole. The mechanical behaviour (displacement, stress, strain etc.) of each individual element is incrementally calculated by applying boundary conditions to the system equation.

The commercially available finite element solver Abaqus is used for the finite element simulations of the work presented in this thesis, with two numerical approaches applied. The first of these is Abaqus Standard, an ‘implicit’ general purpose code used to solve linear and non-linear problems. The second is Abaqus Explicit, an ‘explicit’ special purpose code used to solve dynamic and highly non-linear problems involving large amounts of contact. The choice of solution method for a particular analysis depends on the type of problem to be solved. The following section provides a brief description of the theory behind each numerical approach, summarised from Fagan (1992) and the Abaqus Theory Manual (Abaqus, 2011) where a more in depth discussion can be found.

3.4.1 Implicit Finite Element Solution Method

An ‘implicit’ finite element solution is one that is solved by updating the state of the model incrementally from time t to $t + \Delta t$. In this type of solution, the state of the model at $t + \Delta t$ is determined based on the information at $t + \Delta t$ thereby solving the solution iteratively, requiring convergence at each time point. Abaqus uses a range of solution procedures to solve finite element solutions implicitly. The solution procedure used for the implicit numerical approach applied to the work presented here is the Newton Raphson method. For simplicity, it is presented here in vector matrix notation for the small strain case. This method of solution is based the principle of virtual work. Considering a reference volume (V) bounded by a surface (S), the internal and external virtual work can be represented as:

$$\int_V \delta \boldsymbol{\varepsilon}^T \boldsymbol{\sigma} dV = \int_S \delta \mathbf{u}^T \mathbf{t} dS \quad (3.97)$$

$\boldsymbol{\sigma}$ and \mathbf{t} are the stress and traction vectors respectively, $\delta \boldsymbol{\varepsilon}$ and $\delta \mathbf{u}$ are the virtual strain and virtual displacement vectors respectively. The integrals of equation (3.97) are taken over a finite element mesh with individual elements “ e ” of volume V_e and surface S_e and are evaluated using the following shape functions:

$$\delta \boldsymbol{\varepsilon} = \mathbf{B}_e \delta \mathbf{u}_e \quad (3.98)$$

$$\delta \mathbf{u} = \mathbf{N}_e \delta \mathbf{u}_e \quad (3.99)$$

\mathbf{N}_e is the element shape function matrix, \mathbf{B}_e is the element shape function gradient matrix and $\delta \mathbf{u}_e$ are the nodal displacements. The following expression is obtained if equations (3.98) and (3.99) are substituted into equation (3.97) such that equation (3.100) can be arranged and summed over all the elements in the mesh:

$$\sum_e \int_{V_e} \delta \mathbf{u}_e^T \mathbf{B}_e^T \boldsymbol{\sigma}(\mathbf{u}_e) dV = \sum_e \int_{S_e} \delta \mathbf{u}_e^T \mathbf{N}_e^T \mathbf{t} dS \quad (3.100)$$

The stress matrix is dependent on the elemental vector of nodal displacements, $\delta \mathbf{u}_e$. Assembling elemental quantities into global quantities and eliminating the arbitrary virtual quantities yields the following global expression:

$$\int_V \mathbf{B}^T \boldsymbol{\sigma}(\mathbf{u}) dV = \int_S \mathbf{N}^T \mathbf{t} dS \quad (3.101)$$

\mathbf{u} is the global nodal displacement vector for the finite element mesh. A set of global equations in \mathbf{u} for the out of balance force, \mathbf{G} , can then be assembled and solved as follows:

$$\mathbf{G}(\mathbf{u}) = \int_V \mathbf{B}^T \boldsymbol{\sigma}(\mathbf{u}) dV - \int_S \mathbf{N}^T \mathbf{t} dS = 0 \quad (3.102)$$

In general, for non-linear problems involving non-linear geometries, materials, constitutive laws and/or boundary conditions, equation (3.102) is non-linear, and therefore must be solved incrementally. The loads/displacements are applied in time steps, Δt , from an initial time increment ($t_{initial}$), to an ultimate time, t_{final} . At the end of each increment, the structure of the non-linear geometries, materials, constitutive laws and/or boundary conditions may have changed and therefore equation (3.100) must be updated to represent this. After each increment of an implicit analysis, the analysis performs Newton-Raphson iterations from time t to $t + \Delta t$ to solve for all nodal displacements at $\mathbf{u}^{t+\Delta t}$ to enforce equilibrium of the internal structure forces with the externally applied boundary conditions and/or loads. An estimation of the roots of equation (3.100) is made using the Newton-Raphson formula, such that for the i^{th} iteration:

$$\delta \mathbf{u}_{i+1} = \mathbf{u}_{i+1}^{t+\Delta t} - \mathbf{u}_i^{t+\Delta t} = - \left(\frac{\partial \mathbf{G}(\mathbf{u}_i^{t+\Delta t})}{\partial \mathbf{u}} \right) \mathbf{G}(\mathbf{u}_i^{t+\Delta t}) \quad (3.103)$$

where $\mathbf{u}_i^{t+\Delta t}$ is the vector of nodal displacements for the i^{th} iteration at time $t + \Delta t$ and $\mathbf{u}_{i+1}^{t+\Delta t}$ is an improved estimate of the nodal displacements relative to $\mathbf{u}_i^{t+\Delta t}$. The partial derivative on the right hand side of the equation is known as the Jacobian matrix of the governing equations and can also be referred to as the global stiffness matrix, \mathbf{K}_G . Equation (3.103) is manipulated and inverted to produce a system of linear equations:

$$\mathbf{K}_G(\mathbf{u}_i^{t+\Delta t}) \delta \mathbf{u}_{i+1} = -\mathbf{G}(\mathbf{u}_i^{t+\Delta t}) \quad (3.104)$$

Equation (3.104) must be solved for each iteration for the change in incremental displacements, $\delta \mathbf{u}_{i+1}$. In order to solve for $\delta \mathbf{u}_{i+1}$, the global stiffness matrix, \mathbf{K}_G , must be inverted. Although this is more computationally expensive than

the explicit solution method, it ensures accuracy of the solution using a relatively large time increment.

Following iteration i , $\delta \mathbf{u}_{i+1}$ is determined and a better approximation of the solution is made, $\mathbf{u}_{i+1}^{t+\Delta t}$, through equation (3.103). This in turn is used as the current approximation to the solution for the subsequent iteration ($i + 1$). The accuracy of the solution is also dictated by the convergence criterion where the updated value for \mathbf{G} must be less than a tolerance value. Complications can arise in an analysis that has a highly non-linear stress-strain response or where there is contact and sliding between two surfaces. In such cases many iterations are usually needed to solve for an increment leading to progressively smaller time steps being used. If large non-linearities are encountered, convergence may be impossible to achieve in practical terms. In contrast to the implicit method, the explicit method does not involve iteration and hence convergence issues are not an issue.

3.4.2 Explicit Finite Element Solution Method

The explicit method was developed for analysis simulating dynamic events in which large changes in geometries, materials, constitutive laws and/or boundary conditions occur in a small time period. An advantage to the explicit method is its ability to deal with complex contact and large deformation problems. An explicit analysis can converge on a solution to problems which may be a serious challenge using an implicit solution method due to the complexity of the problem.

For the explicit solution method accelerations and velocities at a particular point in time, t , are assumed to be constant and are used to solve for the next point in time, i.e. it solves for $t + \Delta t$ based on information at time t . The central difference integration scheme is used (Abaqus, 2011) where:

$$\mathbf{u}^{i+1} = \mathbf{u}^i + \Delta t^{i+1} \dot{\mathbf{u}}^{i+\frac{1}{2}} \quad (3.105)$$

$$\dot{\mathbf{u}}^{i+\frac{1}{2}} = \dot{\mathbf{u}}^{i-\frac{1}{2}} + \frac{\Delta t^{i+1} + \Delta t^i}{2} \ddot{\mathbf{u}}^i \quad (3.106)$$

\mathbf{u} is the displacement vector and the superscripts refer to the time increment. In the explicit method iteration is not performed and i refers to the time increment number (unlike the implicit method described previously where i refers to the iteration number within a certain time increment). The accelerations are computed at the start of the increment by:

$$\dot{\mathbf{u}}^i = \mathbf{M}^{-1}(\mathbf{F}^i - \mathbf{I}^i) \quad (3.107)$$

\mathbf{M} is the lumped mass matrix:

$$\mathbf{M} = \int_V \rho \mathbf{N} dV \quad (3.108)$$

\mathbf{I}^i is the vector of internal element forces given by:

$$\mathbf{I}^i = \int_V \mathbf{B}^T \boldsymbol{\sigma}^i dV \quad (3.109)$$

\mathbf{F}^i is the vector of externally applied forces:

$$\mathbf{F}^i = \int_S \mathbf{N}^T \mathbf{t}^i dS + \int_V \mathbf{N}^T \mathbf{P}^i dV \quad (3.110)$$

\mathbf{P}^i is the vector of nodal forces and ρ denotes the current material density. All other quantities are defined through equation (3.101). Equation (3.107), rearranged as $\mathbf{M}\ddot{\mathbf{u}} = (\mathbf{F} - \mathbf{I})$, is analogous to the system of linear equations in the implicit method, equation (3.107). Each time increment is computationally efficient to solve as the lumped mass matrix \mathbf{M} is diagonalised and therefore easily inverted, unlike the global stiffness matrix \mathbf{K}_G in the implicit method.

For the explicit method, as the solution progresses through the increments, and as the displacement vector \mathbf{u}^i is updated for each increment, it is necessary to

calculate the stresses σ^i to form equation (3.107) which necessitates an accurate stress update algorithm. A stability limit determines the size of the time increment:

$$\Delta t \leq \frac{2}{\omega_{max}} \quad (3.111)$$

where ω_{max} is the maximum element eigenvalue. A conservative and practical way of implementing the inequality in the equation above is by using equation (3.112) where L^e is the characteristic element length, c^d is the dilatational wave speed and λ and μ are the Lamé elastic constants.

$$\Delta t = \min\left(\frac{L^e}{c^d}\right) \quad (3.112)$$

$$\text{where } c^d = \sqrt{\frac{\lambda+2\mu}{\rho}} \quad (3.113)$$

As shown above, there is a linear relationship between the size of the model and the solution time, as dictated by the characteristic element length L^e and the number of elements in the model. However, in order to obtain an accurate solution, changes in acceleration between subsequent time increments must be small. Using the explicit method, although the incremental solution is easy to obtain, a quasi-static analysis can therefore often take up to 100,000 increments to solve due to an extremely small time increment. To ensure efficiency of the analysis it is important to ensure the element size is as regular as possible so that a single element doesn't reduce the time increment for the whole model. Due to the large runtime it is often impractical to run quasi-static analysis using its true time scale. A number of methods can be used to artificially reduce the run time of the simulation including speeding up the applied deformation or loading rate and scaling the material density in the model. It is evident from equations (3.112) and (3.113), when the density ρ is scaled by a factor, f^2 , the runtime is reduced by a factor f . When performing a quasi-static simulation, in order to prevent unrealistic dynamic results it is important that the internal forces do not affect the mechanical response. It is recommended that

the ratio of kinetic energy to total internal strain energy in the model is less than 5% in order to ensure dynamic effects are negligible in quasi-static analysis (Abaqus, 2011).

In this thesis, both implicit and explicit finite element solution methods are used. Where possible, implicit solution methods are applied to the analyses of Chapter 4. Explicit solution methods are applied in Chapters 4, 5 and 6 where the analyses consist of superelastic Nitinol properties, hyperelastic tissue properties, large deformations and complex contact conditions.

3.5 Figures

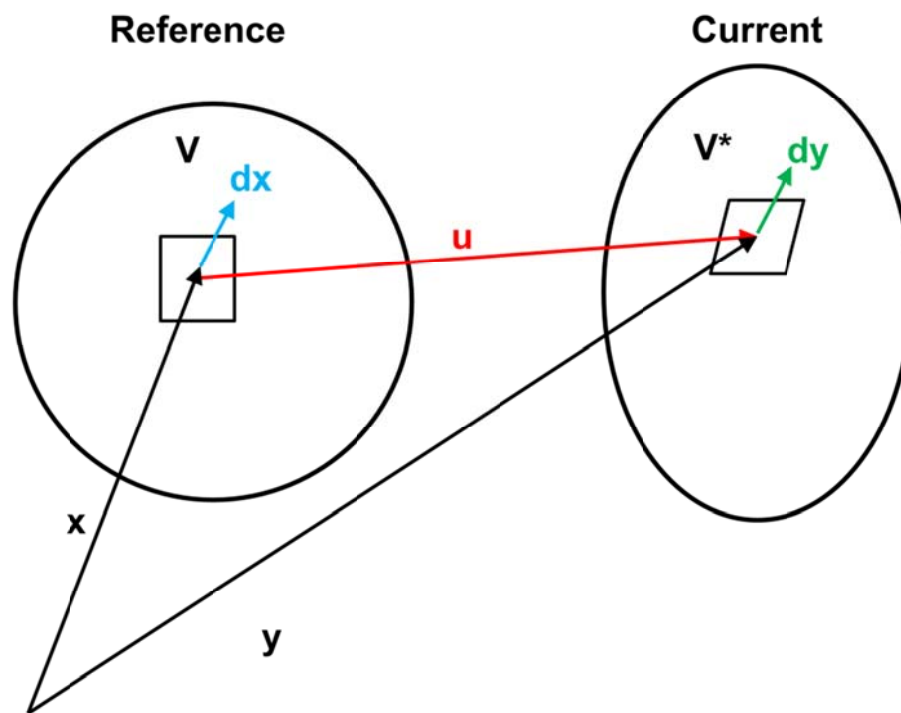
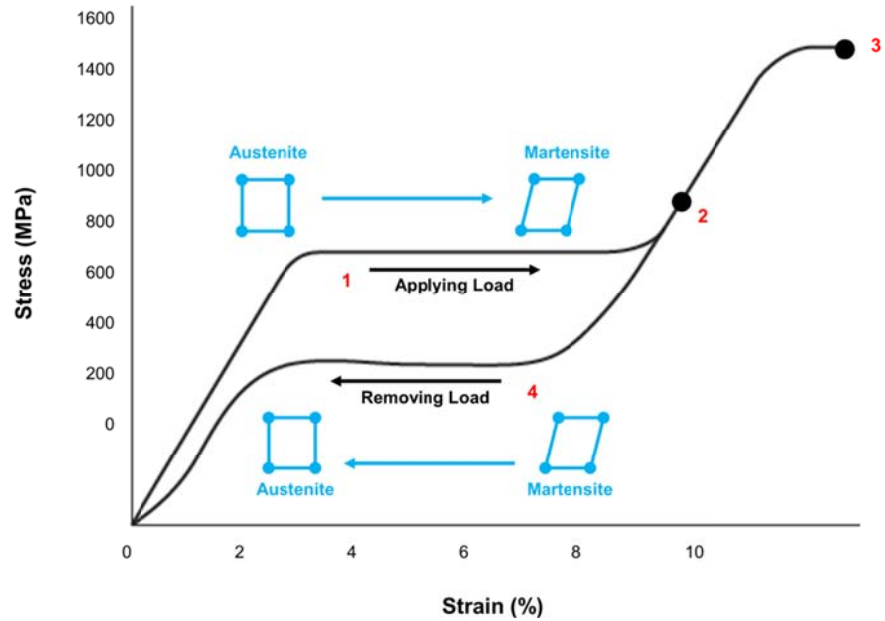


Figure 3.1 Schematic diagram of finite deformation kinematics where V is a reference volume which changes to a current volume V^* and u is a displacement vector of a material point defined by vectors x and y (Fagan, 1992).



- 1 – Applying Load – Start of superelastic loop, austenite transforms to martensite
- 2 – Proportional Limit
- 3 – Elastic Limit
- 4 – Removing Load – Reverse of superelastic loop - martensite transforms back to austenite

Figure 3.2 Nitinol superelastic transformations (Auricchio et al., 1997a, Auricchio et al., 1997b, O'Brien et al., 2011).

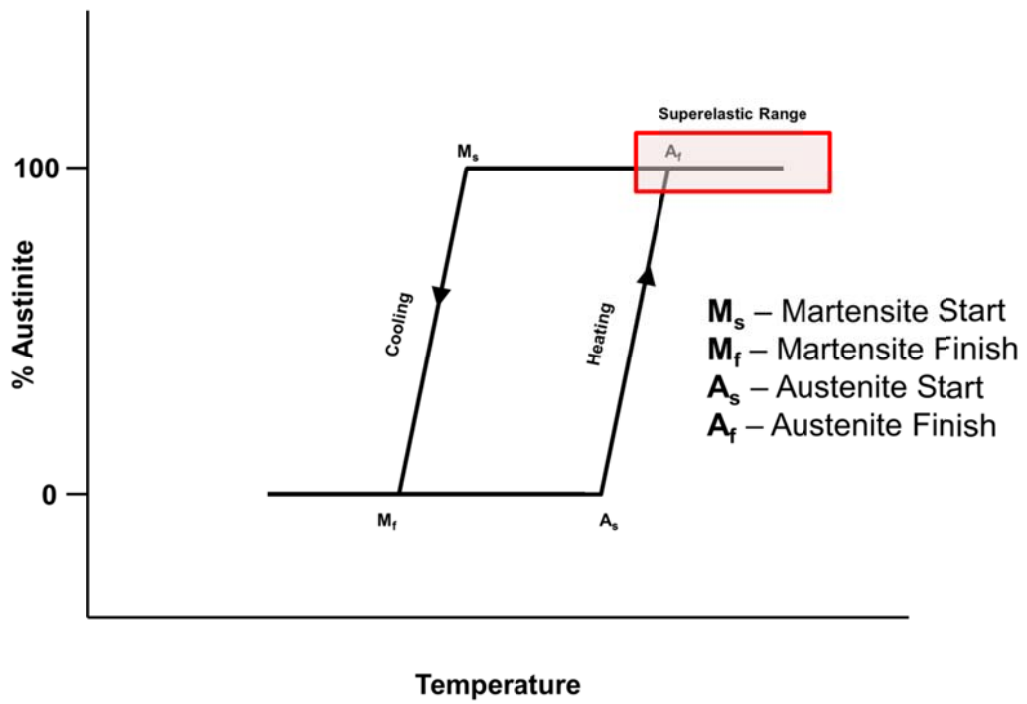
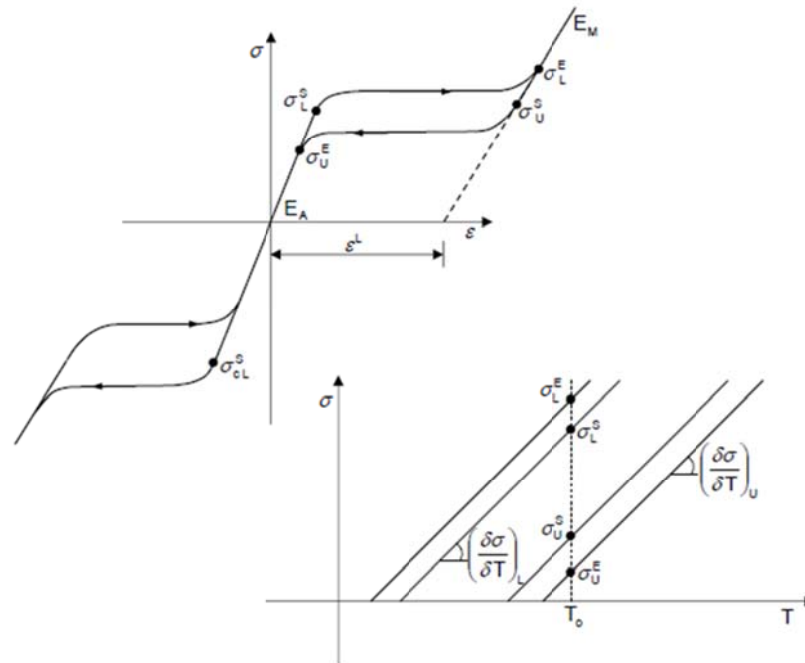
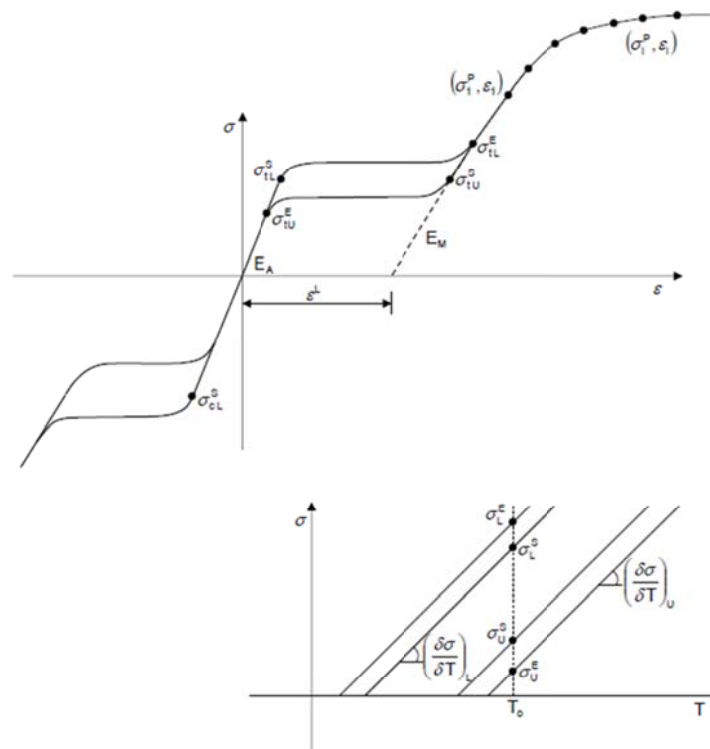


Figure 3.3 Shape memory transformation temperatures (Auricchio et al., 1997a, Auricchio et al., 1997b, O'Brien et al., 2011).



E_A	Austenite elasticity
ν_A	Austenite Poisson's ratio
E_M	Martensite elasticity
ν_M	Martensite Poisson's ratio
ε^L	Transformation strain
$\left(\frac{\delta\sigma}{\delta T}\right)_L$	$\delta\sigma/\delta T$ loading
σ_L^S	Start of transformation loading
σ_L^E	End of transformation loading
T_0	Reference temperature
$\left(\frac{\delta\sigma}{\delta T}\right)_U$	$\delta\sigma/\delta T$ unloading
σ_U^S	Start of transformation unloading
σ_U^E	End of transformation unloading
σ_{cL}^S	Start of transformation stress during loading in compression, as a positive value
ε_V^L	Volumetric transformation strain. If $\varepsilon_V^L = \varepsilon^L$, an associated algorithm is used, with ε_V^L computed based on σ_L^S and σ_{cL}^S
N_A	Number of annealings to be performed during the analysis
$N_{S1} - N_{SNA}$	Step numbers at which all state dependent variable are set to zero

Figure 3.4 Material constants required for Abaqus UMAT of superelastic material (Abaqus, 2011).



E_A	Austenite elasticity
ν_A	Austenite Poisson's ratio
E_M	Martensite elasticity
ν_M	Martensite Poisson's ratio
ε^L	Transformation strain
$\left(\frac{\delta\sigma}{\delta T}\right)_L$	$\delta\sigma/\delta T$ loading
σ_L^S	Start of transformation loading
σ_L^E	End of transformation loading
T_0	Reference temperature
$\left(\frac{\delta\sigma}{\delta T}\right)_U$	$\delta\sigma/\delta T$ unloading
σ_U^S	Start of transformation unloading
σ_U^E	End of transformation unloading
σ_{CL}^S	Start of transformation stress during loading in compression, as a positive value
ε_V^L	Volumetric transformation strain. If $\varepsilon_V^L = \varepsilon^L$, an associated algorithm is used, with ε_V^L computed based on σ_L^S and σ_{CL}^S
N_p	Number of stress-strain pairs to define yield curve
$\sigma_1^p, \varepsilon_1^p, \dots, \sigma_{N_p}^p, \varepsilon_{N_p}^p$	Stress-strain points in the yield curve

Figure 3.5 Material constants required for Abaqus VUMAT of superelastic material (Abaqus, 2011).

3.6 References

- Abaqus. 2011. Abaqus Theory Manual (v.6.11). Dassault Systèmes.
- Auricchio, F and Taylor, RL. 1997a. Shape-memory alloys: modelling and numerical simulations of the finite-strain superelastic behavior. *Computer Methods in Applied Mechanics and Engineering*. 143: 175-194.
- Auricchio, F, Taylor, RL, and Lubliner, J. 1997b. Shape-memory alloys: macromodelling and numerical simulations of the superelastic behavior. *Computer Methods in Applied Mechanics and Engineering*. 146: 281-312.
- Dobrin, PB, Vascular Mechanics, in *Comprehensive Physiology*, 2011, John Wiley & Sons, Inc.
- Fagan, J, *Finite Element Analysis: Theory and Practice*, 1992, Longman Scientific & Technical: Essex.
- Fung, Y. 1967. Elasticity of soft tissues in simple elongation. *American Journal of Physiology*. 213: 1532-1544.
- Fung, Y, *Biomechanics: mechanical properties of living tissues*, 1993, Springer: New York.
- Gasser, TC, Ogden, RW, and Holzapfel, GA. 2006. Hyperelastic modelling of arterial layers with distributed collagen fibre orientations. *Journal of the Royal Society Interface*. 3: 15-35.
- Holzapfel, G, Gasser, T, and Ogden, R. 2000. A New Constitutive Framework for Arterial Wall Mechanics and a Comparative Study of Material Models. *Journal of Elasticity*. 61: 1-48.

- Holzapfel, GA. 2006. Determination of material models for arterial walls from uniaxial extension tests and histological structure. *Journal of theoretical biology*. 238: 290-302.
- Holzapfel, GA and Ogden, RW. 2010. Constitutive modelling of arteries. *Proceedings of the Royal Society A: Mathematical, Physical and Engineering Science*. 466: 1551-1597.
- Holzapfel, GA, Sommer, G, Gasser, CT, and Regitnig, P. 2005. Determination of layer-specific mechanical properties of human coronary arteries with non atherosclerotic intimal thickening and related constitutive modeling. *American Journal of Physiology - Heart and Circulatory Physiology*. 289: H2048-H2058.
- Holzapfel, GA, Sommer, G, and Regitnig, P. 2004. Anisotropic mechanical properties of tissue components in human atherosclerotic plaques. *Journal of Biomechanical Engineering*. 126: 657-665.
- Humphrey, JD. 1995. Mechanics of the arterial wall: review and directions. *Critical Reviews in Biomedical Engineering*. 23: 1-162.
- Humphrey, JD. 2003. Review Paper: Continuum biomechanics of soft biological tissues. *Proceedings of the Royal Society of London. Series A: Mathematical, Physical and Engineering Sciences*. 459: 3-46.
- O'Brien, B and Bruzzi, M, 1.104 - Shape Memory Alloys for Use in Medicine, in *Comprehensive Biomaterials*, 2011, Elsevier: Oxford.
- Spencer, AJM. *Constitutive Theory for Strongly Anisotropic Solids*, in *Continuum Theory of the Mechanics of Fibre-Reinforced Composites*, 1984, Springer-Verlag New York.

Zienkiewicz, OC and Taylor, RL, The finite element method for solid and structural mechanics, 2005, Butterworth-Heinemann: Oxford.

Chapter 4. Local Analysis of Stent-Artery Interactions in the Superficial Femoral Artery

4.1 Introduction

Computational simulations of balloon expandable and self-expanding stents using finite element analysis are commonly used as a tool to determine the structural integrity of the stent as well as to investigate the nature of the interaction between the stent and the artery. As there are many stent designs available in today's market, understanding the effects of different stent designs is vitally important in the development of new stent designs as shown in previous studies (Barth et al., 1996, Capelli et al., 2009, David Chua et al., 2004b, Kastrati et al., 2000, Wang et al., 2006b). Such studies have shown that stent design has a significant impact on the success or failure of the stent *in-vivo*. These experiments not only assessed stent designs and determined their chronic performance, but also investigated links with thrombosis and neointimal hyperplasia. It has been shown that upon deployment and contact with the blood vessel wall, stent struts cause immediate vascular injury (Barth et al., 1996, David Chua et al., 2004a, Kastrati et al., 2000) and it is believed that the degree of restenosis is related to the extent of damage done at the time of stent implantation (Gunn et al., 1999). It is also believed from experimental results that stent design influences neointimal growth after deployment (Carter et al., 1997, Gunn et al., 1999). These results highlight the necessity of accurately modelling stent-artery interaction.

More recently, computational simulations investigating the effects of stent deployment, contact interactions between stent struts and the accurate representation of arterial tissue have become increasingly popular in assessing the viability of stent designs (Auricchio et al., 2011, Balossino et al., 2008, Capelli et al., 2009, Conti et al., 2009, David Chua et al., 2004b, Early et al., 2009, Gasser et al., 2007, Gastaldi et al., 2010, Gervaso et al., 2008, Holzapfel et al., 2005b, Holzapfel et al., 2002, Lally et al., 2005, Liang et al., 2005, Moore et al., 2002, Mortier et al., 2009, Pericevic et al., 2009, Prendergast et al., 2003, Qiu et al., 2000, Rebelo et al., 2006, Timmins et al., 2008, Walke et al., 2005, Wu et al., 2007a, Wu et al., 2007b, Zunino et al., 2009).

Not only are computational simulations cheaper than experimental studies, they allow for focus on specific areas of interest and provide a means of comparing *in-vivo* and *in-vitro* experiments that can complement each other to give ground breaking conclusions. Many research groups have published results of complex computational investigations simulating the deployment of stents into blood vessels. The models created in these studies consist of a number of complex components such as user defined material models for stent materials (Auricchio et al., 2011, Conti et al., 2009, Rebelo et al., 2006, Wu et al., 2007a); user defined material models for arterial tissue and remodelling (Holzapfel et al., 2005b, Holzapfel et al., 2002, Lally et al., 2004, Prendergast et al., 2003); curved, branched and tapered arterial geometry (Liang et al., 2005, Mortier et al., 2009, Rebelo et al., 2009, Timmins et al., 2008, Wu et al., 2007b); regular and irregular plaque geometries along with various plaque material models (Gasser et al., 2007, Gastaldi et al., 2010, Pericevic et al., 2009); fluid interactions (Balossino et al., 2008, Moore et al., 2002, Qiu et al., 2000, Zunino et al., 2009) and *in-vivo* loading including pulsatile, torsion and bending of stented arteries (Early et al., 2009). Furthermore, many of these studies use combinations of these complex components delivering results of powerful simulations that accurately capture the interactions involved in stent deployment processes. Results of such investigations allow for the evaluation of stent-artery interactions both during and following stent deployment and can provide much insight into the behaviour of specific stent designs in a physiological surrounding and depict the behaviour of the stented vessel. However, most of these studies require large computational models which require the use of large amounts of solver time on large scale super computers which can increase the costs of such investigations. There is no doubt that recent studies published have pushed the boundaries of stent-artery modelling and reveal highly complex models that will become more and more complex in the future hence increasing the computational resources required. Each additional component of the analysis attempts to improve accuracy of the computational simulation by making a more realistic model. However, using all of these elements simultaneously within one model represents a significant challenge. Hence there is a need to assess the effect of simplifying these problems and modelling approaches in an effort to reduce computational time and increase the efficiency of such studies. In the past, many researchers have used unit cell models when analysing stent performance. These models reduce the amount of

the stent modelled in an analysis, assuming symmetry or periodicity of the stent and artery in axial planes and planes transverse to the artery central axis. One such study by McGarry et al. (2004) compared the performance of a 2D representation of the repeating unit cell of the NIR stent (Boston Scientific, Natick, MA, USA) during expansion, recoil and cyclic pulsatile loading when its material behaviour was defined using either macroscopic or microscopic mathematical material models. Whilst this study demonstrates the usefulness of unit cell models in comparative studies, providing a means of reducing the size of a computational analysis, unit cell models cannot be used in all computational investigations of stents. For example, for the investigation of stents in combination with physiological loading (bending, compression or torsion), a full representation of the stent geometry must be modelled. Furthermore, in most cases, physiological loads cannot be applied in a symmetric or periodic way. It is therefore necessary to find a means of reducing the computational expense of stent models whilst keeping the full geometry.

Stent foreshortening is a feature of stent design where the axial length of the stent changes as the stent expands i.e. the crimped length of the stent is different to that of the expanded stent length. This foreshortening effect is commonly recognised within the literature and the clinical community (Wang et al., 2006a). It is a key quality of stent design as almost all stents have some degree of foreshortening which affects precise placement of the stent upon expansion in the target vessel. Incorrect positioning of the stent can lead to injury of the vessel wall and effect stent patency. Therefore, accurate modelling of stent foreshortening in computational models is essential for models that contain both the stent and artery geometries that aim to investigate stent-artery interactions. However foreshortening effects present considerable challenges to computational modelling methods of stent-artery interactions. As the length of the stent changes from the initial crimped configuration to the expanded configuration it is difficult to determine the initial geometry of the artery for symmetric and periodic boundary stent geometries, such that the combined deployed stent-artery is also symmetric and/or periodic.

With the objective of reducing computational cost of stent models, Hall and Kasper (2006) carried out a study that compared the performance of different element types in the modelling of stent deployment. The BX Velocity stent was

represented with a number of different models using 3D solid, 2D shell and beam elements. Results highlighted that significant reductions in computational time can be achieved by modelling stents with beam elements in place of shell or solid elements with similar stress and strain magnitudes and locations predicted by all three element types. The appropriate use of the various element types in stent-artery interactions, however, was not investigated.

This chapter presents two studies. Firstly, a study of appropriate modelling approaches for stent-artery interactions is presented. These modelling approaches are then applied in a second study to a model that investigate the effect of physiological loading conditions on the stented SFA.

4.2 Radial Force Accuracy and Modelling Approach

In this investigation, finite element analysis is used to simulate the expansion of a stent geometry based on that of the Cordis SMART™ femoral artery stent, in order to investigate computational modelling approaches of stent-artery interactions. Specifically, the aim of this study is to investigate how different methods of modelling approaches can affect the predicted radial force values and stress concentrations imposed by the self-expanding stent during deployment, the computational time taken and the computational size of the model. Total radial force of the stent during crimp and deployment is computed and compared for the various modelling approaches and, in specific cases, the resulting stress concentrations in the artery after deployment are computed and compared for each case. The different modelling approaches used to simulate the stent delivery, represent increasing levels of complexity, negating the many assumptions and simplifications that could be proposed or which have been used in other similar studies to date (Conti et al., 2009, Gong et al., 2004, Kleinstreuer et al., 2008, Pelton et al., 2008, Wu et al., 2007a). Three different representations for the stent geometry are considered; the geometry represented by a 1/6th constrained unit cell, a 2-ring periodic unit cell, and a reduced length version of the full stent geometry. As each of these geometrical representations (dependent on the specific stent geometry) requires certain assumptions in order to ensure accurate modelling, the focus of this initial study is to explore the effects of periodic and symmetric boundary condition assumptions when modelling stent geometries. Stent crimping and deployment is simulated for all models and the resulting radial displacement and radial force of each stent is compared. Comparisons are made of different techniques for simulating stent crimping including the use of radial displacement boundary conditions and using contact with a rigid cylinder to effect the change in diameter. The effect of self contact of the stent during crimping, and the effect of this on the radial force of the stent upon deployment is also investigated. Finally, the incorporation of large strain or small strain geometrical effects is investigated to establish if there is any effect on the subsequent radial force of the stent during the crimping-deployment cycle.

4.2.1 Materials and Methods

Abaqus/Standard and Abaqus/Explicit finite element software were used to develop the models compared in this study. The models aimed to represent the geometry, material properties and loading conditions of both the stent and blood vessel throughout the stenting procedure.

Stent Geometry

The stent used for the model was based on the Cordis SMART™ stent (outer diameter (OD) 7mm, length 20mm). This self-expanding stent is made of a Ni-Ti alloy, 'Nitinol', a material commonly used for self-expanding stents used in peripheral arteries (Kleinstreuer et al., 2008). The stent is composed of a repeating multi segmented design with connecting offset bridges as shown in Figure 4.1. As mentioned, the stent was modelled with three different representations of the geometry; a 1/6th constrained unit cell, a 2 ring periodic unit cell, and a reduced length version of the full stent geometry. The terminology detailed in Table 4.1 will be used to differentiate between the different geometries. It is necessary to model two rings and not just a single ring as the connecting offset bridges cause the two rings to rotate in respect to one another upon expansion of the stent, leaving the adjacent crown structures off-set from one another. This relative rotation can only be represented by incorporating two rings within the periodic model. A tangentially constrained version of the 1/6th unit cell was chosen to represent a reduced geometry of the 2 ring periodic geometry model. Ideally, a true 1/6th periodic unit segment of a full 2 ring periodic unit cell should allow for ring rotation and therefore on deployment lead to a configuration of two offset rings as previously described. However, in order to match this periodic stent geometry with an appropriate periodic artery geometry to determine contact stresses on the artery, a prediction of the final artery segment geometry in contact with a 1/6th periodic unit cell of the stent would be required. Such a representative artery section would take the shape of the section shown in Figure 4.1(a) (highlighted by the red lines) but is difficult to predict, and would have to be determined iteratively. Therefore, boundary conditions were used to constrain the 1/6th periodic unit cell representation to not allow any relative motion of the 2 rings with respect to each other leading to a 1/6th constrained unit cell

geometry. This represents a significant over-constraint of the real stent behaviour, but is interesting to see how it affects the overall radial force imposed on the artery.

As shown in Figure 4.2(a) the manufacturing process of the SMART™ stent typically involves the stent geometry being cut from 3 mm outer diameter (OD) Nitinol tubing, and expanded to 7 mm OD by placing the stent over a cylindrical mandrel. The stent is then shape set by heat treating the stent and mandrel, resulting in a stress free configuration of the stent at 7 mm OD. This is then crimped to approximately 2 mm OD during loading of the stent into its delivery sheath. In order to accurately represent this manufacturing process, and the stress state of the stent in this analysis, the following modelling steps were used (Figure 4.2 (b)). The ‘as cut’ geometry of each configuration was created using SolidWorks 3D CAD design software 2008 (Dassault Systèmes Simula Corp, Vélizy, France). It was then imported into Abaqus/Standard (Version 6.8, Dassault Systèmes Simula Corp, Vélizy, France) in a planar state, meshed, wrapped into a cylindrical state (by mapping the nodes into a cylindrical coordinate system from the Cartesian coordinate system of the planar state) and offset to create a thickness of 0.2mm. When required, nodes were merged at the connecting ends of the cylindrical configuration. The 1/6th constrained unit cell, 2 ring periodic and full geometries were meshed with 10,515, 65,866 and 127,050 8-node linear 3D stress elements (C3D8R) respectively. The suitability of the mesh density used in the analysis was determined from a mesh dependency study. The mesh density was increased from 2,698 elements to 12,269 elements for each periodic unit. The percentage difference in maximum Von Mises stress (MPa) in the stent between the mesh selected and the finest mesh studied was 0.024MPa. There are 4 elements over the thickness and width of the stent strut. Once meshed, each stent model was expanded from the ‘as cut’ geometry of 3 mm OD to 7 mm OD using a rigid cylindrical body placed inside the stent and expanded out to 7 mm OD using radial displacement boundary conditions applied to the rigid cylinder. The expanded geometry of each stent representation was exported and used as the ‘stress free’ configuration for the study. It is worth highlighting that this expanded (stress free) geometry (shown in Figure 4.3) is not uniformly cylindrical due to deformation within the stent struts as highlighted in Figure 4.3. Abaqus/Standard was used for the simulations that compare the use of self contact, alternative crimping methods and the effect of a

small or large strain analysis. For the remainder of simulations – those that involve stent-artery contact, Abaqus/Explicit was used due to the non-linear material behaviour and contact conditions within the models. Quasi-static Abaqus/Explicit simulations were performed, allowing the simulations to run at a reasonable computational cost. Computational cost was reduced by using mass scaling, enabling the minimum stable time increment to be increased. For all simulations, static equilibrium was ensured within the analysis and verified by a ratio of kinetic energy (ALLKE) to internal energy (ALLIE) of less than 5%. Simulations were performed on a Bull Novascale high performance computer using 4 nodes each with two 2.8GHz quad-core processors.

Artery Geometry

For the purpose of investigating the effects of the various modelling approaches, described, on resulting local stress concentrations on the vessel wall, a vessel was modelled with OD 7.2 mm and wall thickness 0.6 mm, representative of the SFA in which Nitinol stents such as the 7mm OD Cordis SMART™ stent would be used (Smilde et al., 1998, Tai et al., 1999). Each of the three representations of stent geometry, 1/6th constrained unit cell; 2 ring periodic and full geometry required individual corresponding artery geometries to ensure periodicity of the entire model. For the 1/6th constrained unit cell, just a corresponding 1/6th segment of the artery was modelled and similarly for the 2-ring-periodic representation a corresponding periodic segment – that which only those rings of that specific stent representation would be in contact with was modelled. Finally, for the full geometry an infinitely long piece of artery was modelled as this full geometry had no periodic or unit cell entities. This allowed the end effects of the stent within the artery to accurately be assessed. The dimensions of the 1/6th segment of the artery were determined by measuring the 1/6th constrained unit cell of the SMART™ stent upon deployment to determine the associated contact area of the arterial segment. Similarly, the length of the segment for the 2 ring periodic geometry stent model was determined by measuring the expanded length of the stent so as to model only the portion of the artery that would be in contact with the two rings of the stent modelled. Stent foreshortening was considered, using Figure 4.4 to determine the artery periodic length for the simulation.

In contrast to other computational studies (Auricchio et al., 2011, Gijzen et al., 2008) which focus on patient specific vessel geometries, this study focuses on the methodologies of computational modelling such as boundary conditions, non-linear geometry and methods of simulating stent crimping. Therefore, idealised cylindrical vessel geometries are used in this work which may not be directly relevant to patient specific diseased vessels, but they do allow comparisons of symmetric, periodic and whole stent geometries which is the primary focus of the study.

The artery was meshed using 391,625 8-node linear brick reduced integration elements with hourglass control (C3D8R) for the full geometry model and 110,458 of the same element type for the 2-ring-periodic geometry model. The 1/6th constrained unit cell geometry artery was meshed with 20,160 elements of the same element type. Mesh convergence was carried out to ensure accuracy of the mesh density used in the analysis where the percentage difference in Von Mises stress between the mesh selected and the finest mesh studied was 0.016%.

Analysis Steps

The analysis of each stent model contained two steps; stent crimping and stent deployment. The crimp step involves reducing the stent diameter to 2 mm from its stress free (near cylindrical) diameter of 7 mm. The stent deployment step allows the stent to expand out to its original stress free diameter through release of its internal strain energy. Both steps require the definition of boundary conditions and contact interactions, in the following sections. Appropriate boundary conditions are an important aspect of the comparative study presented here as each geometrical representation requires different levels of assumptions in order to ensure accurate representation of the geometry. For the models used to model stent-artery contact of the three representations of stent geometry, a third step was added to the analysis in which stent-artery contact was initiated.

Stent Crimping

In this step, the Nitinol SMART™ stent was crimped to have an OD of 2mm. It is necessary to crimp the stent in a realistic fashion as part of the analysis due to the hysteresis in the loading-unloading properties of superelastic Nitinol. This

was achieved by imposing a radial displacement boundary condition on a rigid cylinder, and allowing surface to surface frictionless tangential and hard normal contact between the outer surface of the stent and the inner surface of the rigid cylinder. The 2-ring periodic geometry model was used to compare this method of crimping with that of imposing a radial displacement constraint on the outer surface of the stent to simulate crimping. The radial displacement boundary condition was assigned directly onto the nodes on the outer surface of the stent that reduced the stent outer diameter to 2 mm.

Stent Deployment

After the crimping, the stent was allowed to feely expand due to its stored elastic strain energy and the reversal of the Nitinol stress induced phase transformation. In order to analyse the contact force during this step, contact is maintained between the rigid cylinder (used to crimp the stent) and the outside surface of the stent as in the previous step. All displacement boundary conditions (conditions imposed during crimp) are removed and the stent expands due to the internal energy of the Nitinol material, resuming its stress free state. For the radial displacement crimp model, the rigid cylinder used in the other analyses is introduced in the deploy step to allow computation of radial force by initiating contact between the outside surface of the stent and inside surface of the rigid cylinder.

Throughout both analysis steps, the stent was restrained as follows: A tangentially constrained version of the 1/6th constrained unit cell was chosen to represent a reduced geometry of the 2 ring periodic geometry model. This required the nodes on the four periodically symmetric faces at the top and bottom of the unit cell to be constrained in the tangential direction. The radial displacements of the two periodically symmetric faces at the sides of the unit cell were coupled to prevent out of plane motion. Additionally, to prevent rigid body motion, one node of the stent was restrained in the axial (z) direction. For the 2 ring periodic geometry model, nodes on the crown faces of the struts at one end of the model were constrained to allow for periodicity, with one node restrained in the axial direction to prevent rigid body motion. For the full geometry model, only a single node was constrained in the axial direction, preventing rigid body motion.

Arterial Contact

For the models used to model stent-artery contact of the three representations of stent geometry, a third step was added to the analysis in which surface to surface frictionless tangential contact and hard normal contact behaviour was initiated between the outside surface of the stent and inner surface of the artery. Contact between the stent and rigid cylinder is de-activated for these models upon expansion of the stent once the stent is within close proximity to the vessel. Frictionless contact was deemed appropriate for this investigation. Whilst it is recognised and accepted that friction will influence contact conditions, it can be assumed negligible in terms of effect on the outward radial force of the stent on the vessel wall, the primary focus of this study. Furthermore it is accepted that the effect that friction may have on the results will be the same for all models, and by using frictionless contact as a standard for each model, that a rational simplification has been made that ensures comparable and meaningful results to be obtained.

Stent Material

A constitutive model that simulates superelastic behaviour of shape memory alloys such as Nitinol is used in this study to model the material of the stent. It is implemented by an in built user-defined mechanical material behaviour (UMAT for Abaqus/Standard or VUMAT for Abaqus/Explicit). This allowed both the loading and unloading hysteresis of Nitinol to be represented. Figure 4.5 shows a schematic stress strain curve of Nitinol material behaviour on which this UMAT is based. The values that accompany the stress strain curve, used in the UMAT are listed in Table 4.2, obtained from a tensile test performed on the stent material. The tensile test of the material was conducted in another study by a commercial partner on samples of Nitinol at 37 degrees centigrade.

Artery Material

The vessel tissue is modelled using a sixth-order reduced polynomial strain energy density function for isotropic hyperelasticity (discussed in Chapter 3, section 3.2.3 of this thesis) previously used by Gastaldi et al. (2010). This model employs a constitutive law which models incompressible materials allowing for large strains based on experimental data by Holzapfel et al. (2005b) of stress strain tests of

arterial layers. Despite the findings of Holzapfel et al. that arterial tissue exhibits anisotropic behaviour, isotropic data was included in this study. The main objectives of the study are to assess the impact of different computational stent models on the outward radial force of the stent. Whilst the impact that this has on arterial tissue is considered in the results, directional dependence of the tissue does not relate back to the radial force of the stent as the radial force of the stent will be the same regardless of the model used for the arterial tissue. Therefore isotropic material properties are used for simplicity. Each arterial layer is represented by different parameters in the model thereby allowing a layer specific (intima, media, and adventitia) artery to be represented. The material constants required for implantation of the model in Abaqus are listed in Table 4.3.

4.2.2 Results

Stress, strain, deformation and radial force values of the stent were evaluated for each model simulation performed. Radial force was computed by summing the radial force in the circumferential direction (acting on a surrounding rigid cylinder) at every node on the outside surface of the stent during the crimp and deployment steps. This captured the effects of stent behaviour during the unloading portion of the analysis (at which stent-artery interactions are significant) and how this varies with modelling approaches. (Note that for the radial displacement crimp model, the radial force during crimp is computed by the summing the reaction force at every node on the outside surface of the stent where radial displacements are applied). The stress and deformation fields imposed by the stent on the artery were also evaluated for each geometrical representation of the stent.

Self Contact

The 1/6th constrained unit cell geometry was used to investigate the effect of neglecting self contact of the stent on its radial force during the analysis. Figure 4.6 shows a Von Mises stress contour plot and strain contour plot of the geometry after crimping. Figure 4.7 compares the radial force profile with radial displacement of the stent with and without self-contact. Although significant differences in the crimped geometry can be observed in the Von Mises stress of the stent (Figure 4.6(a) and Figure 4.6(b)), there is not a significant difference in the radial force imposed by the stent as it unloads from its crimped configuration. This is discussed in more detail in section 4.2.3. There is also no significant difference in the strains observed in the stent (Figure 4.6(c) and Figure 4.6(d)).

Crimp Method

Two techniques of simulating stent crimping were considered in this study. The 2 ring periodic geometry was used for this comparison. Firstly, the use of a cylindrical rigid body, with contact between the inner surface of the rigid body and outer surface of the stent was used. Using this technique, radial displacement boundary conditions were applied to the rigid body in order to crimp the stent to an OD of 2 mm. Secondly; the use of radial displacement boundary conditions, directly

applied to the outer surface of the stent to achieve the same crimp was considered. Figure 4.8 compares the different geometries, stress and strain concentrations in the two models at the end of the crimp step, in which both models are crimped to 2 mm. Maximum strains in the rigid body crimp and radial displacement crimp models are 8.39% and 7.40% respectively. It is clear that the different crimp methods result in different crimped geometries. As seen in Figure 4.8(c), the rigid body crimp method provides a highly cylindrical crimped geometry. In comparison, Figure 4.8(d) displays a significantly less cylindrical configuration.

At first, the geometric results shown in Figure 4.8 appear counter-intuitive. However, on closer examination, the starting geometry of the stent was not perfectly cylindrical at its shape formed 7 mm diameter, and the radial offset of the stent struts from a perfectly cylindrical configuration appear magnified at the crimped 2 mm diameter. This is discussed in more detail in the discussion section of this study. Figure 4.9 compares radial force profile with radial displacement of the stent for both crimping methods. There is a significant difference in the loading (crimping) curves for both methods with higher radial displacements. This is discussed in more detail in the discussion section of this study.

Geometry

Figure 4.10 shows the three different geometry representations at the end of the analysis i.e. at the end of the deployment step. The two middle rings of the full geometry model represent the 2 ring periodic geometry. When comparing these models it can be seen that the deployed configurations of the geometries have slight differences in stress concentrations. Figure 4.10 focuses on identical locations in each geometry and shows the different Von Mises stress concentrations of each representation. Arrows in Figure 4.10 highlight regions of differing stress locations and differing deployed geometry. The radial force results, as shown in Figure 4.11, show that the $1/6^{\text{th}}$ constrained unit cell geometry displays up to 30% higher radial force during the deployment step. The maximum strain result for the $1/6^{\text{th}}$ -constrained-unit-cell, 2-ring-periodic and full stent geometry are 5.34%, 6.03% and 7.02% respectively at the hinges of the struts with average strains in the bars of the struts at 0.0089%, 0.0050% and 0.0059% respectively.

Large Strain versus Small Strain Analysis/Geometric Non-Linearity

The 2 ring periodic geometry was used for the comparison of a ‘small-displacement’ and ‘large-displacement’ analysis of the SMART™ stent. Geometric non-linearity was accounted for using the NLGEOM function in Abaqus. The 2 ring periodic geometry was crimped using a rigid body for this comparison. As expected, differences exist in the results of simulations conducted with small and large strain configurations. Similar levels of Von Mises stress are found in the two models. However, the contour plots show slight variations in stress concentrations between the models, these are highlighted in Figure 4.13(a) and Figure 4.13(b). Furthermore, differences are found between the maximum and minimum stresses of the models. Although these locations of maximum and minimum stress are in identical regions of the models, the values differ by a margin between 8.9% and 3.2% as shown in Table 4.4. Comparison of radial force values of the models shows that upon the crimp step, the radial force of the two models differs, but is broadly similar for stent deployment (i.e. stent unloading) as shown in Figure 4.14. The strain result of the models is also broadly similar as shown in Figure 4.13(c) and Figure 4.13(d) with maximum strains of 0.070% and 0.075% in the ‘small displacement’ and ‘large displacement’ models respectively.

Artery Contact

Stress concentrations on an artery as a result of stent deployment were assessed for the models. Figure 4.12 compares the arterial stresses at the end of stent deployment step. Stress concentrations are similar for the three models with bands of higher stress seen at the end regions of the artery section associated with the full geometry highlighting the presence of end effects due to a stiffness mismatch between the stented and un-stented portions of the artery. This is discussed in more detail in the following section which investigates stresses in the stented SFA due to stent deployment and physiological loading.

4.2.3 Discussions

The aim of this study was to investigate the effects of modelling approaches on the predicted radial force values imposed by a self-expanding stent, hence leading to stress concentrations within an artery. The effects of self contact, crimp method, model geometry and geometric non-linearity were investigated in an effort to assess how modelling approaches may be made simpler without significant effects on accuracy. A clear difference in the crimped geometry is observed when self contact is included. However, this difference in resulting geometry at the end of crimp does not translate to a notable difference in radial force, as shown in Figure 4.7, when the material is assumed to behave purely elastically. The radial force differs by only 0.02% when self contact is neglected. However, it is worth noting that plastic deformation and damage mechanisms that are not represented in this computational model may, in reality, be initiated resulting in a different level of radial support.

As highlighted, the different crimp methods result in different crimped geometries, shown in Figure 4.8. This, at a first glance, does not appear to be intuitive. However, as mentioned previously, the geometry of each stent representation at the beginning of the analysis is taken from a previous analysis that expanded the stent from its 'as cut' to a 'stress free' configuration. This change in diameter (from 3 mm to 7 mm OD) was achieved through simulating the expansion of the stent by contact with a cylinder and not through radial displacement constraints that would ensure that the stent would remain perfectly cylindrical at all diameters. This method of shape setting the stent at its nominal 7mm diameter represents the physical processing of the stent. As a result of this method of expansion, the stent is not a 'perfect cylindrical' at the start of the crimping analysis. This is shown in Figure 4.4. Following this (i.e. during the radial displacement crimp) these deviations are translated to the crimped (2 mm OD) configuration as a fixed displacement is applied to each node on the outer surface of the stent. Once translated through the crimp step, these deviations become more pronounced as can be seen in Figure 4.8(d) where it is apparent that there are clear deviations of the stent struts from a cylindrical configuration. This is reflected also when comparing the ratio of the average radius of the outside nodes to the 3.5 mm radius of the stress free configuration which is 1.048, to the ratio of the average radius of the outside

nodes to the 1 mm radius of the crimped configuration which is 1.167. This ‘non uniform’ crimped geometry is not the case with the rigid body crimp method. In this method, the nodes on the outer surface of the ‘stress free’ configuration are in contact with a cylindrical body throughout the crimp step and therefore conform to a more cylindrical crimp. Deviations are still seen in the crimped (2 mm OD) configuration but are very small, similar to those at the start of the analysis. This method of crimp is more representative of the manufacturing process of the stent. Figure 4.9 shows the comparison of the resultant radial force of the stent due to the different methods of crimping. It can be seen that the radial displacement crimp displays a lower radial force than that of the rigid body crimp upon deployment. This can be explained by the fact that the stent crimped with radial displacements does not conform to a perfectly cylindrical configuration on its outside surface due to the translation of deviations from a perfectly cylindrical shape of the stress free configuration. Consequently, the contact area of the stent crimped with radial displacements will be less than that crimped with the rigid cylinder leading to a lower contact force. (‘Contact area’ in this case is the term given to the outer surface of the stent that will be in contact with any surrounding surface upon deployment. Therefore as the stent is deployed in an artery, the contact area will be the regions of arterial tissue that is contacted by the outer surface of the stent as it deploys. This influences contact force as the amount of arterial tissue (area) contacted by the stent is directly proportional to the force experienced by the arterial tissue).

Three different representations of the stent geometry were considered in this study; the geometry represented by a $1/6^{\text{th}}$ constrained unit cell of a 2 ring periodic unit cell, a full 2 ring periodic unit cell, and a reduced length version of the full stent geometry. The focus of this was to explore the effects of periodic boundary conditions and assumptions when modelling stent geometries on stent-artery interactions during deployment. Results show that although different geometrical representations of the stent lead to similar deployed configurations of the stent with similar stress concentrations, the $1/6^{\text{th}}$ constrained unit cell geometry overestimates radial force, as displayed in Figure 4.11. It is important to remember that this geometry has additional constraints in order to match it to a periodic arterial segment for accurate modelling of stent-artery interactions. These constraints lead to altered stress concentrations in the $1/6^{\text{th}}$ constrained unit cell geometry predominantly at the

connecting bridges as shown in Figure 4.10. Whilst these differing stress configurations of the stent are significant when focusing on the stent alone, they can be overlooked in the context of this study as the focus is on the effect of geometry reduction on the artery upon stent deployment. In this case it is the radial force result that is most important and it can be seen here that due to constraints applied to the 1/6th constrained unit cell model, radial force is overestimated by 8%, leading to the conclusion that at a minimum, two full rings should be modelled for the analysis.

Although the prime objective of this study is centred on computational modelling approaches and assumptions that are commonly made in such analysis to expedite results, the results presented here can be compared to experimental results of previous studies that measured the radial force of an 8 mm SMART[™] stent (Duda et al., 2000). Duda et al. carried out an experimental study to compare the physical properties of 10 endovascular stents, including the SMART[™] stent. Stents were typically 4 cm in length with a nominal diameter of 8 mm and subjected to a number of standardized physical tests. These tests included measurement of ‘chronic outward force’, the measure of the force the stent exerts radially as it deploys to its nominal diameter. Chronic outward force was determined by a loop test and calculated at expansion of the stent to 7 mm (nominal stent diameter minus 1 mm). The 8 mm SMART[™] stent was reported to have a chronic outward radial force of 0.31 ± 0.08 N/cm according to the study. Taking a proportional approach to calculate a corresponding value for the 7 mm SMART[™] stent modelled in this study, chronic radial force is calculated as 0.091 N/cm for the same level of diameter reduction from the nominal diameter. Although these values differ they are of the same order and it is important to highlight that two different stent sizes are being compared. Furthermore, the inevitable processing conditions of the stent, exact material composition, surface finish/defects, and friction during methods of measuring radial force will lead to differences between the results. The material properties used for the stent model were obtained from a material test carried out on Nitinol samples at 37 degrees centigrade and not on struts of a laser cut stent. Therefore this provides challenge to making a direct comparison of the results presented in this work with experimental results of Duda et al. for the SMART[™] stent.

Focusing on the effects on the artery of stent deployment of the three geometrical representations of the stent, it can be seen from Figure 4.12(a) that the stress concentrations of the 1/6th constrained unit cell model are more pronounced than the other two models. This is expected, as results have shown that the radial force of this geometry is higher upon expansion of the stent. It can also be seen that Figure 4.12(c) displays bands of high stresses at the end regions of the stent due to the stiffness mismatch between the stented and non-stented regions of the artery. These regions are not seen in contact stresses of the 2 ring periodic geometry in Figure 4.12(b). For computational models focusing on assessing the effect of the stent on the artery it is important that these end effects are assessed and therefore a full model provides greater insight into stent-artery interactions. Drawing on this result, the representation of a ‘complete stent’ may be interesting to add in this case, however, a representation such as this would simply be a longer version of the full geometry representation, it would not lead to any further results and therefore would not merit the additional computational time/expense. It is worth noting that stents exist in a variety of lengths, typically from 30mm – 120mm, and the only difference is the number of reinforcing ‘ring structures’.

This study has used an idealised cylindrical vessel geometry to compare the three geometrical representations of the stent. It does not account for the presence of plaque, its stiffness and the resulting discontinuity in radial force. However, even though this study does not directly relate to any patient specific geometry, it does allow for the comparisons presented in this study, of symmetric, periodic and whole stent geometries. As the aims of this study were focused on computational modelling approaches, and how methods of modelling stent-artery interactions can affect the results, computational time and size of the analysis, the idealised cylindrical vessels used for the models were considered as suitable geometries to use. It is acknowledged however, that the results presented here may not be directly relevant to patient specific diseased vessels, where the stiffness may be affected and the geometry may deviate significantly from a cylindrical vessel. As mentioned previously, the findings of Holzapfel et al. showed that arterial tissue exhibits anisotropic behaviour, but that isotropic data was included in this study. It is acknowledged that the results of levels of arterial stress produced here will differ depending on the material model that is applied for the arterial tissue and that an

anisotropic material model may give a more accurate representation of its behaviour. However, as discussed, the directional dependence of the tissue does not relate back to the radial force of the stent as the radial force of the stent will be the same regardless of the model used for the arterial tissue. The isotropic material model therefore allows a reasonable simplification to the models in this case.

Non-linear geometric effects arise with large displacements and deformations. In some analysis, the non-linear geometric effects of displacements on the structure due to applied loads are relatively small, and therefore can be ignored. In such cases, Abaqus defines the problem as a ‘small-displacement’ analysis, which means that geometric non-linearity is ignored in the element calculations and the kinematic relationships are linearized. The elements in a small-displacement analysis are formulated in the original configuration, using original nodal co-ordinates. As a result of this approximation, care should be taken when interpreting the results of such an analysis may not be entirely accurate. For example, the approximation also eliminates any possibility of capturing bifurcation buckling, which can be an important characteristic of a structure’s response. By default, Abaqus Standard defines all problems as ‘small-displacement’ problems and does not account for the effects of non-linear geometry. For large-displacements the elements are formulated in the current configuration using current nodal positions.

Non-linear problems exist when the material properties, geometry and/or contact/boundary conditions are not linear, in which case, the stiffness matrix and force vector are functions of the nodal displacements. The focus of comparison for the models in this paper is that of geometric non-linearity. During the deploy step of this analysis, when the stent contacts the vessel, relatively small levels of strain/deformation may exist (depending on the level of stent oversizing). It could be postulated that therefore this analysis could be represented as a small strain analysis. However, through the stent crimping process, the stent experienced a prior loading history, where the geometry deforms significantly and where a small strain analysis cannot be expected to give an accurate representation of the stress and strain levels. Therefore the purpose of this study was to examine if, using a purely elastic formulation to represent material behaviour, small strain analysis can give an accurate representation of the stent’s behaviour when deployed (i.e. close to its

stress-free diameter). As described above, differences are seen in the results of the Von Mises stress concentrations of the small and large strain configurations, with differences in maximum Von Mises stress in the stent of the order of 9%. Furthermore, it is noted that the difference does translate to the radial force result of the two models on the deploy step of the analysis where the radial force of the two models is largely similar for stent deployment (i.e. stent unloading). The differences in stress concentrations are expected as the SMART™ stent geometry undergoes large displacements due to the applied load required for crimping. In order to accurately compute results, the elemental stiffness matrix must be adjusted accordingly by recalculating the matrix incorporating the nodal rotations and or translations due to the calculated displacements of the nodes during the analysis. As the small strain simulations do not require adjustment of the stiffness matrix with displacement, the converged solution is a miss-representation of the results, and when focusing on maximum stresses within the stent, a small strain analysis will lead to inaccuracies in the order of 9%. The large strain analysis is more accurate as it accounts for the nodal displacements/rotations whilst converging on a solution. However, if the purpose of the analysis is to examine the radial pressure imposed on the vessel wall upon stent expansion, a small strain solution is sufficient as this result shows little difference in radial force upon expansion, where stent-artery contact will occur. This is a significant result as choosing a small strain analysis leads to reductions in computational time of the simulation and convergence of a solution as shown in Table 4.5. It is important to note that plasticity or damage mechanisms of the stent, which were not incorporated in these models may account for lower stresses than those predicted by the models presented here.

As seen from Table 4.5, the time taken for each analysis to complete is directly related to the complexity of the model. For some comparisons, specifically the small versus large strain analysis, the increase in computational cost is not significant and does not merit a reduction in model complexity. For other comparisons, specifically the geometry choice and stent self contact analysis, the differences in computational costs are large and the merit in reducing computational costs can be seen clearly. It is therefore worthwhile to consider the results of these models in terms of radial force. Specifically the stent self contact comparison has shown little effect on radial force upon deployment as discussed. This result, along

with those presented in Table 4.5 confirms that a reduction in computational cost would be seen by excluding the effects of self contact of the stent struts whilst not affecting the accuracy of the result in terms of radial force of the stent, which is of interest in this study. It is also worth noting the large increase in computational time of the full geometry model in comparison to that of the 2 ring periodic geometry. It could be justified that if a ‘complete stent’ was modelled (i.e. any more than four rings within an idealised cylindrical geometry), that there would be a significant increase in the time taken for such an analysis to run without yielding any further information or result as this representation would simply be a longer version of the full geometry representation.

4.3 Stresses in the Stented Superficial Femoral Artery due to Physiological Loading

This study applies the approaches to stent-artery interaction modelling established in the initial study to a model that investigates the effect of known physiological loading conditions on the stented SFA. Stenting in the femoropopliteal artery has been associated with high failure rates due to the challenge faced by the environment of dynamic forces of the superficial femoral and popliteal arteries including compression and torsion. The problems associated with these loading conditions include increased levels of stress on the arterial tissue local to the stented portion of the vessel, along with the fracture risk of the stent due to excessive loading conditions. High stress concentrations in the stented region may be associated with local damage to the arterial tissue leading to restenosis and eventually device failure. Similarly, high loading levels on the stent may lead to device failure by stent fracture (Duda et al., 2002, Nikanorov et al., 2008, Scheinert et al., 2005). There is therefore a need for investigation of stent-artery interaction in combination with physiological loading conditions to thoroughly investigate the effects of stenting in the SFA.

A number of experimental studies of both stented and unstented arteries have been undertaken to evaluate the physiological displacements which occurs in the SFA and popliteal artery. These have been reviewed in section 2.5 and are listed in Table 2.1 of this thesis. Results of these studies provide experimentally measured values for a range of physiological deformations of unstented and stented vessels. From the results of these studies, physiological load levels are selected and applied to the stented artery of this study.

The results of the radial force accuracy and modelling approach study (section 4.2) established that it is necessary to model a full stent model to capture accurate stent-artery interactions during stent deployment. A full model will give an accurate prediction of radial force values and also allow determination of stress concentrations at the end regions of the stent due to the stiffness mismatch between the stented and non-stented regions of the artery. Therefore, the model used in this study is the reduced length version of the full stent geometry shown in Figure 4.1(i).

Firstly, deployment of the stent in the SFA was simulated, followed by the application of known physiological loading levels of axial compression and torsion to the stented vessel.

4.3.1 Materials and Methods

Abaqus/Explicit finite element software was used to develop the model of this study which aimed to represent the geometry, material properties and loading conditions of the stent and SFA throughout the stenting procedure and due to known physiological deformation of the artery.

Stent Geometry

The same stent model was used in this study as in the radial force accuracy and modelling approach study described in section 4.2. This model was based on the Cordis SMART™ stent (outer diameter (OD) 7mm, length 20mm). A reduced length version of the full stent geometry was modelled as shown in Figure 4.1(i).

The processing history of the stent was included in the models as described previously. Briefly, this was achieved by creating an ‘as cut’ geometry of the stent model which was then imported into Abaqus, meshed, and then wrapped into a cylindrical state by mapping the nodes into a cylindrical coordinate system. The stent model was then expanded from the ‘as cut’ geometry of 3 mm OD to 7 mm OD using a rigid cylindrical body placed inside the stent and expanded out to 7 mm OD using radial displacement boundary conditions applied to the rigid cylinder. The expanded geometry of the stent was exported and used as the ‘stress free’ configuration for the study.

The full stent model used for this study was meshed with 127,050 8-node linear 3D stress elements (C3D8R). The suitability of this mesh density was determined from a mesh dependency study on a periodic unit of the stent geometry where the mesh density was increased from 2,698 elements to 12,269 elements. The percentage difference in maximum Von Mises stress (MPa) in the stent between the mesh selected and the finest mesh studied was 0.024MPa. There are 4 elements over the thickness and width of each stent strut.

Quasi-static Abaqus/Explicit simulations were performed, allowing the simulations to run efficiently. Computational cost was reduced and static equilibrium ensured as previously described in section 4.2.1 (page 96). Simulations were

performed on a Bull Novascale high performance computer using 4 nodes each with two 2.8GHz quad-core processors.

Artery Geometry

A vessel was modelled with OD 7.2 mm and a wall thickness of 0.6 mm, representative of the SFA in which Nitinol stents such as the 7mm OD Cordis SMART™ stent would be used (Smilde et al., 1998, Tai et al., 1999). An ‘infinitely long’ piece of artery was modelled for this study allowing the end effects of the stent within the artery to be accurately assessed.

In contrast to other computational studies (Auricchio et al., 2011, Gijssen et al., 2008) which focus on patient specific vessel geometries, this study focuses on the effects of physiological loading conditions of the artery, and the resulting stress concentrations in the artery as a result of this loading. Therefore, an idealised cylindrical vessel geometry was used in this study which may not be directly relevant to patient specific diseased vessels, but allows for investigation of the effects of physiological loading on the arterial tissue which is the primary focus of the study. The artery was meshed using 391,625 8-node linear brick reduced integration elements with hourglass control (C3D8R). Mesh convergence was carried out as previously described in section 4.2.1 (page 97).

Analysis Steps

The loading conditions for the model contained four steps; stent crimping, stent deployment, axial compression and torsion. The crimp step involves reducing the stent diameter to 2 mm from its stress free (near cylindrical) diameter of 7 mm. The stent deployment step allows the stent to expand out to its original stress free diameter through release of its internal strain energy. The physiological loading conditions of axial compression and torsion are then applied to represent physiological loading cases of the stented artery. All steps of the simulation require the definition of boundary conditions and contact interactions, as detailed in the following sections.

Stent Crimping

In this step, the Nitinol SMART™ stent was crimped to have an OD of 2mm. The method of stent crimping was determined from the results of the radial force accuracy study which showed that crimping with a rigid cylinder gives a more accurate method of simulating stent crimping than applying radial displacements directly to the stent. Not only is the rigid cylinder method more representative of the manufacturing process of the stent, but it was shown that the radial displacement crimp method displays a lower radial force than that of the rigid cylinder method upon deployment (Figure 4.9), therefore affecting radial force on the artery during stent deployment. As discussed previously, the contact area of the stent crimped with radial displacements will be less than that crimped with the rigid cylinder leading to a lower contact force on the arterial tissue in the model. In order to ensure an accurate reflection of contact force, stent crimping using a rigid cylinder was chosen. This was achieved as described in the radial force accuracy and modelling approach study in section 4.2. A radial displacement boundary condition was imposed on a rigid cylinder, with surface to surface frictionless tangential and hard normal contact between the outer surface of the stent and the inner surface of the rigid cylinder that reduced its diameter, and therefore the stent outer diameter, to 2 mm.

Stent Deployment

After the crimping, the stent was allowed to freely expand due to its stored elastic strain energy and the reversal of the Nitinol stress induced phase transformation. All displacement boundary conditions (conditions imposed during crimp) are removed and the stent expands due to the internal energy of the Nitinol material, towards its stress free state. Throughout both crimp and deployment steps, a single node of the stent was constrained in the axial direction, preventing rigid body motion.

Arterial Contact

Surface to surface tangential penalty contact with friction coefficient of 0.2 (Mortier et al., 2010) and hard normal contact behaviour was initiated between the outside surface of the stent and inner surface of the artery. Contact between the stent

and rigid cylinder is de-activated for these models upon expansion of the stent once the stent is within close proximity to the vessel.

Physiological Loading

The physiological loading conditions of axial compression and torsion are investigated in this study. The magnitudes of these load cases are listed in Table 4.6. For this part of the analysis, a kinematic coupling constraint is set up at one side of the stented artery. Kinematic coupling constraints are used to control the displacement of nodes to the rigid body motion defined by a reference node; a point which is in the centre of a local coordinate system. There are six degree of freedom constraints available for selection in the kinematic coupling, three translational and three rotational. For the model of this study a reference point (RP) and local coordinate system were created at a point at the centre of the face of one end of the artery. The displacements of all nodes in all degrees of freedom of that end face of the artery were then coupled to this RP using a kinematic coupling constraint (Figure 4.15). Displacement loads were then applied to the RP. The other end of the artery was fixed in all directions.

Stent Material

The same constitutive model that simulates superelastic behaviour of the shape memory alloy, Nitinol, is used in this study to model the material of the stent, implemented by an in built user-defined mechanical material behaviour (VUMAT for Abaqus/Explicit). This allowed both the loading and unloading hysteresis of Nitinol to be represented.

Artery Material

The vessel tissue of this study is modelled using the Holzapfel-Gasser-Ogden form of the strain energy function for anisotropic hyperelasticity (discussed in Chapter 3, section 3.2.5 of this thesis) proposed by Gasser et al. (2006) for modelling arterial layers with two families of fibres orientated helicoidally. Each arterial layer (intima, media, and adventitia) is modelled as a separate material in the model which captures the strong stiffening effect of collagen fibres that make up the vessel wall (Holzapfel et al., 2005b). The strain energy of the material is calculated as the sum of

an isotropic and anisotropic term which represent the matrix material (isotropic term) and embedded collagen fibres (anisotropic term) of the vessel tissue. This model has been shown to correlate well with experimental test data for non-atherosclerotic arterial tissue (Holzapfel et al., 2005b). The material constants required for implantation of the model in Abaqus are listed in Table 4.7 and are based on experimental data by Holzapfel et al. (2005a).

4.3.2 Results

Von Mises stress concentrations imposed by the stent on the artery wall from axial compression and torsion loads are shown in Figure 4.16 and Figure 4.17 respectively. The maximum stress in the vessel tissue after 10% axial compression is 0.086 MPa, almost a threefold increase from the maximum stresses after stent deployment. Addition of torsional displacement of $0.28^\circ \text{ mm}^{-1}$ results in maximum stress in the vessel tissue of 0.156 MPa, almost a five-fold increase from stress levels after stent deployment. The scales on the contour plot legends in Figure 4.16 and Figure 4.17 are the same for the purpose of making a visual comparison of the stress levels.

4.3.3 Discussions

The aim of this study was to investigate the effect of known physiological loading conditions on the stented SFA. The results of the radial force accuracy and modelling approach study were used in this study to ensure accurate capture of stent-artery interactions during the physiological loading. Results show that the stresses in the arterial wall are increased due to physiological loads of axial compression and torsion.

This study has shown that stent-artery interactions result in significantly higher stresses on the artery wall than those due to stent deployment alone (three times and five times greater than those after stent deployment for compression and compression-torsion respectively). Focusing on the effects on the artery of compression, it can be seen from the results of this study that the stress on the artery wall increases due to the compressive load, with stress concentrations more pronounced, specifically at the ends of the stented portion where maximum stresses are found. Similar trends are seen in the effects of axial compression and torsion on the stented vessel where highest stress concentrations are found in regions closest to the stent rings and again at the end portions of the stented region. This is expected, as results of stent deployment in the previous analysis showed high stress concentrations, also at the end of the stented portion, understood to be due to the stiffness mismatch between the stented and unstented artery. The analysis of the stented artery in combination with physiological loads confirms that these are still the regions most affected by stent placement, and this should be considered in stent design. Controlling radial force at the end portions of the stent, with an aim towards matching the stiffness at the ends of the stented artery portion to the unstented artery portion would reduce stress in the artery in these locations.

A limitation of this study is the use of the idealised cylindrical vessel geometry to evaluate the results of the physiological loads applied which does not account for the presence of plaque, its stiffness and the resulting effect on deformation of the artery due to the applied loads. However, even though this study does not directly relate to any patient specific geometry, it does allow for the comparison of physiological loads and the effect they have on a healthy, non-diseased artery which is important for gaining a further understanding of the

behaviour of the artery due to its physiological loads, an important consideration for device design.

Thus far, many studies have focused on investigating stent-artery interactions in coronary vessels. Few studies have investigated the effects of stenting in combination with physiological loads in the femoropopliteal artery. One study by Early et al. (2009). investigated the stresses in a peripheral artery after placement of a stainless steel stent followed by the application of a bending load with results also showing that similar levels of high stresses occur at the proximal and distal ends of the stent. However, typically, Nitinol stents are used for peripheral arteries due to their ability to deform super-elastically. For this reason, the Cordis SMART™ Nitinol stent was modelled in this study. Due to the distinctively unique mechanical environment of the femoropopliteal artery, it is necessary to investigate the behaviour of stent-artery interactions for the peripheral arteries (specifically femoropopliteal artery) with models that will account for this environment. Therefore, the finite element models presented in this study are designed to predict stresses in the SFA following self expanding stent placement and combinations of the dominant physiological deformation (i.e. axial compression and torsion) of the vessel. Bending was not considered in this study, as it is recognised that the levels of bending determined through angiography images (outlined in Table 2.1) are highly dependent on the location of the stent within the femoropopliteal artery. In addition, the overall deformation pattern of the artery is likely to be altered as a result of stenting, altering the critical bending locations to the unstented segments of the artery. This warrants a more thorough analysis, which is the focus of Chapter 5 of this thesis.

4.4 Conclusions

Due to the high failure rates associated with stents placed in the femoropopliteal artery, there is a great need to further investigate stent designs and stent-artery interactions. A thorough understanding of the effects of stent placement is necessary for femoropopliteal stent design parameters and considerations. The studies of this chapter are focused on both the methods of computational modelling, specifically investigating how different methods of modelling stent-artery interactions can affect the accuracy of the results, along with implementing the methods to simulate the effects of stenting on the femoropopliteal artery in combination with its associated physiological loads.

The results presented in the radial force accuracy study may prove valuable in helping reduce the computational time associated with future models of self expanding stent-artery interactions. In the highly complex computational models employed by researchers, each additional element of the analysis aims to improve accuracy of the computational simulation by making a more realistic model. However, using all of these elements in combination is a challenge for one computational model and there is a need to assess the effect of simplifying these problems and modelling approaches in whatever way possible. This study has highlighted where such simplifications can be made without significantly reducing the accuracy of an analysis, when the focus of the analysis is on the effect of stent deployment on arterial stress concentrations and radial force imposed on the artery.

Firstly, this study has shown that methods employed in crimping the self-expanding stent before deployment into the artery has significant implications on the resulting predicted radial force of the stent. The application of a rigid cylinder on the outside of the stent which reduces the outer diameter of the stent in the crimping process more accurately captures the crimping process of the stent than the application of radial displacement to the stent nodes themselves. The latter method results in a lower level of radial force upon deployment and therefore stress concentrations as a result of stent-artery interactions may not be as accurate.

Results have also shown that the most accurate representations of stent-artery interactions can only be made when modelling the full length of the stent as

accurately matching a periodic artery segment and a stent segment would have to be determined iteratively due to relative motion of stent struts upon stent expansion. Results have shown that a 1/6th-constrained-unit cell, used to approximate such a model, over-estimates the radial force of the stent upon deployment and those stent-artery interactions. Where necessary, 2-ring-periodic geometries could be used for stent-artery models as radial force upon unloading and subsequent stress concentrations in the artery due to deployment are similar to a full geometry model. However a 2-ring-periodic geometry would not capture end effects which are captured by the full geometry model and may lead to important conclusions of stent designs being neglected.

Additionally this study has shown that whilst including self contact of the stent struts with each other in the analysis greatly affects the stress concentrations within the stent, the effect of this on the unloading behaviour and resulting radial force of the stent is negligible (assuming elastic behaviour of the Nitinol only). Therefore, as the objective of the analysis is to investigate arterial stress concentrations, self contact of the stent can be excluded to simplify the model. Similarly, the inclusion of 'large strain' effects of the model in comparison to having including only 'small strain' effects does not significantly alter radial force values as shown by the results presented here. Whilst consideration should be taken to assess whether small or large strain models are required for accurate modelling of arterial displacements as a result of stenting, the magnitude of the radial force from the stent, and subsequent loading on the artery from the stent is not affected by reducing to a small strain analysis.

In a second analysis, the results determined from the radial force accuracy study were implemented to create a model of the stented SFA with applied physiological loading conditions, typical of those reported in the literature for the femoropopliteal artery. This study has shown that stresses in the artery are dramatically increased by the addition of physiological loads to the stented artery, with a significant impact to stress concentrations at the end of the stented region of the vessel. Therefore this study highlights the importance of computational models that focus on the effect of stent-artery interactions, specifically in the context of physiological loads which have a huge impact on vessel stresses. It is important to

note however, that stenting will affect the global characteristic deformation of the femoropopliteal artery due to deformations such as knee bending as seen from previous research (Jonker, 2008, Smouse et al., 2005). These changes to deformations characteristics may in turn cause changes to vessel stresses which must be investigated. This is the subject matter of Chapters 5 and 6 of this thesis.

4.5 Tables and Figures

Name	Geometrical Representation
1/6 th -Constrained-Unit Cell Geometry	1/6 th symmetric segment of a periodic 2 ring geometry constrained in the tangential directions
2-Ring-Periodic Geometry	Periodic 2 ring unit cell
Full Geometry	Reduced length version (8mm) of the full stent

Table 4.1 Terminology for geometrical representation of the stent.

Material Parameter	Value
Austenite Elasticity - E_A	44071 MPa
Austenite poisson's ratio - ν_A	0.3
Martensite Elasticity - E_M	24131MPa
Martensitepoisson's ratio - ν_M	0.3
Transformation strain - ε^L	0.051
Start of transformation loading - σ_L^S	420MPa
End of transformation loading - σ_L^E	441MPa
Reference Temperature - T_o	37°C
Start of transformation unloading - σ_U^S	93.08MPa
End of transformation unloading - σ_U^E	82.74MPa
Start of transformation stress during loading in compression - σ_{CL}^S	420MPa
Volumetric transformation strain - ε_V^L	0.051

Table 4.2 Experimentally determined Nitinol material properties for the stent.

	C₁₀ (MPa)	C₂₀ (MPa)	C₃₀ (MPa)	C₄₀ (MPa)	C₅₀ (MPa)	C₆₀ (MPa)
Intima	6.79E-03	5.40E-01	-1.11	10.65	-7.27	1.63
Media	6.52E-03	4.89E-02	9.26E-03	0.76	-0.43	8.69E-02
Adventitia	8.27E-03	1.20E-02	5.20E-01	-5.63	21.44	0.00

Table 4.3 Material constants of sixth order reduced polynomial strain energy density function for the isotropic artery material model (Gastaldi et al., 2010).

	Maximum Von Mises Stress (MPa)	Minimum Von Mises Stress (MPa)
Large Strain Simulations	779.9	3.0
Small Strain Simulations	710.3	3.1
% Difference	8.9%	3.2%

Table 4.4 Maximum and minimum stress levels as found in the 2-ring-periodic geometry models at the end of the deploy step with and without geometric non-linearity effects.

Model Details	Number of Nodes in Model	Analysis Run Time	Analysis Type
1/6 th -constrained-unit cell geometry with self contact conditions	18,003	10.33 hours	Standard
1/6 th -constrained-unit cell geometry without self contact conditions	18,003	4.5 hours	Standard
2-ring-periodic geometry crimped with an outer surface	186,360	18.22 hours	Standard
2- ring-periodic geometry crimped with radial displacements	185,880	0.45 hours	Standard
Small strain analysis of 2-ring-periodic geometry	186,360	13.37 hours	Standard
Large strain analysis of 2-ring-periodic geometry	186,360	18.22 hours	Standard
1/6 th -constrained-unit cell geometry with artery contact	41,601	20.83 hours	Explicit
2-ring-periodic geometry with artery contact	196,480	31.48 hours	Explicit
Full geometry with artery contact	334,205	106.53 hours	Explicit

Table 4.5 Impact of model complexity on analysis run time.

Reference	Load	Magnitude
Denison et al. (2004)	Axial compression	10%
Cheng et al. (2009)	Torsion	0.28° mm ⁻¹

Table 4.6 Physiological load levels applied to the stented SFA.

	μ (MPa)	k_1 (MPa)	k_2 (-)	κ (-)	θ (°)
Intima	46.777E-03	9992.9E-03	80.24	0	53.9
Media	19.021E-03	21.045E-03	79.362	0	26.348
Adventitia	6.623E-03	118.48E-03	373.38	0	42.291

Table 4.7 Material constants of the Holzapfel-Gasser-Ogden form of the strain energy density function for the anisotropic artery material model (Holzapfel et al., 2005a).

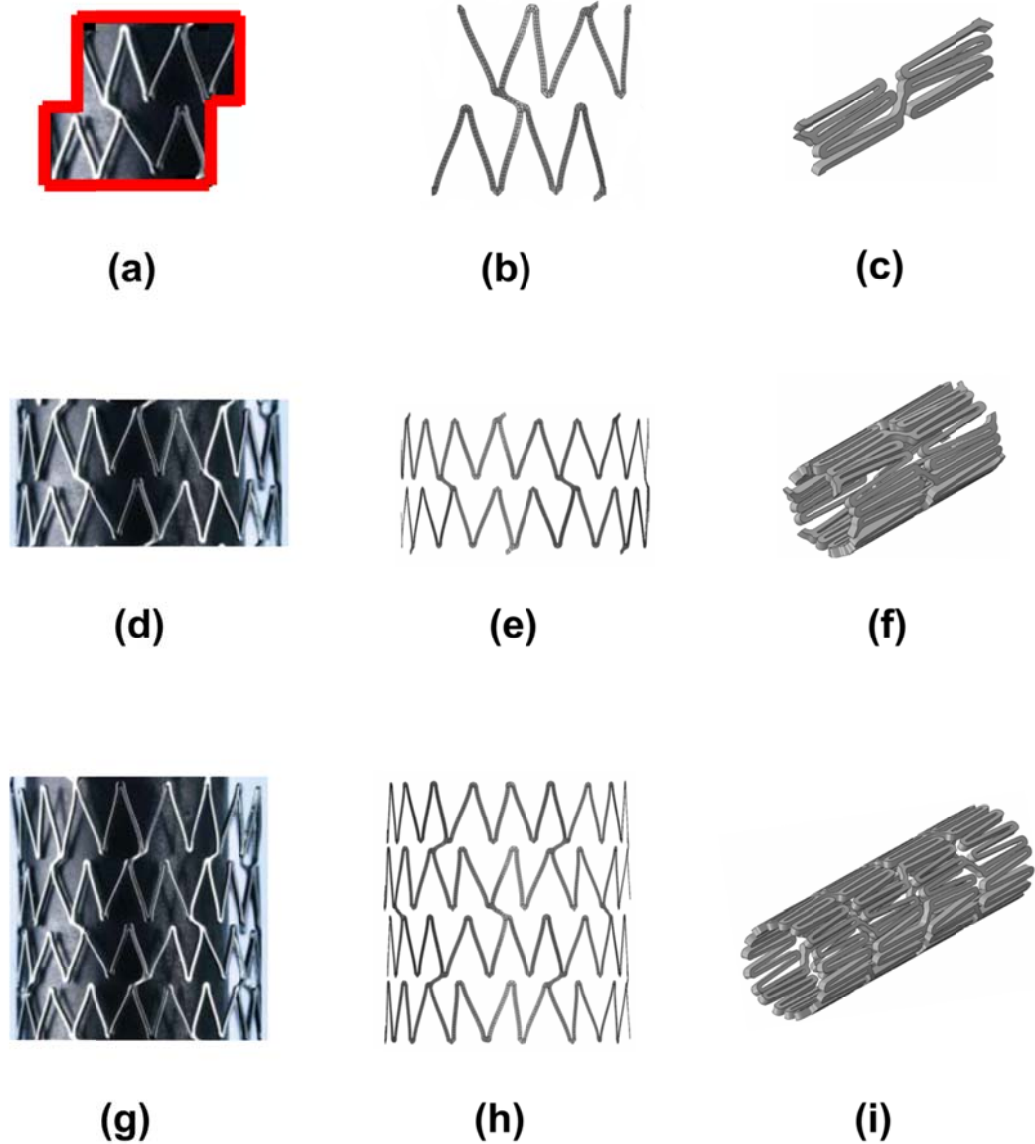


Figure 4.1 SMART™ stent: 1/6th-constrained-unit-cell geometry (a), (b) and (c); 2-ring-periodic geometry (d), (e) and (f); full geometry (g), (h) and (i). Models (c), (f) and (i) represent crimped configurations while all other models represent deployed configurations. Red lines on (a) represent associated periodic artery geometry shape.

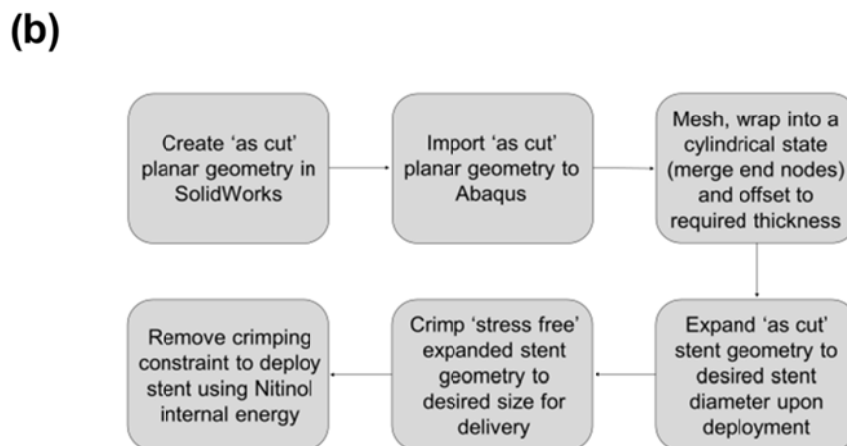
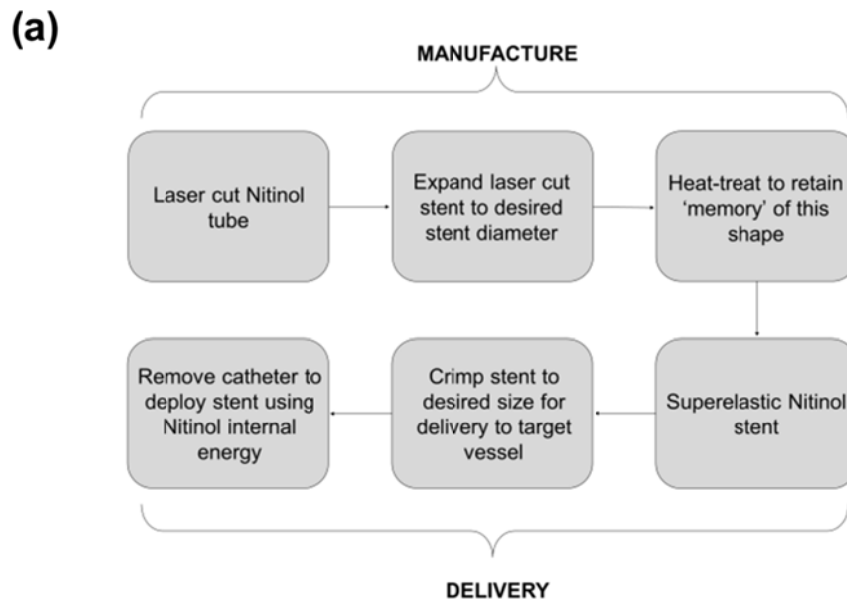


Figure 4.2 The manufacturing and delivery process of a Nitinol stent (a) and the model generation process for the analysis (b).

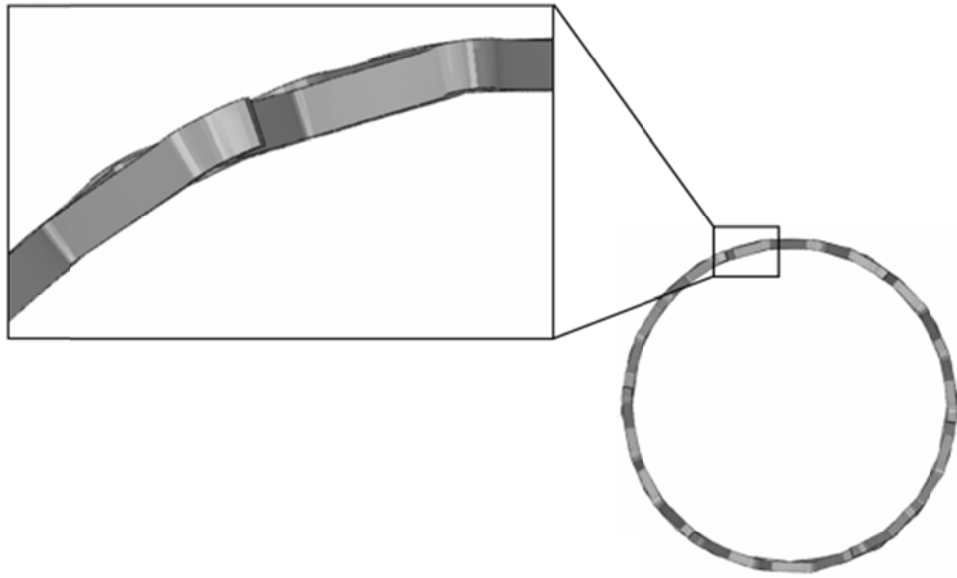


Figure 4.3 The ‘stress free’ stent geometry after expansion where deviations from a perfectly cylindrical shape are observed.

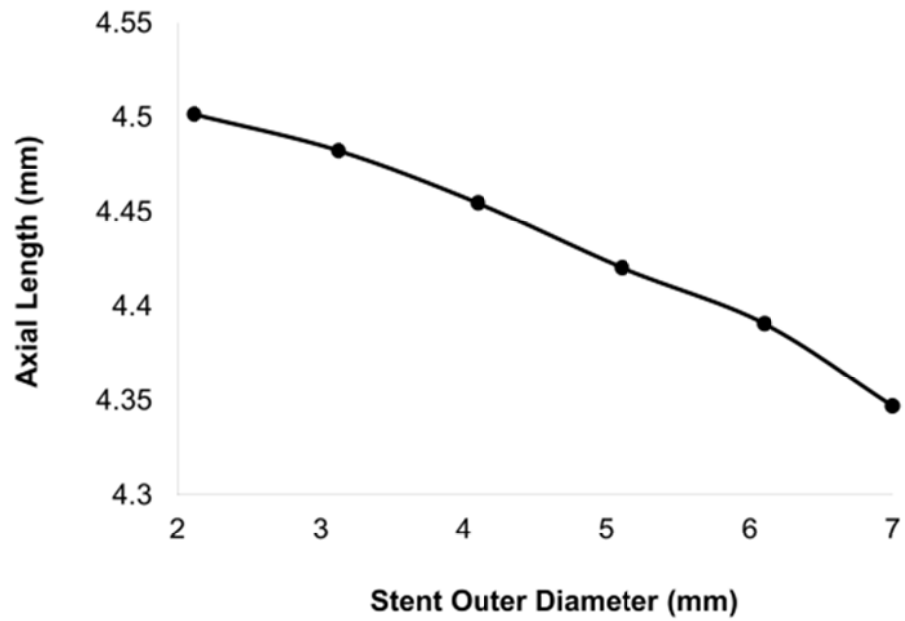


Figure 4.4 Axial length of stent versus stent outer diameter upon deployment used to determine the artery periodic length due to stent foreshortening.

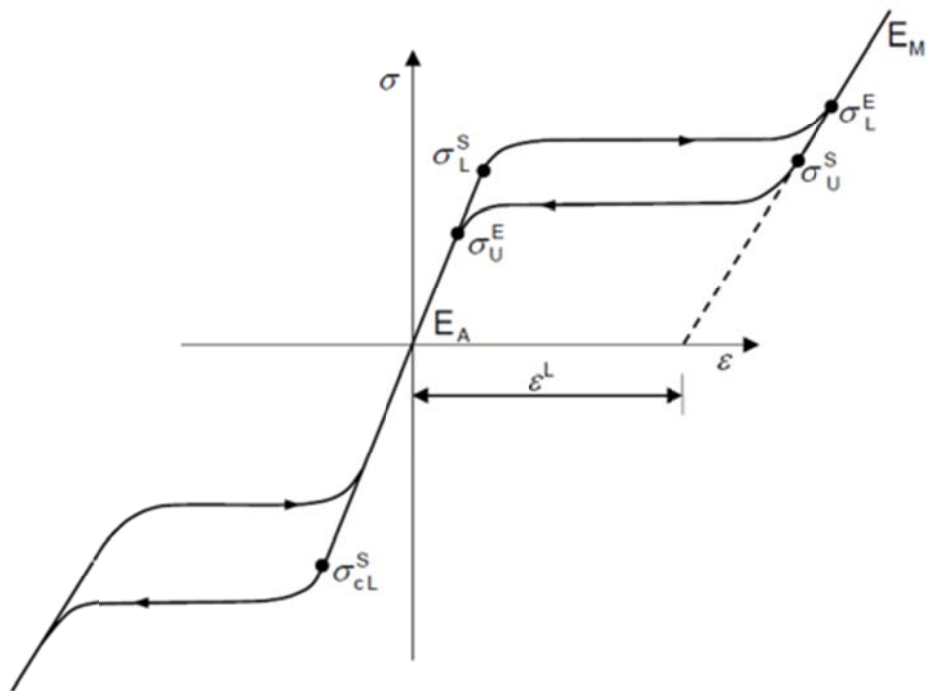


Figure 4.5 Stress-strain curve of Nitinol material behavior.

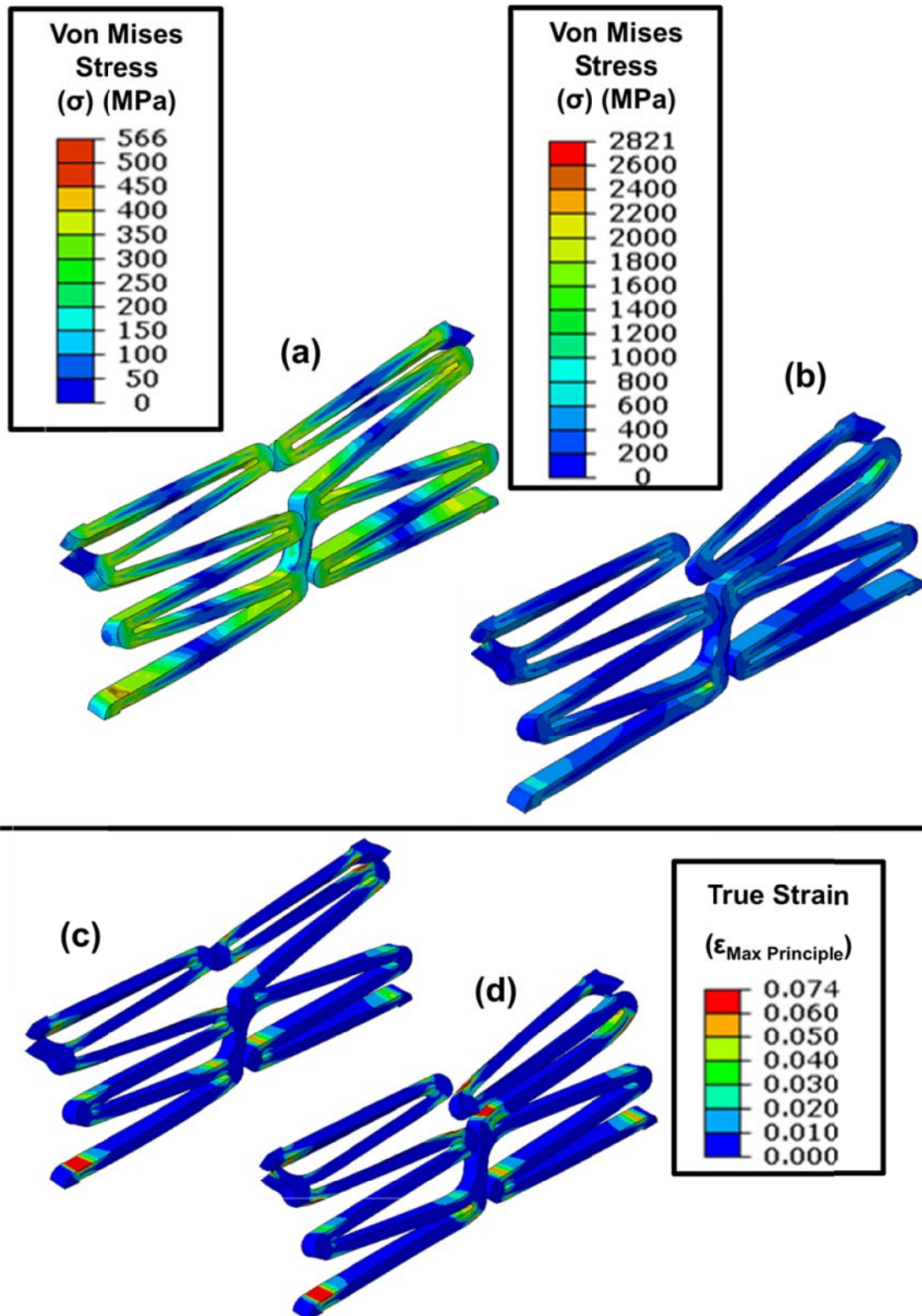


Figure 4.6 1/6th-constrained-unit-cell geometry crimped to 1.5 mm OD (a) and (c) neglecting the effects of self contact and (b) and (d) including the effects of self contact.

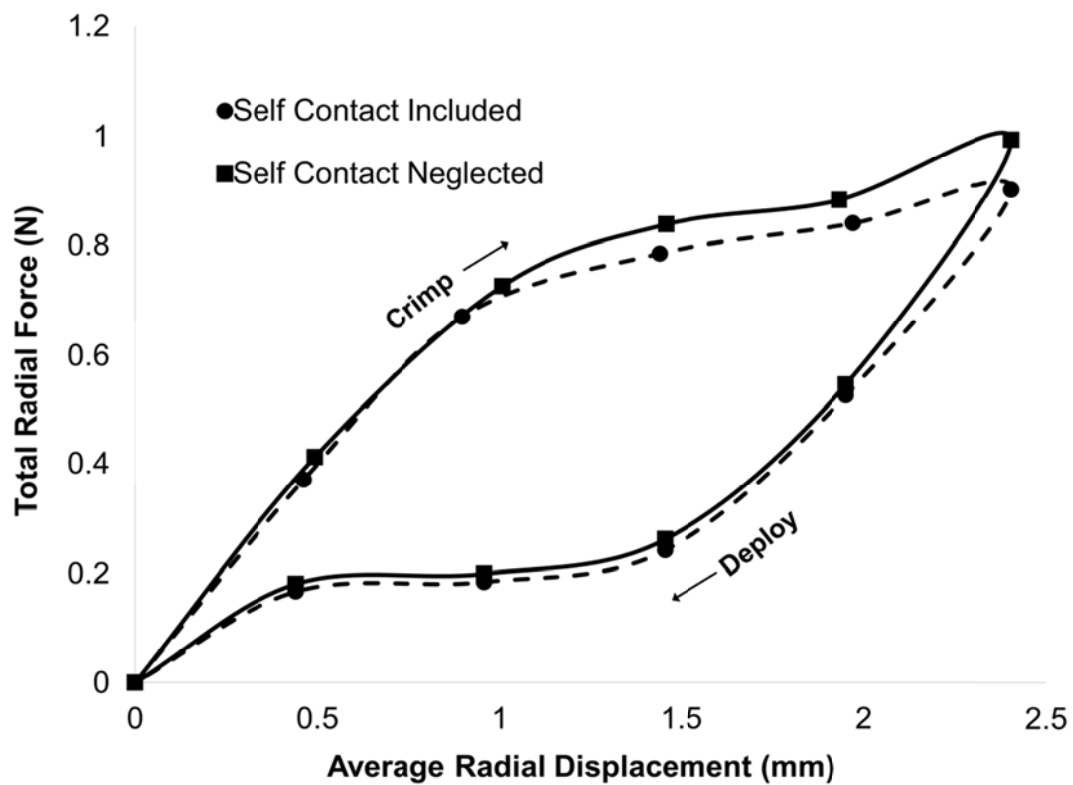


Figure 4.7 Comparison of self contact modelling on the 1/6th-constrained-unit-cell geometry radial force.

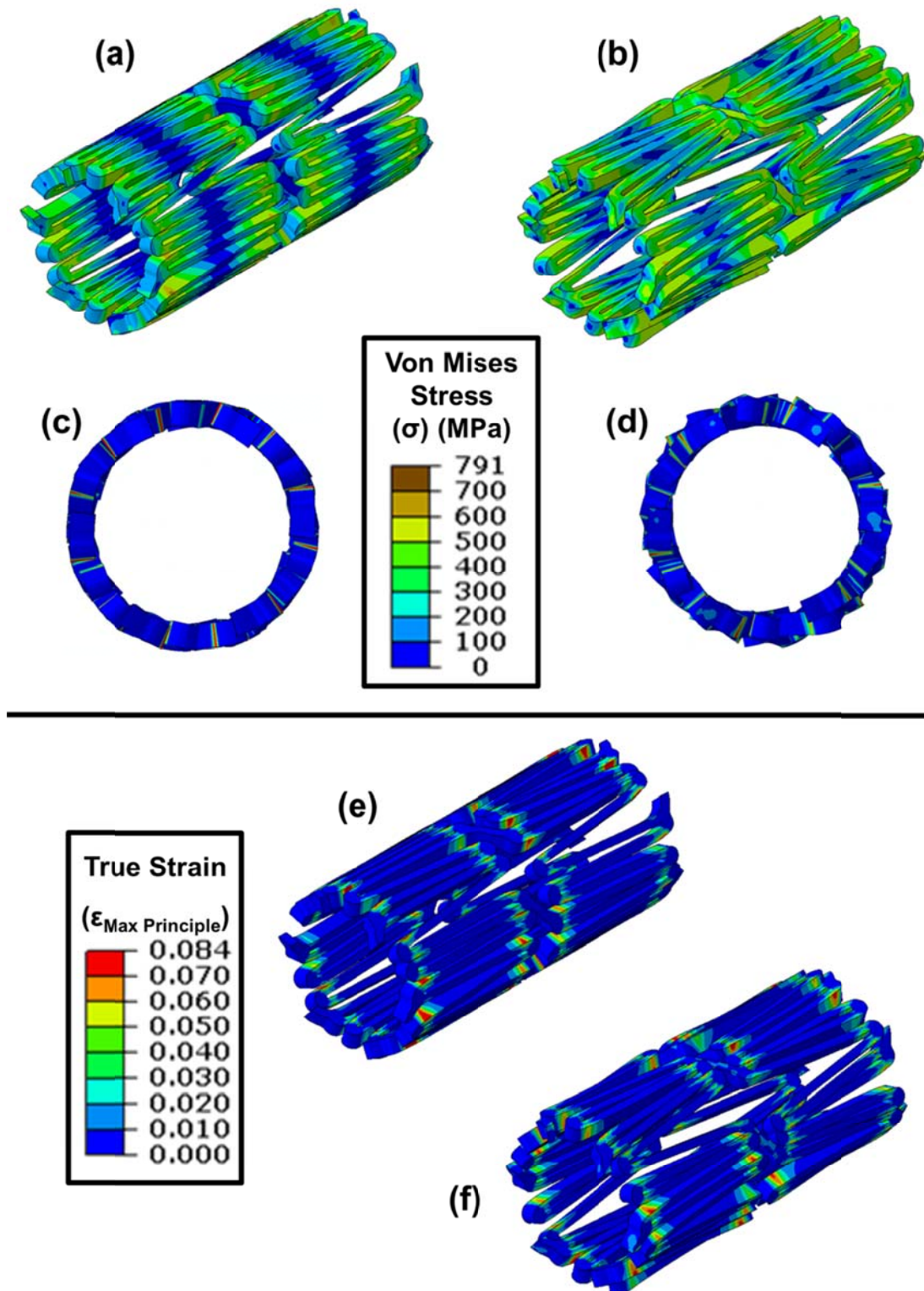


Figure 4.8 Contour plots of the 2-ring-periodic geometry model at the end of the crimp step, (a), (c) and (e) crimped by a rigid body and (b), (d) and (f) crimped by radial displacements applied directly to the stent outer surface.

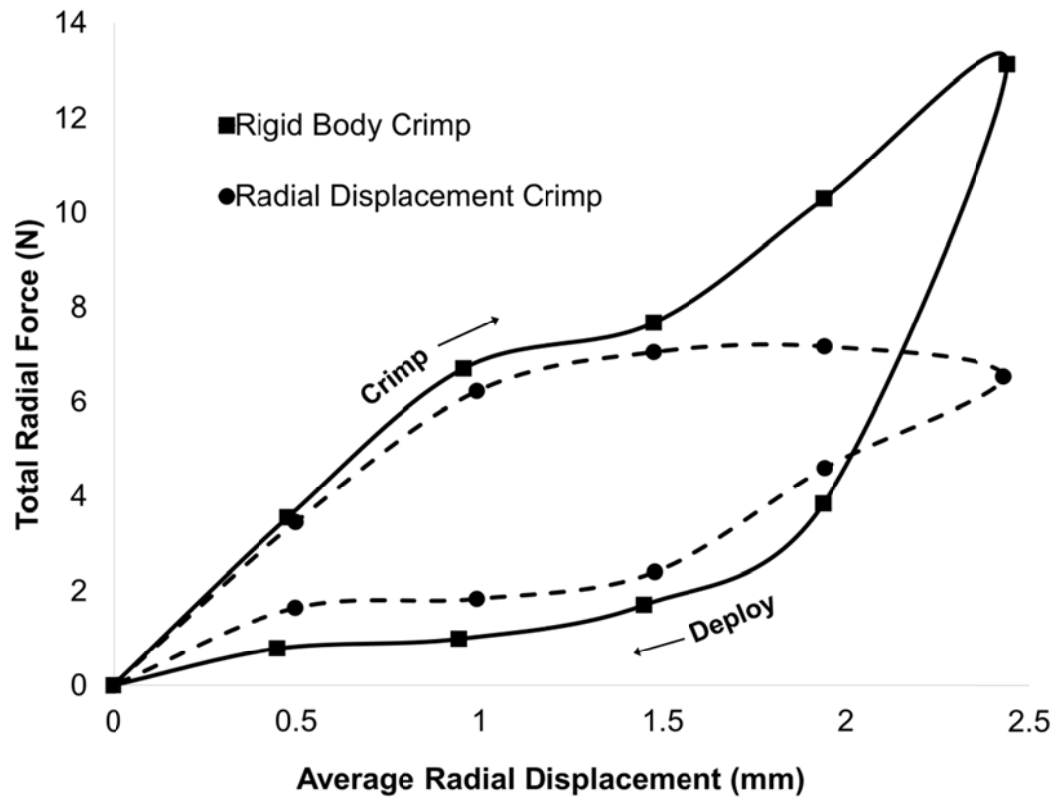


Figure 4.9 Comparison of crimp methods on 2-ring-periodic geometry radial force.

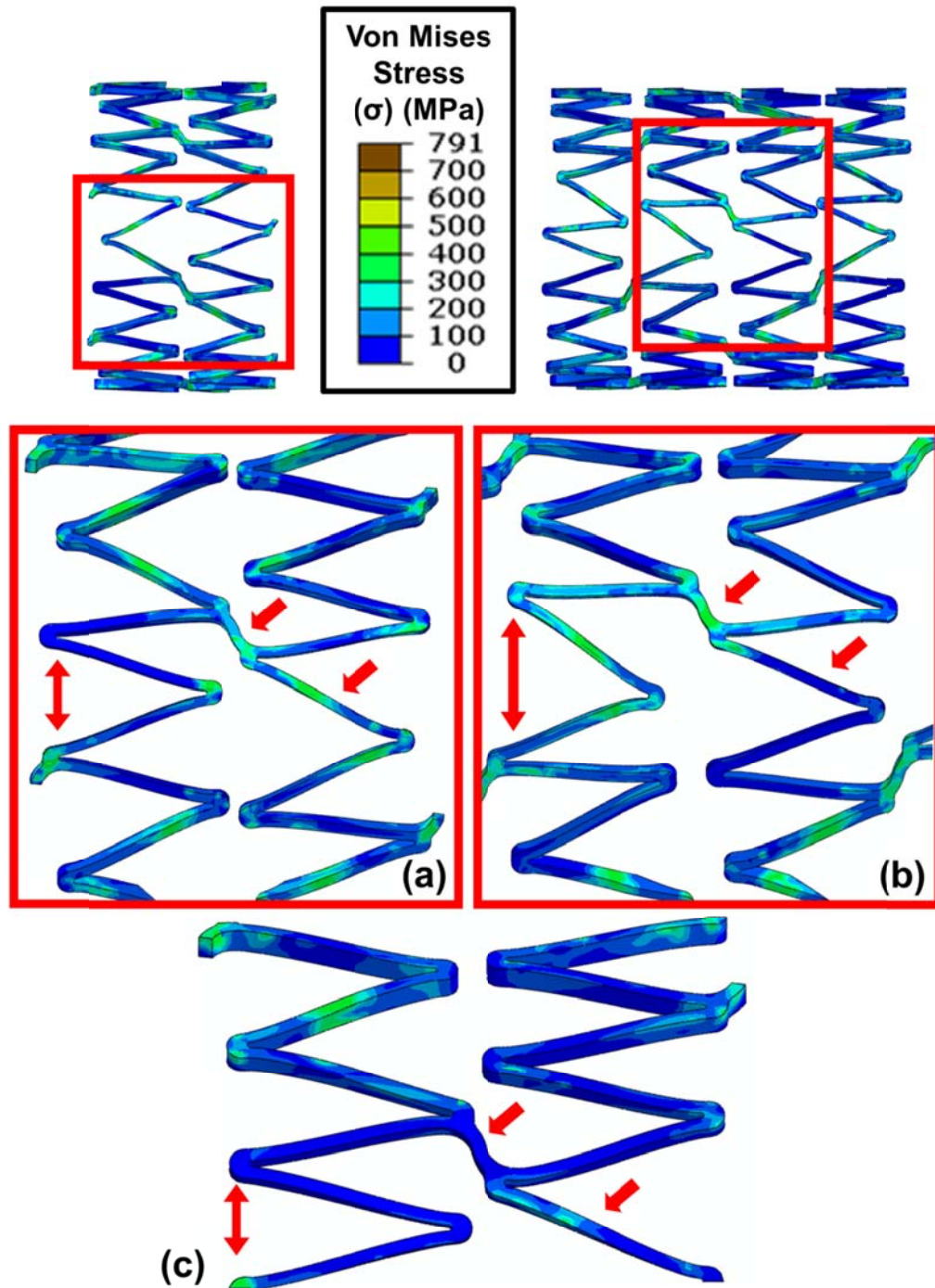


Figure 4.10 Close up comparison of Von Mises stress (MPa) concentrations of the 1/6th-constrained-unit-cell geometry(c), 2-ring-periodic geometry (a) and full geometry (b) at the end of the deploy step. Arrows highlight differences in stress locations and deployed geometry.

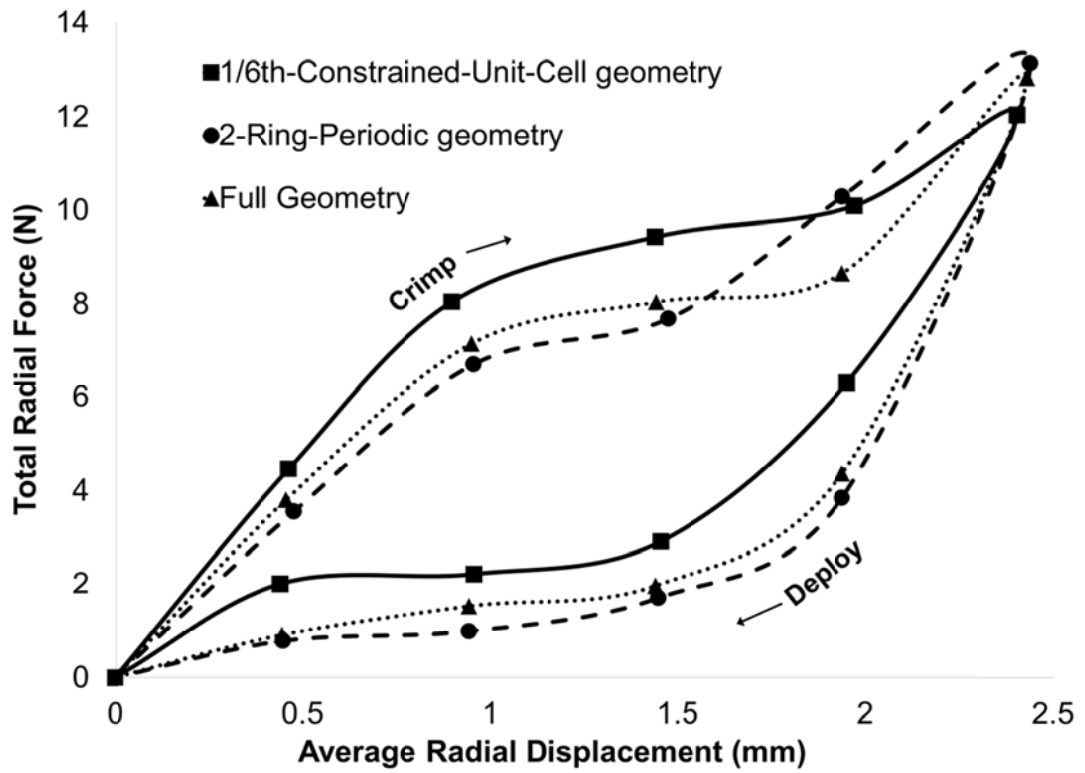


Figure 4.11 Comparison of geometry on radial force.

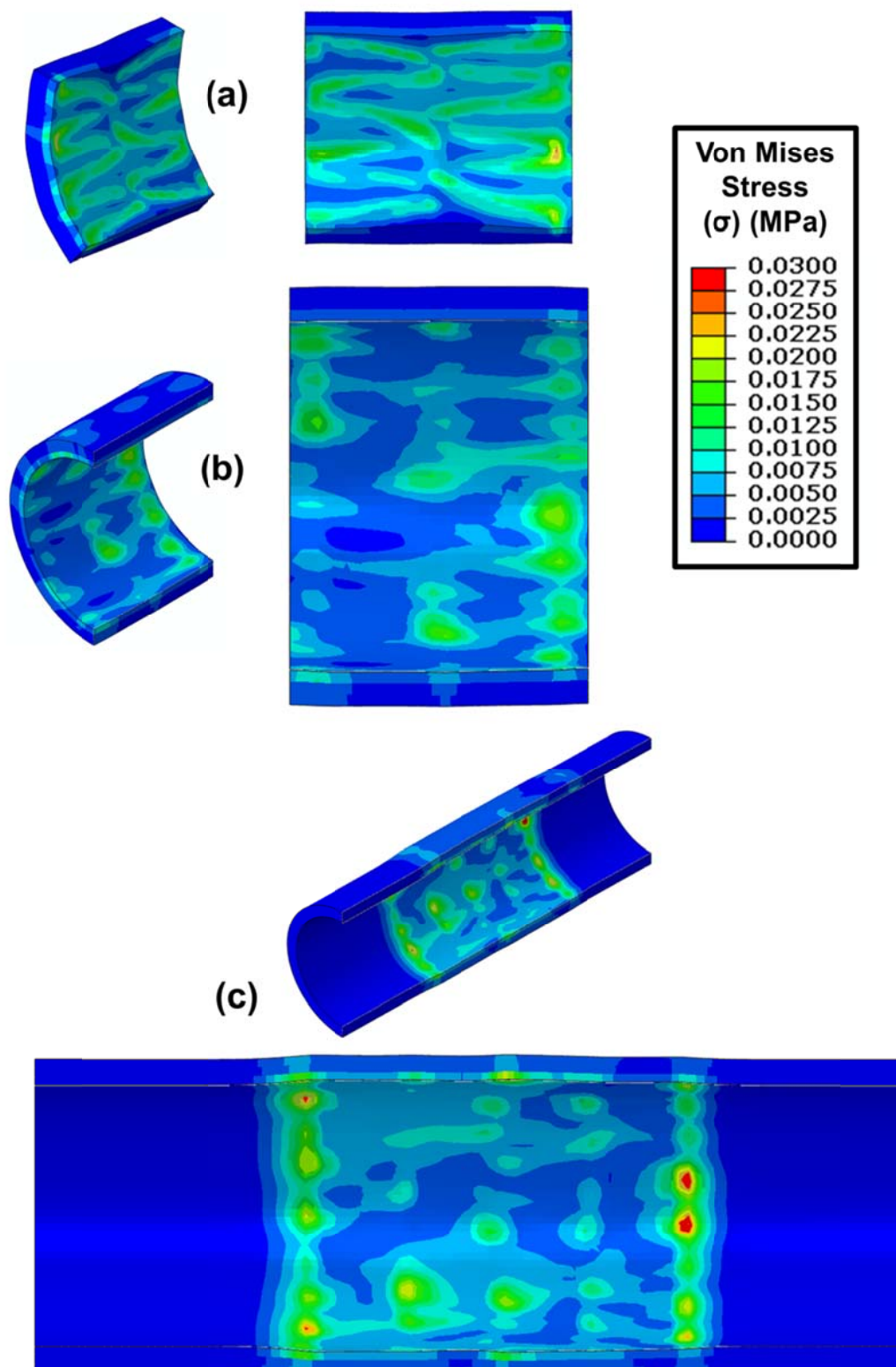


Figure 4.12 Von Mises stresses (MPa) in the 1/6th-constrained-unit-cell geometry (a) Von Mises stresses (MPa) in the 2-ring-periodic geometry (b) Von Mises stresses (MPa) in the full geometry (c) after stent deployment.

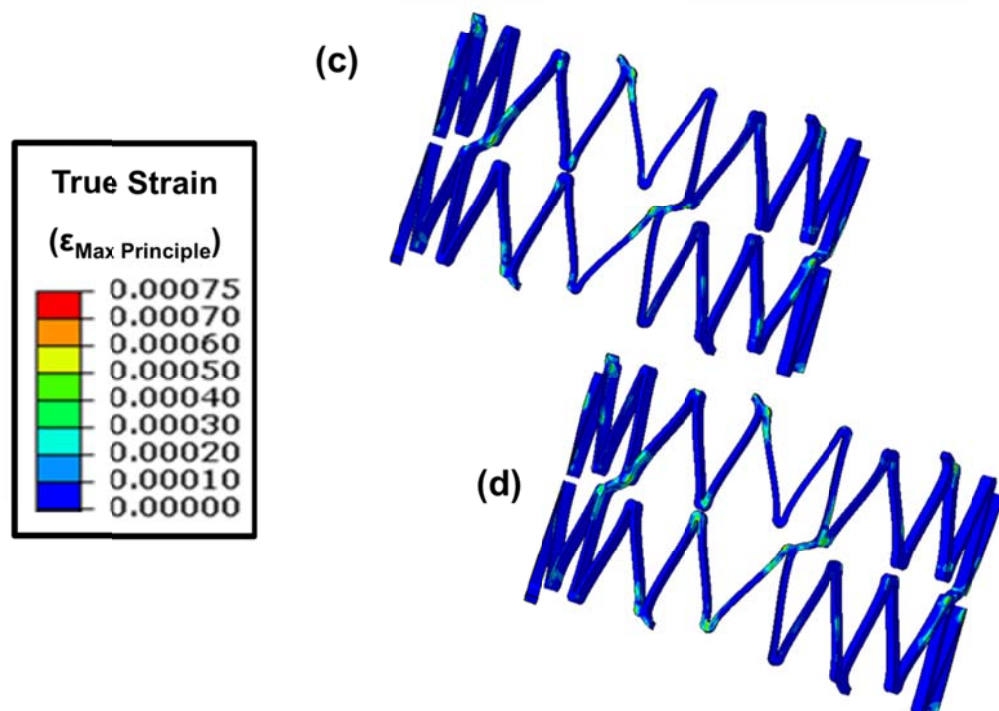
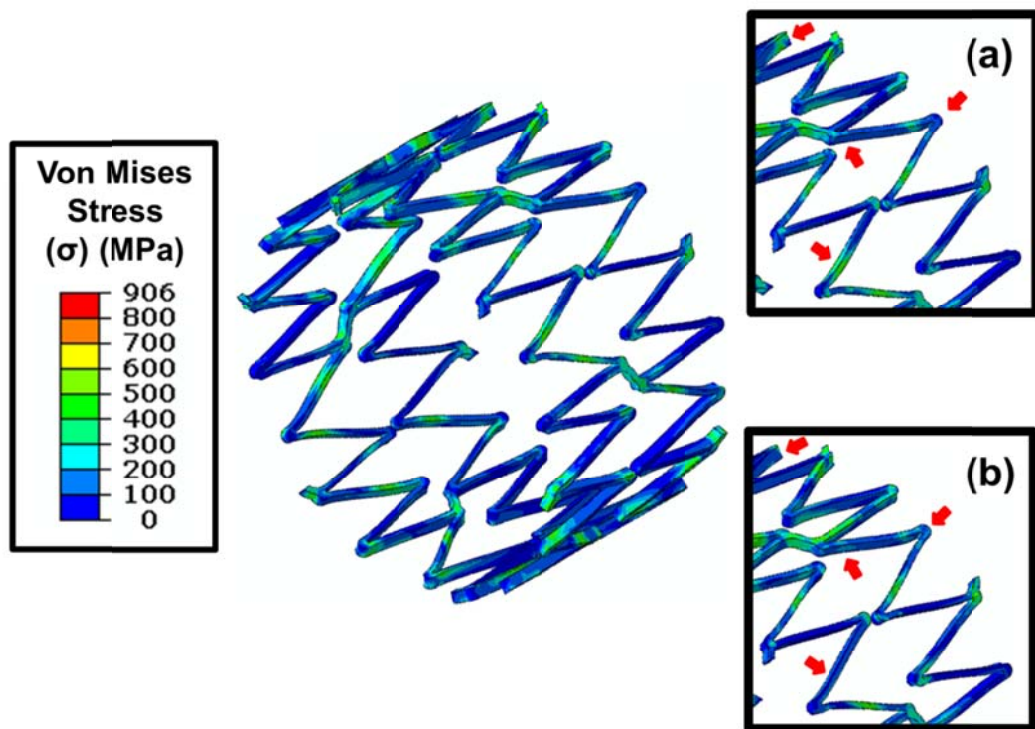


Figure 4.13 Differences in stress concentrations (MPa) of the 2-ring-periodic geometry model at the end of the deploy step for a small strain analysis (a) and a large strain analysis (b). Strains in the 2-ring-periodic geometry model at the end of the deploy step for small strain analysis (c) and large strain analysis (d).

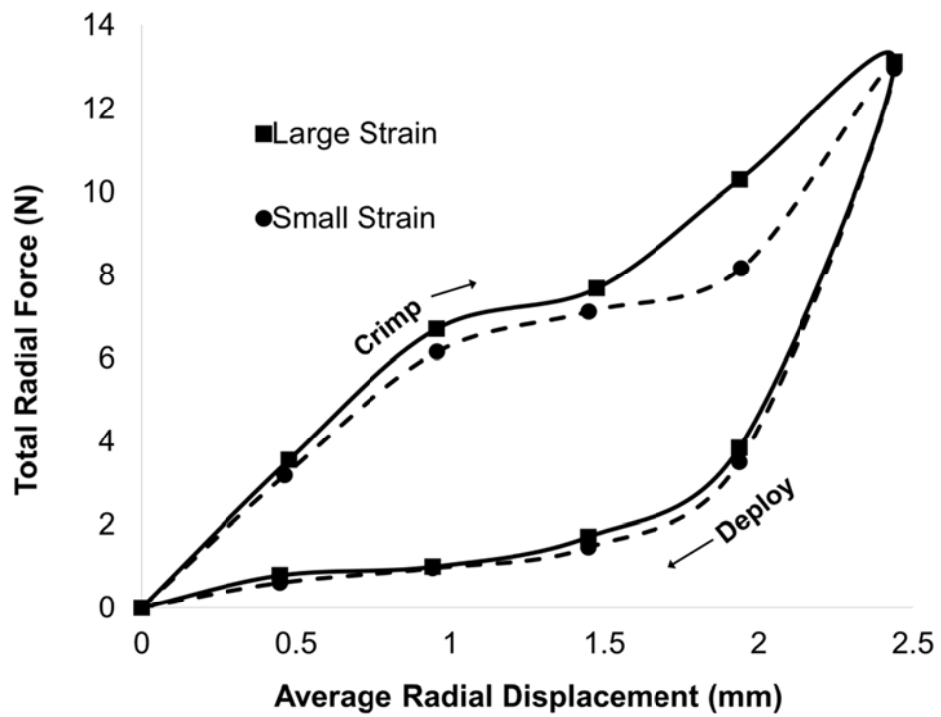


Figure 4.14 Comparison of non-linear geometry analysis effects on 2-ring-periodic geometry radial force.

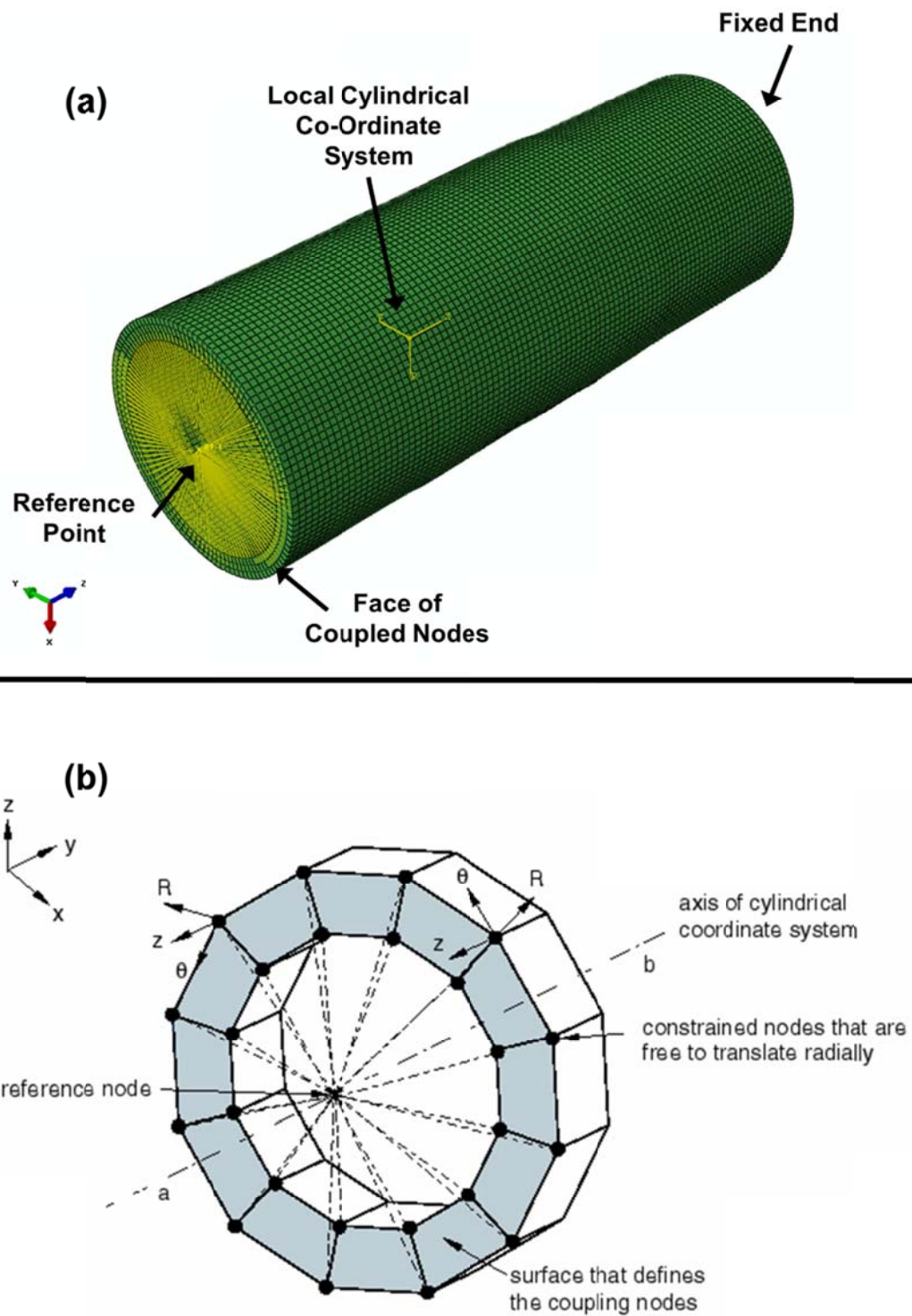


Figure 4.15 The kinematic coupling constraint used to apply physiological loading conditions to the artery in the analysis (a) and a schematic of the features of a kinematic coupling constraint (b) (Abaqus, 2011).

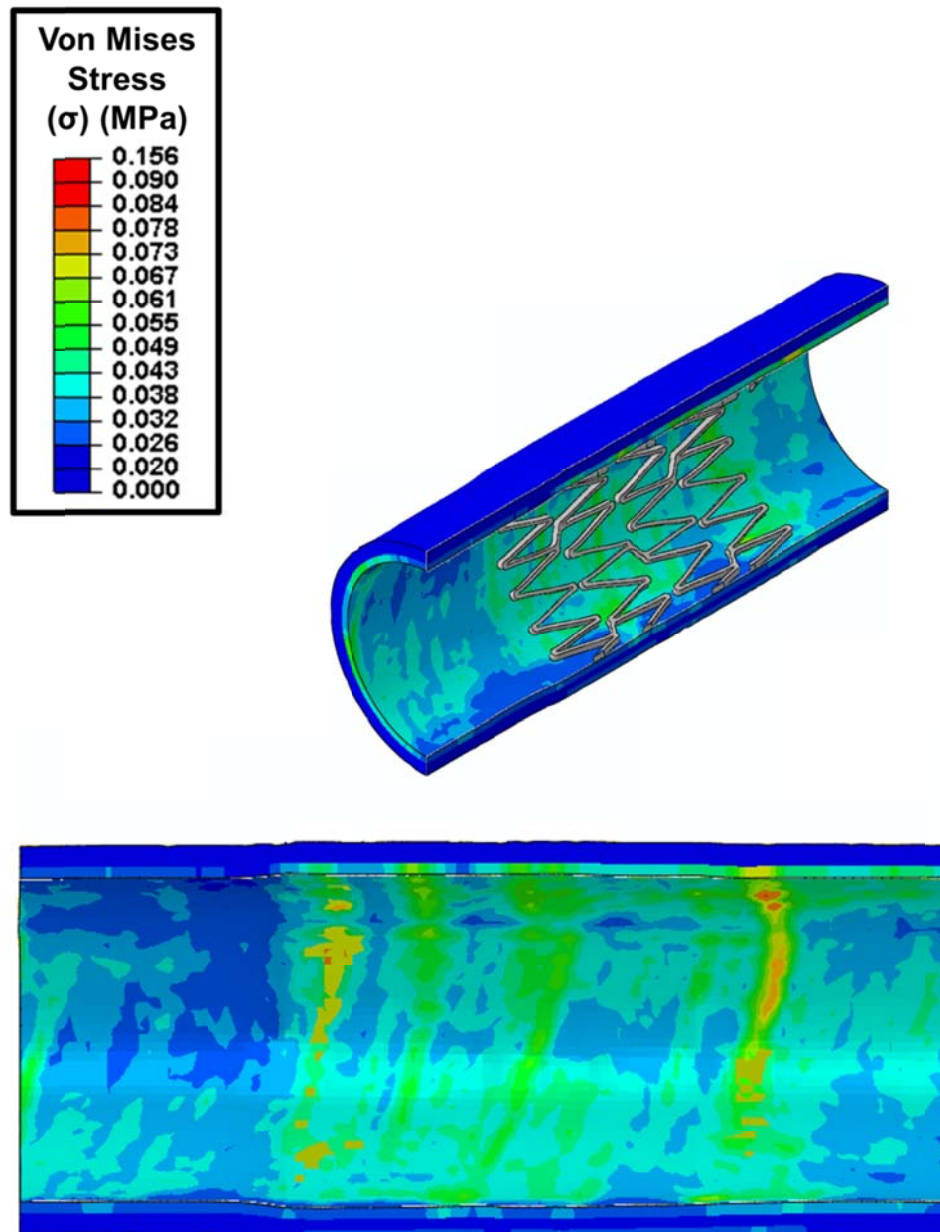


Figure 4.16 Von Mises stresses (MPa) in the stented artery segment after 10% axial compression.

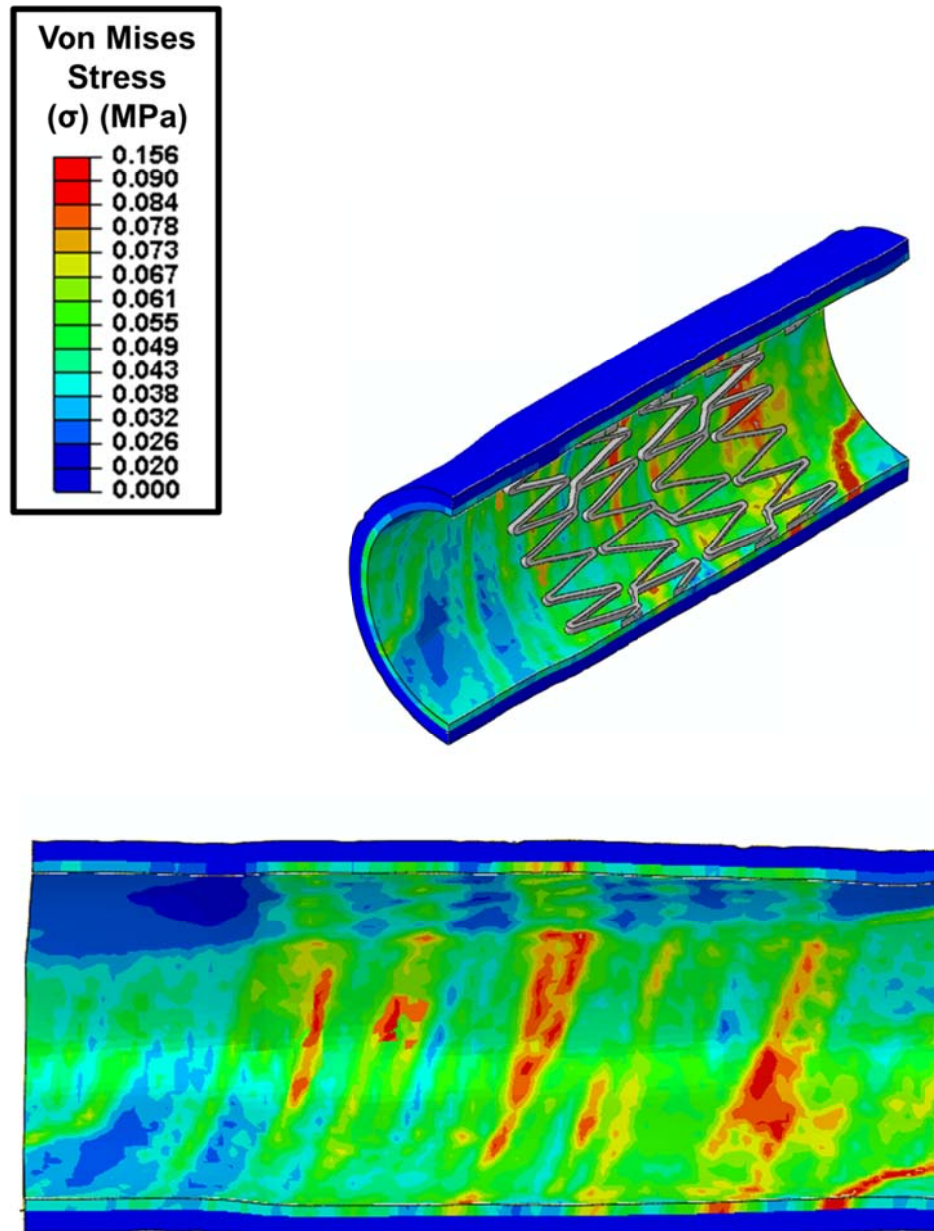


Figure 4.17 Von Mises stresses (MPa) in the stented artery segment after 10% axial compression and $0.28^\circ \text{ mm}^{-1}$ torsion.

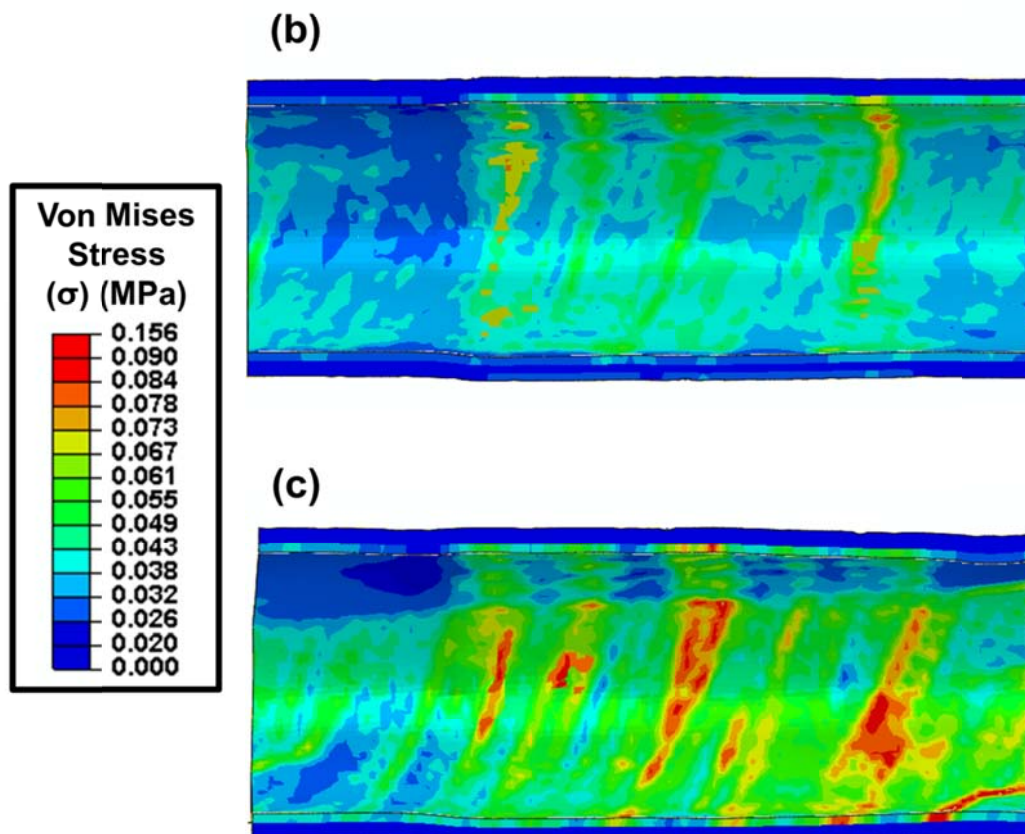
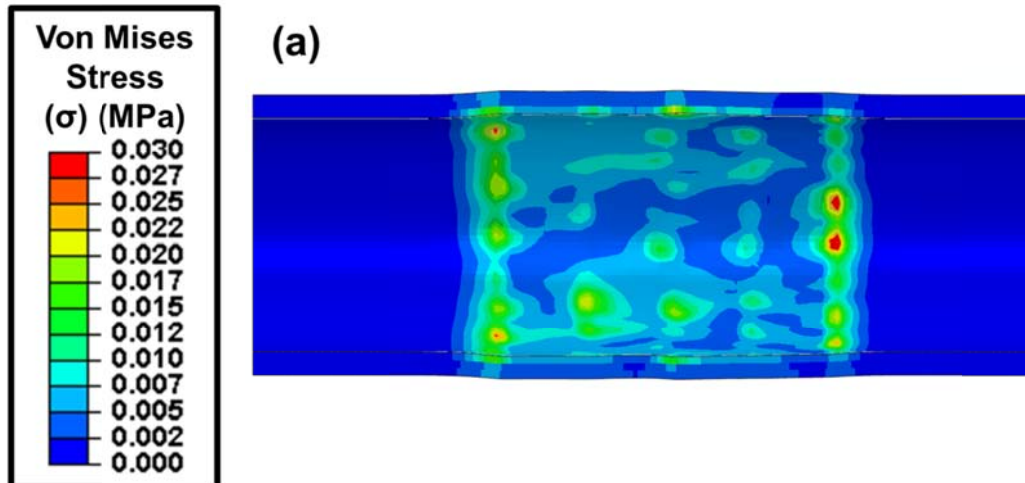


Figure 4.18 Comparison of Von Mises stresses (MPa) in the artery (a) after stent deployment (b) after 10% axial compression (c) after 10% axial compression and $0.28^\circ \text{ mm}^{-1}$ torsion.

4.6 References

- Abaqus. 2011. Abaqus Analysis Users Manual (v.6.11). Dassault Systèmes.
- Auricchio, F, Conti, M, De Beule, M, De Santis, G, et al. 2011. Carotid artery stenting simulation: From patient-specific images to finite element analysis. *Medical engineering & physics*. 33: 281-289.
- Balossino, R, Gervaso, F, Migliavacca, F, and Dubini, G. 2008. Effects of different stent designs on local hemodynamics in stented arteries. *Journal of Biomechanics*. 41: 1053-1061.
- Barth, KH, Virmani, R, Froelich, J, Takeda, T, et al. 1996. Paired comparison of vascular wall reactions to Palmaz stents, Strecker tantalum stents, and Wallstents in canine iliac and femoral arteries. *Circulation*. 93: 2161-2169.
- Capelli, C, Gervaso, F, Petrini, L, Dubini, G, et al. 2009. Assessment of tissue prolapse after balloon-expandable stenting: influence of stent cell geometry. *Medical engineering & physics*. 31: 441-447.
- Carter, A, Scott, D, Bailey, L, Jones, R, et al. 1997. Stent design: in the “ends” it matters. *Circulation*. 96: 1-402.
- Choi, G, Cheng, CP, Wilson, NM, and Taylor, CA. 2009. Methods for quantifying three-dimensional deformation of arteries due to pulsatile and nonpulsatile forces: implications for the design of stents and stent grafts. *Annals of Biomedical Engineering*. 37: 14-33.
- Conti, M, Auricchio, F, De Beule, M, and Verheghe, B. Numerical simulation of Nitinol peripheral stents: from laser-cutting to deployment in a patient specific anatomy. in 8th European Symposium on Martensitic Transformations. 2009. Prague, Czech Republic.

- David Chua, S, MacDonald, B, and Hashmi, M. 2004a. Effects of varying slotted tube (stent) geometry on its expansion behaviour using finite element method. *Journal of Materials Processing Technology*. 155: 1764-1771.
- David Chua, S, MacDonald, B, and Hashmi, M. 2004b. Finite element simulation of slotted tube (stent) with the presence of plaque and artery by balloon expansion. *Journal of Materials Processing Technology*. 155: 1772-1779.
- Denison, A. Axial and bending fatigue resistance of nitinol stents. in *International Conference on Shape Memory and Superelastic Technologies*. 2004. Baden-Baden, Germany.
- Duda, SH, Pusich, B, Richter, G, Landwehr, P, et al. 2002. Sirolimus-Eluting Stents for the Treatment of Obstructive Superficial Femoral Artery Disease. *Circulation*. 106: 1505-1509.
- Duda, SH, Wiskirchen, J, Tepe, G, Bitzer, M, et al. 2000. Physical Properties of Endovascular Stents: An Experimental Comparison. *Journal of Vascular and Interventional Radiology*. 11: 645-654.
- Early, M, Lally, C, Prendergast, PJ, and Kelly, DJ. 2009. Stresses in peripheral arteries following stent placement: a finite element analysis. *Computer Methods in Biomechanics and Biomedical Engineering*. 12: 25-33.
- Gasser, TC and Holzapfel, GA. 2007. Modeling plaque fissuring and dissection during balloon angioplasty intervention. *Annals of Biomedical Engineering*. 35: 711-723.
- Gasser, TC, Ogden, RW, and Holzapfel, GA. 2006. Hyperelastic modelling of arterial layers with distributed collagen fibre orientations. *Journal of the Royal Society Interface*. 3: 15-35.
- Gastaldi, D, Morlacchi, S, Nichetti, R, Capelli, C, et al. 2010. Modelling of the provisional side-branch stenting approach for the treatment of atherosclerotic

coronary bifurcations: effects of stent positioning. *Biomechanics and Modeling in Mechanobiology*. 9: 551-561.

Gervaso, F, Capelli, C, Petrini, L, Lattanzio, S, et al. 2008. On the effects of different strategies in modelling balloon-expandable stenting by means of finite element method. *Journal of Biomechanics*. 41: 1206-1212.

Gijsen, FJH, Migliavacca, F, Schievano, S, Socci, L, et al. 2008. Simulation of stent deployment in a realistic human coronary artery. *Biomedical Engineering Online*. 7: 23-34.

Gong, XY, Pelton, AR, Duerig, TW, Rebelo, N, et al. Finite element analysis and experimental evaluation of superelastic Nitinol stent. in *International Conference on Shape Memory and Superelastic Technologies*. 2004. Pacific Grove, California, USA.

Gunn, J and Cumberland, D. 1999. Does stent design influence restenosis? *European Heart Journal*. 20: 1009-1013.

Hall, GJ and Kasper, EP. 2006. Comparison of element technologies for modeling stent expansion. *Journal of Biomechanical Engineering*. 128: 751-756.

Holzapfel, G, Stadler, M, and Gasser, T. 2005a. Changes in the mechanical environment of stenotic arteries during interaction with stents: computational assessment of parametric stent designs. *Journal of Biomechanical Engineering*. 127: 166-209.

Holzapfel, GA, Sommer, G, Gasser, CT, and Regitnig, P. 2005b. Determination of layer-specific mechanical properties of human coronary arteries with non atherosclerotic intimal thickening and related constitutive modeling. *American Journal of Physiology - Heart and Circulatory Physiology*. 289: H2048-H2058.

- Holzapfel, GA, Stadler, M, and Schulze-Bauer, CAJ. 2002. A Layer-Specific Three-Dimensional Model for the Simulation of Balloon Angioplasty using Magnetic Resonance Imaging and Mechanical Testing. *Annals of Biomedical Engineering*. 30: 753-767.
- Jonker, FS, F. Moll, F. Muhs, B. 2008. Dynamic Forces in the SFA and Popliteal Artery During Knee Flexion. *Endovascular Today*.
- Kastrati, A, Dirschinger, J, Boekstegers, P, Elezi, S, et al. 2000. Influence of stent design on 1-year outcome after coronary stent placement: A randomized comparison of five stent types in 1,147 unselected patients. *Catheterization and Cardiovascular Interventions*. 50: 290-297.
- Kleinstreuer, C, Li, Z, Basciano, C, Seelecke, S, et al. 2008. Computational mechanics of Nitinol stent grafts. *Journal of Biomechanics*. 41: 2370-2378.
- Lally, C, Dolan, F, and Prendergast, P. 2005. Cardiovascular stent design and vessel stresses: a finite element analysis. *Journal of Biomechanics*. 38: 1574-1581.
- Lally, C, Reid, A, and Prendergast, P. 2004. Elastic behavior of porcine coronary artery tissue under uniaxial and equibiaxial tension. *Annals of Biomedical Engineering*. 32: 1355-1364.
- Liang, D, Yang, D, Qi, M, and Wang, W. 2005. Finite element analysis of the implantation of a balloon-expandable stent in a stenosed artery. *International Journal of Cardiology*. 104: 314-318.
- McGarry, J, O'donnell, B, McHugh, P, and McGarry, J. 2004. Analysis of the mechanical performance of a cardiovascular stent design based on micromechanical modelling. *Computational Materials Science*. 31: 421-438.
- Moore, JE and Berry, JL. 2002. Fluid and solid mechanical implications of vascular stenting. *Annals of Biomedical Engineering*. 30: 498-508.

- Mortier, P, De Beule, M, Van Loo, D, Verheghe, B, et al. 2009. Finite element analysis of side branch access during bifurcation stenting. *Medical engineering & physics*. 31: 434-440.
- Mortier, P, Holzapfel, G, De Beule, M, Van Loo, D, et al. 2010. A Novel Simulation Strategy for Stent Insertion and Deployment in Curved Coronary Bifurcations: Comparison of Three Drug-Eluting Stents. *Annals of Biomedical Engineering*. 38: 88-99.
- Nikanorov, A, Smouse, HB, Osman, K, Bialas, M, et al. 2008. Fracture of self-expanding nitinol stents stressed in vitro under simulated intravascular conditions. *Journal of Vascular Surgery*. 48: 435-440.
- Pelton, A, Schroeder, V, Mitchell, M, Gong, XY, et al. 2008. Fatigue and durability of Nitinol stents. *Journal of the Mechanical Behavior of Biomedical Materials*. 1: 153-164.
- Pericevic, I, Lally, C, Toner, D, and Kelly, DJ. 2009. The influence of plaque composition on underlying arterial wall stress during stent expansion: the case for lesion-specific stents. *Medical engineering & physics*. 31: 428-433.
- Prendergast, P, Lally, C, Daly, S, Reid, A, et al. 2003. Analysis of prolapse in cardiovascular stents: a constitutive equation for vascular tissue and finite-element modelling. *Journal of Biomechanical Engineering*. 125: 692-699.
- Qiu, Y and Tarbell, JM. 2000. Numerical simulation of pulsatile flow in a compliant curved tube model of a coronary artery. *Journal of Biomechanical Engineering*. 122: 77-85.
- Rebelo, N, Fu, R, and Lawrenchuk, M. 2009. Study of a nitinol stent deployed into anatomically accurate artery geometry and subjected to realistic service loading. *Journal of Materials Engineering and Performance*. 18: 655-663.

- Rebelo, N, Prabhu, S, Feezor, C, and Denison, A. Deployment of a Self-Expanding Stent in an Artery. in International Conference on Shape Memory and Superelastic Technologies. 2006. Baden-Baden, Germany.
- Scheinert, D, Scheinert, S, Sax, J, Piorkowski, C, et al. 2005. Prevalence and clinical impact of stent fractures after femoropopliteal stenting. *Journal of the American College of Cardiology*. 45: 312-315.
- Smilde, TJ, van den Berkmortel, FWPJ, Boers, GHJ, Wollersheim, H, et al. 1998. Carotid and femoral artery wall thickness and stiffness in patients at risk for cardiovascular disease, with special emphasis on hyperhomocysteinemia. *Arteriosclerosis, Thrombosis, and Vascular Biology*. 18: 1958-1963.
- Smouse, B, Nikanorov, A, and LaFlash, D. 2005. Biomechanical forces in the femoropopliteal arterial segment. *Endovascular Today*. 4: 60-66.
- Tai, NRM, Giudiceandrea, A, Salacinski, HJ, Seifalian, AM, et al. 1999. In vivo femoropopliteal arterial wall compliance in subjects with and without lower limb vascular disease. *Journal of Vascular Surgery*. 30: 936-945.
- Timmins, LH, Meyer, CA, Moreno, MR, and Moore, JE. 2008. Mechanical modeling of stents deployed in tapered arteries. *Annals of Biomedical Engineering*. 36: 2042-2050.
- Walke, W, Paszenda, Z, and Filipiak, J. 2005. Experimental and numerical biomechanical analysis of vascular stent. *Journal of Materials Processing Technology*. 164: 1263-1268.
- Wang, W-Q, Liang, D-K, Yang, D-Z, and Qi, M. 2006a. Analysis of the transient expansion behavior and design optimization of coronary stents by finite element method. *Journal of Biomechanics*. 39: 21-32.

- Wang, WQ, Liang, DK, Yang, DZ, and Qi, M. 2006b. Analysis of the transient expansion behavior and design optimization of coronary stents by finite element method. *Journal of Biomechanics*. 39: 21-32.
- Wu, W, Qi, M, Liu, XP, Yang, DZ, et al. 2007a. Delivery and release of nitinol stent in carotid artery and their interactions: A finite element analysis. *Journal of Biomechanics*. 40: 3034-3040.
- Wu, W, Wang, WQ, Yang, DZ, and Qi, M. 2007b. Stent expansion in curved vessel and their interactions: A finite element analysis. *Journal of Biomechanics*. 40: 2580-2585.
- Zunino, P, D'Angelo, C, Petrini, L, Vergara, C, et al. 2009. Numerical simulation of drug eluting coronary stents: mechanics, fluid dynamics and drug release. *Computer Methods in Applied Mechanics and Engineering*. 198: 3633-3644.

Chapter 5. Effects of Knee Flexion on the Femoropopliteal Artery: A Computational Study

5.1 Introduction

The femoropopliteal artery is a branch of the femoral artery, the main artery in the upper leg, providing blood to all muscles and superficial tissues in the thigh. It is the largest of the femoral artery branches, composed of the superficial femoral artery (SFA) in the proximal region and popliteal artery in the distal region which twists around the femur as it runs behind the knee. It is characterised by its tortuous geometry.

The femoropopliteal artery is entirely encased in the firm muscles of the thigh that extend and flex the knee. The SFA passes anterior of the thigh at the femoral triangle between the vastus and adductor muscles in a region termed the adductor canal. Once past through the adductor canal, the artery runs posterior of the thigh at the adductor hiatus where it becomes the popliteal artery (Brown et al., 2009). These surrounding muscles translate various deformations on the underlying artery including radial compression, bending, torsion and axial extension and axial compression.

The femoropopliteal artery often has a high levels of peripheral arterial disease and atherosclerotic plaque burden and requiring treatment by percutaneous transluminal angioplasty (PTA) followed by stenting to restore vessel patency and uncompromised blood flow. Due to these dynamic forces, peripheral stents placed in the femoropopliteal artery are reported to have high fracture rates (Jonker, 2008, Müller-Hülsbeck et al., 2010, Schlager et al., 2005), predominantly due to bending of the artery as a result of knee flexion. Worst case bending of the artery is observed in regions of the SFA/popliteal artery behind and just above the knee, proving detrimental to stent patency in this region (Allie et al., 2004, Ganguly et al., 2011, Jonker, 2008, Lederman, 2009, Smouse et al., 2005). Measuring the dynamic forces of the femoropopliteal artery and its deformation characteristics represents a great challenge *in vivo*, hence making it impossible to quantify the load levels imposed on the stent due to the dynamic forces from surrounding muscles. Further investigations

quantifying load levels imposed by surrounding muscles, taken together with characteristic properties of the femoropopliteal artery will give further insight into deformation trends of the artery due to leg movement.

As discussed previously, finite element analysis is a tool widely used to determine the structural integrity of stent designs as well as to investigate the nature of the interaction between the stent and the artery. Computational simulations allow for focus on specific areas of interest and provide a means of comparing *in-vivo* and *in-vitro* experiments that can complement each other to give important insights. Many research groups have published results of computational investigations simulating the deployment of stents into blood vessels. The models created in these studies, most of which investigate coronary arteries, consist of a number of complex components such as user defined material models for stent materials (Auricchio et al., 2011, Conti et al., 2009, Rebelo et al., 2006, Wu et al., 2007a, Wu et al., 2007b); user defined material models for arterial tissue and remodelling (Holzapfel et al., 2002a, Holzapfel et al., 2005, Lally et al., 2004, Prendergast et al., 2003); curved, branched and tapered arterial geometry (Liang et al., 2005, Mortier et al., 2009, Rebelo et al., 2009, Timmins et al., 2008, Wu et al., 2007b); regular and irregular plaque geometries along with various plaque material models (Gasser et al., 2007, Gastaldi et al., 2010, Pericevic et al., 2009); fluid interactions (Balossino et al., 2008, Moore et al., 2002, Qiu et al., 2000, Zunino et al., 2009) and *in-vivo* loading including pulsatile, torsion and bending of stented arteries (Early et al., 2009). Many of these studies use combinations of these complex components in order to accurately capture the interactions involved in stent deployment processes. However these simulations fail to capture the dynamic nature of the physiological surroundings of the vessel which in the case of the femoropopliteal artery are highly complex and greatly impact the artery in terms of deformation characteristics responsible for stent failure.

Although various studies have quantified deformation characteristics of the artery by analysing angiographic images and three dimensional models based on these images, measurements of deformation characteristics and links to levels of stress and strain within the artery have never been assessed (Cheng et al., 2010, Cheng et al., 2006, Klein et al., 2009). Due to this lack of investigation, stent design

parameters of stiffness/flexibility, diameter, length, geometry and the altered deformation characteristics of the artery as a result of the location of stent placement cannot be thoroughly investigated before device implantation in a clinical setting.

According to physicians, there is an advantage to matching the native physiological properties of the vessel after stenting, by maintaining radial stiffness at a level that will ensure vessel compliance close to physiological levels (Duerig et al., 2002). Therefore understanding the native behaviour of the vessel *in vivo* is an essential input for device design.

The overall goal of this study is to create an anatomically accurate, three dimensional finite element model capable of capturing the deformation characteristics of the femoropopliteal artery during knee flexion. An anatomically precise model is essential in order to accurately simulate the biomechanical behaviour of the femoropopliteal artery where the bones, muscles, and soft tissues that surround it are the boundary conditions for its deformational behaviour during knee flexion. The specific objectives were to create a model that can be used to link deformation characteristics (length change, curvature change, lumen reduction (radial compression) and axial twist) as a result of the various dynamic loads of the femoropopliteal artery with stress and strain levels. In addition, it can also be used to quantify the physiological loads applied to the artery as a result of knee flexion.

5.2 Materials and Methods

5.2.1 Geometry

In order to achieve an anatomically accurate geometry, DICOM images produced in a CT scan of the leg from hip to ankle were acquired. The images were imported into MIMICS[®] (Materialise Interactive Medical Image Control System, Leuven, Belgium, Version 14.1) where Hounsfield values were used to separate bone, muscle, artery and soft tissues based on their material densities and density masks created to separate the different tissues. Following separation of tissue using masks, anatomies of individual bones, muscles, arteries and other soft tissue was accomplished by manual editing and edge detection in each slice.

5.2.2 Meshing

Three dimensional geometries of the muscle, bone, arterial and soft tissues were then constructed for each anatomical part and these geometries were meshed in 3-matic[®] (Materialise, Leuven, Belgium, Version 6.0) for finite element analysis. Using mesh control methods volume and surface meshes of high quality, triangular elements were generated. The equi-angle skewness was controlled as defined in equation (5.1) where α was the smallest angle of the triangle and β was the largest angle of the triangle (3-matic, 2011).

$$\min\left(\frac{\alpha}{60}; \frac{180 - \beta}{180 - 60}\right) \quad (5.1)$$

Ratios of this would idyllically be unity, with lowest value set as 0.4 as adopted by previous researchers (Gíslason et al., 2010, Ito et al., 2006). Meshes were smoothed to remove sharp edges by rearranging the position of nodes, whilst simultaneously compensating for volume changes resulting from the smoothing.

Meshed geometries were exported to Abaqus Explicit (Version 6.11 Simulia, DassaultSystèmes, Vélizy-Villacoublay, France) and assembled to form the finished finite element model shown in Figure 5.1. The model consisted of 1 artery part, 3 bone parts, 8 muscle parts and an encasing soft tissue part. Table 5.1 lists the parts of

the analysis along with details of finite element meshes. The bones, muscles and soft tissue geometries were modelled as 3D surfaces with shell elements (S3R) whilst the artery was modelled as a 3D solid with 3D elements (S3D8R). This was appropriate as the bones, muscles and soft tissue parts were included in the model to provide boundaries and stability for the embedded artery. 3D surfaces ensured accurate modelling of this whilst also providing a practically sized computational model. The suitability of the mesh density of each part of the analysis was determined from a mesh dependency study. Final mesh density was chosen once increases to the number of elements of each mesh resulted in changes in computed stress of less than 2% in the part.

5.2.3 Material Properties

Bone

The femur, tibia and patella were modelled using linear elastic isotropic material properties with Young's modulus of 18GPa and Poisson's ratio of 0.2 (Rho et al., 1993). This value represents the Young's modulus of cortical bone. All bone material was assumed as cortical, justified by the fact that the deformation of the bones in comparison to that of the neighbouring soft tissue, muscle and artery is negligible. Furthermore the effect of the knee flexion on the femur, tibia and patella is not of interest in this analysis.

Muscle and Soft Tissue

Skeletal muscles and their mechanical properties have been extensively studied (Gasser et al., 1924, Huxley, 1957, Zajac, 1989). These studies have provided validations of biomechanical models created by numerous researchers who have dedicated significant effort to modelling realistic muscle. Such models focus on accurate anatomical representation of muscle shape and its deformable behaviours during muscle contraction using mass spring systems and finite volume methods (Aubel et al., 2001, Chadwick et al., 1989, Lee et al., 1995, Nedel et al., 1998, Teran et al., 2005). Finite element methods have also been widely investigated for studying skeletal muscles. Various muscle models have been proposed to analyze and predict accurate strain distribution of muscle during contraction and its functional properties.

Chen et al., (1992) proposed an approach for human muscle modelling by integrating a Hill-based muscle model into a linear elastic solid model where active muscle forces were approximated as parametric functions implemented through a finite element mesh which approximated muscle geometry. Muscle flexion was animated and validated by comparing the results of the model to experimental measurements. Hirota et al., (2001) combined the Mooney-Rivlin hyperelastic material model, Veronda material model (Veronda et al., 1970) and a fiber-reinforcement material model (Klisch et al., 1999) to represent passive response of tissues during body contact. Lemos et al., (2001) used a hyperelastic material model to aligned Hill-based muscle forces to fibre orientations within finite element meshes created to represent muscle. Gielen et al., (2000) and Oomens et al., (2003a) incorporated the Huxley model to represent contractile properties of skeletal muscle. In these studies, the equations developed by Huxley (1957) are approximated using a distributed moments approach (Zahalak 1981) and combined with a constitutive equation to describe nonlinear and incompressible material responses. Yucesoy et al., (2002) modelled the mechanical behaviour of skeletal muscle as the interaction between muscle fibres and connective tissues. Muscle geometry was represented by two separate meshes elastically linked to account for the force transmissions between these them. Blemker et al., (2005) developed simulations of complex muscle geometries and architecture created from magnetic resonance images. Moment arms of muscles (measurements calculated from cadavers), were applied to the geometries and the predicted changes to muscle shape were compared to magnetic resonance images of deformed muscles. Tang et al., (2009) proposed a constitutive muscle model in which active contraction of muscle fibres and hyperelastic material properties are coupled using a strain energy density function. They demonstrated concentric and eccentric contraction, and the effects of muscle geometry and fibre orientation on stress distributions.

In this study, the muscles were modelled with surface meshes (shell elements) and a Mooney-Rivlin strain energy density function for hyperelasticity (discussed in Chapter 3, section 3.2.4 of this thesis). The corresponding material parameters are listed in Table 5.2. This approach was chosen to approximate muscle behaviour as it is well established in the literature that non-linear hyperelastic isotropic material models are a good compromise between physical reality and

computational efficiency when dealing with human-body soft tissue (Bader et al., 1983, Chow et al., 1978, Grujicic et al., 2009, Krouskop et al., 1987, Mak et al., 1992, Oomens et al., 2003b, Tang et al., 2010, Todd et al., 1994, Vannah et al., 1996, Yongping et al., 2001, Yongping et al., 1999). This study is not concerned with the detailed internal mechanics of the muscle tissue, but instead, the way in which the muscles act as a boundary for the allowable movement or restraint of the underlying femoropopliteal artery. Whilst the assumptions of the Mooney-Rivlin model include isotropy, homogeneity and non-viscoelastic behaviour, it was deemed as an appropriate choice as it accounts for the large non-linear elastic deformations of muscle. Material constants applied to the Mooney-Rivlin material model in this study were shown by Grujicic et al., (2009) to accurately model the stiffness of bulk muscle, modelled with shell elements, under large deformations. This corresponds to the application in the work of this thesis.

Grujicic et al., (2009) established parameters for the Mooney-Rivlin model by fitting an experimental compression-force versus compression-strain curve from the study by Vannah et al., (1996) (indentor experimental tests on muscular tissue of lower limbs) to their corresponding results obtained from a matching finite element model. Model parameterization (parameter identification) was carried out in an iterative process so as to determine the unknown material model parameters allowing the experimentally predicted load versus nominal strain curves to be matched from the finite element model. Whilst the modelling strategies of other researchers (Blemker et al., 2005, Chen et al., 1992, Gielen et al., 2000, Hirota et al., 2001, Lemos et al., 2001, Oomens et al., 2003b, Tang et al., 2009, Yucesoy et al., 2002) was investigated and considered, it was apparent that these approaches are most applicable to models of the musculoskeletal system where joint kinematics and the loads exerted on joints is of primary interest. These include orthopaedic procedures such as tendon transfer and lengthening operations, joint replacements and gait analysis studies. The necessary inputs for these models (mathematical descriptions of joint kinematics, muscle path geometries and muscle fibre architectures), all dependent on many other parameters (such as activation mechanisms, muscle and tendon length, velocity of movement) would increase computational and experimental requirements and validations and is beyond the scope of this thesis.

Similarly, the soft tissue surrounding the muscles was modelled as a linearly elastic isotropic nearly-incompressible material also as per Grujicic et al. (2009), with a Young's modulus of 0.15 MPa and a Poisson's ratio of 0.46.

Artery

The vessel tissue is modelled using a sixth-order reduced polynomial strain energy density function for isotropic hyperelasticity (discussed in Chapter 3, section 3.2.3 of this thesis) previously used by Gastaldi et al. (2010). This model employs a constitutive law which models incompressible materials allowing for large strains based on experimental data by Holzapfel et al. (2005b) of stress strain tests of arterial layers. Despite the findings of Holzapfel et al. that arterial tissue exhibits anisotropic behaviour, isotropic data was included in this study to simplify the models. The main objective of the study is to create a model capable of capturing the deformational characteristic of the femoropopliteal artery. Anisotropic behaviour of the individual arterial layers was considered to be too complex to include in such a global anatomical model of the leg. Each arterial layer is represented by different parameters in the model thereby allowing a layer specific (intima, media, and adventitia) artery to be represented. The material constants required for implementation of the model in Abaqus are listed in Table 5.3.

Loads, Boundary Conditions and Interactions

A knee bend of approximately 90° was simulated in this analysis. This was simulated by displacing the tibia with respect to the femur. The tibia was moved from a 180° angle to the femur, to a 90° to the femur. This was applied assuming that all muscles were initially in a stress-free configuration. Previous studies on lower limb movements suggest that when lying down, muscles of a straight leg are in a stress free state (Fleuren et al., 2009). Knee flexion was simulated by keeping the femur fixed and prescribing displacement of the tibia along the articulating surfaces of the femur and tibia. For this, a cylindrical co-ordinate system and continuum distributing coupling constraint were initiated at the knee joint, where surfaces of articulation of the femur and tibia were created and movement constrained around a reference point, at an anatomically accurate location for joint articulation. A

displacement boundary condition was then applied to the end surface of the tibia to move the bone along the articulating surfaces, around the reference point.

The model was fixed at the proximal end of the femur where all parts of the femur, muscles, artery and soft tissue parts were fully fixed. It is important to note that the precise movement and interaction of bones, muscle and soft tissue surrounding the artery must be simulated in order to ensure accurate effects on the artery to be captured. This was achieved by ensuring the origin and insertion of muscle tendons to anatomically precise locations on the underlying bone, determined by referencing a human anatomy atlas (Netter, 2006). Insertions of muscles (by tendon attachment to bone) were modelled by creating tie constraints between the tendon regions of the muscles and the relevant bones. General contact conditions were activated between all parts of the model (excluding the surface between the tibia and femur for efficient simulation) with tangential normal contact behaviour specified with a friction coefficient of 0.4 (Shacham et al., 2010, Tang et al., 2010).

5.2.4 Quantification of Deformation

Axial Length Change

Axial length change of the vessel is quantified by calculating the difference between the centreline arc length of the straight leg and flexed knee configurations. In both configurations, the vessel length is divided into equi-spaced sections at each element layer of the artery which corresponds to approximately 0.5mm intervals along the vessel length. A centre point node is found by calculating the average coordinate of the nodes around the inside layer of the vessel wall (Figure 5.2). The distance between each point is calculated and the sum of the distances is used to define the vessel length.

Curvature Change

Artery curvature is defined as the inverse of the radius of a circle fitted to a curve as shown in Figure 5.3. A circle is circumscribed around three equi spaced nodes of a segment of the vessel mesh to create an osculating circle (Figure 5.3). The inverse of the osculating circle is taken as the curvature of the vessel segment. The size of the vessel segments are chosen to be equal to the diameter of the vessel,

following methods validated in a previous study by Choi et al. (2009). Measurements for curvature are calculated for the portion of the vessel behind the knee where the most extreme curvatures have been observed in previous studies (Cheng et al., 2010, Choi et al., 2009, Klein et al., 2009).

Radial Compression

Radial compression is defined as the change in vessel lumen cross sectional area (CSA) as a result of knee flexion. At each element layer of the vessel (which corresponds to approximately 0.5mm intervals along the vessel length), images were captured in Abaqus of the CSA of the vessel lumen in the straight leg and flexed knee configuration. The lumen CSA is calculated using ImageJ software (Rasband, 1997-2011). Best fit circles/ellipses were traced over the vessel lumen of the images and the area of the shape calculated. The change in lumen CSA is the difference between the same section in the straight leg and flexed knee configurations. The aspect ratio of the vessel lumen is quantified as the ratio of the major to minor axis of the best fitting circle/ellipse of the lumen.

Axial Twist/Torsion

Axial twist is defined as the change in degrees of the angle of separation between two arbitrary vectors on the vessel. A twisting metric, developed by Choi et al. (2009) to measure 3D characteristics of vessel geometry was used to quantify the twisting of the vessel due to knee flexion. As described by Choi et al. this method measures the axial twist of the artery by determining the difference between the angle of separation between adjacent branches of the artery (profunda femoris (PF) artery branch and superior geniculate (SG) artery branch) in a current configuration (i.e. straight leg) and reference configuration (i.e. flexed knee). Due to bending and twisting effects acting together during vessel deformation, the effect of twist of the artery from knee flexion is not co-planar, making it necessary to separate the bending component from the total deformation to quantify the pure twisting component of the vessel (Choi et al., 2009). The centre point nodes (used in the axial length change calculation (Figure 5.2) are used to subdivide the length of the vessel into short segments that can be assumed co-planar (Figure 5.4). Referring to the CT scan, locations of the profunda femoris (PF) artery and superior geniculate (SG) artery

branch are identified and correlated with a node on the outside surface of the vessel mesh where that branch would stem. A vector C_iP_i is calculated, from the co-ordinates of the identified node of the PF branch origin on the outside surface of the vessel mesh (P_i of Figure 5.4) to the co-ordinates of the centre point node of the vessel at that section (C_i of Figure 5.4). Following the methods of Choi et al. (2009), this vector is translated along the length of the vessel as far as the segment of the SG artery branch using equation (5.2). This translation is calculated using the rotation axis $\vec{\omega}_i$ (equation (5.5)) and rotation angle ψ_i (equation (5.6)).

$$\overrightarrow{C_{i+1}P_{i+1}} = Rot(\omega_i, \psi_i) \cdot \overrightarrow{C_iP_i} \quad (5.2)$$

$$Rot(\omega_i, \psi_i) = e^{[\vec{\omega}_i]\psi_i} \quad (5.3)$$

$$[\omega_i] = \begin{pmatrix} 0 & -\omega_{iz} & \omega_{iy} \\ \omega_{iz} & 0 & -\omega_{ix} \\ -\omega_{iy} & \omega_{ix} & 0 \end{pmatrix} \quad (5.4)$$

$$\vec{\omega}_i = \frac{\vec{n}_i \times \vec{n}_{i+1}}{\|\vec{n}_i \times \vec{n}_{i+1}\|} \quad (5.5)$$

$$\vec{\psi}_i = \cos^{-1} \left(\frac{\vec{n}_i \cdot \vec{n}_{i+1}}{\|\vec{n}_i\| \cdot \|\vec{n}_{i+1}\|} \right) \quad (5.6)$$

A vector C_jQ_j is calculated, from the co-ordinates of the identified node of the SG branch origin on the outside surface of the vessel mesh (Q_j of Figure 5.4) to the co-ordinates of the centre point node of the vessel at that section (C_j of Figure 5.4). This is done in both the straight leg and flexed knee configurations. An angle of separation Θ is calculated as the angle between the vector C_jP_j and C_jQ_j in the straight leg configuration (equation (5.7)). Similarly, an angle of separation θ is calculated as the angle between the vector C_jP_j and C_jQ_j in the flexed knee configuration. The twist angle for the vessel is the found by calculating the difference between the angles of separation in each configuration, $(\theta - \Theta)$.

$$\Theta = \cos^{-1} \left(\frac{\overline{C_b P_b} \cdot \overline{C_b Q_b}}{\|\overline{C_b P_b}\| \cdot \|\overline{C_b Q_b}\|} \right) \quad (5.7)$$

5.3 Results

The main objective of this study was to develop a finite element model of the femoropopliteal artery to capture its dynamic load levels and deformation characteristics. Specific deformations of length change, curvature change, and axial twist were measured and used to validate the deformed artery from the model presented here by comparing its shape to similar experimental studies that investigate arterial deformation through angiographic images. This comparison is made in Figure 5.5(a) which shows a good correlation between arterial shape of the finite element model presented here and that of angiographic images from a previous study by Klein et al. (2009).

5.3.1 Axial Length Change

Shortening of the vessel was observed after knee flexion. The straight leg length and flexed knee length of the vessel are 22.11cm and 20.29cm respectively. The change in length caused by knee flexion is 1.82cm, representing vessel shortening of 8.23%.

5.3.2 Curvature Change

Curvature of the vessel imposed by knee flexion can be seen in Figure 5.5(b) which shows contour plots in multiple views of the artery after knee flexion. Values for artery curvature after flexion in the distal portion of the vessel are summarised in Table 5.4. Maximum artery curvature observed in the flexed knee was 0.601cm^{-1} , proximal to the knee joint. After comparing the curvatures at each measurement location before and after knee flexion proximal to the knee joint, it was found that the average change in vessel curvature in this region is $0.18 \pm 0.03\text{cm}^{-1}$. Maximum stress and strain as a result of induced curvatures in the vessel are 61.17 kPa and 0.16% respectively (Figure 5.5(c) and Figure 5.5 (d)).

5.3.3 Radial Compression

Radial compression of the vessel lumen is summarised in Figure 5.6 which shows typical lumen CSA profiles in the straight leg and flexed knee configurations. These profiles are a selection of those from which the values for radial compression

were calculated. More extreme radial compression and distortion of the vessel lumen CSA is seen in the region of the vessel behind the knee as shown in Figure 5.6(a) (S_4 and S_5). CSA of the vessel lumen in the straight and flexed knee position is summarised in Table 5.5. The average change in CSA of all sections taken is $12.32 \pm 3.1 \text{ mm}^2$. Aspect ratios of the vessel lumen in straight leg and flexed knee position are shown in Figure 5.6(b). The average change in aspect ratio from the straight leg to flexed knee position for all sections is 0.51.

5.3.4 Axial Twist/Torsion

The twist angle for the entire vessel from the straight leg to flexed knee configurations was calculated to be 32.71° . The axial twist gradient was determined to be $0.161^\circ/\text{mm}$, found by dividing the twist of the entire vessel by its length. Arterial stress and strain as a result of induced twist in the vessel can be seen in the contour plots of Figure 5.5(c) and Figure 5.5 (d).

5.4 Discussions and Conclusions

The goal of this study was to create an anatomically accurate three dimensional finite element model to capture dynamic load levels and deformation characteristics of the femoropopliteal artery (length change, curvature change, lumen reduction (radial compression) and axial twist) during knee flexion. Results show that the model developed here is capable of replicating the *in vivo* deformation of the femoropopliteal artery and is applied, for the first time in this work to quantify femoropopliteal artery deformation and associate deformation characteristics with stress and strain levels within the arterial tissue. The resulting deformation of the artery presented here can be validated by comparing it to similar experimental studies that investigate arterial deformation through angiographic images such as Klein et al. (2009) (Figure 5.5(a)). Accurate biomechanical behaviour of the artery was captured through the use of a precise model of the human leg where the bones, muscles and surrounding soft tissues of the artery are used as boundary conditions for its deformation behaviour. Furthermore, using realistic material models for the soft tissue, muscle and artery also allow the model to mimic arterial deformation characteristics and more importantly to model stress and strain levels within the arterial tissue.

The shortening of the vessel from the straight leg to flexed knee positions of 8.23% observed in the model presented here compares well to results of other studies that determine vessel shortening after similar replication of lower limb movement. Choi et al. (2009) reported 8.8% shortening of the SFA from the straight leg to flexed knee position. This was determined from the measurement of centrelines calculated on three dimensional models of the main arterial tree, created from MRI scans of the SFA in both the supine and fetal positions. Applying similar methods, Cheng et al. (2010) and Klein et al. (2009) reported 6.9% and 6.1% shortening of the vessel respectively after knee flexion. The close correlation of these values from studies carried out on geometries from a range of MRI and CT scans validates the model created here and the methods used to simulate knee flexion.

This study has, for the first time, linked deformation of the femoropopliteal artery to stress and strain levels. As shown in Figure 5.5, maximum curvatures of

0.601 cm⁻¹ in the flexed knee position are linked with stresses of 36.24kPa and strains of 0.16% are prevalent in locations behind and above the knee as can be seen in many clinical angiographic images. The mean curvature of the flexed vessel determined by the model in this study is 0.294 ± 0.26 cm⁻¹. This value compares well with the published data of vessel curvature from 3D models generated from angiographic images, as shown in Figure 5.5(b) (Cheng et al., 2010, Choi et al., 2009, Klein et al., 2009). This comparison highlights the accuracy of the finite element model of this study in simulating deformation of the artery.

The artery is seen to be compressed radially due to the movement of the knee from the straight leg to flexed position with resulting changes in vessel lumen cross sectional area and aspect ratio, with more extreme radial compression and distortion of the vessel lumen seen directly behind the knee. Compression and alteration of the vessel lumen cross sectional profile can lead to altered blood flow within the vessel with consequences on hemodynamic forces of wall shear stress (WSS), radial pressure and tensile hood strain (THS). Hemodynamic force mechanisms and their effects have been investigated extensively and it is known that alterations to hemodynamic force influences the development of vascular pathologies (Barron et al., 2007, Dartsch et al., 1989, Lehoux et al., 2006, Levesque et al., 1985, Malek et al., 1999, Moore et al., 1994, Moretti et al., 2004, Neidlinger-Wilke et al., 2001, Wang et al., 1995, Wang et al., 2001, Ziegler et al., 1998).

From a clinical perspective the results of this study provides deformation levels of the artery that can be linked with the various vascular disease states observed *in vivo*. With regard to medical device design, stent radial compression can be determined by assessing the reduced diameter of the stent due to the application of external pressure from the surrounding artery (Duerig et al., 2002). Therefore, the vessel compression results of this study can be used to gain further insight into the flexibility required by the stented vessel. Furthermore, in reference to stent design parameters, it has been suggested that preserving the native physiologically correct vessel properties is an advantageous trait (Duerig et al., 2002). Again, vessel compression results provided by this study can be used as inputs for device design.

This study has quantified the axial twist of the femoropopliteal artery as a result of knee flexion using a finite element model, linking axial twist of the artery to

stress and strain levels for the first time (Figure 5.5). The angle of twist quantified by the model compares well with the results of other studies. Choi et al. (2009) reported an angle of twist of $0.8 \pm 0.4^\circ/\text{mm}$. Klein et al. (2009) reported an angle of twist of $0.346 \pm 1.9^\circ/\text{mm}$.

A limitation of the model is the simulation of knee flexion using only a displacement boundary condition to the tibia. Another method considered when creating the model was to apply active contraction of the eight muscles surrounding the artery which may more accurately reflect the biomechanics of the muscle tissue during knee flexion. However, as previously mentioned, it is the way in which the muscles act as a boundary for the allowable movement or restraint of the underlying femoropopliteal artery that is of interest in this study and it is important to recognise that precise arterial deformation characteristics have been shown in this work. This is achieved in the model by ensuring accurate geometries, insertion of muscles in anatomically accurate locations and employing material properties that have been proven to correspond well to experimental models of muscle movement. As an active muscle and soft tissue model would negatively impact on computational efficiency without necessarily increasing the accuracy of the resulting deformations of the artery, the methods taken were deemed appropriate. Furthermore, as discussed, quantification of deformation values from this study compare well to previous studies that quantify deformation to the artery from knee flexion, confirming the validity of the approach taken to apply knee flexion in this study.

This study has shown that deformation of the femoropopliteal artery due to knee flexion occurs in three dimensions, and therefore multiple viewing planes must be assessed in order to fully determine the artery deformation during knee flexion. This is not typically considered with angiographic images as it would be very time consuming. There are many potential applications of this model in industry to benefit stent design. In order to ensure safe and effective endovascular device design, dynamic changes to vessels from *in vivo* deformations must be thoroughly understood. Strict guidelines for testing the mechanical performance of devices are enforced by regulatory bodies including a number of bench top tests and finite element simulations. These tests ensure the durability of the device within the *in vivo* loading environment in which it must perform. As the femoropopliteal artery is

susceptible to extreme deformations due to repetitive knee flexion occurring during walking, stair climbing and sitting; linking the repetitive deformation of the artery with device fatigue should be an essential input when seeking regulatory approval for a medical device. A finite element model such as that presented in this study allows for simulation of a realistic loading environment in order for *in vivo* arterial load levels to be established. These load levels, established from 'global' models of entire arteries can be inputs for 'local' models of artery segments and implanted devices for durability analysis. Furthermore, the model can be adapted to incorporate stent placement (through stiffness changes) to investigate the effect of stented artery portions on its deformation. Moreover, the model could be applied clinically using patient specific models.

In conclusion, we have presented a finite element model that captures the deformation characteristics of the femoropopliteal artery during knee flexion. This model can be used to assess the biomechanical behaviour of the femoropopliteal artery after knee flexion due to the interaction of surrounding anatomical structures of bone, muscle, and soft tissues. The model associates deformation characteristics of axial length change, curvature change, radial compression and axial twist with stress and strain levels in the artery.

5.5 Tables and Figures

Part	Number of Elements
Femoral Artery	58,945
Tibia	7,803
Femur	12,318
Patella	4,040
Adductors (Brevis, Longus, Magnus)	51,218
Vastus (Lateralis, Medialis, Intermedius)	61,671
Rectus Femoris	11,504
Gracillis	16,306
Sartorius	18,790
Semimembranosus	20,818
Semitendinosus	25,634
Biceps Femoris	44,652
Soft Tissue/Outer Skin	161,165

Table 5.1 Details of meshes for the parts of the finite element model of the leg.

C₁₀ (MPa)	C₀₁ (MPa)	D₁
0.00165	0.00335	0.49

Table 5.2 Material constants of the Mooney-Rivlin strain energy density function for the muscle material model (Grujicic et al., 2009).

	C₁₀ (MPa)	C₂₀ (MPa)	C₃₀ (MPa)	C₄₀ (MPa)	C₅₀ (MPa)	C₆₀ (MPa)
Intima	6.79E-03	5.40E-01	-1.11	10.65	-7.27	1.63
Media	6.52E-03	4.89E-02	9.26E-03	0.76	-0.43	8.69E-02
Adventitia	8.27E-03	1.20E-02	5.20E-01	-5.63	21.44	0.00

Table 5.3 Material constants of sixth order reduced polynomial strain energy density function for the isotropic artery material model (Gastaldi et al., 2010).

	Maximum (cm⁻¹)	Mean (cm⁻¹)
Straight Leg Curvature	0.089	0.061 ± 0.03
Flexed Knee Curvature	0.601	0.294 ± 0.26

Table 5.4 Maximum and mean curvature of the femoropopliteal artery in straight leg and flexed knee positions.

	Minimum (mm²)	Maximum (mm²)	Mean (mm²)
Straight Leg FP Lumen CSA	32.67	54.87	37.91 ± 6.1
Flexed Knee FP Lumen CSA	10.42	52.40	28.32 ± 3.2

Table 5.5 Minimum, maximum and mean lumen cross sectional area (CSA) of the femoropopliteal (FP) artery in straight and flexed knee positions.

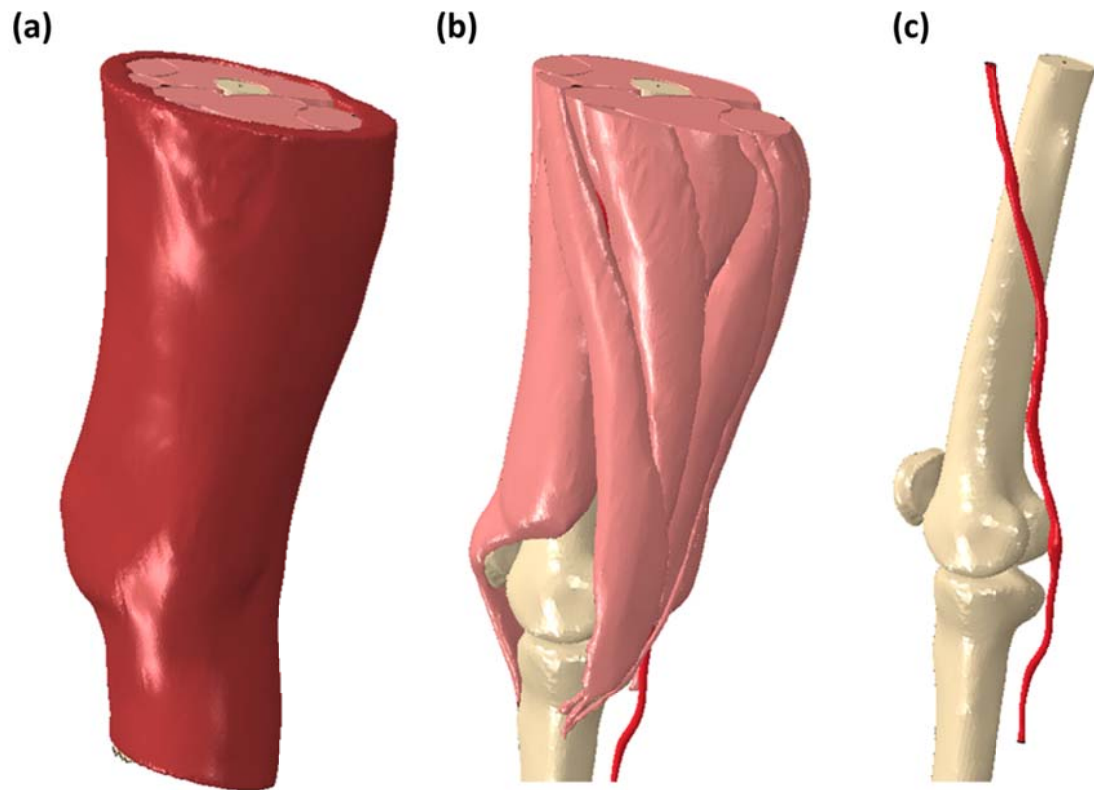


Figure 5.1 Finite Element Model of the Leg: (a) the complete model (b) outer soft tissue (skin) removed to reveal individual muscles (c) outer skin and muscles removed to reveal the underlying bones and femoropopliteal artery.

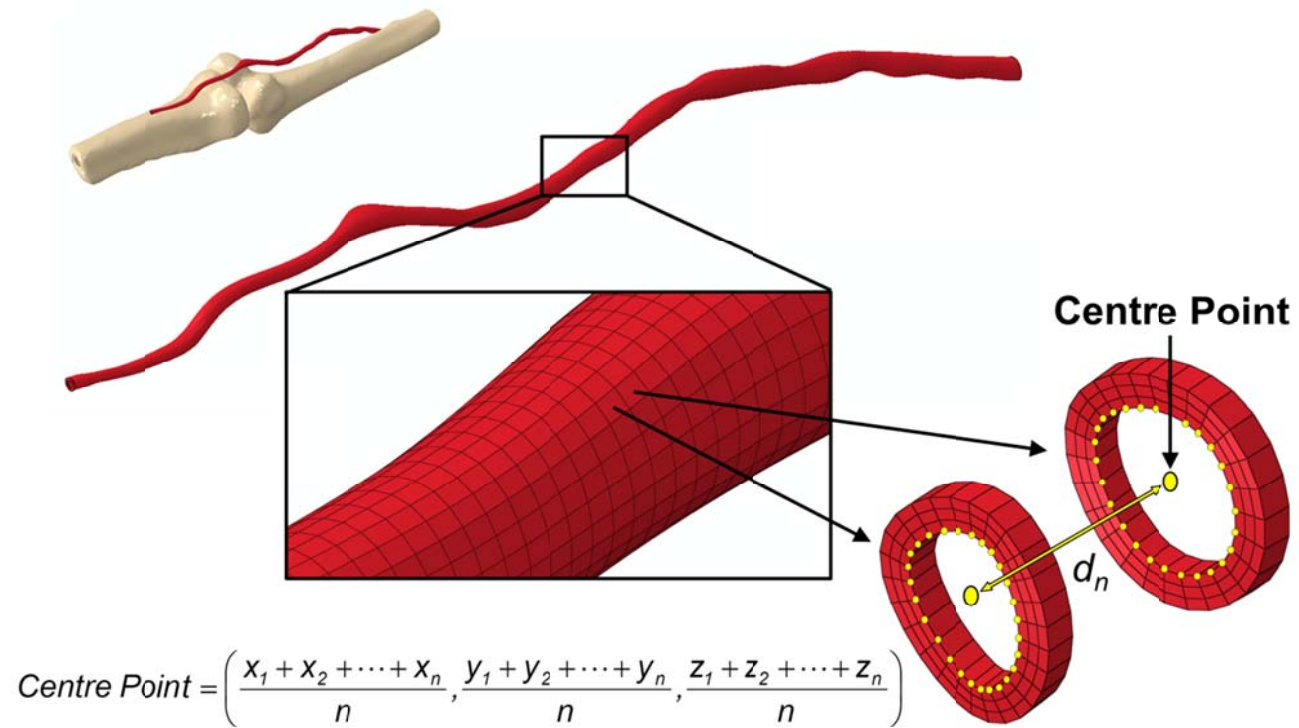


Figure 5.2 Schematic of methods used to calculate vessel length.

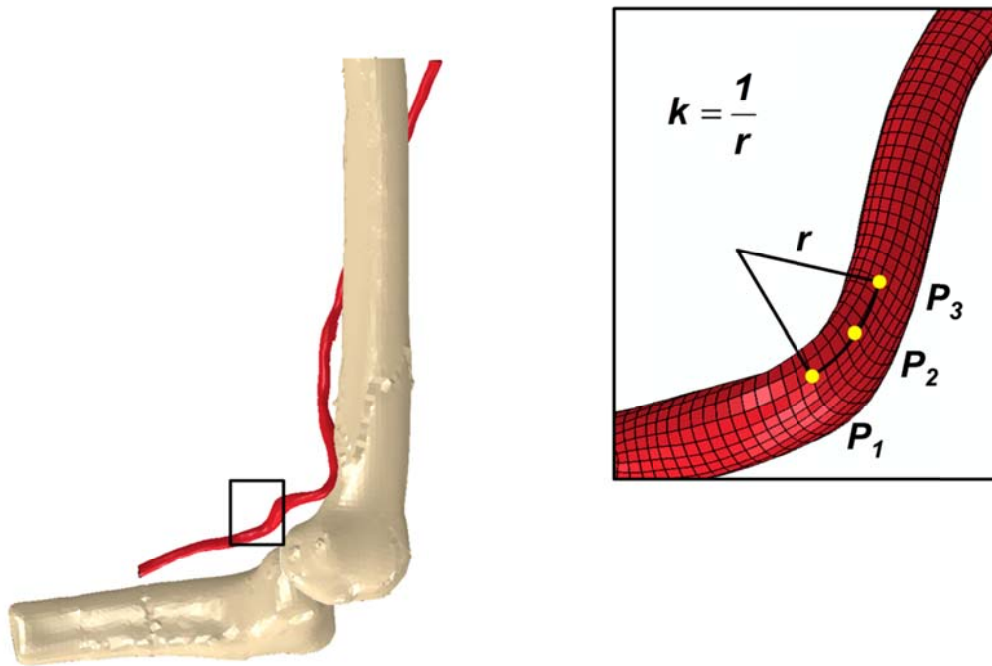


Figure 5.3 Schematic of methods used to calculate vessel curvature.

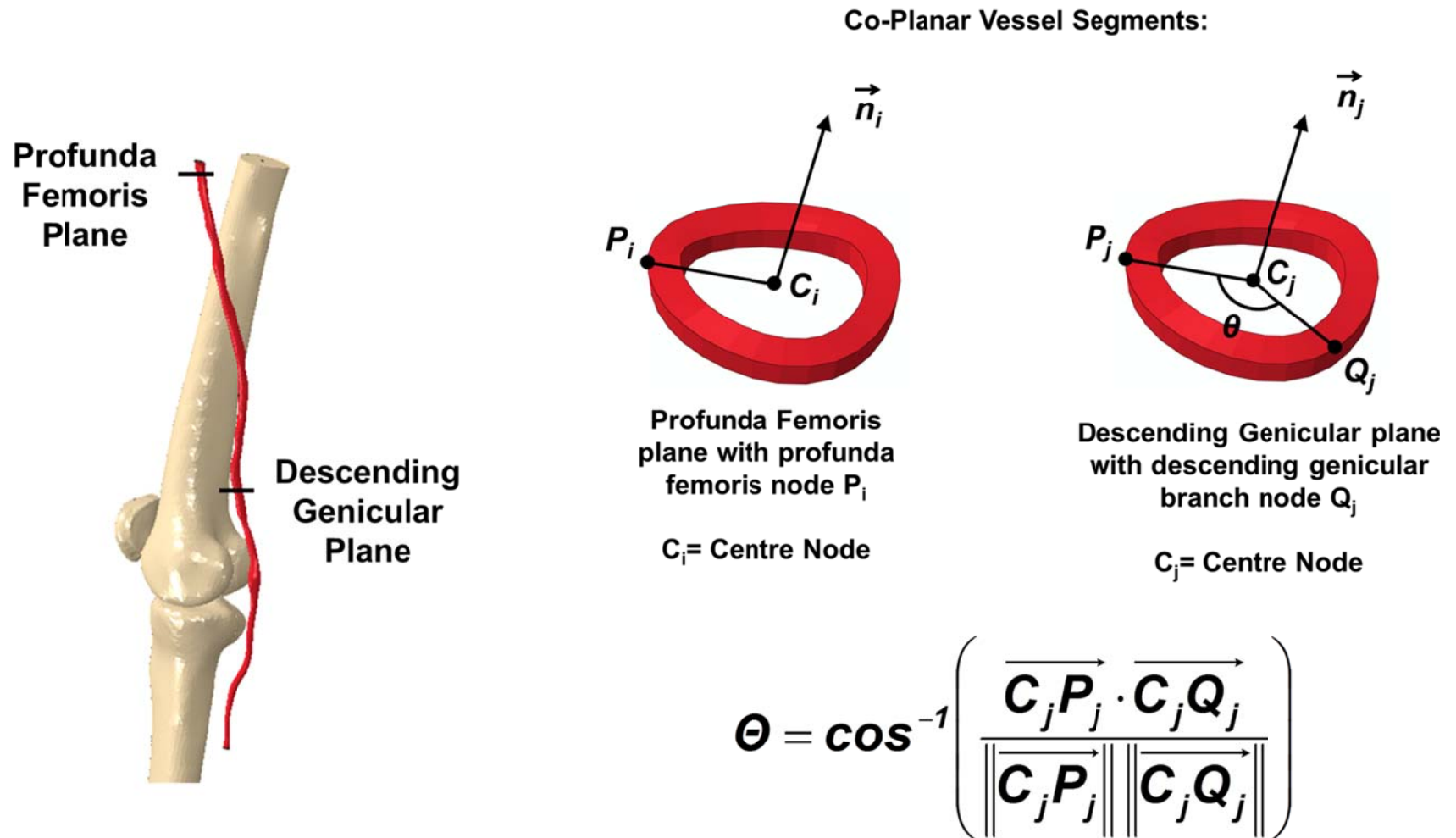


Figure 5.4 Schematic of methods used to calculate vessel twist.

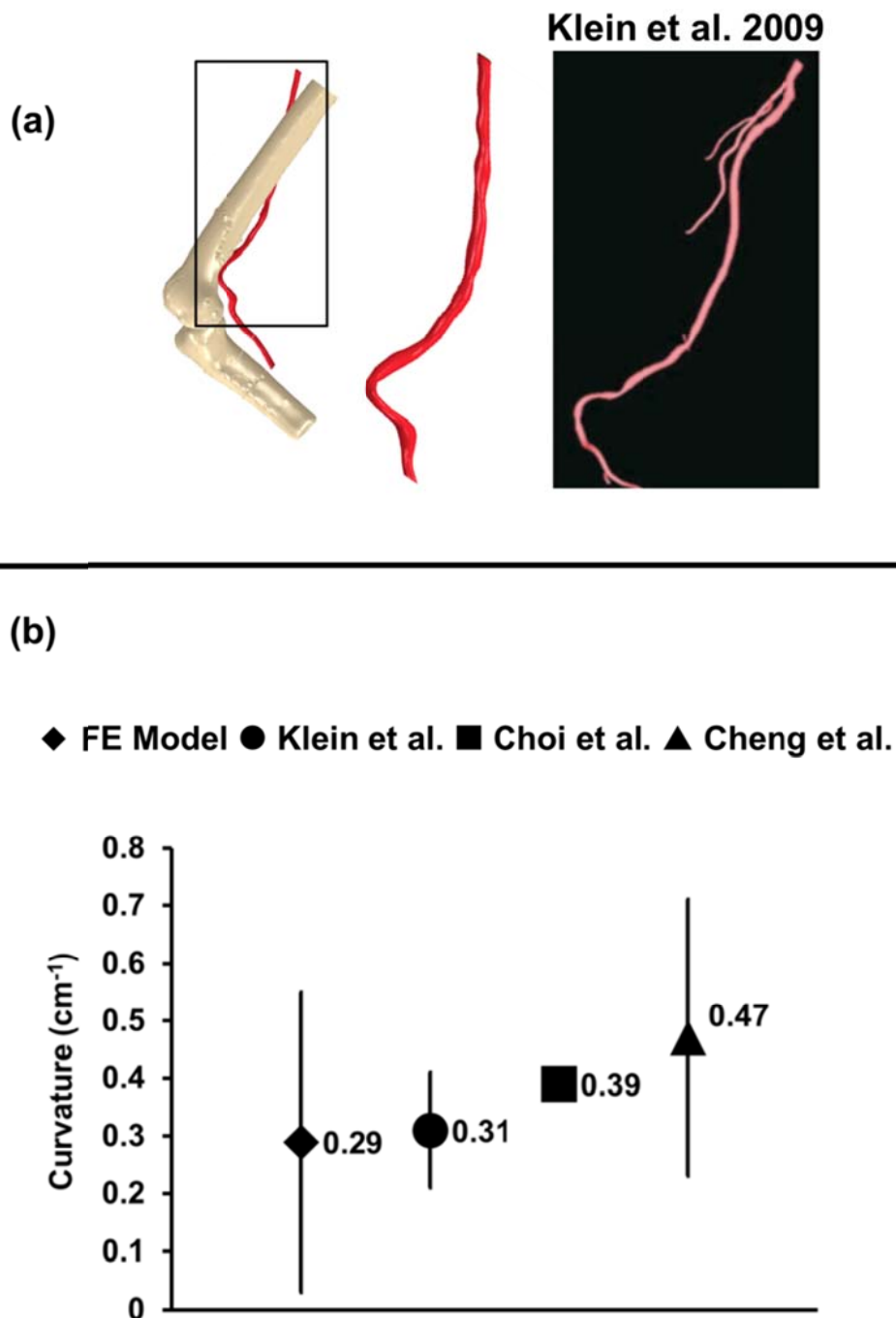


Figure 5.5 Deformation results: (a) comparison of the deformed vessel of this study and that of the model created from angiographic images of Klein, et al. 2009 (b) comparison of curvature results of other studies (Cheng, et al. 2010, Klein, et al. 2009b, Choi, et al. 2009) with error bars representing standard deviations of the curvature measurements (taken along the length of the vessel) (standard deviations not reported by Choi, et al. 2009) (c) contour plot showing Von Mises stress results (MPa) in the vessel after knee flexion and (d) contour plot showing strain in regions of extreme curvature.

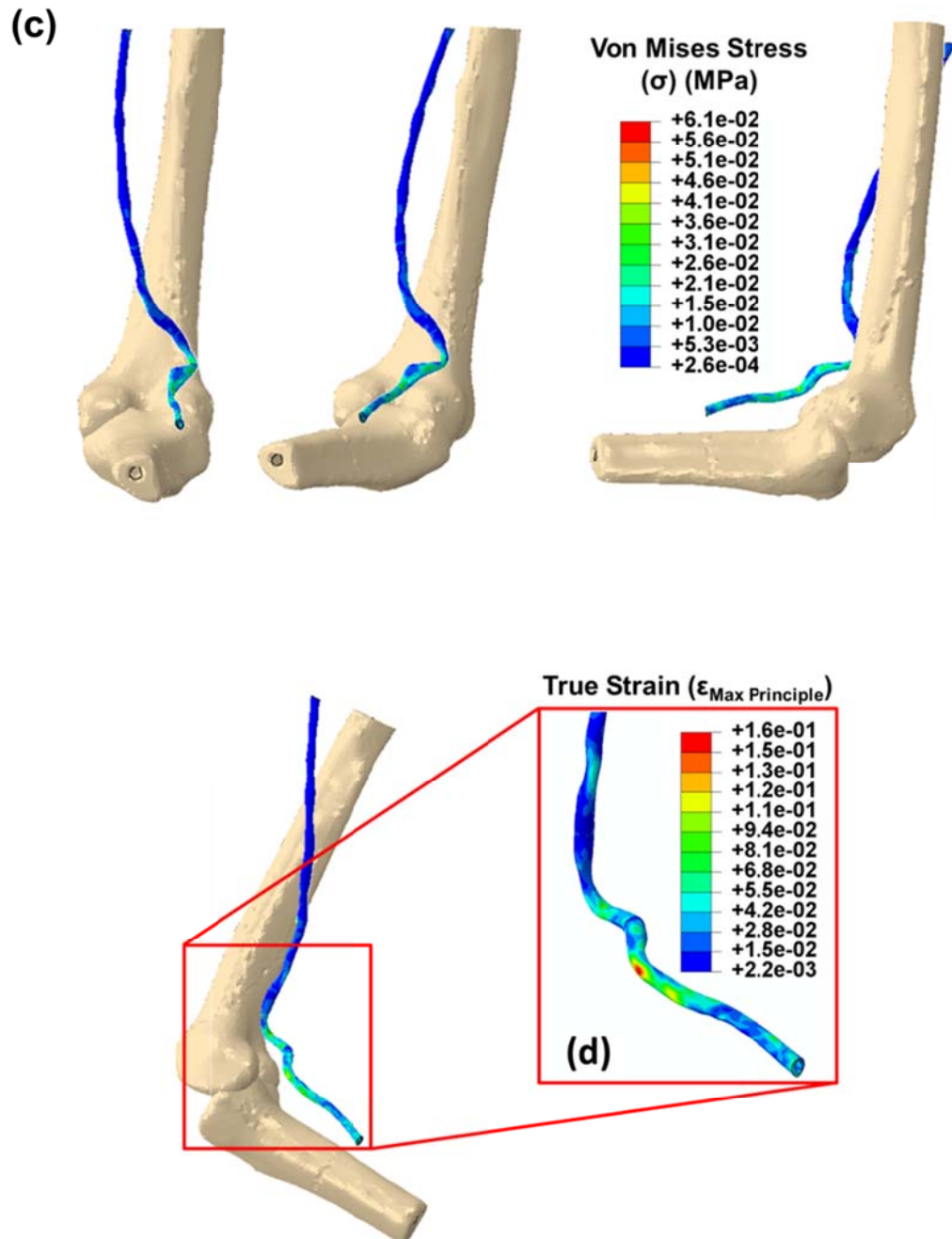


Figure 5.5 (c) contour plot showing Von Mises stress results (MPa) in the vessel after knee flexion and (d) contour plot showing strain in regions of extreme curvature.

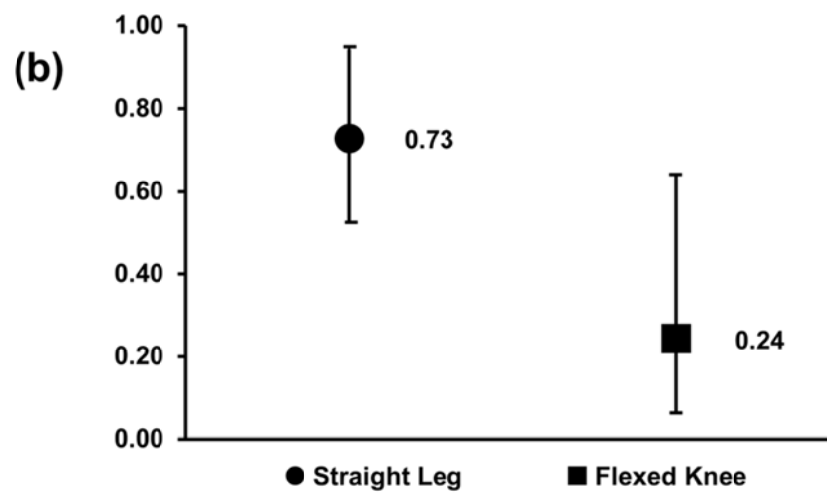
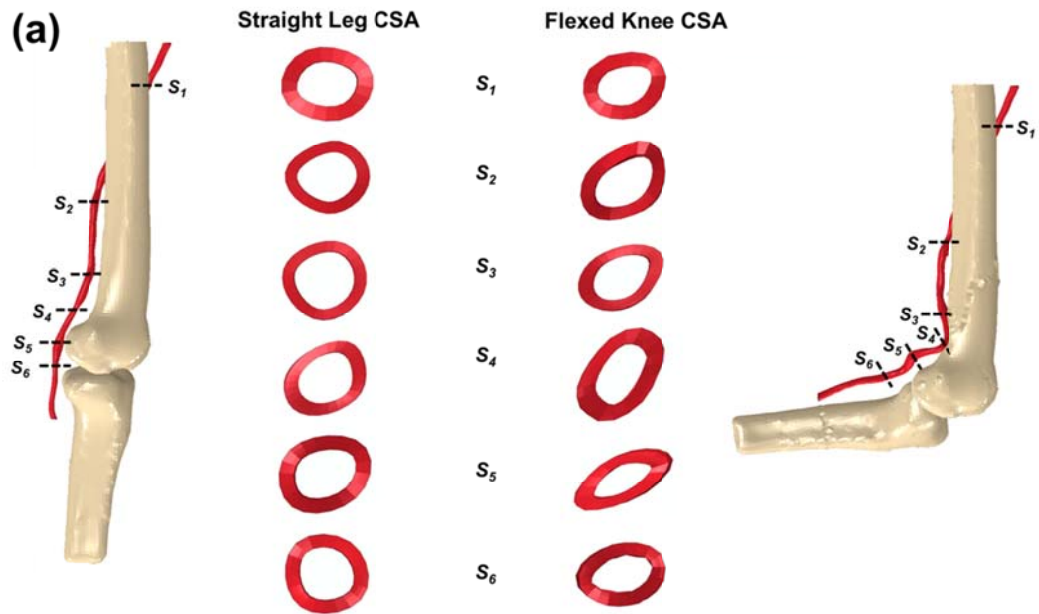


Figure 5.6 Cross sectional area results: (a) cross sectional area of vessel lumen in straight leg and flexed knee position (b) average lumen aspect ratio before and after knee flexion. Error bars represent maximum and minimum values.

5.6 References

- 3-matic. 2011. Reference Manual, Materialise.
- Allie, DE, Hebert, CJ, and Walker, CM. 2004. Nitinol stent fractures in the SFA. *Endovascular Today*. 3: 22-34.
- Aubel, A and Thalmann, D. 2001. Interactive modelling of the human musculature. *Proceedings of the 14th annual on conference: Computer Animation*: 167-255.
- Auricchio, F, Conti, M, De Beule, M, De Santis, G, et al. 2011. Carotid artery stenting simulation: From patient-specific images to finite element analysis. *Medical engineering & physics*. 33: 281-289.
- Auricchio, F, Taylor, RL, and Lubliner, J. 1997. Shape-memory alloys: macromodelling and numerical simulations of the superelastic behavior. *Computer Methods in Applied Mechanics and Engineering*. 146: 281-312.
- Bader, DL and Bowker, P. 1983. Mechanical characteristics of skin and underlying tissues in vivo. *Biomaterials*. 4: 305-308.
- Balossino, R, Gervaso, F, Migliavacca, F, and Dubini, G. 2008. Effects of different stent designs on local hemodynamics in stented arteries. *Journal of Biomechanics*. 41: 1053-1061.
- Barron, V, Brougham, C, Coghlan, K, McLucas, E, et al. 2007. The effect of physiological cyclic stretch on the cell morphology, cell orientation and protein expression of endothelial cells. *Journal of Materials Science: Materials in Medicine*. 18: 1973-1981.
- Blemker, SS and Delp, SL. 2005. Three-dimensional representation of complex muscle architectures and geometries. *Annals of Biomedical Engineering*. 33: 661-673.

- Brown, R, Nguyen, TD, Spincemaille, P, Prince, MR, et al. 2009. In vivo quantification of femoralpopliteal compression during isometric thigh contraction: Assessment using MR angiography. *Journal of Magnetic Resonance Imaging*. 29: 1116-1124.
- Capelli, C, Gervaso, F, Petrini, L, Dubini, G, et al. 2009. Assessment of tissue prolapse after balloon-expandable stenting: influence of stent cell geometry. *Medical engineering & physics*. 31: 441-447.
- Chadwick, JE, Haumann, DR and Parent, RE. 1989. Layered construction for deformable animated characters. *SIGGRAPH Proceedings of the 16th annual conference: Computer Graphics and Interactive Techniques*: 243-252
- Chen, DT and Zeltzer, D. 1992. Pump it up: computer animation of a biomechanically based model of muscle using the finite element method. *Proceedings of the 19th annual conference on computer graphics and interactive techniques*: 89-98.
- Cheng, CP, Choi, G, Herfkens, RJ, and Taylor, CA. 2010. The Effect of Aging on Deformations of the Superficial Femoral Artery Resulting from Hip and Knee Flexion: Potential Clinical Implications. *Journal of Vascular and Interventional Radiology*. 21: 195-202.
- Cheng, CP, Wilson, NM, Hallett, RL, Herfkens, RJ, et al. 2006. In vivo MR angiographic quantification of axial and twisting deformations of the superficial femoral artery resulting from maximum hip and knee flexion. *Journal of Vascular and Interventional Radiology*. 17: 979-987.
- Choi, G, Cheng, CP, Wilson, NM, and Taylor, CA. 2009. Methods for quantifying three-dimensional deformation of arteries due to pulsatile and nonpulsatile forces: implications for the design of stents and stent grafts. *Annals of Biomedical Engineering*. 37: 14-33.

- Chow, WW and Odell, EI. 1978. Deformations and Stresses in Soft Body Tissues of a Sitting Person. *Journal of Biomechanical Engineering*. 100: 79-87.
- Conti, M, Auricchio, F, De Beule, M, and Verhegghe, B. Numerical simulation of Nitinol peripheral stents: from laser-cutting to deployment in a patient specific anatomy. in 8th European Symposium on Martensitic Transformations. 2009. Prague, Czech Republic.
- Dartsch, P and Betz, E. 1989. Response of cultured endothelial cells to mechanical stimulation. *Basic research in cardiology*. 84: 268-281.
- David Chua, S, MacDonald, B, and Hashmi, M. 2004a. Effects of varying slotted tube (stent) geometry on its expansion behaviour using finite element method. *Journal of Materials Processing Technology*. 155: 1764-1771.
- David Chua, S, MacDonald, B, and Hashmi, M. 2004b. Finite element simulation of slotted tube (stent) with the presence of plaque and artery by balloon expansion. *Journal of Materials Processing Technology*. 155: 1772-1779.
- Duerig, T and Wholey, M. 2002. A comparison of balloon-and self-expanding stents. *Minimally Invasive Therapy & Allied Technologies*. 11: 173-178.
- Early, M, Lally, C, Prendergast, PJ, and Kelly, DJ. 2009. Stresses in peripheral arteries following stent placement: a finite element analysis. *Computer Methods in Biomechanics and Biomedical Engineering*. 12: 25-33.
- Fleuren, JFM, Snoek, GJ, Voerman, GE, and Hermens, HJ. 2009. Muscle activation patterns of knee flexors and extensors during passive and active movement of the spastic lower limb in chronic stroke patients. *Journal of Electromyography and Kinesiology*. 19: e301-e310.
- Ganguly, A, Simons, J, Schneider, A, Keck, B, et al. 2011. In-vivo imaging of femoral artery Nitinol stents for deformation analysis. *Journal of Vascular and Interventional Radiology*. 22: 244-249.

- Gasser, H and Hill, A. 1924. Proceedings of the Royal Society of London. Series B. Biological Sciences. 96: 398-437.
- Gasser, TC and Holzapfel, GA. 2007. Modeling plaque fissuring and dissection during balloon angioplasty intervention. *Annals of Biomedical Engineering*. 35: 711-723.
- Gastaldi, D, Morlacchi, S, Nichetti, R, Capelli, C, et al. 2010. Modelling of the provisional side-branch stenting approach for the treatment of atherosclerotic coronary bifurcations: effects of stent positioning. *Biomechanics and Modeling in Mechanobiology*. 9: 551-561.
- Gervaso, F, Capelli, C, Petrini, L, Lattanzio, S, et al. 2008. On the effects of different strategies in modelling balloon-expandable stenting by means of finite element method. *Journal of Biomechanics*. 41: 1206-1212.
- Gielen, A, Oomens, C, Bovendeerd, P, Arts, T and Janssen, J. 2000. A finite element approach for skeletal muscle using a distributed moment model of contraction. *Computer Methods in Biomechanics and Biomedical Engineering*. 3: 231-244.
- Gíslason, MK, Stansfield, B, and Nash, DH. 2010. Finite element model creation and stability considerations of complex biological articulation: The human wrist joint. *Medical Engineering & Physics*. 32: 523-531.
- Grujicic, M, Pandurangan, B, Arakere, G, Bell, WC, et al. 2009. Seat-cushion and soft-tissue material modeling and a finite element investigation of the seating comfort for passenger-vehicle occupants. *Materials & Design*. 30: 4273-4285.
- Hirota, G, Fisher, S, Lee, C and Fuchs, H. 2001. An implicit finite element method for elastic solids in contact. *Computer Animation: The Fourteenth Conference on Computer Animation Proceedings*: 136-254.

- Holzapfel, G, Gasser, T, and Stadler, M. 2002a. A structural model for the viscoelastic behavior of arterial walls: continuum formulation and finite element analysis. *European Journal of Mechanics-A/Solids*. 21: 441-463.
- Holzapfel, GA, Sommer, G, Gasser, CT, and Regitnig, P. 2005. Determination of layer-specific mechanical properties of human coronary arteries with non atherosclerotic intimal thickening and related constitutive modeling. *American Journal of Physiology - Heart and Circulatory Physiology*. 289: H2048-H2058.
- Holzapfel, GA, Stadler, M, and Schulze-Bauer, CAJ. 2002b. A Layer-Specific Three-Dimensional Model for the Simulation of Balloon Angioplasty using Magnetic Resonance Imaging and Mechanical Testing. *Annals of Biomedical Engineering*. 30: 753-767.
- Huxley, AF. 1957. Muscle structure and theories of contraction. *Progress in Biophysics and Biophysical Chemistry*. 7: 255-318.
- Ito, Y, Corey Shum, P, Shih, AM, Soni, BK, et al. 2006. Robust generation of high-quality unstructured meshes on realistic biomedical geometry. *International Journal for Numerical Methods in Engineering*. 65: 943-973.
- Jonker, FS, F. Moll, F. Muhs, B. 2008. Dynamic Forces in the SFA and Popliteal Artery During Knee Flexion. *Endovascular Today*.
- Klein, AJ, James Chen, S, Messenger, JC, Hansgen, AR, et al. 2009. Quantitative assessment of the conformational change in the femoropopliteal artery with leg movement. *Catheterization and Cardiovascular Interventions*. 74: 787-798.
- Klisch, SM and Lotz, JC. 1999. Application of a fibre-reinforced continuum theory to multiple deformations of the annulus fibrosus. *Journal of Biomechanics*. 32: 1027-1036.

- Krouskop, TA, Muilenberg, AL, Dougherty, DR, and Winningham, DJ. 1987. Computer-aided design of a prosthetic socket for an above-knee amputee. *Journal of Rehabilitation Research and Development*. 24: 31-38.
- Lally, C, Dolan, F, and Prendergast, P. 2005. Cardiovascular stent design and vessel stresses: a finite element analysis. *Journal of Biomechanics*. 38: 1574-1581.
- Lally, C, Reid, A, and Prendergast, P. 2004. Elastic behavior of porcine coronary artery tissue under uniaxial and equibiaxial tension. *Annals of Biomedical Engineering*. 32: 1355-1364.
- Lederman, RJ. 2009. Legs bend: Why dynamic angiography is important. *Catheterization and Cardiovascular Interventions*. 74: 799-799.
- Lee, D, Glueck, M, Khan, A, Fiume, E, et al. 2010. A survey of modeling and simulation of skeletal muscle. *ACM Transactions on Graphics*. 28.
- Lee, Y, Terzopoulos, D and Waters, K. 1995. Realistic modelling for facial animation. *Proceedings of the 22nd annual conference: Computer Graphics and Interactive Techniques*: 55-62
- Lehoux, S, Castier, Y, and Tedgui, A. 2006. Molecular mechanisms of the vascular responses to haemodynamic forces. *Journal of Internal Medicine*. 259: 381-392.
- Lemos, R, Epstein, M, Herzog, W, Wyvill, B. 2001. Realistic skeletal muscle deformation using finite element analysis. *Proceedings of XIV Brazilian Symposium on Computer Graphics and Image Processing*: 192-199.
- Levesque, MJ and Nerem, RM. 1985. The Elongation and Orientation of Cultured Endothelial Cells in Response to Shear Stress. *Journal of Biomechanical Engineering*. 107: 341-347.

- Liang, D, Yang, D, Qi, M, and Wang, W. 2005. Finite element analysis of the implantation of a balloon-expandable stent in a stenosed artery. *International Journal of Cardiology*. 104: 314-318.
- Mak, AFT, Wang, Q, and Huang, L. 1992. The biomechanical responses of a skin layer to surface loadings. *Journal of Biomechanics*. 25: 809-821.
- Malek, AM, Alper, SL, and Izumo, S. 1999. Hemodynamic Shear Stress and Its Role in Atherosclerosis. *JAMA: The Journal of the American Medical Association*. 282: 2035-2042.
- Moore, JE and Berry, JL. 2002. Fluid and solid mechanical implications of vascular stenting. *Annals of Biomedical Engineering*. 30: 498-508.
- Moore, JE, Burki, E, Suciu, A, Zhao, S, et al. 1994. A device for subjecting vascular endothelial cells to both fluid shear stress and circumferential cyclic stretch. *Annals of Biomedical Engineering*. 22: 416-422.
- Moretti, M, Prina-Mello, A, Reid, A, Barron, V, et al. 2004. Endothelial cell alignment on cyclically-stretched silicone surfaces. *Journal of Materials Science: Materials in Medicine*. 15: 1159-1164.
- Mortier, P, De Beule, M, Van Loo, D, Verheghe, B, et al. 2009. Finite element analysis of side branch access during bifurcation stenting. *Medical engineering & physics*. 31: 434-440.
- Mortier, P, Holzapfel, G, De Beule, M, Van Loo, D, et al. 2010. A Novel Simulation Strategy for Stent Insertion and Deployment in Curved Coronary Bifurcations: Comparison of Three Drug-Eluting Stents. *Annals of Biomedical Engineering*. 38: 88-99.
- Müller-Hülsbeck, S, Schäfer, PJ, Charalambous, N, Yagi, H, et al. 2010. Comparison of Second-Generation Stents for Application in the Superficial Femoral

-
- Artery: An In Vitro Evaluation Focusing on Stent Design. *Journal of Endovascular Therapy*. 17: 767-776.
- Nedel, LP. and Thalmann, D. 1998. Real time muscle deformations using mass-spring systems. *Proceedings of Computer Graphics International*. 156-165.
- Neidlinger-Wilke, C, Grood, E, Wang, JHC, Brand, R, et al. 2001. Cell alignment is induced by cyclic changes in cell length: studies of cells grown in cyclically stretched substrates. *Journal of orthopaedic research*. 19: 286-293.
- Netter, FH, *Atlas of Human Anatomy*, 2006, Saunders/Elsevier: Philadelphia.
- Oomens, CWJ, Bressers, OFJT, Bosboom, EMH, Bouten, CVC, et al. 2003a. Can Loaded Interface Characteristics Influence Strain Distributions in Muscle Adjacent to Bony Prominences? *Computer Methods in Biomechanics and Biomedical Engineering*. 6: 171-180.
- Oomens, C, Maenhout, M, Van Oijen, C, Drost, M and Baaijens, F. 2003b. Finite element modelling of contracting skeletal muscle. *Philosophical Transactions of the Royal Society of London. Series B: Biological Sciences*. 358: 1453-1460.
- Pericevic, I, Lally, C, Toner, D, and Kelly, DJ. 2009. The influence of plaque composition on underlying arterial wall stress during stent expansion: the case for lesion-specific stents. *Medical engineering & physics*. 31: 428-433.
- Prendergast, P, Lally, C, Daly, S, Reid, A, et al. 2003. Analysis of prolapse in cardiovascular stents: a constitutive equation for vascular tissue and finite-element modelling. *Journal of Biomechanical Engineering*. 125: 692-699.
- Qiu, Y and Tarbell, JM. 2000. Numerical simulation of pulsatile flow in a compliant curved tube model of a coronary artery. *Journal of Biomechanical Engineering*. 122: 77-85.

- Rasband, WS. 1997-2011. Available from: <http://imagej.nih.gov/ij/>
- Rebelo, N, Fu, R, and Lawrenchuk, M. 2009. Study of a nitinol stent deployed into anatomically accurate artery geometry and subjected to realistic service loading. *Journal of Materials Engineering and Performance*. 18: 655-663.
- Rebelo, N, Prabhu, S, Feezor, C, and Denison, A. Deployment of a Self-Expanding Stent in an Artery. in *International Conference on Shape Memory and Superelastic Technologies*. 2006. Baden-Baden, Germany.
- Rho, JY, Ashman, RB, and Turner, CH. 1993. Young's modulus of trabecular and cortical bone material: Ultrasonic and microtensile measurements. *Journal of Biomechanics*. 26: 111-119.
- Schlager, O, Dick, P, Sabeti, S, Amighi, J, et al. 2005. Long-Segment SFA Stenting—The Dark Sides: In-Stent Restenosis, Clinical Deterioration, and Stent Fractures. *Journal of Endovascular Therapy*. 12: 676-684.
- Shacham, S, Castel, D, and Gefen, A. 2010. Measurements of the Static Friction Coefficient Between Bone and Muscle Tissues. *Journal of Biomechanical Engineering*. 132: 084502-4.
- Smouse, B, Nikanorov, A, and LaFlash, D. 2005. Biomechanical forces in the femoropopliteal arterial segment. *Endovascular Today*. 4: 60-66.
- Tang, C, Zhang, G, and Tsui, C. 2009. A 3D skeletal muscle model coupled with active contraction of muscle fibres and hyperelastic behaviour. *Journal of Biomechanics*. 42: 865-872.
- Tang, C, Chan, W, and Tsui, C. 2010. Finite Element Analysis of Contact Pressures between Seat Cushion and Human Buttock-Thigh Tissue. *Engineering*. 2: 720-726.

- Teran, J, Sifakis, E, Blemker, SS, Ng Thow Hing, V, Lau, C and Fedkiw, R. 2005. Creating and simulating skeletal muscle from the visible human data set. *IEEE Transactions on Visualization and Computer Graphics*. 11: 317-328
- Timmins, LH, Meyer, CA, Moreno, MR, and Moore, JE. 2008. Mechanical modeling of stents deployed in tapered arteries. *Annals of Biomedical Engineering*. 36: 2042-2050.
- Todd, B and Thacker, J. 1994. Three-dimensional computer model of the human buttocks in vivo. *Journal of Rehabilitation Research and Development*. 31: 111-119.
- Vannah, WM and Childress, DS. 1996. Indentor tests and finite element modeling of bulk muscular tissue in vivo. *Journal of Rehabilitation Research and Development*. 33: 239-252.
- Veronda, D and Westmann, R. 1970. Mechanical characterization of skin – finite deformations. *Journal of Biomechanics*. 3: 111-124
- Walke, W, Paszenda, Z, and Filipiak, J. 2005. Experimental and numerical biomechanical analysis of vascular stent. *Journal of Materials Processing Technology*. 164: 1263-1268.
- Wang, H, Ip, W, Boissy, R, and Grood, ES. 1995. Cell orientation response to cyclically deformed substrates: experimental validation of a cell model. *Journal of Biomechanics*. 28: 1543-1552.
- Wang, JHC, Goldschmidt-Clermont, P, Wille, J, and Yin, FCP. 2001. Specificity of endothelial cell reorientation in response to cyclic mechanical stretching. *Journal of Biomechanics*. 34: 1563-1572.
- Wu, W, Qi, M, Liu, XP, Yang, DZ, et al. 2007a. Delivery and release of nitinol stent in carotid artery and their interactions: A finite element analysis. *Journal of Biomechanics*. 40: 3034-3040.

- Wu, W, Wang, WQ, Yang, DZ, and Qi, M. 2007b. Stent expansion in curved vessel and their interactions: A finite element analysis. *Journal of Biomechanics*. 40: 2580-2585.
- Yongping, Z, Arthur, M, and Leung, A. 2001. State-of-the-art methods for geometric and biomechanical assessments of residual limbs: A review. *Journal of Rehabilitation Research and Development*. 38: 487-504.
- Yongping, Z and Mak, AFT. 1999. Effective elastic properties for lower limb soft tissues from manual indentation experiment. *Rehabilitation Engineering, IEEE Transactions on*. 7: 257-267.
- Yucesoy, CA, Koopman, BH, Huijing, PA, and Grootenboer, HJ. 2002. Three-dimensional finite element modelling of skeletal muscle using a two-domain approach: linked fibre-matrix mesh model. *Journal of Biomechanics*. 35: 1253-1262.
- Zahalak, GI, 1981. A distribution-moment approximation for kinetic theories of muscular contraction. *Mathematical Biosciences*. 55: 89-114.
- Zajac, FE. 1989. Muscle and tendon: properties, models, scaling, and application to biomechanics and motor control. *Critical Reviews in Biomedical Engineering*. 17: 359-411.
- Ziegler, T, Bouzourène, K, Harrison, VJ, Brunner, HR, et al. 1998. Influence of Oscillatory and Unidirectional Flow Environments on the Expression of Endothelin and Nitric Oxide Synthase in Cultured Endothelial Cells. *Arteriosclerosis, Thrombosis, and Vascular Biology*. 18: 686-692.
- Zunino, P, D'Angelo, C, Petrini, L, Vergara, C, et al. 2009. Numerical simulation of drug eluting coronary stents: mechanics, fluid dynamics and drug release. *Computer Methods in Applied Mechanics and Engineering*. 198: 3633-3644.

Chapter 6. Effect of Stenting on the Deformation Characteristics of the Superficial Femoral Artery: A Computational Study

6.1 Introduction

As discussed already in this thesis, the superficial femoral artery (SFA) is a prevalent location for peripheral arterial disease often requiring percutaneous transluminal angioplasty (PTA) followed by stenting to restore vessel patency and uncompromised blood flow. However, due to loading conditions from the surrounding muscles of the SFA, stents placed in this location are reported to have high fracture rates commonly observed as a result of bending of the artery during knee flexion (Jonker, 2008, Smouse et al., 2005, Wensing et al., 1995). Understanding the loading conditions of the unstented SFA could aid greatly in device design, helping to combat fracture rates of peripheral stent devices.

It has been shown that in healthy vessels, bending of the femoropopliteal artery mostly occurs behind the knee, becoming more exaggerated as hip and knee flexion angles increase in magnitude (Cheng et al., 2010, Klein et al., 2009, Smouse et al., 2005). A study carried out by Smouse et al. (2005), in which deformations of the unstented and stented SFA were evaluated, showed minor bends appear in the SFA region of the vessel after hip and knee bending of unstented arteries as shown in Figure 6.1. It is postulated that whilst elastic and collagenous components of the arterial wall allow for some axial compression during movement, out of plane buckling and twisting also occurs in order to allow further shortening of the vessel length during knee bending. Stent placement provides the required scaffolding of the artery, however it alters the vessel's axial rigidity hence reducing the arteries ability to shorten as it innately would. As elastic arterial compression allows some axial shortening of the vessel during knee bending, and hence keeps localized bending and twisting (described as 'concertina effect' by Wensing et al. (1995) and Kalmár et al. (2002)) to a minimum, any increase in axial stiffness of the artery (due to stent placement for example), could cause an increase in such localized bending to allow the required shortening of the artery to occur as the knee flexes. Severe bending

could occur with extreme stent rigidity and long stent lengths. It has been observed in angiographic images that unstented artery portions bend in a severe manner when adjacent to stented regions as shown in Figure 6.2. This may contribute to vascular injury of the vessel, and can result in intimal hyperplasia and restenosis (Smouse et al., 2005).

The investigations of Smouse et al. (2005), Klein et al. (2009), and Cheng et al. (2006) have provided important data regarding the highly complex deformation characteristics of the femoropopliteal artery. However, there are currently no investigations that have linked deformation characteristics of the stented SFA to levels of stress and strain within the artery. Due to this lack of investigation, stent design parameters of stiffness/flexibility, diameter, length, geometry and the altered deformation characteristics of the artery as a result of the location of stent placement and stent sizing cannot be thoroughly investigated before device implantation in a clinical setting. As previously mentioned, the musculoskeletal forces that surround the vessel causing deformation patterns also act on the stent and it has been proposed that the dynamic forces which act on the SFA during knee flexion leads to stent buckling and fracture (Jonker, 2008). Therefore, stents designed for the femoropopliteal artery must be able to withstand this loading and in order to design such a stent, load levels and modes must be thoroughly understood.

The overall goal of this study is to determine the effect of stent placement on the deformation characteristics of the SFA using an anatomically accurate, three dimensional finite element model of the leg, previously shown in Chapter 5 to accurately capture the deformation characteristics of the femoropopliteal artery during knee flexion. The study focuses on the effect of different stent lengths and locations. Deformation characteristics (length change, curvature change and axial twist) that result from dynamic loading of the vessel are linked with stress and strain levels within the SFA.

6.2 Materials and Methods

In this chapter, the femoropopliteal vessel within a ‘global’ leg model developed in Chapter 5 was adapted to represent various ‘stented’ cases of the SFA. Two investigations were conducted in this study:

1. An investigation of the effect of stent length. This investigation included three models with differing stent lengths 40mm, 60mm and 90mm all located in the distal portion of the vessel (placed in the same distal location, see Figure 6.3)
2. An investigation of the effect of stent location. This investigation included three models of a 60mm stent placed in the distal, mid and proximal SFA (Figure 6.3).

Portions of the artery were assigned stiffened material properties, to represent the SFA stented with a Cordis SMART™ Nitinol stent. Linear elastic material properties were used in this portion of the artery model for efficient simulation. Simons et al., (2010) reported axial, torsional and bending stiffness values of mock arteries stented with a SMART™ stent. Using this data, which showed the stented vessel exhibits worst case axial stiffness of 3.38 times that of the bare vessel, linear elastic properties of the artery, as described by Mozersky et al., (1972) were adapted to represent this stiffness. Therefore, Young’s modulus of 1.14 MPa and Poisson’s ratio of 0.3 were assigned to the stiffened vessel portions.

A knee bend of 90° was simulated by prescribing displacement to the tibia resulting in movement along the articulating surfaces of the femur and tibia around a reference point created at an anatomically accurate location for joint articulation, as described in Chapter 5.

The axial length change, curvature and axial twist of the vessels in each of the six stented cases was quantified by applying the methods previously employed in Chapter 5 (section 5.2.4).

6.2 Results

In this section, the axial length change, curvature and axial twist results of the six stented models created in this study are presented. For clarity, presentation of the results is given in three parts:

- Firstly, in section 6.2.1, the results of the investigation of the effect of stent length are reported.
- Secondly, in section 6.2.2, the results of the investigation of the effect of stent location are reported.
- Finally, in section 6.2.3, the results of this study are compared to those of the unstented vessel model of Chapter 5.

6.2.1 Stent Length Investigation

Axial Length Change

The 40mm, 60mm and 90mm stented vessel models all shortened in length after knee flexion. Vessel shortening values for these models are reported in Table 6.1. The greatest amount of vessel shortening was observed in the 40 mm (shortest stent) model which showed a change in length of 1.59cm (7.19% shortening) of the entire arterial segment. The least amount of shortening was observed in the longest (90mm) stent model which showed changes in length of 1.38cm (6.26% shortening) of the entire arterial segment. Results show that the amount of vessel shortening reduces with increasing stent length. This is an expected result as increasing the axial stiffness of a portion of the artery through stenting will inevitably increase the total axial stiffness of the modelled SFA. However, as the unstented artery shortened by 8.23%, the change in axial shortening observed here may cause other modes of deformation (i.e. bending, twisting) in the SFA or elsewhere (e.g. popliteal artery). This is discussed in more detail in section 6.3.

Axial Twist/Torsion

Axial twist results for the 40mm, 60mm and 90mm stented vessel models are reported in Table 6.2. Results show that stent length has an effect on the amount of axial twist/torsion of the vessel. Axial twist angle of the stented vessel was shown to

decrease with increasing stent length. This is expected due to the increase in torsional stiffness of a stented vessel. The 40 mm (shortest stent) model exhibited an axial twist angle of 24.23° whilst the 90 mm (longest stent) exhibited an axial twist angle of 12.81° . Figure 6.4, Figure 6.5 and Figure 6.6 show contour plots of the artery for the three stent length models after knee flexion where stress and strain in the vessel as a result of axial twist/torsion can be observed.

Curvature Change

Figure 6.4, Figure 6.5 and Figure 6.6 show contour plots of the deformed artery for the models of the stent length investigation where curvature of the vessels after knee bending can be observed. Results show that stenting with 40mm, 60mm and 90mm stent lengths leads to large curvatures in the vessel after knee flexion. It is evident from the multiple views of the models that three dimensional curvature changes occur. It can also be seen from Figure 6.4, Figure 6.5 and Figure 6.6 that the portion of the vessel above the knee changes shape only slightly due to stenting. This portion of the vessel remains relatively straight in all stent length models, with an arched conformation apparent in some views. Stenting within this region, which only occurs in the 90mm stent length model leads to very slight changes to this shape. Values for mean and maximum artery curvature for the models of the stent length investigation are reported in Table 6.3 and compared in Figure 6.7 and Figure 6.8. Results show that maximum vessel curvatures occur in the vessel stented with the shortest stent length. The 40mm (shortest stent) model showed mean and maximum curvatures of $0.394 \pm 0.12 \text{ cm}^{-1}$ and 0.693 cm^{-1} respectively. Lowest curvatures were observed in the 90 mm (longest stent) model, which displayed mean and maximum curvatures of $0.303 \pm 0.11 \text{ cm}^{-1}$ and 0.642 cm^{-1} respectively. It may seem counter intuitive that the highest curvatures are observed in the 40 mm model. However, it can be seen from Figure 6.9 and Figure 6.10 that curvatures are induced as the vessel deforms at the proximal end of the stented portion of the 40 mm stent. This does not occur in the 60 mm or 90 mm vessels and is discussed further in section 6.3. Largest curvatures of these models can be seen directly behind the knee and in the popliteal portion of the artery below the knee (Figure 6.4, Figure 6.5 and Figure 6.6). Furthermore, each specific stent length model results in unique stress concentrations in the vessel tissue as highlighted in Figure 6.9 and Figure 6.10. Maximum vessel

stress levels of 130 kPa are observed in the 40mm stent length model (Figure 6.4). The maximum vessel stresses in the 90mm stent length model are observed to be 100 kPa (Figure 6.6).

6.2.2 Stent Location Investigation

Axial Length Change

The distal SFA, mid SFA and proximal SFA stented vessel models all shortened in length after knee flexion. Vessel shortening values for these models are reported in Table 6.4. The greatest amount of vessel shortening was observed in the distal model which showed a change in length of 1.53cm (6.91% shortening) of the entire arterial segment. The least amount of shortening was observed in the proximally placed which showed a change in length of 1.25cm (5.65% shortening) of the entire arterial segment.

Axial Twist/Torsion

Axial twist results for the distal SFA, mid SFA and proximal SFA stented vessel models are reported in Table 6.5. Results show that stent location has an effect on the amount of axial twist/torsion of the vessel. Specifically it was shown in the results that the axial twist angle of the stented vessel is greater in a vessel stented in the distal SFA portion of the vessel and that stenting towards the hip decreases axial twist/torsion. The distal SFA stented portion leads to an axial twist angle of 20.95°. In contrast the proximal SFA stented portion leads to an axial twist angle of 11.31° within the vessel. Figure 6.11, Figure 6.12 and Figure 6.13 show contour plots of the artery for the three stent location models after knee flexion where stress and strain in the vessel as a result of axial twist/torsion can be observed.

Curvature Change

Results show that placing a 60mm stent in the distal SFA, mid SFA and proximal SFA also leads to large curvatures in the vessel after knee flexion. Figure 6.11, Figure 6.12 and Figure 6.13 show contour plots of the deformed artery for the models of the stent location investigation where curvature of the vessels after knee bending can be observed which again highlight three dimensional curvature changes

to the vessel. It is also observed in Figure 6.11, Figure 6.12 and Figure 6.13 that the portion of the vessel above the knee changes shape only slightly due to stenting, remaining relatively straight in all the models. Small deformations can be seen in the models in which this region is stented (mid SFA and proximal SFA models). Values for mean and maximum artery curvature of the models are reported in Table 6.6 and compared in Figure 6.7 and Figure 6.8. Results show that maximum vessel curvatures occur in the vessel stented in the proximal SFA. The proximal stent portion leads to mean and maximum curvatures of $0.419 \pm 0.13 \text{ cm}^{-1}$ and 0.831 cm^{-1} respectively. In contrast, the distal stented portion leads to lower curvatures with mean and maximum curvatures of $0.327 \pm 0.13 \text{ cm}^{-1}$ and 0.651 cm^{-1} respectively. Largest curvatures of these models can be seen directly behind the knee. Whilst the largest curvatures can be observed behind the knee for the proximally placed stent, the location of the largest curvatures is in the popliteal portion of the artery below the knee for the distally stented SFA model (Figure 6.11, Figure 6.12 and Figure 6.13). Furthermore, each stent location model can be associated with unique stress concentrations in the vessel tissue as highlighted in Figure 6.14 and Figure 6.15. Maximum vessel stress levels of 130 kPa are observed in the proximal SFA stent location model (Figure 6.13). Maximum vessel stresses of 120 kPa are observed in both the distal SFA and mid SFA stent location models (Figure 6.12).

6.2.3 Changes in deformation characteristics for stented vessels

Axial Length Change

In comparison with unstented vessels, shortening of the stented vessel models was less than those of the unstented model. Results from Chapter 5 showed a change in length of the unstented vessel of 1.82cm (8.23% shortening) when going from the straight leg to flexed knee position, a higher value than those presented in Table 6.1 and Table 6.4 of the stented models of this study.

Axial Twist/Torsion

It was shown in Chapter 5 that knee flexion of the unstented artery results in a twist angle of 32.71° of the vessel when going from the straight leg to flexed knee

configuration. This equates to an axial twist gradient of $0.161^\circ/\text{mm}$. In the stented vessels of this study, knee flexion resulted in reduced axial twist angles in all six models. Axial twist angles of all stented models after knee flexion are listed in Table 6.2 and Table 6.5. Values for axial twist are on average 43.6% lower than that of the unstented model. Figure 6.4 - Figure 6.6 and Figure 6.9 - Figure 6.15 show contour plots of the artery for all six stented models after knee flexion where stress and strain in the vessel as a result of axial twist/torsion can be observed. Comparison of stress and strain levels of the stented models to those of the unstented model (reproduced in Figure 6.16) highlights an increase in the resulting stress concentrations of the vessel tissue due to the combination of axial twist/torsion and stenting.

Curvature Change

Results show that location and magnitude of stented vessel curvatures, induced by knee flexion, differ to those of an unstented vessel after knee flexion. Comparing vessel conformation of the six stented models presented here (shown in Figure 6.4 - Figure 6.6 and Figure 6.9 - Figure 6.15) to that of the unstented model (reproduced in Figure 6.16) highlights the different vessel configurations that arise after knee bending in stented vessels. Average and maximum curvatures of the unstented vessel after knee flexion, as reported in Chapter 5 were $0.294 \pm 0.26 \text{ cm}^{-1}$ and 0.601 cm^{-1} respectively. From the six stented cases of this study, maximum curvatures of 0.831 cm^{-1} are observed, an increase of 38.2% from maximum curvatures in the unstented vessel (Chapter 5). It was shown in Chapter 5 that curvatures in the unstented vessel arising from knee flexion are associated with arterial stresses in the order of 61.17 kPa. Maximum stresses in the vessel tissue as a result of curvatures arising from knee flexion of the stented models of this study are in the order of 130.47 kPa.

6.3 Discussions and Conclusions

The overall goal of this study was to determine the effect of stent placement on the deformation characteristics of the SFA. An anatomically accurate finite element model of the leg, developed in Chapter 5, was used to examine length change, axial twist, and curvature change of the stented vessel during knee flexion. Deformation characteristics were then linked to stress and strain levels in the vessel tissue.

The study leads to three main conclusions. Firstly, that stenting portions of the SFA leads to a change in global deformation characteristics from the unstented vessel. Secondly, that stress and strain values in the vessel tissue are increased with the combination of stented ‘stiffened’ portions of the vessel and dynamic loads of the vessel during knee flexion. Finally, results implicate that changing stent length and location results in a corresponding change in deformation characteristics of the vessel.

With regard to axial length changes in the vessel, this study confirms that stiffening portions of the vessel (i.e. stenting) leads to reduced shortening capability of the SFA. This is not a surprising result as previous studies have highlighted that the artery shortens due to the vessels inherent elastic and collagenous components (Wensing et al., 1995). Stiffening a portion of the vessel, by addition of a stent with greater rigidity than that of the bare vessel tissue does not allow the elastic and collagenous components of the arterial wall to behave as they usually would, therefore effecting length change.

It was shown that longer stent lengths, and locations of stenting in the proximal SFA portion of the vessel (towards the hip), results in the lowest vessel axial shortening levels. The result regarding longer stent length is intuitive, as increasing the length of the stiffened portion would therefore result in lower overall axial shortening levels in the model. Regarding stent location, a conclusion can be made that large amounts of vessel shortening by axial compression occur in this straighter proximal region of the vessel towards the hip. To investigate this further, the shortening of the vessel portions of the three regions of the stent location investigation (distal, mid and proximal) were measured in the unstented model.

Table 6.7 presents the results of this comparison which gives some insight into the different shortening percentages of specific regions of the artery. For the unstented artery, values for percentage shortening are greater for the proximal regions of the artery. Consequently, by stiffening portions of the artery that may be key regions of axial shortening, overall shortening of the vessel will be significantly reduced.

With regard to axial twist, the results have shown reduced twist angles of the vessels of the stented models of this study. This is intuitive due to the change in torsional stiffness of the stiffened region. Increasing stent length and stent location in the proximal SFA results in the lowest axial twist/torsion of the vessel.

Regarding curvature, the study confirms that regions of increased rigidity (i.e. stent placement) cause changes to the location and magnitude of curvature configurations of the artery. As the stenting in the proximal SFA results in least amounts of vessel shortening and twist, it is expected that curvature is the mode in which it will most deform. This is indeed the case, as stent location towards the proximal SFA results in the most extreme induced curvatures behind the knee. Also, it was observed in the 40 mm stent model that curvature is induced at the proximal end of the stented portion. This is less apparent in the 60 mm and 90 mm stent models. This is due to the anatomical constraints that surround the mid and proximal portions of the SFA that cause stiffness mismatch between the stent and artery to result in more diffuse curvatures of the vessel in this region. There is less support of the vessel behind the knee, causing buckling of the tissue at the ends of the stented portion.

Comparing the unstented vessel deformations (presented in Chapter 5) with the stented vessel deformations presented in this study, confirms that stenting prevents the vessel from moving as it innately would. This results in changes to ‘global’ deformation characteristics of the entire artery, not just the stented portion. Furthermore, stenting creates a stiffness mismatch between the artery and stented portion. This can result in buckling of the artery local to the ends of the stented portion causing high stresses in these locations, as seen in all models of this study (Figure 6.9 and Figure 6.14). It has been shown from this work that in these regions, stresses reach levels 53.08% higher than those of the unstented models. It is concluded that the stiffness mismatch at the ends of the stiffened portions of the

vessel results in increased pressure and stress as the entire vessel tries to axially compress and twist simultaneously.

Conclusions about the deformation characteristics of the vessel can be made by examining curvature, length change and axial twist results in combination. It can be seen from the results that the highest artery curvatures are found in the model where the vessel is stiffened in the proximal SFA as this model shows the least axial shortening. It is concluded that the increased curvatures observed compensate for the reduced amount of shortening. This is supported by previously studies where angiographic images of femoropopliteal arteries after knee and hip flexion showed that extreme curvatures form in the artery in order to allow the vessel length to shorten and compress in response to external *in vivo* loads that act on the vessel (Wensing et al., 1995). Furthermore, by combining the results presented in this study, it is observed that maximum stresses observed in the vessel are caused by bending of the vessel rather than axial compression or axial twist. The results show that the models with the most amount of shortening and axial twist do not correspond to the models with maximum stresses. It is the models with highest curvatures (as a result of a reduced capability to axially shorten and twist) that show maximum stresses in the vessel, although these maximum stress locations do not occur within the stented region.

There are few published studies with which to compare the results of the study presented here. One particular study that presents angiographic images of stented femoropopliteal artery confirms that extreme curvatures are induced below the stented region of the vessel (Smouse et al., 2005). The results of the study of Chapter 5 confirmed that the model adapted for this study is capable of replicating accurate deformation behavior of the femoropopliteal artery. However, accuracy and validation could be added to enhance this study in future work. As discussed in Chapter 5, active contraction of the eight muscles surrounding the artery, using an active material model would more accurately reflect the biomechanics of the muscle tissue during knee flexion but is beyond the scope of this work. Furthermore, the models of this study do not allow for the contribution of the dense network of fibres that surround the artery *in vivo* which anchor its position anatomically. Validation of the results, by comparison to angiographic images of stented peripheral arteries

imaged in straight knee and flexed knee configurations would confirm the validity of the approach taken of stiffening portions of the vessel to simulate stenting for this study. This could be considered in future work.

Understanding the changes in deformation characteristics due to stenting and the associated effects on the mechanical response of vessel tissue is important when deciding on stent design parameters. Understanding the loads of which the stent must withstand *in vivo* along with understanding the effects to the artery of a stented portion of the vessel is of great benefit to both clinicians and engineers. Therefore the model presented here has many potential applications. It can be adapted to model various stent sizes, locations, stiffness's and combinations of devices (overlapping stents) for use clinically in patient specific evaluations or within an industrial setting for investigation of stent design parameters and characteristics. Future applications of the model, incorporating an anisotropic material model for the stiffened portion would allow axial and radial stiffness's to be separated and investigated independently of each other to elucidate the effects of these two characteristics on deformation behavior of the artery.

In conclusion, this study presents a finite element model capable of capturing the deformation characteristics of the stented femoropopliteal artery during knee flexion. The model is used to investigate the effect of various stent lengths and locations on vessel deformation characteristics (axial length change, curvature change and axial twist) and stress and strain levels. To the author's knowledge, this study presents for the first time the effects of stenting on the deformation characteristics of the artery combined with the mechanical behavior of the vessel tissue.

6.4 Tables and Figures

	Change in vessel length (cm)	% Shortening
Unstented	1.82	8.23
40mm stent	1.59	7.19
60mm stent	1.53	6.91
90mm stent	1.38	6.26

Table 6.1 Axial shortening of stented femoropopliteal artery of the stent length investigation from straight leg to flexed knee configuration (axial shortening of unstented vessel added for comparison).

	Axial Twist (°)	Axial Twist Gradient (°/mm)
Unstented	32.71°	0.161
40mm stent	26.23	0.129
60mm stent	20.95	0.103
90mm stent	12.81	0.063

Table 6.2 Axial twist angles of stented models of the stent length investigation after knee flexion (axial twist of unstented vessel added for comparison).

	Maximum Curvature (cm⁻¹)	Mean Curvature (cm⁻¹)
Straight knee	0.089	0.061 ± 0.03
Flexed knee unstented	0.601	0.294 ± 0.26
Flexed knee 40mm stent	0.693	0.394 ± 0.12
Flexed knee 60mm stent	0.651	0.327 ± 0.13
Flexed knee 90mm stent	0.642	0.303 ± 0.11

Table 6.3 Maximum and mean curvature of the femoropopliteal (FP) artery in the stented vessels of the stent length investigation (curvature of unstented vessel added for comparison).

	Change in vessel length (cm)	% Shortening
Unstented	1.82	8.23
Distal SFA 60mm stent	1.53	6.91
Mid SFA 60mm stent	1.41	6.38
Proximal SFA 60mm stent	1.25	5.65

Table 6.4 Axial shortening of stented femoropopliteal artery of the stent location investigation from straight leg to flexed knee configuration (axial shortening of unstented vessel added for comparison).

	Axial Twist (°)	Axial Twist Gradient (°/mm)
Unstented	32.71°	0.161
Distal SFA 60mm SFA	20.95	0.103
Mid SFA 60mm SFA	18.36	0.090
Proximal SFA 60mm SFA	11.31	0.056

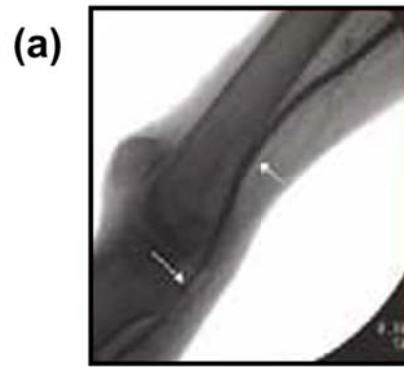
Table 6.5 Axial twist angles of stented models of the stent location investigation after knee flexion (axial twist of unstented vessel added for comparison).

	Maximum Curvature (cm⁻¹)	Mean Curvature (cm⁻¹)
Straight knee	0.089	0.061 ± 0.03
Flexed knee unstented	0.601	0.294 ± 0.26
Flexed knee distal SFA 60 mm stent	0.651	0.327 ± 0.13
Flexed knee mid SFA 60 mm stent	0.786	0.401 ± 0.09
Flexed knee proximal SFA 60 mm stent	0.831	0.419 ± 0.13

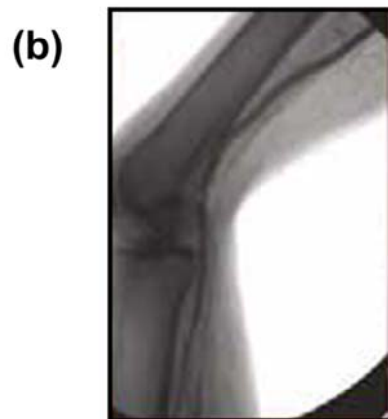
Table 6.6 Maximum and mean curvature of the femoropopliteal (FP) artery in the stented vessels of the stent location investigation (curvature of unstented vessel added for comparison).

% Shortening of vessel portion	
Distal	11.26
Mid	11.85
Proximal	12.30

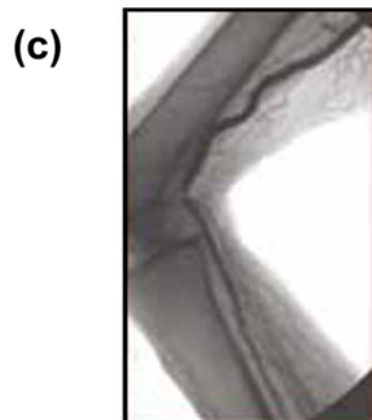
Table 6.7 Comparison of percentage shortening of the unstented model in the portion of the vessel to which stiffer properties were applied to represent stented cases for the stent location investigation.



**0° Knee Flexion
0° Hip Flexion**



**70° Knee Flexion
20° Hip Flexion**



**90° Knee Flexion
90° Hip Flexion**

Figure 6.1 Artery configuration after various angles of hip and knee flexion as reported by Smouse et al. (2005).

Image Removed Due To Copyright

Figure 6.2 Severe bending of unstented artery tissue when adjacent to stented regions as shown by Duerig et al (2002). The image shows the artery in a straight knee configuration (a) and flexed knee configuration (b). Red lines represent the end of the stented portion which begins in the distal portion of the SFA.

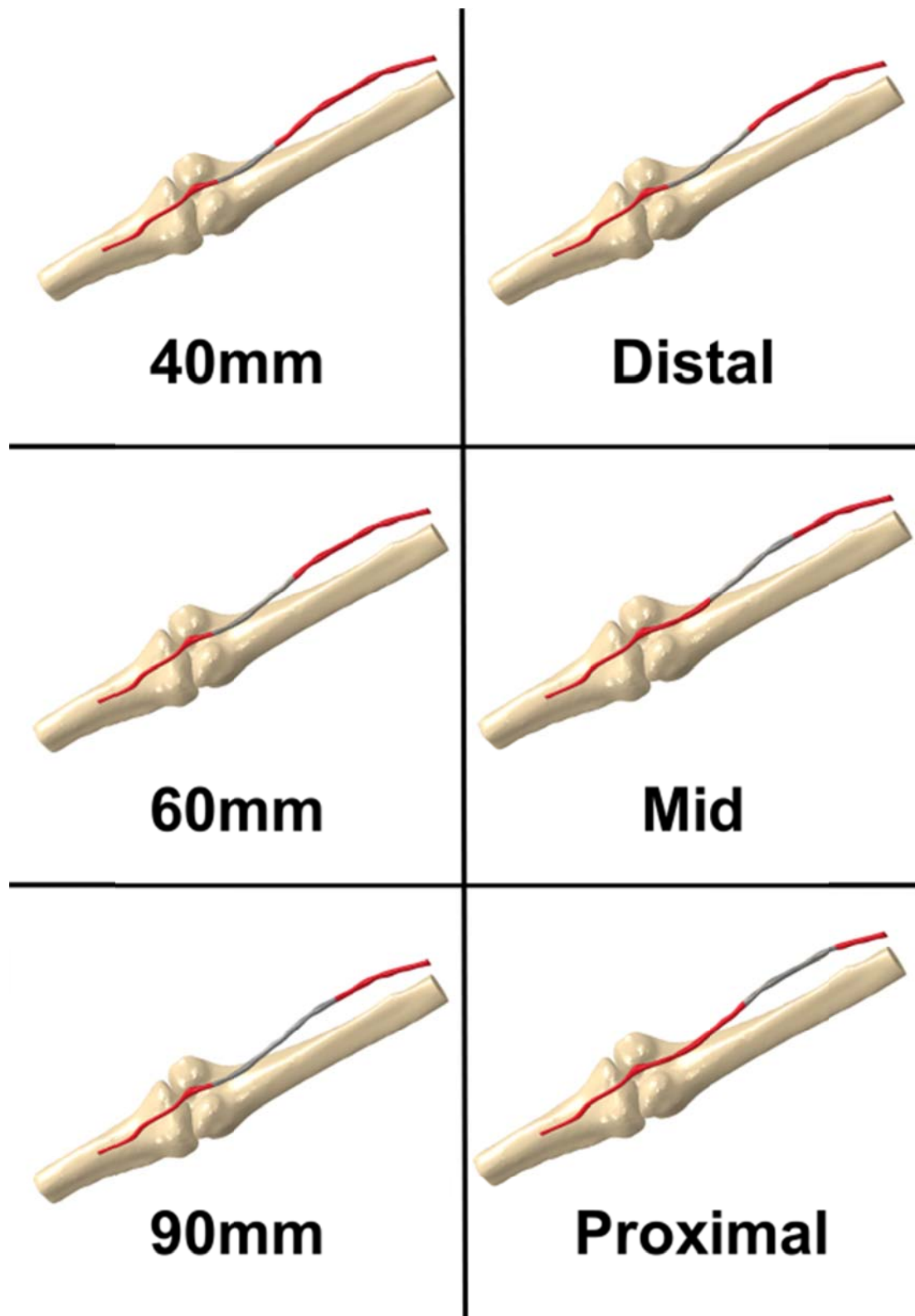


Figure 6.3 Geometries of the six stented vessel models including three stent lengths (40mm, 60mm and 90 mm) and three stent locations (distal SFA, mid SFA and proximal SFA).

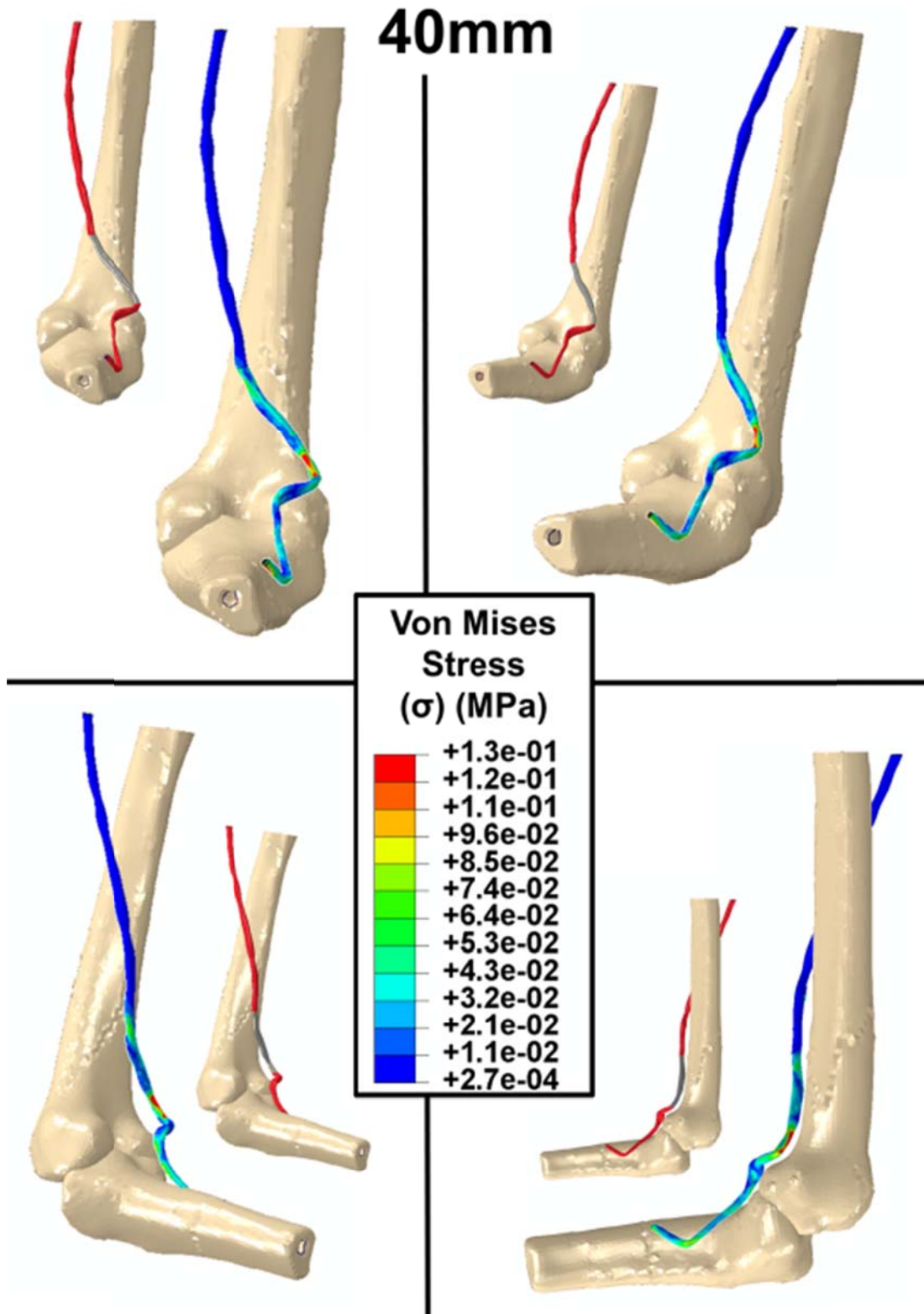


Figure 6.4 Deformation results of the 40mm stented artery model with contour plot of Von Mises stress (MPa) in the vessel after knee flexion. Schematic image (inset on each view) shows stent location.

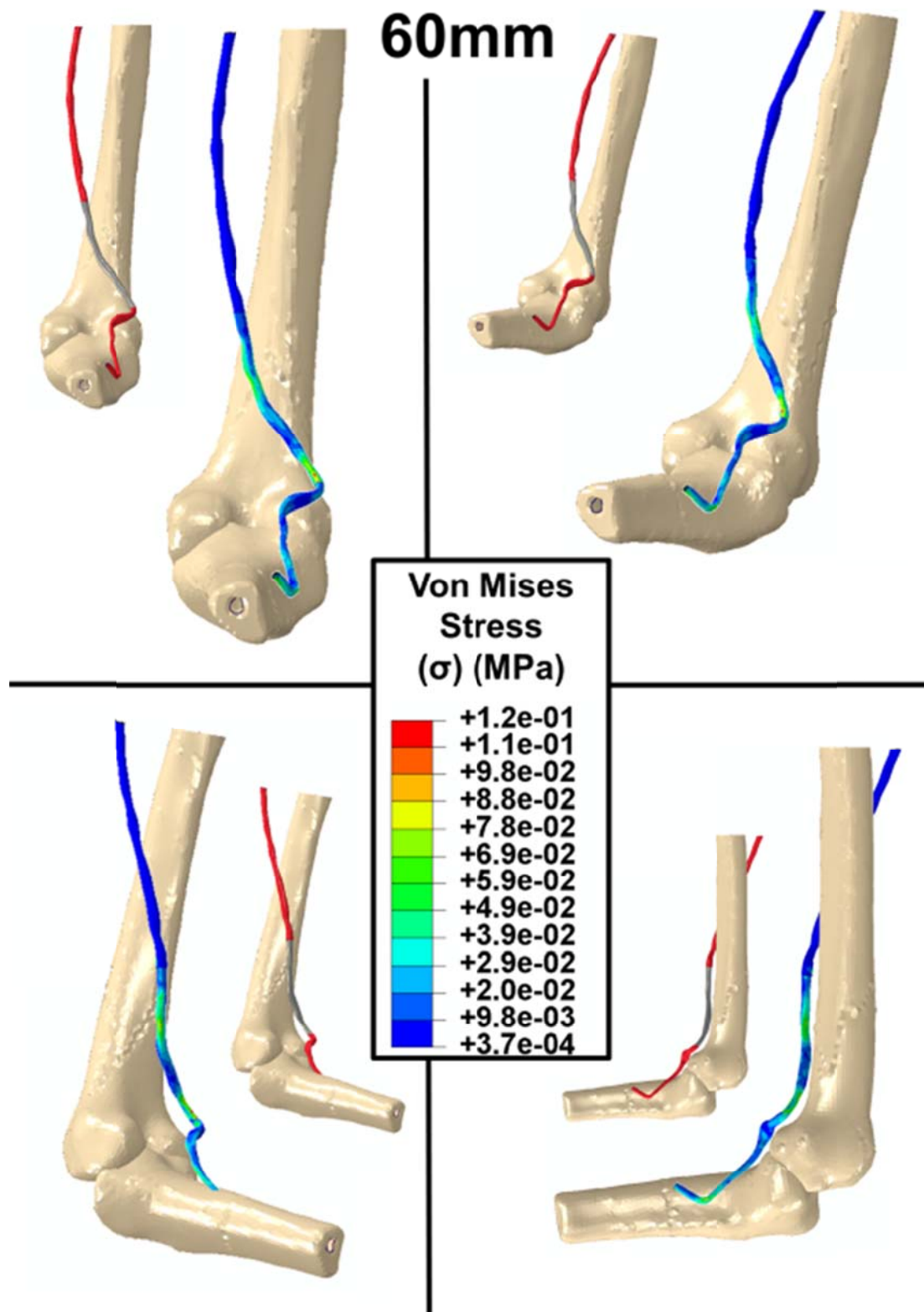


Figure 6.5 Deformation results of the 60mm stented artery model with contour plot of Von Mises stress (MPa) in the vessel after knee flexion. Schematic image (inset on each view) shows stent location.

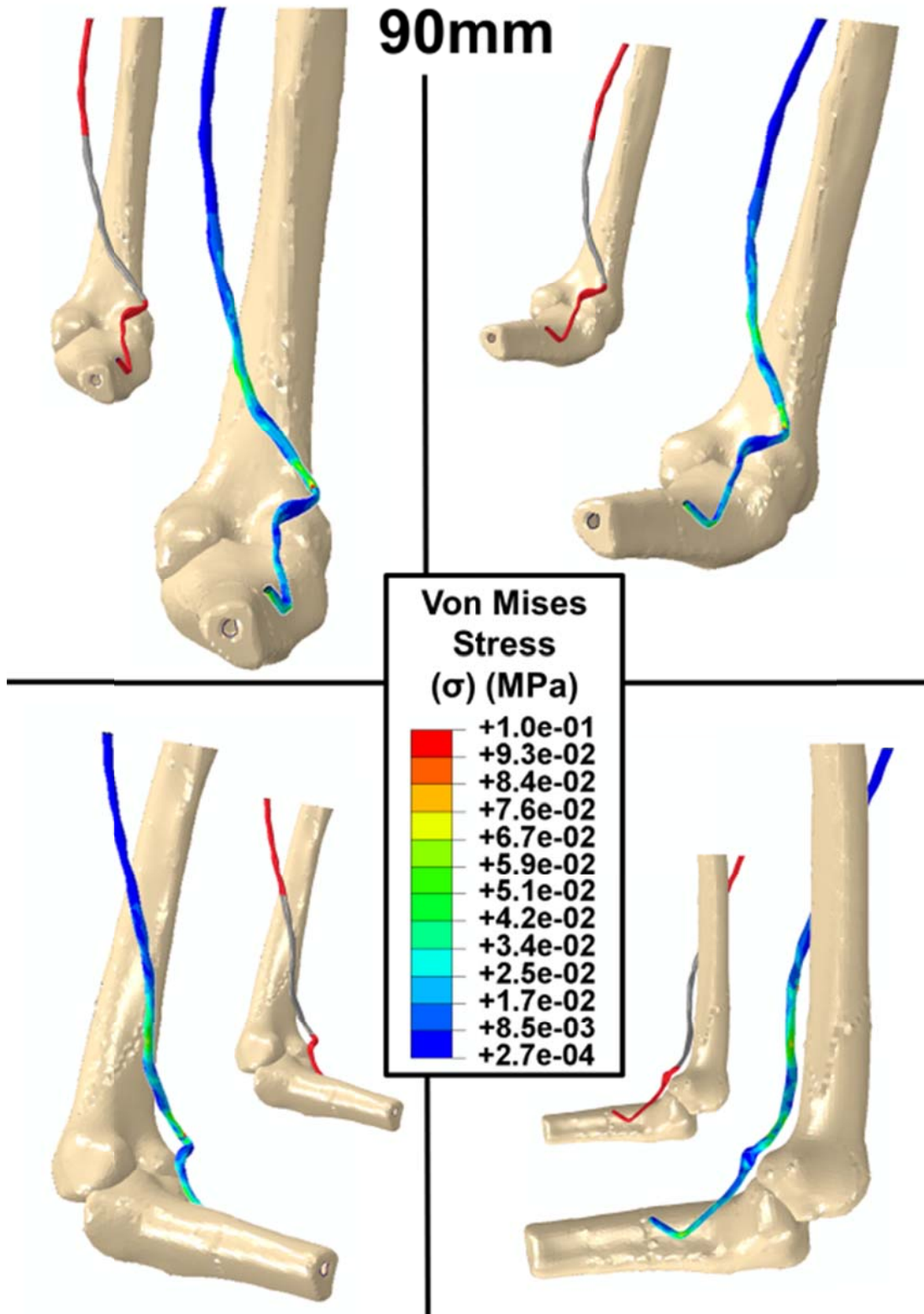


Figure 6.6 Deformation results of the 90mm stented artery model with contour plot of Von Mises stress (MPa) in the vessel after knee flexion. Schematic image (inset on each view) shows stent location.

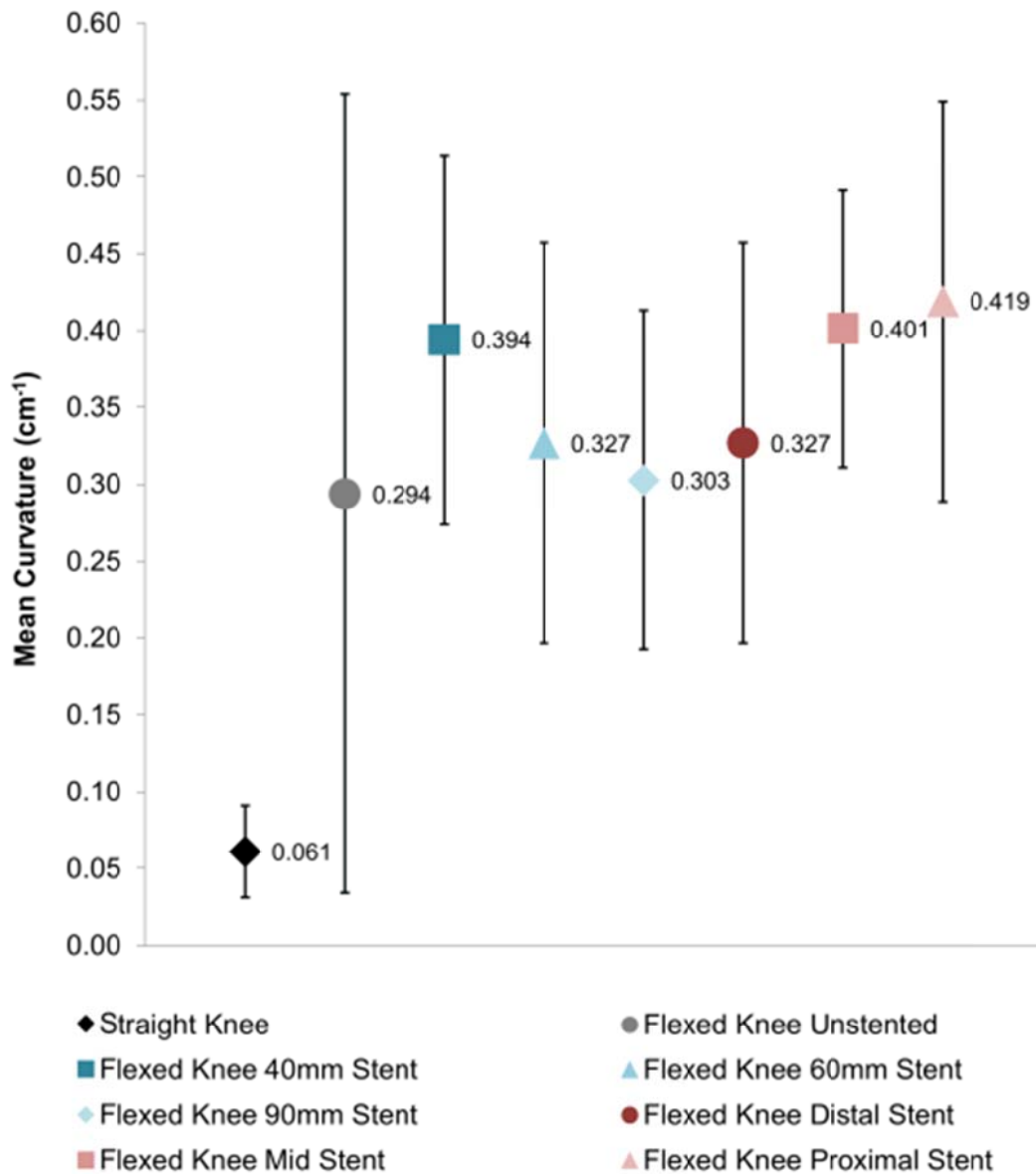


Figure 6.7 Comparison of mean vessel curvature in all models. Error bars represent standard deviations of the curvature measurements (taken along the length of the vessel).

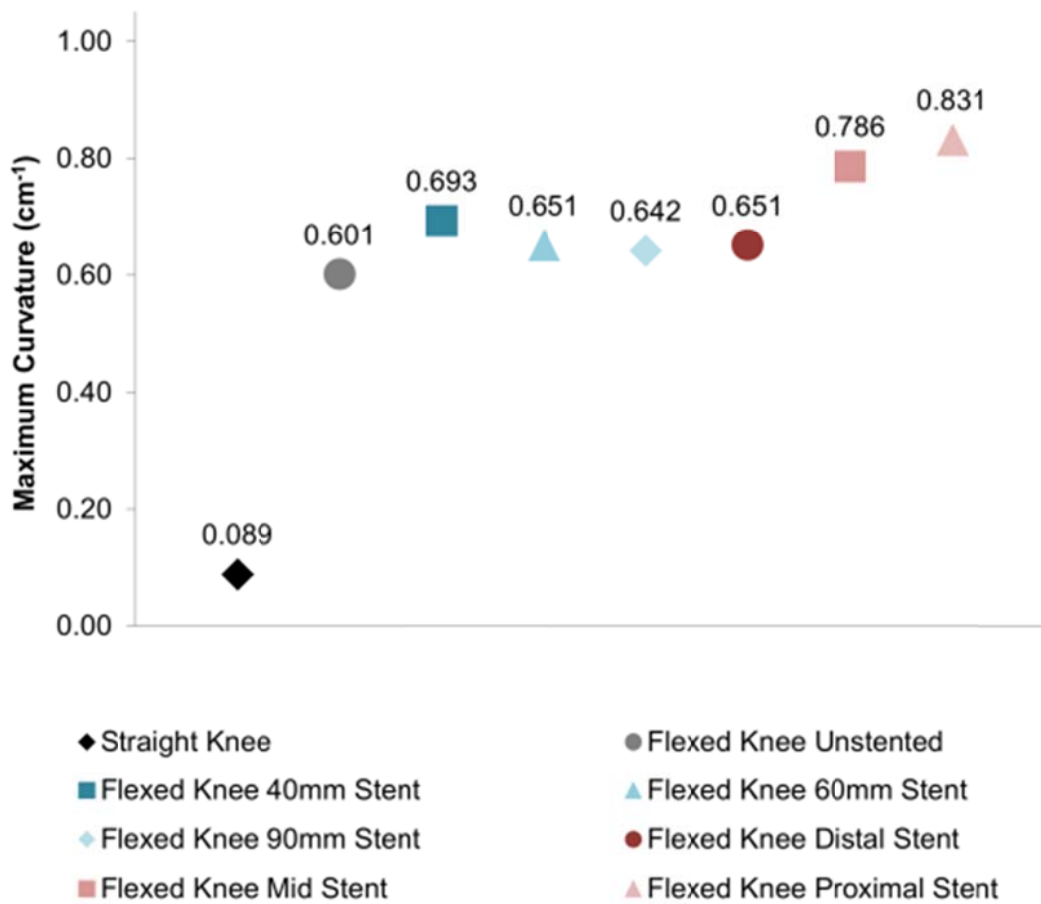


Figure 6.8 Comparison of maximum vessel curvature in all models.

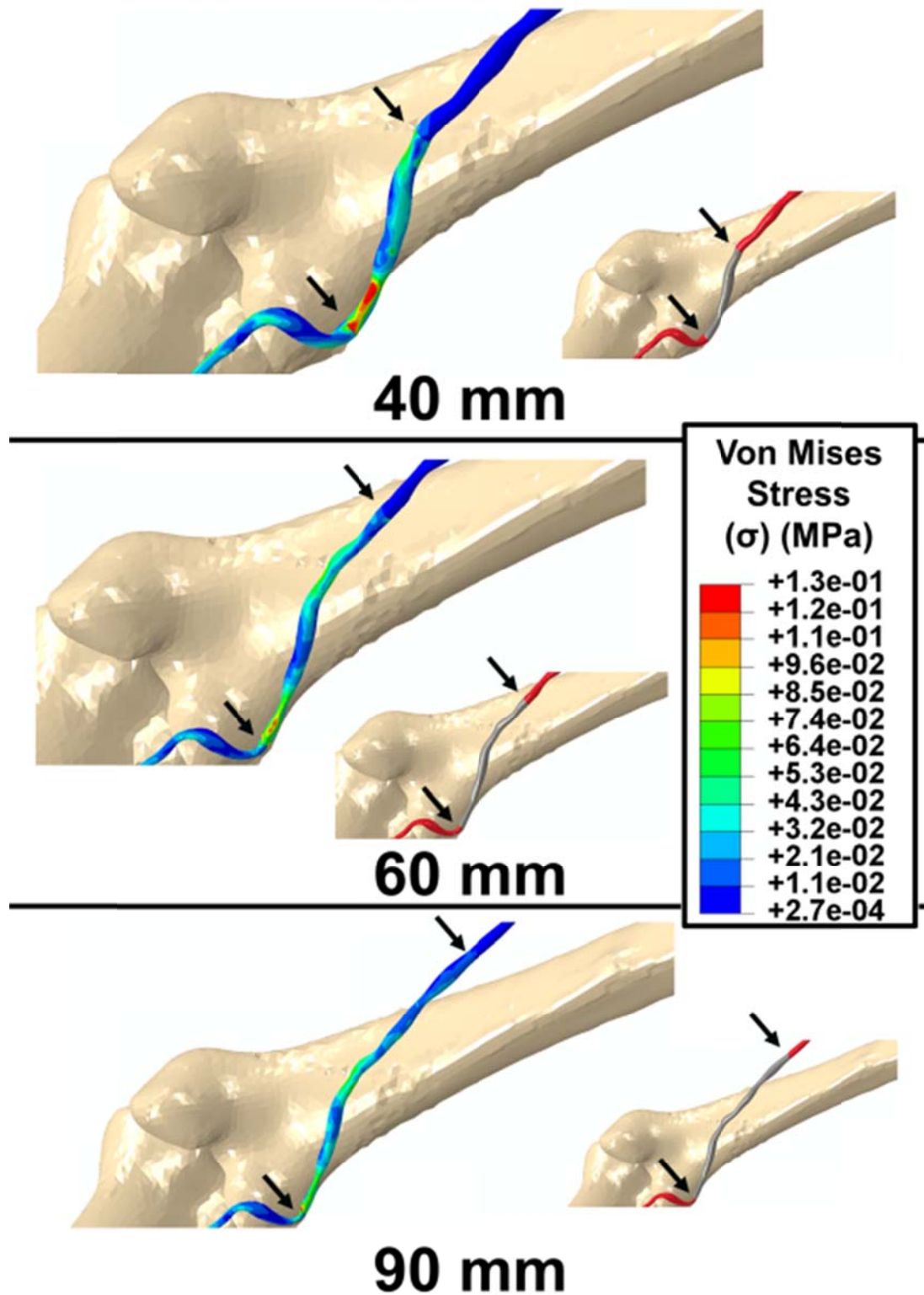


Figure 6.9 Contour plot of the deformed artery models of the stent length investigation showing Von Mises stress (MPa) in the stented region of the artery. Schematic image (inset on each view) shows stent location.

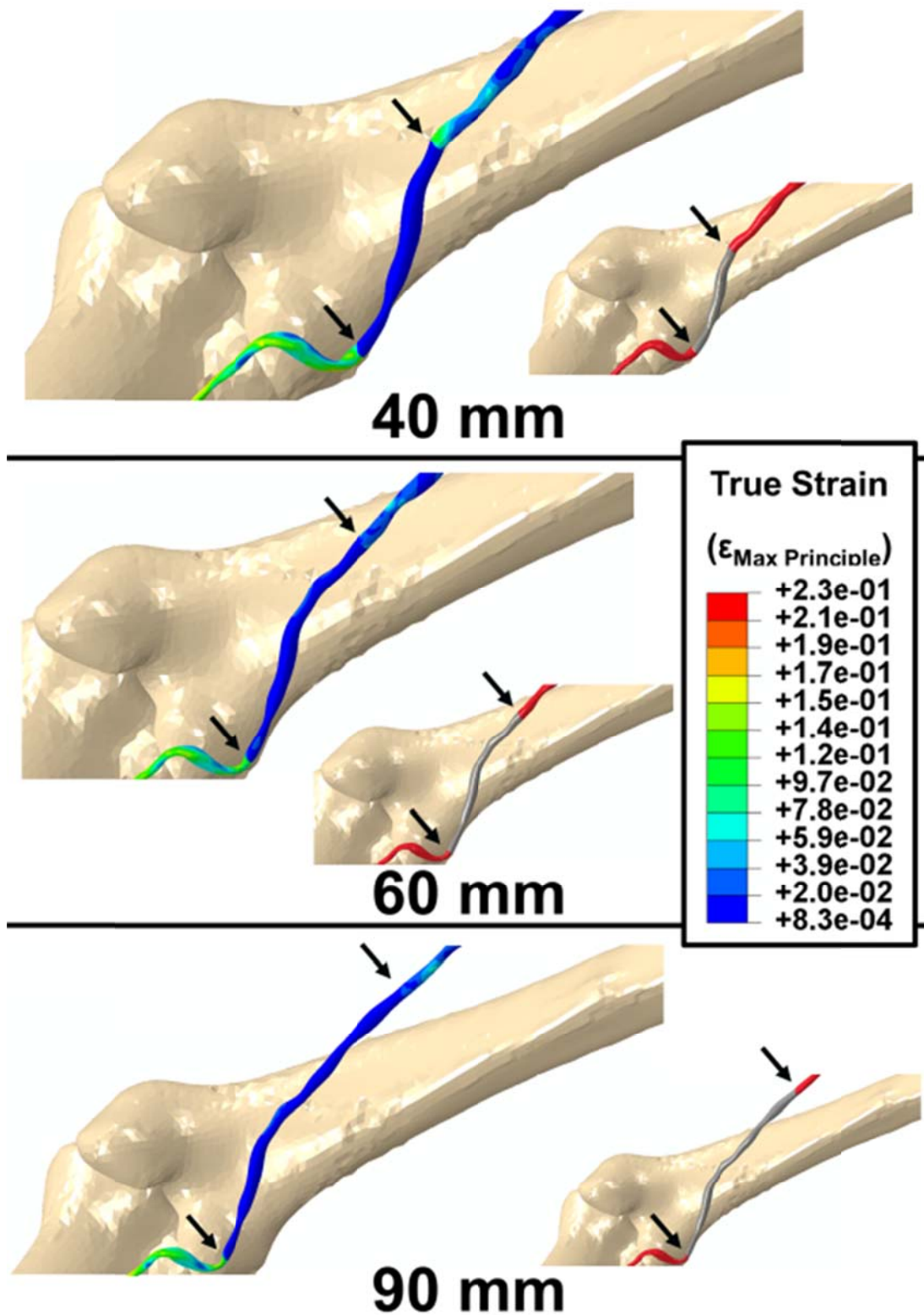


Figure 6.10 Contour plot of the deformed artery models of the stent length investigation showing strain in the stented region of the artery. Schematic image (inset on each view) shows stent location.

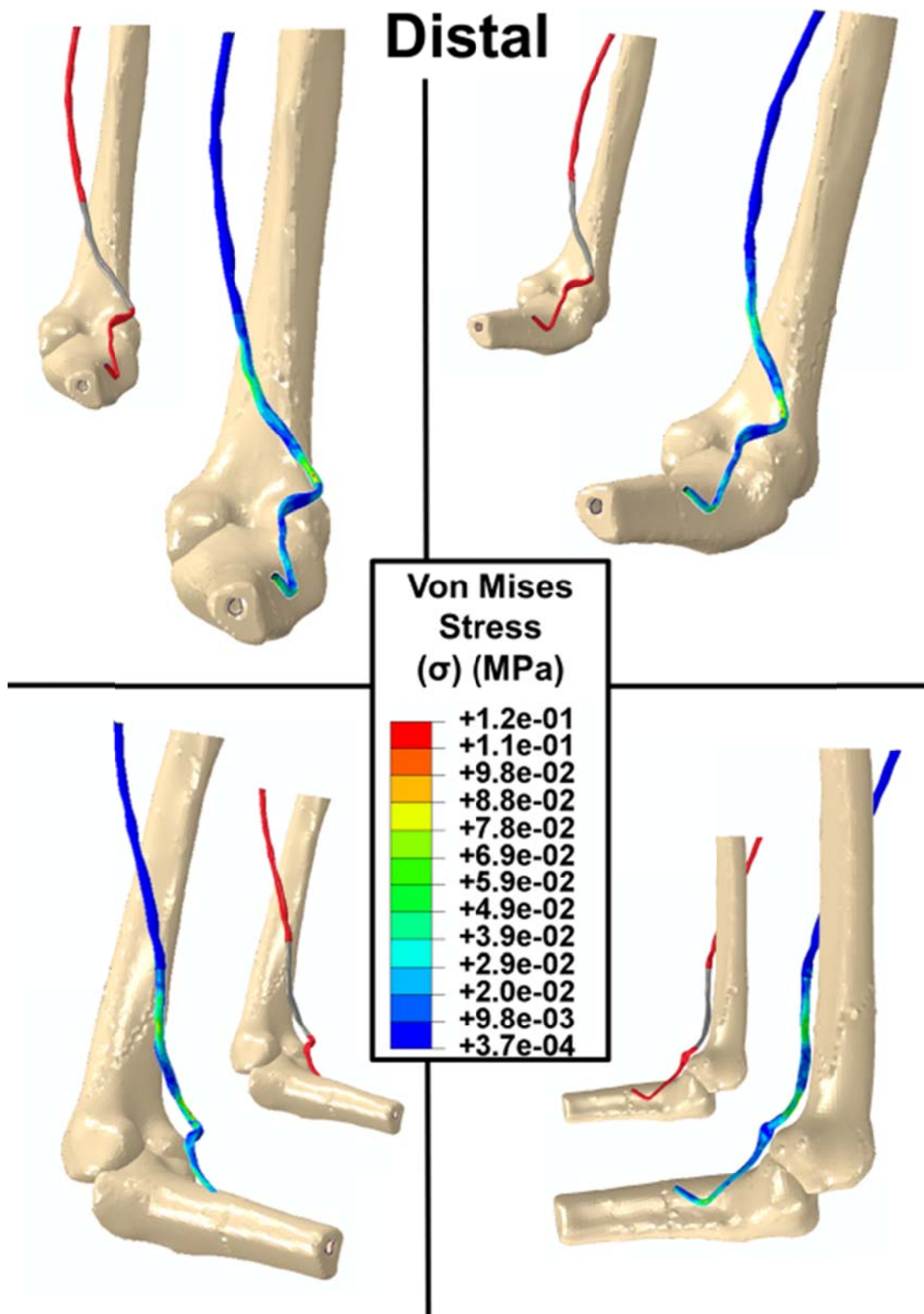


Figure 6.11 Deformation results of the stented (distal SFA location) artery model with contour plot of Von Mises stress (MPa) in the vessel after knee flexion. Schematic image (inset on each view) shows stent location.

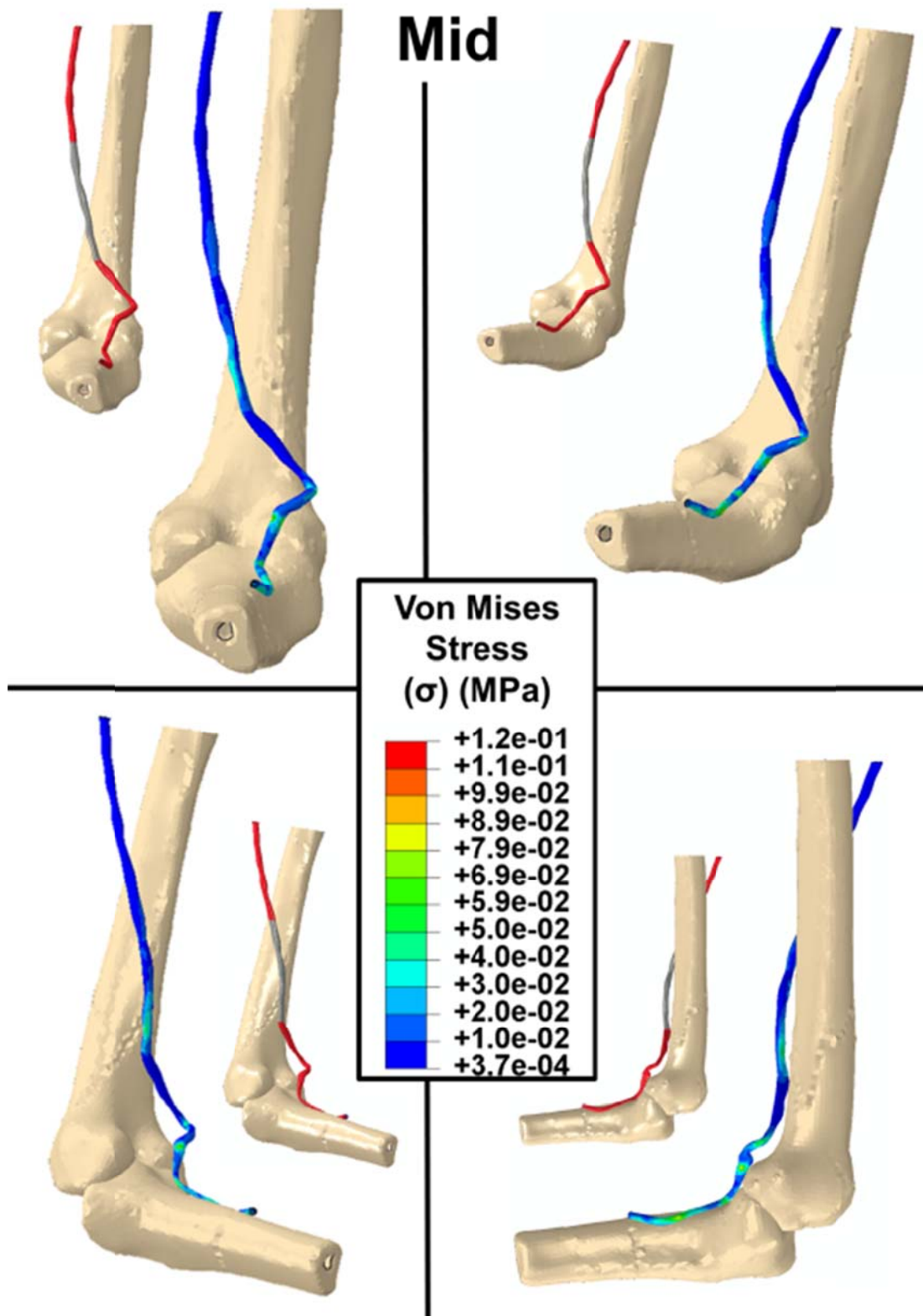


Figure 6.12 Deformation results of the stented (mid SFA location) artery model with contour plot of Von Mises stress (MPa) in the vessel after knee flexion.

Schematic image (inset on each view) shows stent location.

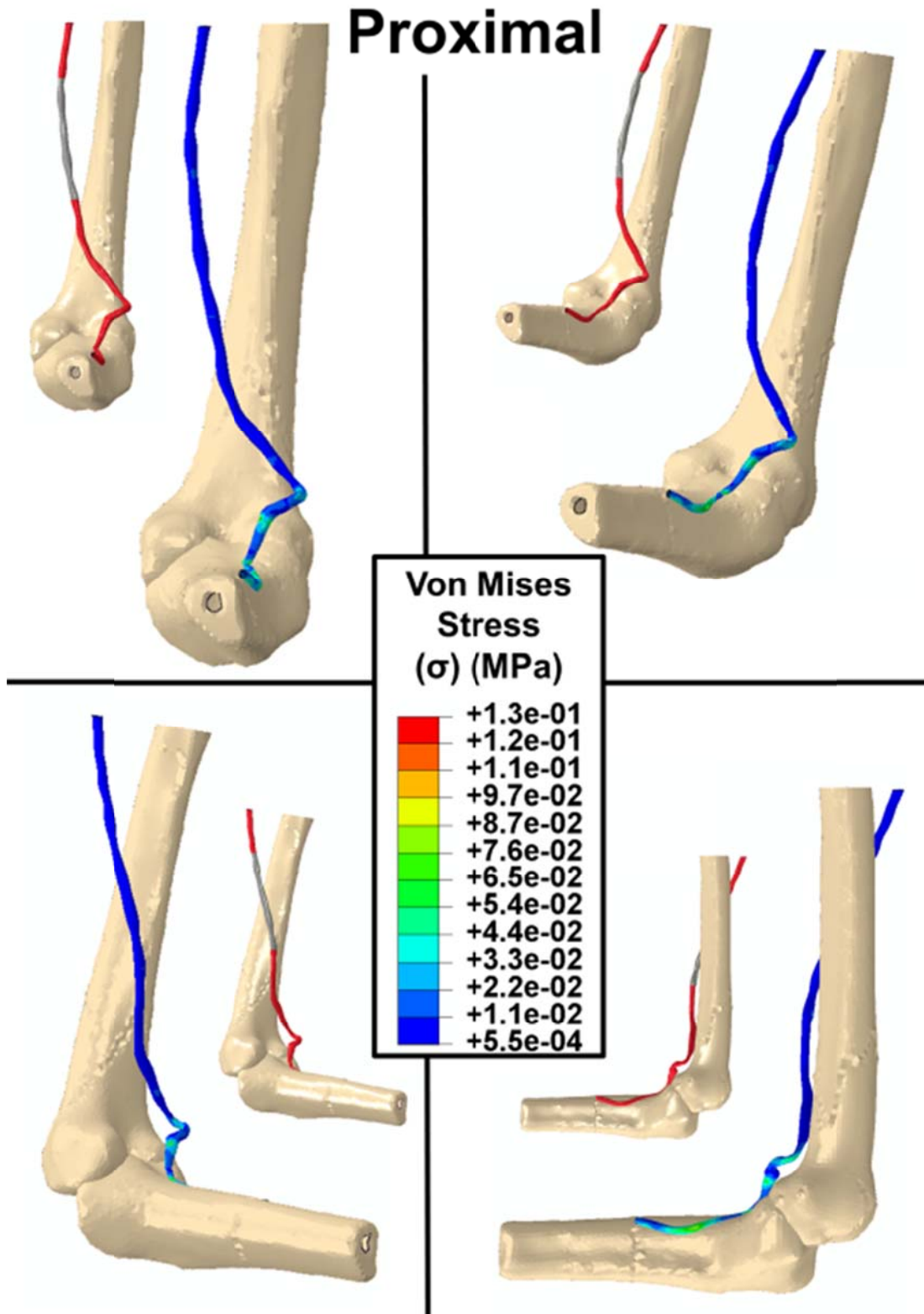


Figure 6.13 Deformation results of the stented (proximal SFA location) artery model with contour plot of Von Mises stress (MPa) in the vessel after knee flexion. Schematic image (inset on each view) shows stent location.

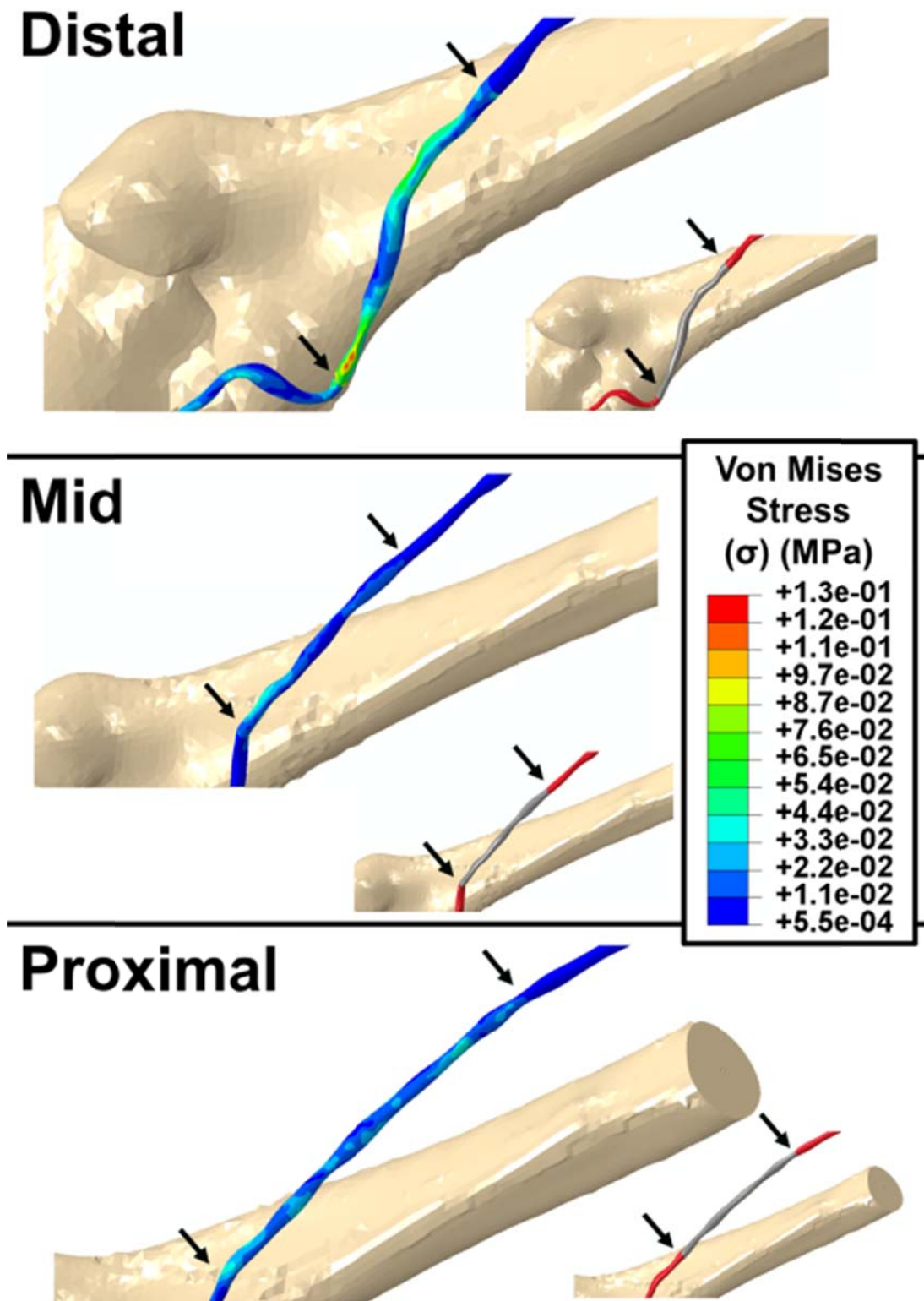


Figure 6.14 Contour plot of the deformed artery models of the stent location investigation showing Von Mises stress (MPa) in the stented region of the artery. Schematic image (inset on each view) shows stent location.

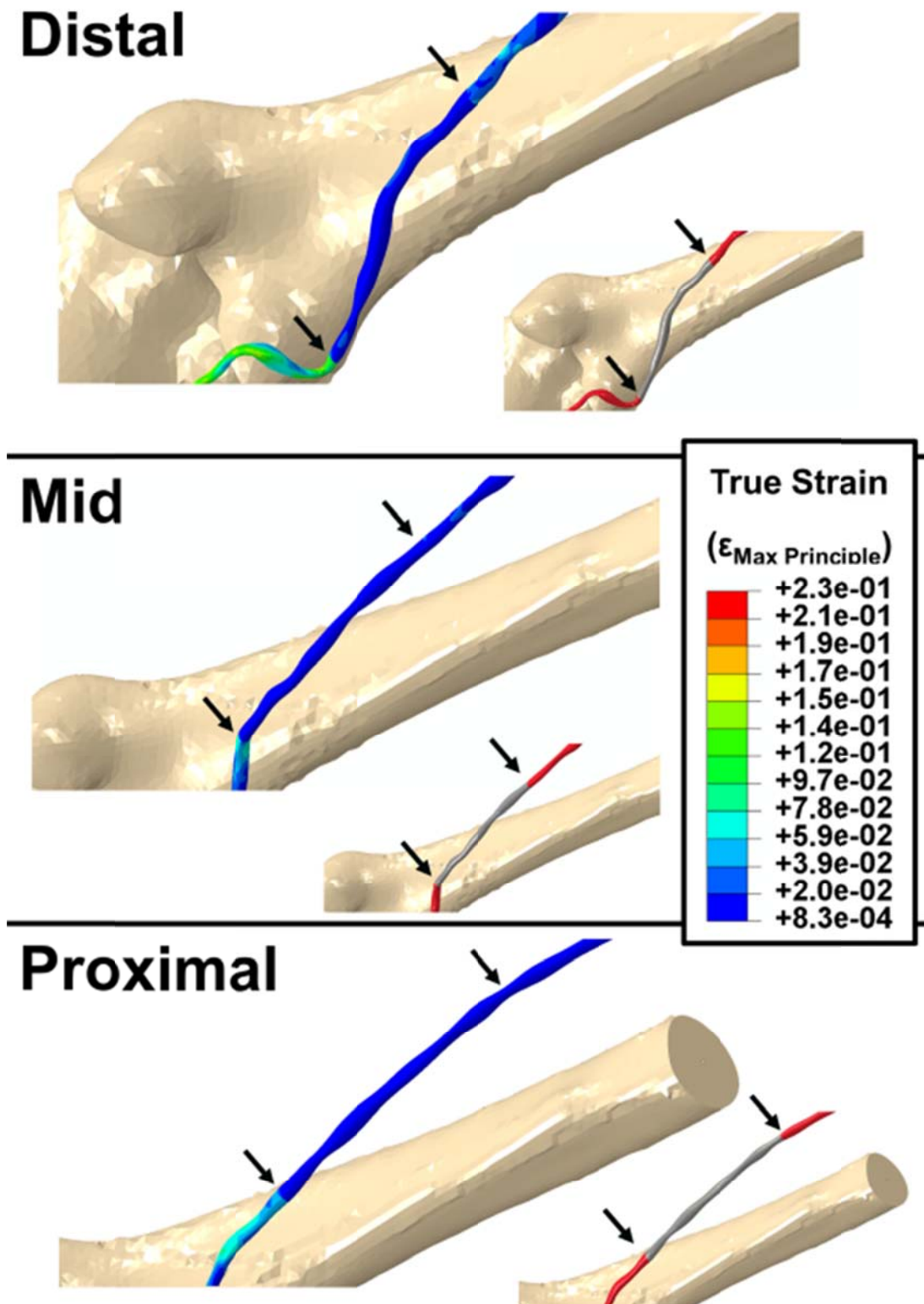


Figure 6.15 Contour plot of the deformed artery models of the stent location investigation showing strain in the stented region of the artery. Schematic image (inset on each view) shows stent location.

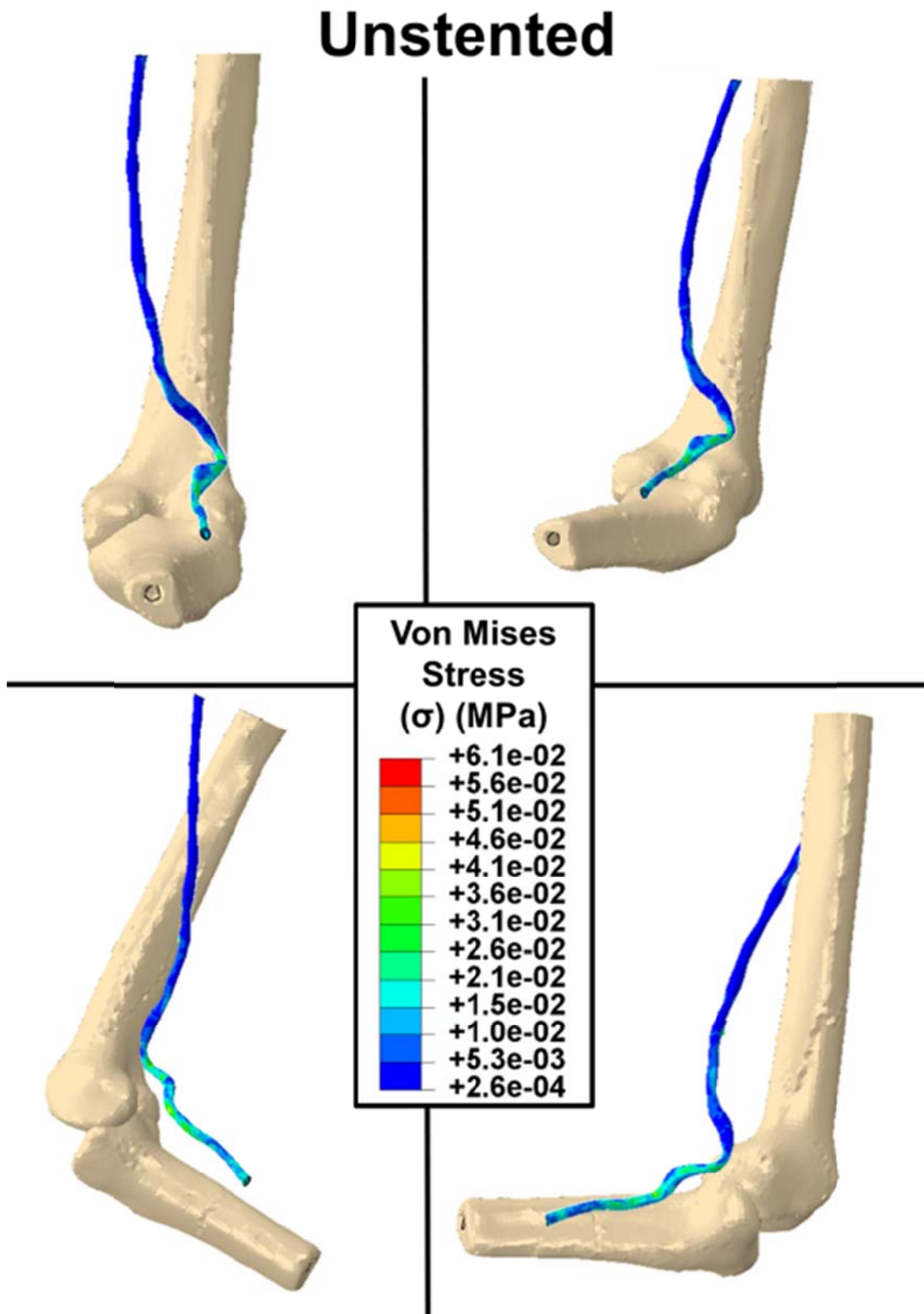


Figure 6.16 Deformation results of the unstented artery model as reported in Chapter 5 with contour plots of Von Mises stress (MPa) in the vessel after knee flexion.

6.5 References

- Cheng, CP, Choi, G, Herfkens, RJ, and Taylor, CA. 2010. The effect of aging on deformations of the superficial femoral artery resulting from hip and knee flexion: potential clinical implications. *Journal of Vascular and Interventional Radiology*. 21: 195-202.
- Cheng, CP, Wilson, NM, Hallett, RL, Herfkens, RJ, et al. 2006. In vivo MR angiographic quantification of axial and twisting deformations of the superficial femoral artery resulting from maximum hip and knee flexion. *Journal of Vascular and Interventional Radiology*. 17: 979-987.
- Choi, G, Cheng, CP, Wilson, NM, and Taylor, CA. 2009. Methods for quantifying three-dimensional deformation of arteries due to pulsatile and nonpulsatile forces: implications for the design of stents and stent grafts. *Annals of Biomedical Engineering*. 37: 14-33.
- Duerig, T and Wholey, M. 2002. A comparison of balloon-and self-expanding stents. *Minimally Invasive Therapy & Allied Technologies*. 11: 173-178.
- Gastaldi, D, Morlacchi, S, Nichetti, R, Capelli, C, et al. 2010. Modelling of the provisional side-branch stenting approach for the treatment of atherosclerotic coronary bifurcations: effects of stent positioning. *Biomechanics and Modeling in Mechanobiology*. 9: 551-561.
- Grujicic, M, Pandurangan, B, Arakere, G, Bell, WC, et al. 2009. Seat-cushion and soft-tissue material modeling and a finite element investigation of the seating comfort for passenger-vehicle occupants. *Materials & Design*. 30: 4273-4285.
- Jonker, FS, F. Moll, F. Muhs, B. 2008. Dynamic Forces in the SFA and Popliteal Artery During Knee Flexion. *Endovascular Today*.

- Kalmár, G, Hübner, F, Voelker, W, Hutzenlaub, J, et al. 2002. Radial force and wall apposition of balloon-expandable vascular stents in eccentric stenoses: an in vitro evaluation in a curved vessel model. *Journal of Vascular and Interventional Radiology*. 13: 499-508.
- Klein, AJ, James Chen, S, Messenger, JC, Hansgen, AR, et al. 2009. Quantitative assessment of the conformational change in the femoropopliteal artery with leg movement. *Catheterization and Cardiovascular Interventions*. 74: 787-798.
- Mozersky, DJ, Sumnfr, DS, Hokanson, DE, and Strandness JR, DE. 1972. Transcutaneous measurement of the elastic properties of the human femoral artery. *Circulation*. 46: 948-955.
- Rho, JY, Ashman, RB, and Turner, CH. 1993. Young's modulus of trabecular and cortical bone material: Ultrasonic and microtensile measurements. *Journal of Biomechanics*. 26: 111-119.
- Simons, J, Dalal, A, and Shockey, D. 2010. Load-Deformation Behavior of Nitinol Stents. *Experimental Mechanics*. 50: 835-843.
- Smouse, B, Nikanorov, A, and LaFlash, D. 2005. Biomechanical forces in the femoropopliteal arterial segment. *Endovascular Today*. 4: 60-66.
- Wensing, P, Scholten, F, Buijs, P, Hartkamp, M, et al. 1995. Arterial tortuosity in the femoropopliteal region during knee flexion: a magnetic resonance angiographic study. *Journal of Anatomy*. 187: 133-139.

Chapter 7. Comparison of *In Vitro* Human Endothelial Cell Response to Self Expanding Stent Deployment in a Straight and Curved Peripheral Artery Simulator

7.1 Introduction

Endothelial cells (EC) on the lining of the arterial wall are continuously subjected to haemodynamic forces of wall shear stress (WSS), radial pressure and tensile hoop strain (THS) from blood flow. These forces regulate numerous biomechanical stimuli and cellular responses that influence blood vessel structure. Haemodynamic forces have been investigated extensively and it is now known that combinations of haemodynamic forces have a synergistic effect on EC proliferation, morphology, biochemical expression and gene expression. Furthermore it is known that alterations to haemodynamic force influences the development of vascular pathologies (Barron et al., 2007, Dartsch et al., 1989, Levesque et al., 1985, Malek et al., 1999, Moore et al., 1994, Neidlinger-Wilke et al., 2001, Wang et al., 1995, Wang et al., 2001). Numerous experiments have shown active responses of the vasculature to altered haemodynamic forces including structural remodelling of the vessel (Asakura et al., 1990, Bennett, 2011, Girerd et al., 1996, Kamiya et al., 1984, Langille et al., 1986, Mattsson et al., 1997, Pedersen et al., 1997, Qiu et al., 2000), altered cell morphologies (Chiu et al., 1998, Ives et al., 1986, Kolpakov et al., 1996, Zhao et al., 1995), proliferation (Asakura et al., 1990, Cho et al., 1997, Förstermann et al., 2011, Gnasso et al., 1997, Pedersen et al., 1997), expression of inflammatory genes ICAM-1 and VCAM-1 (Breen et al., 2009, Cines et al., 1998, Ishida et al., 1997, Nerem et al., 1998) and production of nitric oxide (Barbato et al., 2004, Cines et al., 1998, Förstermann et al., 2011, Gimbrone et al., 2000, Hayashi et al., 2008, Mattsson et al., 1997, Rudic et al., 1998).

Under normal physiological conditions, EC function ensures a stable haemodynamic force environment by maintaining EC proliferation, apoptosis and production of adhesion molecules, inflammatory mediators, vasodilators and

vasoconstrictors at healthy levels. Nitric oxide (NO), a vasoactive autacoid, is synthesized by endothelial NOS (eNOS), expressed by vascular ECs and plays a crucial role in the dilation of blood vessels to regulate WSS (Barbato et al., 2004, Hayashi et al., 2008, Klabunde, 2004). It has been shown that the main role of eNOS is in vessel wall remodelling in response to alterations in WSS (Förstermann et al., 2011, Mattsson et al., 1997, Rudic et al., 1998). Studies have indicated that increasing WSS leads to increased eNOS levels, reduced cellular proliferation, reduced platelet aggregation and initiates apoptosis. This is followed by expansion of the vessel lumen to normalise WSS levels to a baseline level of 15-20 dyne/cm² (Girerd et al., 1996). Studies have also shown that in the presence of physiological WSS levels, ECs display an elongated appearance, with cells aligned in the direction of flow (Levesque et al., 1985). ECs reorientate perpendicular to the direction of pressure-induced THS and as such the combined effect of WSS and THS holds significant physiological relevance to cell morphology (Ives et al., 1986, Wang et al., 2001). THS is also responsible for increasing EC sensitivity to WSS, which results in a lowered threshold level of shear stress to stimulate structural remodelling of the vessel (Zhao et al., 1995). Studies suggest that THS initiates cellular structural integrity and may act as a mediator in vessel wall remodelling in response to altered WSS. Taking the results of these investigations together suggests that in combination, physiological levels of THS and WSS result in inhibited production of vasoconstrictors and enhanced production of vasodilators therefore evoking an anti-atherosclerotic environment, reducing fibrous plaque formation (Breen et al., 2009, Qiu et al., 2000).

Changes to flow conditions are commonly observed in peripheral arteries where the *in vivo* dynamic loading environment continually alters arterial geometry. This is seen in the femoropopliteal artery where curvature is consistently varied along artery length as a result of dynamic loading conditions such as knee bending (Cheng et al., 2010, Klein et al., 2009). The artery undergoes considerable length changes during knee bending which is compensated by curving and tortuosity of the artery (Kröger et al., 2004). This curvature change disrupts the flow pattern within the artery and thereby alters the haemodynamic environment. In a healthy patient, the control of stable physiological haemodynamics, by the regulatory mechanisms of vessel wall remodelling, ensures that deformations to peripheral arteries that cause

geometrical irregularities and alterations in WSS does not lead to a pathological state. However, in patients with risk factors for arterial disease (age, smoking, diabetes, hypertension, obesity and high cholesterol (Aboyans et al., 2006)) where the regulatory mechanisms of haemodynamic conditions are compromised, the effects of additional curvatures in the femoropopliteal artery can lead to disturbed flow and an increased likelihood for vascular pathologies to develop in the vessel (Aboyans et al., 2006, Wood et al., 2006).

For many physicians, percutaneous transluminal angioplasty (PTA) is the treatment of choice for vascular pathologies such as local arterial occlusion (stenosis) after the development of plaque on the inner artery wall resulting from alterations in haemodynamic flow (David Chua et al., 2004). PTA is generally followed by stent implantation, the delivery of a metallic scaffold (stent) to the stenosed region, providing a means of supporting the inside of the artery to maintain lumen patency (Holmes Jr et al., 1984). Whilst stenting initially allows uncompromised blood flow through the artery, studies have shown that the proliferative and thrombotic environment developed at branched and curved regions of the vasculature is also detected in vessels after stent placement (Duraiswamy et al., 2009, Duraiswamy et al., 2007, Frank et al., 2002, He et al., 2005, Moore et al., 2002, Punchard et al., 2009). Many investigations report that stenting causes a change in the haemodynamic flow environment due to stagnation and recirculation of blood flow around stent struts (Duraiswamy et al., 2009, Duraiswamy et al., 2007, Frank et al., 2002, He et al., 2005, Moore et al., 2002, Punchard et al., 2009). As observed in branched and curved regions, this change in haemodynamic flow conditions is coincident with increased EC proliferation, irregular EC morphologies and lower eNOS expression leading to the return of a pathological state inevitably, restenosis of the vessel (Asakura et al., 1990, Caro et al., 1971, Gnasso et al., 1997, Pedersen et al., 1997).

Low WSS (± 4 dyne/cm²), found at branching points, curved and stented regions of the vasculature, are a consequence of flow re-circulation, stasis, separation and directional change (Deplano et al., 2001, Krams et al., 2005, Moore et al., 1999, Pivkin et al., 2005, Prosi et al., 2004, Wood et al., 2006). Changes to flow conditions, and the subsequent disturbed haemodynamic environment that develops

in these regions of geometrical irregularity and curvature has been correlated with regions of diseased states such as atherosclerosis and stenosis in the carotid, coronary and femoral arteries (Asakura et al., 1990, Caro et al., 1971, Gnasso et al., 1997, Pedersen et al., 1997). Analysis of endothelial layers in regions of turbulent, oscillatory and low WSS tend to show a build-up of sub-intimal macrophages and lymphocytes, increased platelet aggregation and EC proliferation, irregular EC morphologies and reduced eNOS production (Chiu et al., 2011, Chiu et al., 1998, Cines et al., 1998, Gimbrone, 1995, Gimbrone et al., 2000, Gnasso et al., 1996, Ishida et al., 1997, Kamiya et al., 1984, Kamiya et al., 1980, Kolpakov et al., 1996, Nerem et al., 1998). Altered EC morphologies have a random orientation, exhibit decreased elongation and shortened actin stress fibres eventually causing EC loss. EC loss resulting from low WSS is a proposed result of apoptosis of ECs which remains persistent in the absence of normal WSS levels, eventually leading to a highly diminished EC layer (Bennett, 2011, Chiu et al., 2011, Cho et al., 1997). Therefore it can be concluded that intimal hyperplasia, fibrous plaque formation and atherosclerosis are due in part to altered flow conditions, which cause haemodynamic forces to change from normal physiological levels.

Previous studies suggest that a strong connection exists between vessel curvature, stenting, disturbed flow, intima thickening and atherosclerosis, with numerous studies having examined the effects of either artery curvature or stenting on haemodynamic forces using computational models, *in vitro* or *in vivo* studies (Asakura et al., 1990, Caro et al., 1971, Chiu et al., 2011, Chiu et al., 1998, Cines et al., 1998, Deplano et al., 2001, Gimbrone, 1995, Gimbrone et al., 2000, Gnasso et al., 1996, Gnasso et al., 1997, Ishida et al., 1997, Kamiya et al., 1984, Kamiya et al., 1980, Kolpakov et al., 1996, Krams et al., 2005, Moore et al., 1999, Nerem et al., 1998, Pedersen et al., 1997, Pivkin et al., 2005, Prosi et al., 2004, Wood et al., 2006). However, no study has focused on the effects of both artery curvature changes and stenting in combination and most importantly, independently of each other. We hypothesise that curved stented arteries create a pro-atherosclerotic environment and that different atherosclerotic responses exist in curved, straight stented and curved stented vessels due to altered haemodynamic forces. Previous studies have shown the potential of *in vitro* systems to deliver *in vivo* haemodynamic forces (Cardinal et al., 2006, Pouchard et al., 2009). Their work also showed the potential of such a system

to study cell response following stent deployment in a coronary artery model and evaluate the performance and interaction of coronary stents with the endothelial layer in a controlled environment.

The objective of this study is to reproduce the peripheral artery haemodynamic environment using an *in vitro* peripheral artery model and apply this model to determine the effects of curvature change and stent placement on the EC monolayer. A novel peripheral artery simulator is developed to model arteries of varying geometries (i.e. varying curvature), based on a previously existing coronary artery simulator capable of delivering *in vivo* haemodynamic forces *in vitro* (O'Cearbhaill et al., 2008, Punchard et al., 2007). Straight and curved sections of silicone tubes (fabricated to match the *in vivo* compliance of the femoropopliteal artery) are seeded with ECs, stented and subjected to haemodynamic flow conditions for 24 hours. EC viability, cell number, orientation and nitric oxide production are analysed.

7.2 Materials and Methods

7.2.1 Bioreactor Design

The bioreactor used in this study was adapted from a previous bioreactor perfusion system designed to deliver combinational forces of coronary arterial distention, pressure, flow and WSS to pseudovessels - specially fabricated using silicone tubes seeded with a monolayer of ECs (Punchard et al., 2009). For the study presented here the existing bioreactor design was augmented to simulate peripheral arterial radial distention, pressure, flow and mean WSS and to incorporate both straight and curved artery configurations. This was achieved by fabricating a specially designed fixture, capable of attaching the pseudovessel into the flow loop in each configuration. The curved configuration imposes a 0.4cm^{-1} curvature on the pseudovessel. This was defined by taking the radius of the average bend of the femoropopliteal artery *in vivo*, 0.4cm^{-1} (Klein et al., 2009). The bioreactor system shown in Figure 7.1 is set up inside a Heraeus Heracell-150 incubator. Pulsatile flow was provided by a peristaltic pump (520U, Watson-Marlow Limited) with the flow profile monitored by a non-invasive ultrasonic flow sensor (H9XL, Transonic Systems Inc.) clipped to the outside of the system tubing to ensure a pulse frequency of 1 Hz. The pressure in the system was monitored by a pressure transducer (BLPR2, World Precision Instruments Inc) connected to the flow loop by a luer connection. The pressure level in the system was controlled by positioning the reservoir to create a pressure head and by means of an adjustable pinch placed on the outside of the system tubing to control the resistance of the flow in the system. In order to monitor the measurements of flow and pressure, a data acquisition system was set up using a computer connected to a CompactRIO chassis (NI cRIO-9074 National Instruments) in combination with an input module to read voltage (NI 9215 Input Module). Voltages from the flow probe and pressure transducer were calibrated to mL/min and mm/Hg respectively using Labview (National Instruments). A Labview program was designed to read the output voltage from the probe and transducer and convert them to mL/min and mm/Hg whilst simultaneously producing live wave-forms so that the flow and pressure values could be continuously monitored. The mean WSS applied to the system was calculated from the Hagen-Poiseuille equation (equation (7.1)) (Cheng et al., 2002).

$$\tau_{mean} = \frac{4\mu Q}{\pi r^3} \quad (7.1)$$

where μ is the dynamic viscosity of the media (7.21×10^{-4} Pa), Q is the average flow rate and r is the tube's inner radius (3 mm). The waveform of the flow profile of the bioreactor system is shown in Figure 7.2. The waveform describes the physiological pulsatile flow conditions applied to the pseudovessel with an average flow rate of 240 ml/min. The average Reynolds number of the flow loop is 391. A fixture was designed to hold the silicone tube in either a straight or curved configuration during the experiment, attached into the flow loop by flow connectors.

7.2.2 Fabrication of *In Vitro* Peripheral Artery Models

Medical grade silicone (RT-601, Elastosil, Wacker) was molded into tubes (ID 6mm, OD 7mm, length 90mm) that have comparable material properties to the native femoropopliteal artery (0.3MPa elastic modulus, 3.5% radial distention (Benetos et al., 1993, Bergel, 1961, Mozersky et al., 1972)). Sterilized silicone tubes were coated with $8\mu\text{g/mL}$ fibronectin (Sigma) and seeded with human umbilical vein ECs (HUVEC) between passages 4 and 6 (Promocell). HUVECs were seeded at a concentration of $171,500$ cells/cm² in EC growth media (C-22010Promocell) (Punchard et al., 2009). Tubes were rotated at slow rotation speed (10rph) for 48 hours (37°C, 5% CO₂). Media was changed after 24 hours. After 48 hours of rotation, a short end portion of the tube was cut off and examined to determine a confluent cell layer. The cut section was washed in phosphate buffered saline (PBS, Sigma) and fixed by immersion in methanol (Sigma) at -21°C for 20 seconds. Once fixed the section was stained with Haematoxylin (Sigma) for 20 seconds followed by Eosin (Sigma) for 20 seconds. It was then longitudinally sectioned with a scalpel and mounted on microscope slides for light microscopy.

7.2.3 Experimental Models

To investigate the effect of curvature on stented peripheral arteries, four experimental models were considered in this study. These included a straight

unstented pseudovessel, a curved unstented pseudovessel, a straight stented pseudovessel and a curved stented pseudovessel (n=3 per experimental model).

7.2.4 Controls

The four models described (straight unstented, curved unstented, straight stented and curved stented) were also investigated in static conditions (no flow) in the bioreactor flow loop as controls (n=3 per control).

7.2.5 Stent deployment

Once the presence of a confluent cell monolayer was confirmed by H&E staining of a segment of a tube, a Nitinol self-expanding stent (Cordis SMART[®] Control[™] Nitinol Stent System) was deployed into the pseudovessel. The SMART[®] stent has regulatory approval for use *in vivo* and therefore has no adverse effect on the EC's of the pseudovessel. The device was received in its original sterile packaging and used in sterile conditions employing aseptic techniques. The stent was deployed by means of a stent delivery system in which the stent is crimped and constrained between the inner and outer sheath of a catheter. For stent deployment, the catheter tip is fed through the centre of the pseudovessel and once the stent is positioned correctly, the outer sheath retracted along the inner sheath, allowing the stent to expand to its nominal diameter within the pseudovessel. Following deployment, the inner sheath is retracted from inside the tube. During deployment, care was taken to ensure there was no contact between the delivery system and the EC lining of the tube. The stent was not dragged or repositioned so as not to damage the EC layer. In this way the innocuousness of the stent deployment is ensured. The stent has a strut profile of 0.1mm x 0.2mm and the surface coverage of the stent is calculated as 27.43% of the pseudovessel. Cell viability was measured immediately after stent deployment using an alamar blue cell viability reagent (Invitrogen). Pseudovessels were washed with phosphate buffered saline (PBS, Sigma) and stained with alamar blue (diluted 1:10 in cell culture media (C-22010 Promocell) under a slow rotation speed (10 rph, 37°C, 5% CO₂) for 2 hours after which the absorbance of the cell conditioned alamar blue reagent was measured at 550 and 595nm using a micro plate reader (Wallac 1420m, Victor). Cell number was

quantified by comparing to a standard curve correlating a known cell number with % reduction of the alamar blue reagent.

7.2.6 Biomechanical Stimulation

Stented pseudovessels were transferred into the bioreactor flow loop by attachment into the specially designed fixture. Pseudovessels were biomechanically conditioned (pressure 80/120 mmHg, radial distention 5%, average flow 240 mL/min, mean WSS 10 dyne/cm²) for 24 hours at 37°C, 5% CO₂.

7.2.7 Cell Number

After 24 hours of biomechanical conditioning cell number was measured as previously described using alamar blue cell viability reagent (Invitrogen). Briefly, pseudovessels were removed from the flow loop, washed with phosphate buffered saline (PBS, Sigma), stained with alamar blue dye under a slow rotation speed (10 rph, 37°C, 5% CO₂) for 2 hours. Absorbance of the cell conditioned alamar blue reagent was measured and cell quantified using the standard curve correlating a known cell number with % reduction of the alamar blue reagent.

7.2.8 Cell Orientation

After 24 hours of biomechanical conditioning the angle of cell orientation was determined. The pseudovessels were washed in phosphate buffered saline (PBS, Sigma) and fixed by immersion in methanol (Sigma) at -21°C for 20 seconds. Once fixed the tubes were then stained with Haematoxylin (Sigma) for 20 seconds followed by Eosin (Sigma) for 20 seconds. Tubes were longitudinally sectioned with a scalpel so that sections from the entire circumference of the tube could be imaged. Sections were mounted on microscope slides for light microscopy and images were captured throughout the length of the sections. ImageJ software was used to determine cell orientation by quantifying the orientation of the cells with the longitudinal axis of the tube using the ellipsis method by thresholding the images and using the particle analysis tool to assign best-fit ellipses to each cell (O'Cearbhaill et al., 2008, Rasband, 1997-2011).

7.2.9 Nitric Oxide Production

Nitric Oxide (NO) production of the cells was monitored during each experiment at 2, 4, 6 and 24 hours of biomechanical stimulation. At 2, 4, 6 and 24 hour time points, the pseudovessel was removed from the flow loop, washed with phosphate buffered saline (PBS, Sigma), filled with cell culture media (C-22010 Promocell) and incubated for 2 hours (37°C, 5% CO₂). Media was then removed from the tubes and the tube placed back into the flow loop. Nitrite concentration was quantified from the cell conditioned media using a Measure-iT™ High-Sensitivity Nitrite Assay Kit according to manufacturer's instructions (Invitrogen).

7.2.10 Statistical Analysis

Results presented here are a representative of three independent experiments for each model and are presented as mean \pm standard deviation. An independent *t*-test was used to determine statistical difference in the fold increase, cell orientation and nitric oxide results of the models. A *p*-value <0.05 was considered statistically significant. *P*-values of significant results are reported.

7.3 Results

7.3.1 Cell Number

Successful fabrication of pseudovessels followed by self-expanding stent deployment was achieved in the model arteries, confirmed by an alamar blue assay showing viability of cells after seeding and rotation for 48 hours. The number of cells at 0 and 24 hours in the bioreactor for both static and flow experiments is shown in Figure 7.3(a). The relative change in cell number from 0 to 24 hours is shown in Figure 7.3(b).

Flow vs. No Flow

All static condition models show a lower increase in cell number after 24 hours compared to their corresponding models subjected to flow conditions (straight unstented, $p=0.0018$; curved unstented, $p=0.0005$; straight stented, $p<0.0001$; curved stented, $p=0.0005$) (Figure 7.3(b)). The highest increase in cell number is seen in the straight stented pseudovessel after addition of flow (1.50 fold increase after 24 hours) (Figure 7.3(b)). The lowest increase in cell number of the flow models was the straight unstented pseudovessel (1.29 fold increase after 24 hours) (Figure 7.3(b)).

Straight vs. Curved

For the unstented models, curved unstented pseudovessels show significantly higher increases in cell number than straight unstented pseudovessels after 24 hours of biomechanical flow conditions. (1.29 and 1.41 fold increase for straight unstented and curved unstented models respectively; $p=0.0182$) (Figure 7.3(b)). Histology of the tubes shows more confluent EC layers in curved unstented tubes versus straight unstented tubes (Figure 7.4). For the stented models, straight stented pseudovessels show significantly higher increases in cell number than curved stented pseudovessels after 24 hours of biomechanical flow conditions. (1.50 and 1.35 fold increase for straight stented and curved stented models respectively; $p=0.0161$) (Figure 7.3(b)).

Stented vs. Unstented

Increase in cell number was significantly higher in the straight stented models in comparison to the straight unstented models after 24 hours of biomechanical flow conditions. (1.29 and 1.50 fold increase for straight unstented and straight stented models respectively; $p < 0.0024$) (Figure 7.3(b)). The fold increase in cell number was lower in the curved stented model than the curved unstented model after 24 hours of biomechanical flow conditions. (1.29 and 1.50 fold increase for curved unstented and curved stented models respectively) (Figure 7.3(b)).

7.3.2 Cell Orientation***Flow vs. No Flow***

Static condition models all showed a random orientation of cells after 24 hours (Figure 7.4). Straight and curved unstented pseudovessels had significantly more cells aligned within 10° and 20° of the longitudinal axis of the tube than their static controls (straight unstented $0-10^\circ$, $p < 0.0001$; straight unstented $11-20^\circ$, $p < 0.0001$; curved unstented $0-10^\circ$, $p < 0.0001$; curved unstented $11-20^\circ$, $p < 0.0001$). The straight stented pseudovessels had significantly more cells aligned within $0-10^\circ$ of the longitudinal axis of the tube than its static controls (straight stented $0-10^\circ$, $p = 0.0165$) (Figure 7.4 and Figure 7.5).

Unstented Pseudovessels

Significantly more cells are seen to align within $0-10^\circ$ of the longitudinal axis of the tube in the straight unstented pseudovessel compared to the curved unstented pseudovessels after 24 hours of biomechanical stimulation ($p < 0.0001$) (Figure 7.4). ECs of the straight unstented pseudovessel are notably more aligned in a particular direction versus the ECs of the curved unstented pseudovessel in histological sections (Figure 7.5(c) and Figure 7.5(d)).

Stented Pseudovessels

The stented flow models display a significantly less aligned orientation of cells in both straight and curved geometries compared to their corresponding

unstented models in the presence of flow (straight stented 0-10°, $p<0.0001$; straight stented 11-20°, $p=0.0026$; curved stented 0-10°, $p<0.0001$; curved stented 11-20°, $p<0.0001$) (Figure 7.4). Significantly less alignment is seen in between stent struts for the curved stented pseudovessel versus the straight stented pseudovessel after 24 hours of biomechanical stimulation (0-10°, $p=0.0001$; 11-20°, $p<0.0014$) (Figure 7.4). In histological sections it can be seen that the curved stented pseudovessel exhibits slightly less confluent regions of EC growth in between stent struts versus the straight stented pseudovessel, with ECs of the curved stented pseudovessel notably less aligned in a particular direction versus ECs of the straight stented pseudovessel (Figure 7.6).

7.3.3 Nitric Oxide Production

Flow vs. No Flow

The static condition models showed low NO production with no statistical difference in NO levels between the different pseudovessels. Addition of biomechanical flow significantly increased NO production in each group (straight unstented, $p<0.0001$ at 2, 4, 6 and 24 hours; curved unstented, $p<0.0001$ at 2, 4, 6 and 24 hours; straight stented, $p<0.0001$ at 2, 4, 6 and 24 hours; curved stented, $p<0.0001$ at 2, 4, 6 and 24 hours) (Figure 7.7).

Straight vs. Curved

Under *in vitro* fluid flow conditions, curved pseudovessels produced significantly less NO than straight pseudovessels in both the unstented and stented case at all time points in the unstented pseudovessels and after 2 hours in the stented pseudovessels (curved unstented 2 hours, $p=0.0001$; curved unstented 4 hours, $p=0.0002$; curved unstented 6 hours, $p=0.0025$; curved unstented 24 hours, $p<0.0001$; curved stented 4 hours, $p<0.0001$; curved stented 6 hours, $p=0.0009$; curved stented 24 hours, $p<0.0001$) (Figure 7.7).

Stented vs. Unstented

Under *in vitro* fluid flow conditions, stented pseudovessels produced significantly less NO than unstented pseudovessels in both the straight and curved

configuration at all time points (straight stented 2 hours, $p=0.0006$; straight stented 4 hours, $p=0.0005$; straight stented 6 hours, $p=0.0001$; straight stented 24 hours, $p<0.0001$; curved stented 2 hours, $p=0.0021$; curved stented 4 hours, $p=0.0038$; curved stented 6 hours, $p<0.0001$; curved stented 24 hours, $p<0.0001$) (Figure 7.7).

7.4 Discussions and Conclusions

Variations of haemodynamic flow (due to geometry changes and stenting of the pseudovessels) will alter levels of haemodynamic force (WSS and THS) on the EC lining of the vessel, and it has been shown in this study that this produces cellular responses that can be linked to pathological conditions in vessels. The responses focused on in this study are those of proliferation (by quantifying changes to cell number), orientation/alignment and NO production. This study shows for the first time the EC response to combinations of straight, curved, stented and unstented peripheral vessel models subjected to 24 hours of stimulation in a peripheral artery bioreactor. After 24 hours of biomechanical stimulation we report that, compared to straight pseudovessels, curved pseudovessels show characteristics of a pro-atherosclerotic environment. Specifically this was indicated by a greater increase in the number of ECs and lower NO production in the curved pseudovessels, with EC orientation in the curved pseudovessels randomly aligned, and not aligned in the direction of flow as seen in straight pseudovessels. Our results showed a reduction in viable ECs immediately after stent deployment in the straight and curved pseudovessels. Furthermore, we report that after 24 hours of biomechanical stimulation, curved stented pseudovessels show less viable cells with lower increases in cell number and lower NO production than straight stented pseudovessels, indicating a pro atherosclerotic environment in the curved stented model.

It has been shown in other studies that ECs found in regions of disturbed flow and low WSS display a response characteristic of increased proliferation including the build-up macrophages, lymphocytes and platelets (Chiu et al., 2011, Chiu et al., 1998, Cines et al., 1998, Gimbrone, 1995, Gimbrone et al., 2000, Gnasso et al., 1996, Ishida et al., 1997, Kamiya et al., 1984, Kamiya et al., 1980, Kolpakov et al., 1996, Nerem et al., 1998). Therefore the altered geometry of the curved pseudovessel and the resulting changes to the flow environment and haemodynamic forces are likely to be responsible for the higher increases in cell number in the curved unstented models. In our study, we report for the first time, that lower levels of EC proliferation (lower increase to EC number) are seen in the straight unstented models where normal physiological conditions exist and ECs maintain normal levels

of proliferation due to an environment of stable haemodynamic force. Furthermore in the absence of haemodynamic forces, in the static condition models, there are little changes to EC number.

The reduction in viable ECs seen in the stented pseudovessels post deployment is assumed to be a result of EC denudation during stent placement, which replicates *in vivo* events. It is well known that stent deployment procedures are associated with immediate injury to the EC lining of the vessel wall (Scott, 2006, Sullivan et al., 2002). In this study it has been shown that increase in EC cell number is lower in the curved pseudovessel than in the straight pseudovessel after stent placement, perhaps due to the movement of the stent against the pseudovessel wall during attachment to the tube curved fixture. This friction between the cell coated tube wall and stent as the tube conforms to a curved configuration would cause additional denudation of ECs which does not occur in the straight stented pseudovessel. As the vasculature consists of many curved regions, with curvature changing due to deformation characteristics of the vessel, the *in vitro* model presented here is a good reflection of *in vivo* occurrences. Specifically it replicates the effects of changing curvature of stented vessels on the vessel lining of the superficial femoral artery (SFA) and popliteal arteries, which are known to change in curvature due to knee flexion (Cheng et al., 2010, Cheng et al., 2006, Klein et al., 2009).

In this study, it has also been shown that regardless of vessel geometry (straight or curved), the presence of a stent will result in random cell orientation; with regions of aligned ECs populating in close to stent struts. It has been shown in previous studies that the morphological response of EC's is dependent on both WSS and THS and also that the combined effect of WSS and THS holds significant physiological relevance, with cell morphology determined by both haemodynamic forces in combination (Breen et al., 2009, Qiu et al., 2000). In the stented models of this study, addition of the stent to the pseudovessel alters its compliance, thereby altering THS. This may be causing the altered morphological EC response seen in the stented pseudovessels, due to changing WSS (around stent struts) and THS (due to compliance changes) in combination. This study also shows that in a straight stented vessel, there is a greater number of EC's orientating local to stent struts than

when the vessel is in a curved configuration. We propose that this is a result of additional changes to flow conditions resulting from the geometry change of the pseudovessel (along with previously mentioned changes to flow conditions due to the presence of stent struts and compliance of the pseudovessel).

It has been shown for the first time that the curvature of a stented vessel has an effect on EC proliferation (changes in EC number) post stent deployment. Specifically it was shown that ECs proliferated less in the curved stented pseudovessel than in the straight stented pseudovessel 24 hours after stent deployment in the presence of biomechanical flow conditions. Interestingly, in the absence of flow (in the straight and curved stented pseudovessels in static conditions) no significant difference was seen in the number of viable cells of the straight stented pseudovessel in comparison to the curved stented pseudovessel after 24 hours. Therefore, the difference in proliferation rates between the straight and curved stented pseudovessels after 24 hours of flow suggests that stenting in combination with artery curvature results in reduced proliferation and viability due to its haemodynamic force environment. As previously stated, it has been shown that EC response is dependent on both WSS and THS in combination, and it has been suggested that the presence of THS neutralizes the athero-prone effect of low of WSS (Breen et al., 2009, Qiu et al., 2000). Studies by both Qiu et al. and Breen et al. have reported that THS influences the production of vasoactive agents and cellular proliferation influencing vascular wall remodeling when combined with WSS. In the curved stented models of this study, the addition of the stent to the pseudovessel (which alters pseudovessel compliance and therefore THS) may be a cause of the viability response of the cells in the curved stented pseudovessels in response to changing WSS and THS in combination.

Previous studies have established correlations between altered WSS levels and EC alignment. Steady flow and high WSS levels result in ECs aligning in the direction of flow. Oscillatory/turbulent flow and low WSS levels results in random orientation of ECs (Levesque et al., 1985, Moore et al., 1994). Cell orientation results of the static models of this study correlate well with studies that show random alignment of ECs in the absence of flow (Levesque et al., 1985). Additionally, results of the straight unstented and straight stented pseudovessels compare well to

reports by previous researchers that have assessed orientation of cells in straight pseudovessels with and without a stent in the presence of flow (Cardinal et al., 2006, Punchard et al., 2009). We confirm that ECs in these models will align within 0-10° of the direction of flow. However in this study we show for the first time how EC orientation is affected in a curved vessel in the presence of biomechanical flow conditions, both with and without a stent. Specifically we show that in unstented pseudovessels, ECs are more randomly orientated when the vessel is of a curved configuration. In this study, the curved pseudovessels represent cases of disturbed flow conditions due to geometry changes and the resulting EC orientation of these models may therefore be a direct result of disturbed flow conditions.

It has been shown that increased NO production, resulting from high WSS levels inhibits cell proliferation, leading to an overall anti-proliferative effect (Förstermann et al., 2011, Golledge et al., 1997). Therefore, high WSS levels, and the resulting production of NO by ECs in the straight unstented model creates an anti-atherosclerotic environment. In our study reduced production of NO is found in the curved and stented models and can be explained by changes to haemodynamic forces. In these models, WSS is reduced which has been shown in previous studies to reduce NO production (Berkels et al., 2001, Peng et al., 2000). Furthermore, Awolesi et al. showed that THS increases EC eNOS expression in bovine aortic ECs (Awolesi et al., 1995). Therefore the reduced levels of NO production in the stented models of this study could be as a result of lower levels of THS. Additionally, as one of the pathways for production of NO is dependent on endothelial receptors on the surface of ECs that form a healthy and complete endothelial layer, allowing binding of ligands essential for NO production (Klabunde, 2004), the reduced NO level of the stented models may be due to the broken, dysfunctional endothelial layers. Altered levels of NO production is associated with inflammatory and thrombotic responses (Klabunde, 2004). Therefore the curved and stented models of this study display indications of biochemical production that would lead to atherosclerosis and restenosis.

One of the limitations of this experiment is the lack of gene expression analysis. Other studies have examined atherosclerotic responses and restenosis by measuring the expression of inflammatory genes such as ICAM-1, VCAM-1 and E-Selectin. However, seen as a complete inflammatory response could only be found

through an *in vivo* model with circulating inflammatory cells, an *in vitro* model could not capture an accurate inflammatory response. It was therefore considered sufficient to focus on EC viability, proliferation, orientation and NO production in measuring the response of ECs to curvature and stenting. However, future applications of the peripheral peripheral artery simulator developed here could include measuring the expression of inflammatory genes of the pseudovessels investigated in this study along with the incorporation of dynamic loading conditions such as flexion and extension to further simulate the physiological loading environment of the femoropopliteal vessel.

As discussed, this study focuses on vascular pathologies influenced by changes in hemodynamic flow conditions. It is important to note that transport and accumulation of macromolecules across the blood vessel wall plays an important role in the physiological regulation of healthy vessels. Therefore, pathological states of the blood vessels such as atherosclerosis are often related to irregular mass transport across the vessel wall (Kennedy et al., 1995). Studies have revealed a correlation between increased permeability to macromolecules (specifically albumin, fibrinogen and low density lipoprotein) and the localization of atherosclerotic plaques (Tarbell, 2003). Therefore mass transport, along with changes to the hemodynamic flow environment is considered to be a significant factor in vascular pathologies.

Stenting in the femoropopliteal artery has been associated with high failure rates due to the challenge faced by the environment of dynamic forces of the SFA and popliteal artery, including bending, tension, torsion and compression which leads to failure by stent fracture (Duda et al., 2002, Nikanorov et al., 2008, Scheinert et al., 2005). However another common cause of stent failure in the femoropopliteal artery is in-stent restenosis, the reoccurrence of blockages in the stented region, generally resulting in re-stenting of the artery (Cheng et al., 2001, Gray et al., 1997). Restenosis is a direct result of the cellular response to changes in flow characteristics which alter the haemodynamic forces of THS and WSS (Chiu et al., 2011, Cines et al., 1998, Gimbrone et al., 2000, Wentzel et al., 2003). Therefore the effects of stenting in combination with artery curvature observed in this study may play a role in in-stent restenosis of femoropopliteal arteries as stenting in combination with artery curvature dramatically affects flow conditions. In this study the effects of both

artery curvature and stenting on the endothelial layer *in vitro* have been examined independently of each other to elucidate the different result of straight stented and curved stented vessels. The breakdown of these factors will identify the most unfavourable haemodynamic condition of peripheral stented vessels. As femoropopliteal artery stenting usually involves long stents that extend beyond the lesion, this study highlights that care should be taken when extending the stented portion of the artery to regions of high curvature. Furthermore, the results presented here have important implications for peripheral stent design. A common feature of femoropopliteal stenting is the ‘straightening’ of the vessel in the stented portion due to a mismatch in stiffness between the stented and unstented portion of the vessel immediately adjacent to the stent. This results in increased deformation at the end portions of the stented region and in turn, geometry changes to the vessel at these locations. Therefore it can be concluded that stent designs that adversely affect the stiffness of the artery and associated altered vessel configuration post deployment, will undesirably affect cell behaviour to the stented portion and the associated cell responses will ensue.

In conclusion this study demonstrates that the combination of vessel geometry changes (curvature) and stent deployment, in the presence of haemodynamic flow, results in cell responses associated with pro-atherosclerotic conditions, in-stent restenosis and other arterial diseased states. Furthermore, results presented here highlight the necessity of investigating the effects of curvature in combination with stenting as it has been shown that the response of the vascular endothelium is dependent on both curvature and stenting combined. The use of *in vitro* systems to accurately model the haemodynamic environment of complex arterial geometries such as the femoropopliteal artery will help to clearly define the effects of altered flow conditions in these regions and the extent of pathophysiological conditions that form as a result.

7.5 Figures

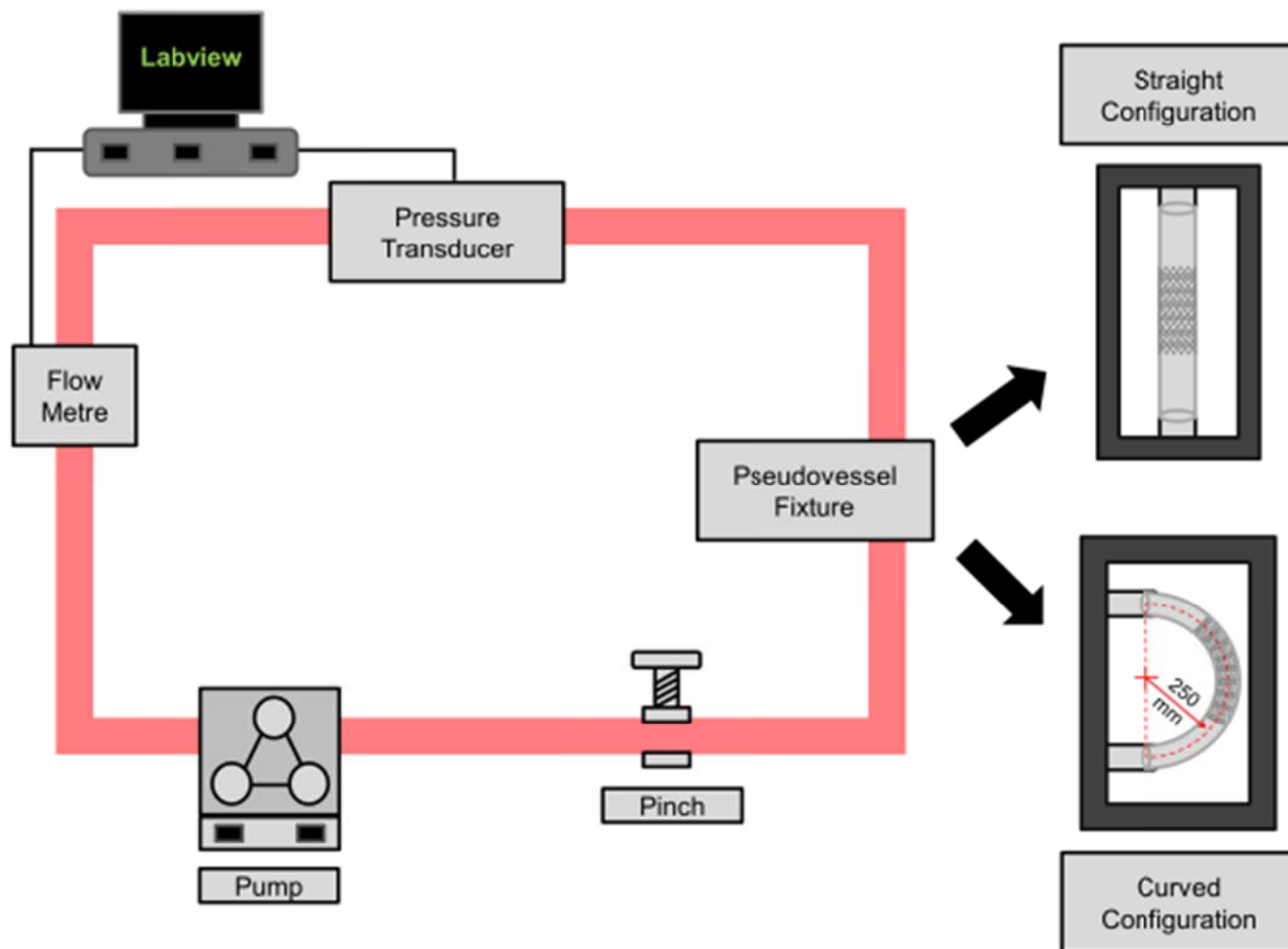


Figure 7.1 Bioreactor Schematic.

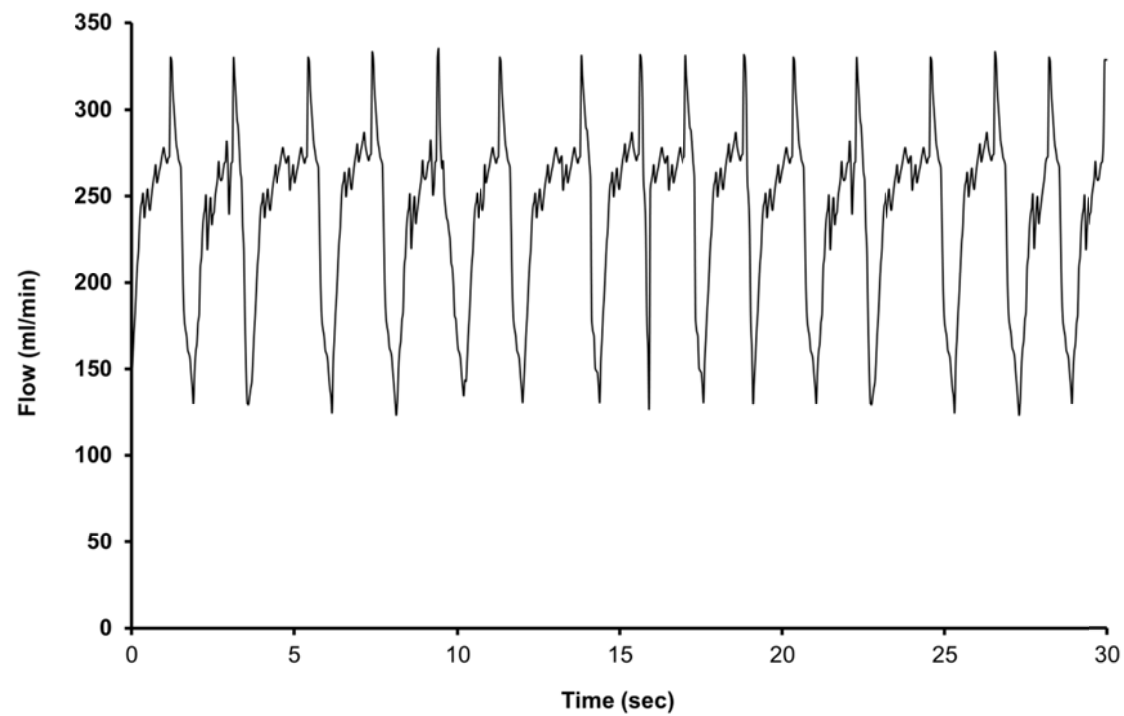


Figure 7.2 The waveform of the pulsatile flow profile of the bioreactor system recorded using an ultrasonic flow probe.

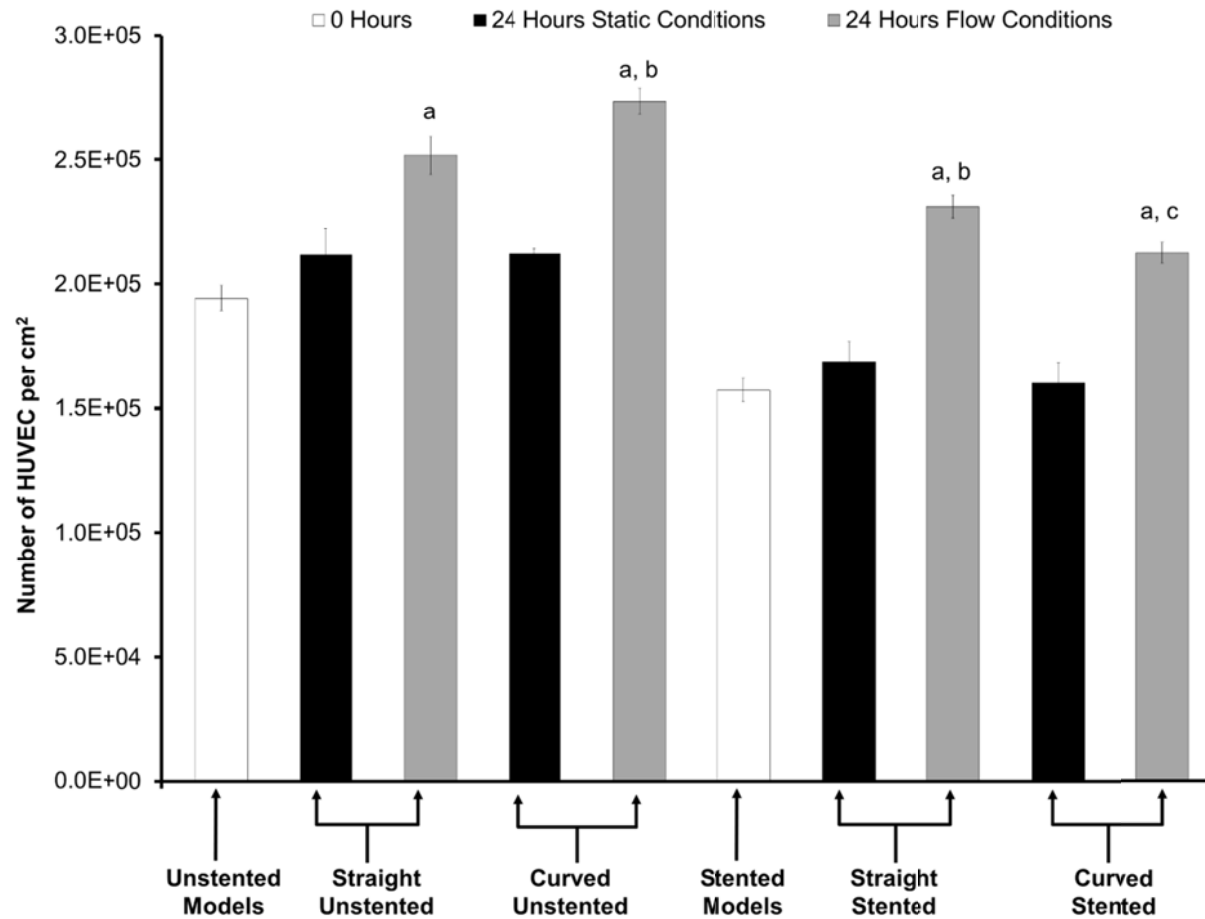


Figure 7.3 (a) Cell number at 0 and 24 hours with and without biomechanical flow conditions. ^a $p < 0.05$ versus its static control; ^b $p < 0.05$ versus straight unstented with flow; ^c $p < 0.05$ versus straight stented with flow.

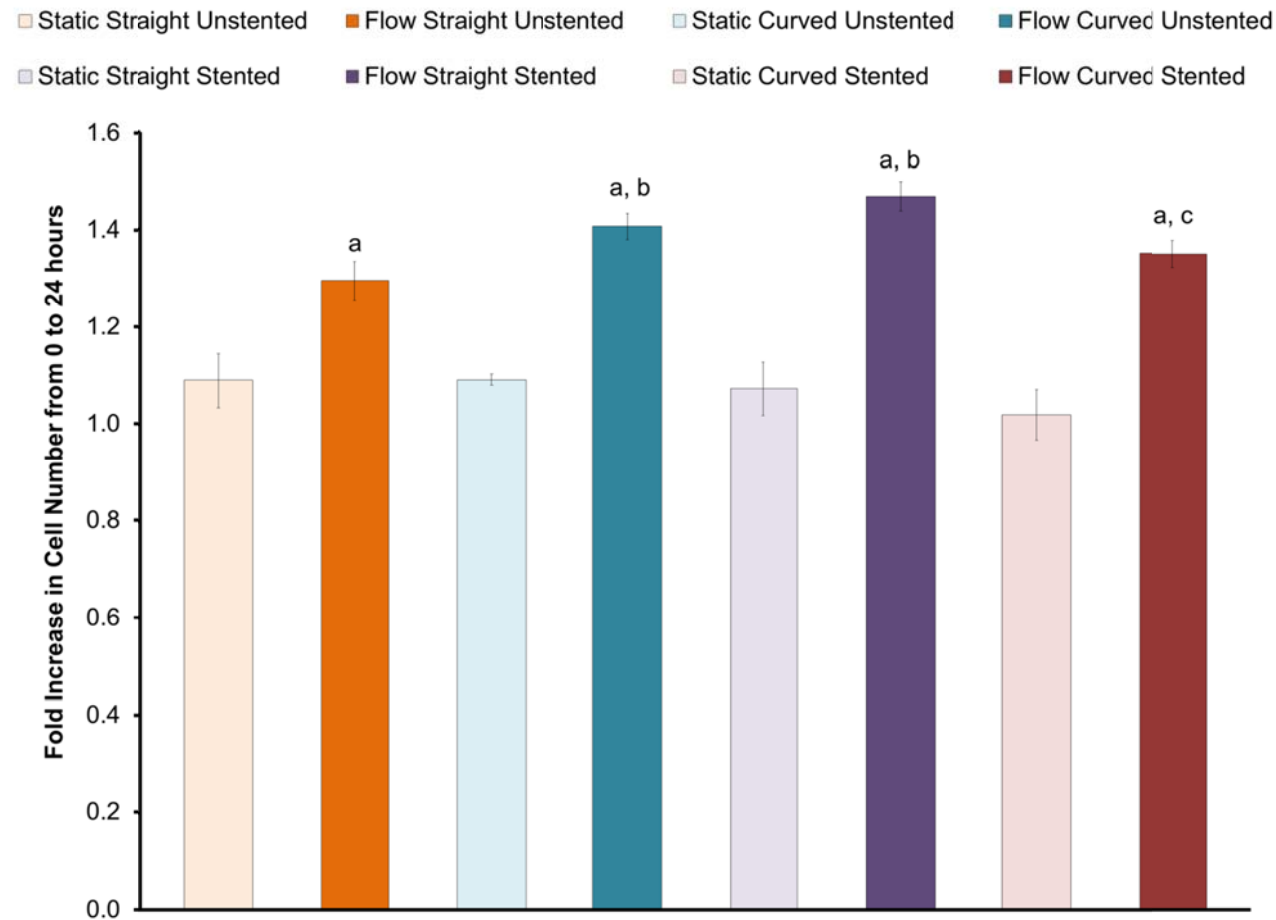


Figure 7.3 (b) Relative cell number increase from 0 to 24 hours with and without biomechanical flow conditions. ^a $p < 0.05$ versus its static control; ^b $p < 0.05$ versus straight unstented with flow; ^c $p < 0.05$ versus straight stented with flow.

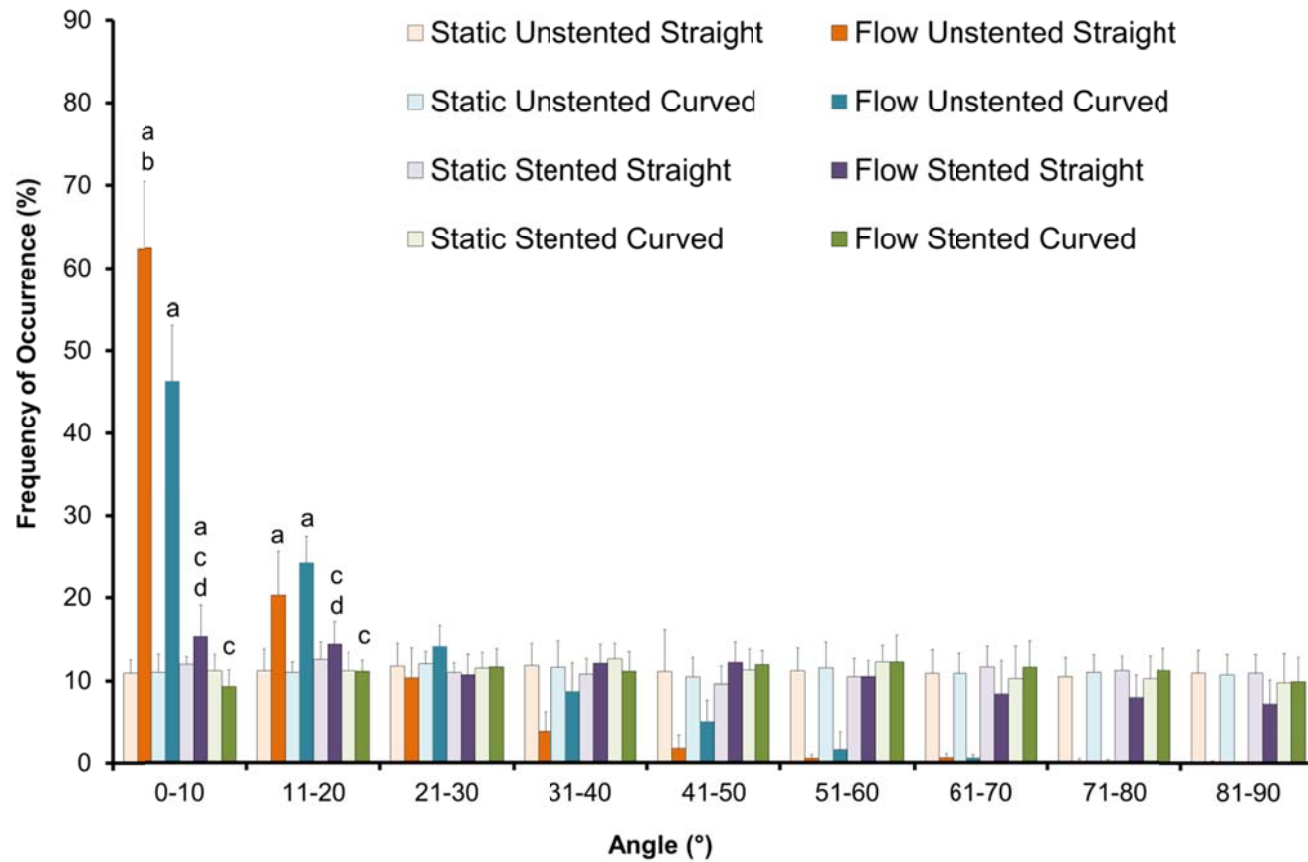


Figure 7.4 Cell orientation angles and frequency of occurrence for pseudovessels with and without biomechanical flow conditions. ^a $p < 0.05$ versus static control; ^b $p < 0.05$ versus curved unstented with flow; ^c $p < 0.05$ versus corresponding unstented model with flow; ^d $p < 0.05$ versus curved stented model.

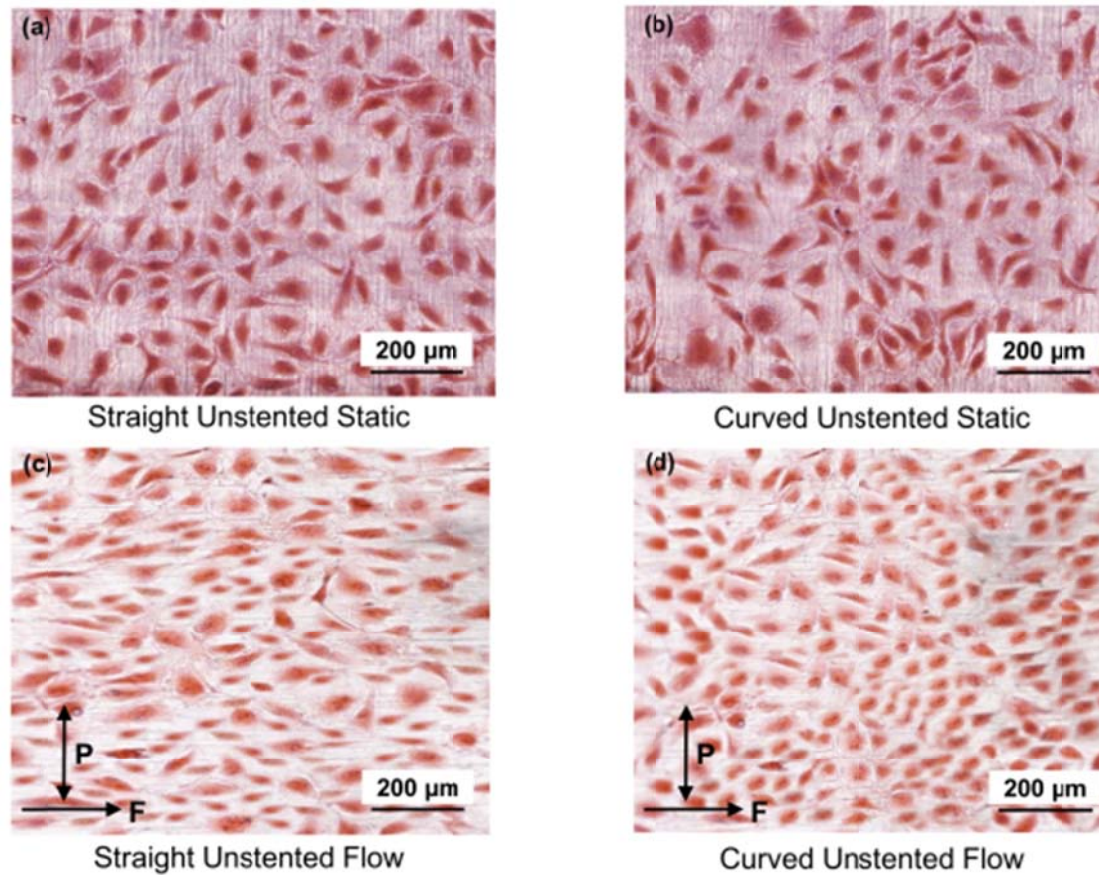


Figure 7.5 Haematoxylin& Eosin stained unstented pseudovessels after 24 hours in the bioreactor. Straight static control pseudovessel (a), curved static control pseudovessel (b), straight pseudovessel with biomechanical flow conditions (c), curved pseudovessel with biomechanical flow conditions (d). P and F correspond to pulsatile and flow directions respectively.

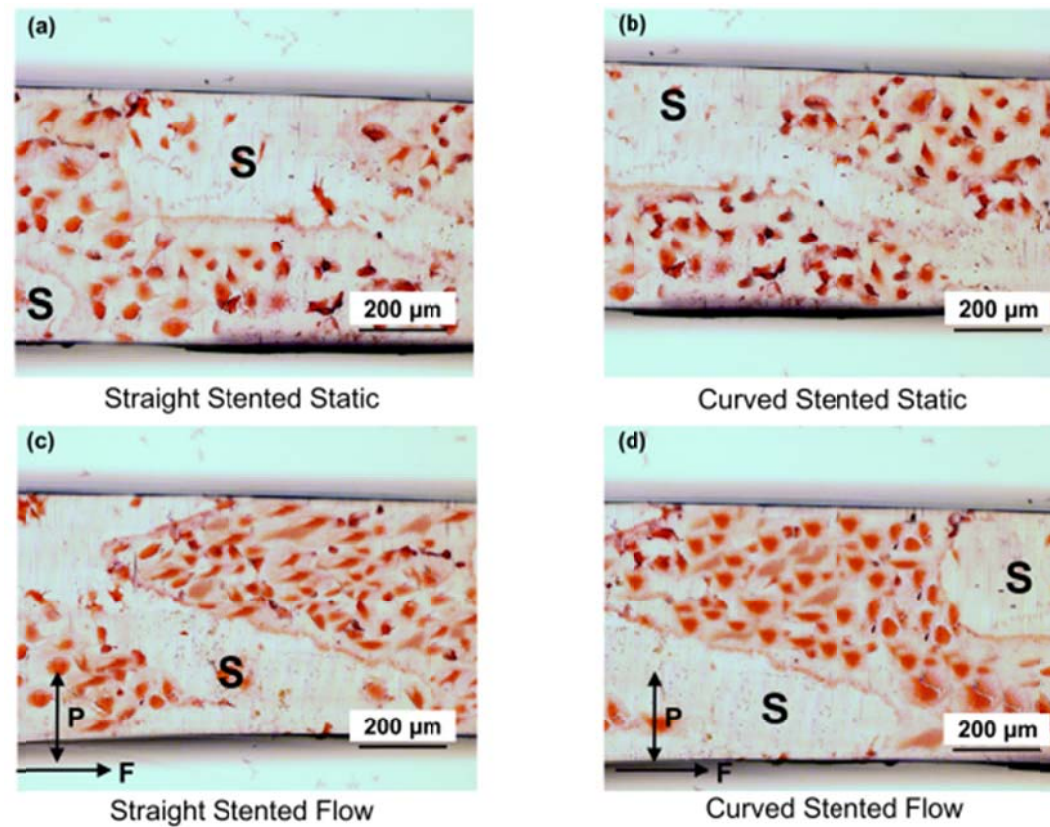


Figure 7.6. Haematoxylin& Eosin stained stented pseudovessels after 24 hours in the bioreactor. Straight static control pseudovessel (a), curved static control pseudovessel (b), straight pseudovessel with biomechanical flow conditions (c), curved pseudovessel with biomechanical flow conditions (d). Nitinol stent (S) removed from stented pseudovessels. P and F correspond to pulsatile and flow directions respectively.

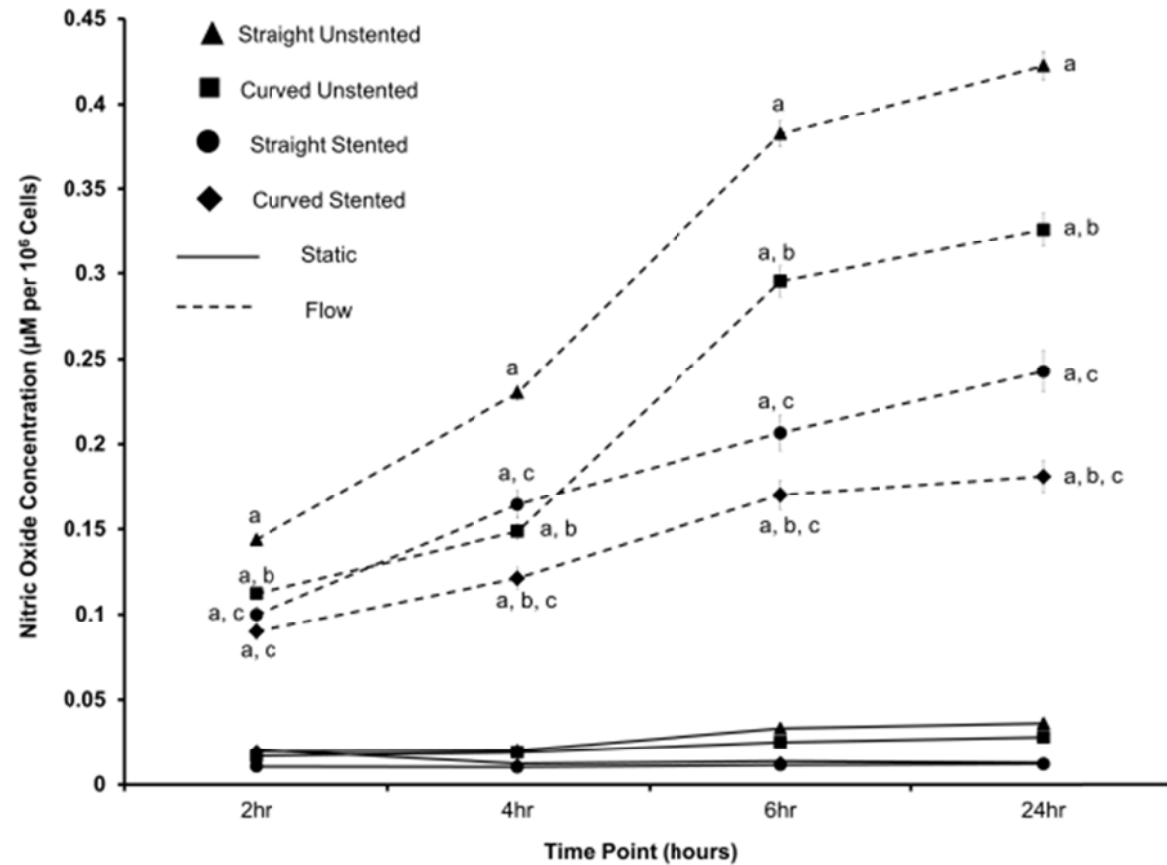


Figure 7.7 Nitric Oxide Production for each pseudovessel model at 2, 4, 6 and 24 hours in the bioreactor with and without biomechanical flow conditions. ^ap < 0.05 versus its static control; ^bp < 0.05 versus corresponding straight pseudovessel with flow; ^cp < 0.05 versus corresponding unstented pseudovessel with flow.

7.6 References

- Aboyans, V, Criqui, MH, Denenberg, JO, Knoke, JD, et al. 2006. Risk factors for progression of peripheral arterial disease in large and small vessels. *Circulation*. 113: 2623-2629.
- Asakura, T and Karino, T. 1990. Flow patterns and spatial distribution of atherosclerotic lesions in human coronary arteries. *Circulation Research*. 66: 1045-1066.
- Awolesi, MA, Sessa, WC, and Sumpio, BE. 1995. Cyclic strain upregulates nitric oxide synthase in cultured bovine aortic endothelial cells. *Journal of Clinical Investigation*. 96: 1449-1454.
- Barbato, JE and Tzeng, E. 2004. Nitric oxide and arterial disease. *Journal of Vascular Surgery*. 40: 187-193.
- Barron, V, Brougham, C, Coghlan, K, McLucas, E, et al. 2007. The effect of physiological cyclic stretch on the cell morphology, cell orientation and protein expression of endothelial cells. *Journal of Materials Science: Materials in Medicine*. 18: 1973-1981.
- Benetos, A, Laurent, S, Hoeks, A, Boutouyrie, P, et al. 1993. Arterial alterations with aging and high blood pressure. A noninvasive study of carotid and femoral arteries. *Arteriosclerosis, Thrombosis, and Vascular Biology*. 13: 90-97.
- Bennett, MR. 2011. Cell Death in Cardiovascular Disease. *Arteriosclerosis, Thrombosis, and Vascular Biology*. 31: 2779-2780.
- Bergel, D. 1961. The dynamic elastic properties of the arterial wall. *The Journal of physiology*. 156: 458-469.

- Berkels, R, Purol-Schnabel, S, and Roesen, R. 2001. A new method to measure nitrate/nitrite with a NO-sensitive electrode. *Journal of Applied Physiology*. 90: 317-320.
- Breen, LT, McHugh, PE, and Murphy, BP. 2009. Multi-axial mechanical stimulation of HUVECs demonstrates that combined loading is not equivalent to the superposition of individual wall shear stress and tensile hoop stress components. *Journal of Biomechanical Engineering*. 131: 1880-1892.
- Cardinal, KOH, Bonnema, GT, Hofer, H, Barton, JK, et al. 2006. Tissue-engineered vascular grafts as in vitro blood vessel mimics for the evaluation of endothelialization of intravascular devices. *Tissue engineering*. 12: 3431-3438.
- Caro, C, Fitz-Gerald, J, and Schroter, R. 1971. Atheroma and arterial wall shear observation, correlation and proposal of a shear dependent mass transfer mechanism for atherogenesis. *Proceedings of the Royal Society of London. Series B. Biological Sciences*. 177: 109-133.
- Cheng, CP, Choi, G, Herfkens, RJ, and Taylor, CA. 2010. The effect of aging on deformations of the superficial femoral artery resulting from hip and knee flexion: potential clinical implications. *Journal of Vascular and Interventional Radiology*. 21: 195-202.
- Cheng, CP, Parker, D, and Taylor, CA. 2002. Quantification of Wall Shear Stress in Large Blood Vessels Using Lagrangian Interpolation Functions with Cine Phase-Contrast Magnetic Resonance Imaging. *Annals of Biomedical Engineering*. 30: 1020-1032.
- Cheng, CP, Wilson, NM, Hallett, RL, Herfkens, RJ, et al. 2006. In vivo MR angiographic quantification of axial and twisting deformations of the superficial femoral artery resulting from maximum hip and knee flexion. *Journal of Vascular and Interventional Radiology*. 17: 979-987.

- Cheng, SWK, W. Ting, AC, and Wong, J. 2001. Endovascular stenting of superficial femoral artery stenosis and occlusions: results and risk factor analysis. *Cardiovascular Surgery*. 9: 133-140.
- Chiu, J-J and Chien, S. 2011. Effects of Disturbed Flow on Vascular Endothelium: Pathophysiological Basis and Clinical Perspectives. *Physiological Reviews*. 91: 327-387.
- Chiu, JJ, Wang, D, Chien, S, Skalak, R, et al. 1998. Effects of disturbed flow on endothelial cells. *Journal of Biomechanical Engineering*. 120: 2-8.
- Cho, A, Mitchell, L, Koopmans, D, and Langille, BL. 1997. Effects of changes in blood flow rate on cell death and cell proliferation in carotid arteries of immature rabbits. *Circulation Research*. 81: 328-337.
- Cines, DB, Pollak, ES, Buck, CA, Loscalzo, J, et al. 1998. Endothelial Cells in Physiology and in the Pathophysiology of Vascular Disorders. *Blood*. 91: 3527-3561.
- Dartsch, P and Betz, E. 1989. Response of cultured endothelial cells to mechanical stimulation. *Basic research in cardiology*. 84: 268-281.
- David Chua, S, MacDonald, B, and Hashmi, M. 2004. Finite element simulation of slotted tube (stent) with the presence of plaque and artery by balloon expansion. *Journal of Materials Processing Technology*. 155: 1772-1779.
- Deplano, V, Bertolotti, C, and Boiron, O. 2001. Numerical simulations of unsteady flows in a stenosed coronary bypass graft. *Medical and Biological Engineering and Computing*. 39: 488-499.
- Duda, SH, Pusich, B, Richter, G, Landwehr, P, et al. 2002. Sirolimus-Eluting Stents for the Treatment of Obstructive Superficial Femoral Artery Disease. *Circulation*. 106: 1505-1509.

- Duraiswamy, N, Schoepfoerster, RT, and James E. Moore, J. 2009. Comparison of Near-Wall Hemodynamic Parameters in Stented Artery Models. *Journal of Biomechanical Engineering*. 131: 061006.
- Duraiswamy, N, Schoepfoerster, RT, Moreno, MR, and Moore, JE. 2007. Stented Artery Flow Patterns and Their Effects on the Artery Wall. *Annual Review of Fluid Mechanics*. 39: 357-382.
- Förstermann, U and Sessa, WC. 2011. Nitric oxide synthases: regulation and function. *European Heart Journal*.
- Frank, AO, Walsh, PW, and Moore, JE. 2002. Computational Fluid Dynamics and Stent Design. *Artificial Organs*. 26: 614-621.
- Gimbrone, MA. 1995. Vascular endothelium: an integrator of pathophysiologic stimuli in atherosclerosis. *The American Journal of Cardiology*. 75: 67B-70B.
- Gimbrone, MA, Topper, JN, Nagel, T, Anderson, KR, et al. 2000. Endothelial Dysfunction, Hemodynamic Forces, and Atherogenesis. *Annals of the New York Academy of Sciences*. 902: 230-240.
- Girerd, X, London, G, Boutouyrie, P, Mourad, JJ, et al. 1996. Remodeling of the radial artery in response to a chronic increase in shear stress. *Hypertension*. 27: 799-803.
- Gnasso, A, Carallo, C, Irace, C, Spagnuolo, V, et al. 1996. Association between intima-media thickness and wall shear stress in common carotid arteries in healthy male subjects. *Circulation*. 94: 3257-3262.
- Gnasso, A, Irace, C, Carallo, C, De Franceschi, MS, et al. 1997. In vivo association between low wall shear stress and plaque in subjects with asymmetrical carotid atherosclerosis. *Stroke*. 28: 993-998.

- Golledge, J, Turner, RJ, Harley, SL, Springall, DR, et al. 1997. Circumferential deformation and shear stress induce differential responses in saphenous vein endothelium exposed to arterial flow. *Journal of Clinical Investigation*. 99: 2719-2726.
- Gray, BH, Sullivan, TM, Childs, MB, Young, JR, et al. 1997. High incidence of restenosis/reocclusion of stents in the percutaneous treatment of long-segment superficial femoral artery disease after suboptimal angioplasty. *Journal of Vascular Surgery*. 25: 74-83.
- Hayashi, T, Yano, K, Matsui-Hirai, H, Yokoo, H, et al. 2008. Nitric oxide and endothelial cellular senescence. *Pharmacology & therapeutics*. 120: 333-339.
- He, Y, Duraiswamy, N, Frank, AO, and James E. Moore, J. 2005. Blood Flow in Stented Arteries: A Parametric Comparison of Strut Design Patterns in Three Dimensions. *Journal of Biomechanical Engineering*. 127: 637-647.
- Holmes Jr, DR, Vlietstra, RE, Smith, HC, Vetrovec, GW, et al. 1984. Restenosis after percutaneous transluminal coronary angioplasty (PTCA): a report from the PTCA Registry of the National Heart, Lung, and Blood Institute. *The American Journal of Cardiology*. 53: C77-C81.
- Ishida, T, Takahashi, M, Corson, MA, and Berk, BC. 1997. Fluid Shear Stress: Mediated Signal Transduction: How Do Endothelial Cells Transduce Mechanical Force into Biological Responses? *Annals of the New York Academy of Sciences*. 811: 12-24.
- Ives, C, Eskin, S, and McIntire, L. 1986. Mechanical effects on endothelial cell morphology: In vitro assessment. *In Vitro Cellular & Developmental Biology - Plant*. 22: 500-507.
- Kamiya, A, Bukhari, R, and Togawa, T. 1984. Adaptive regulation of wall shear stress optimizing vascular tree function. *Bulletin of mathematical biology*. 46: 127-137.

- Kamiya, A and Togawa, T. 1980. Adaptive regulation of wall shear stress to flow change in the canine carotid artery. *American Journal of Physiology-Heart and Circulatory Physiology*. 239: H14-H21.
- Kennedy, JH and Tedgui, A. 1995. Normal and pathological aspects of mass transport across the vascular wall. *Cardiovascular Surgery*. 3: 611-5.
- Klabunde, RE, *Cardiovascular physiology concepts*, 2004, Lippincott Williams & Wilkins: Philadelphia.
- Klein, AJ, James Chen, S, Messenger, JC, Hansgen, AR, et al. 2009. Quantitative assessment of the conformational change in the femoropopliteal artery with leg movement. *Catheterization and Cardiovascular Interventions*. 74: 787-798.
- Kolpakov, V, Polishchuk, R, Bannykh, S, Rekhter, M, et al. 1996. Atherosclerosis-prone branch regions in human aorta: microarchitecture and cell composition of intima. *Atherosclerosis*. 122: 173-189.
- Krams, R, Bambi, G, Guidi, F, Helderman, F, et al. 2005. Effect of vessel curvature on Doppler derived velocity profiles and fluid flow. *Ultrasound in Medicine & Biology*. 31: 663-671.
- Kröger, K, Santosa, F, and Goyen, M. 2004. Biomechanical incompatibility of popliteal stent placement. *Journal of Endovascular Therapy*. 11: 686-694.
- Langille, BL and O'Donnell, F. 1986. Reductions in arterial diameter produced by chronic decreases in blood flow are endothelium-dependent. *Science*. 231: 405-407.
- Levesque, MJ and Nerem, RM. 1985. The Elongation and Orientation of Cultured Endothelial Cells in Response to Shear Stress. *Journal of Biomechanical Engineering*. 107: 341-347.

- Malek, AM, Alper, SL, and Izumo, S. 1999. Hemodynamic Shear Stress and Its Role in Atherosclerosis. *JAMA: The Journal of the American Medical Association*. 282: 2035-2042.
- Mattsson, EJR, Kohler, TR, Vergel, SM, and Clowes, AW. 1997. Increased blood flow induces regression of intimal hyperplasia. *Arteriosclerosis, Thrombosis, and Vascular Biology*. 17: 2245-2249.
- Moore, J, Steinman, D, Prakash, S, Johnston, K, et al. 1999. A numerical study of blood flow patterns in anatomically realistic and simplified end-to-side anastomoses. *Journal of Biomechanical Engineering*. 121: 265-272.
- Moore, JE and Berry, JL. 2002. Fluid and solid mechanical implications of vascular stenting. *Annals of Biomedical Engineering*. 30: 498-508.
- Moore, JE, Burki, E, Suciu, A, Zhao, S, et al. 1994. A device for subjecting vascular endothelial cells to both fluid shear stress and circumferential cyclic stretch. *Annals of Biomedical Engineering*. 22: 416-422.
- Mozersky, DJ, Sumnfr, DS, Hokanson, DE, and Strandness JR, DE. 1972. Transcutaneous measurement of the elastic properties of the human femoral artery. *Circulation*. 46: 948-955.
- Neidlinger-Wilke, C, Grood, E, Wang, JHC, Brand, R, et al. 2001. Cell alignment is induced by cyclic changes in cell length: studies of cells grown in cyclically stretched substrates. *Journal of orthopaedic research*. 19: 286-293.
- Nerem, R, Alexander, R, Chappell, D, Medford, R, et al. 1998. The study of the influence of flow on vascular endothelial biology. *The American journal of the medical sciences*. 316: 169-175.

- Nikanorov, A, Smouse, HB, Osman, K, Bialas, M, et al. 2008. Fracture of self-expanding nitinol stents stressed in vitro under simulated intravascular conditions. *Journal of Vascular Surgery*. 48: 435-440.
- O'Cearbhaill, ED, Punchard, MA, Murphy, M, Barry, FP, et al. 2008. Response of mesenchymal stem cells to the biomechanical environment of the endothelium on a flexible tubular silicone substrate. *Biomaterials*. 29: 1610-1619.
- Pedersen, E, Kristensen, I, and Yoganathan, A. 1997. Wall shear stress and early atherosclerotic lesions in the abdominal aorta in young adults. *European Journal of Vascular and Endovascular Surgery*. 13: 443-451.
- Peng, X, Recchia, FA, Byrne, BJ, Wittstein, IS, et al. 2000. In vitro system to study realistic pulsatile flow and stretch signaling in cultured vascular cells. *American Journal of Physiology - Cell Physiology*. 279: C797-C805.
- Pivkin, IV, Richardson, PD, Laidlaw, DH, and Karniadakis, GE. 2005. Combined effects of pulsatile flow and dynamic curvature on wall shear stress in a coronary artery bifurcation model. *Journal of Biomechanics*. 38: 1283-1290.
- Prosi, M, Perktold, K, Ding, Z, and Friedman, MH. 2004. Influence of curvature dynamics on pulsatile coronary artery flow in a realistic bifurcation model. *Journal of Biomechanics*. 37: 1767-1775.
- Punchard, MA, O'Cearbhaill, ED, Mackle, JN, McHugh, PE, et al. 2009. Evaluation of Human Endothelial Cells Post Stent Deployment in a Cardiovascular Simulator In Vitro. *Annals of Biomedical Engineering*. 37: 1322-1330.
- Punchard, MA, Stenson-Cox, C, O'Cearbhaill, ED, Lyons, E, et al. 2007. Endothelial cell response to biomechanical forces under simulated vascular loading conditions. *Journal of Biomechanics*. 40: 3146-3154.

- Qiu, Y and Tarbell, JM. 2000. Interaction between wall shear stress and circumferential strain affects endothelial cell biochemical production. *Journal of vascular research*. 37: 147-157.
- Rasband, WS. 1997-2011. Available from: <http://imagej.nih.gov/ij/>
- Rudic, RD, Shesely, EG, Maeda, N, Smithies, O, et al. 1998. Direct evidence for the importance of endothelium-derived nitric oxide in vascular remodeling. *Journal of Clinical Investigation*. 101: 731-736.
- Scheinert, D, Scheinert, S, Sax, J, Piorkowski, C, et al. 2005. Prevalence and clinical impact of stent fractures after femoropopliteal stenting. *Journal of the American College of Cardiology*. 45: 312-315.
- Scott, N. 2006. Restenosis following implantation of bare metal coronary stents: Pathophysiology and pathways involved in the vascular response to injury. *Advanced drug delivery reviews*. 58: 358-376.
- Sullivan, TM, Ainsworth, SD, Langan, EM, Taylor, S, et al. 2002. Effect of endovascular stent strut geometry on vascular injury, myointimal hyperplasia, and restenosis. *Journal of Vascular Surgery*. 36: 143-149.
- Tarbell JM. 2003. Mass transport in arteries and the localization of atherosclerosis. *Annual Review of Biomedical Engineering*. 5: 79-118.
- Wang, H, Ip, W, Boissy, R, and Grood, ES. 1995. Cell orientation response to cyclically deformed substrates: experimental validation of a cell model. *Journal of Biomechanics*. 28: 1543-1552.
- Wang, JHC, Goldschmidt-Clermont, P, Wille, J, and Yin, FCP. 2001. Specificity of endothelial cell reorientation in response to cyclic mechanical stretching. *Journal of Biomechanics*. 34: 1563-1572.

Wentzel, JJ, Gijzen, FJH, Stergiopoulos, N, Serruys, PW, et al. 2003. Shear stress, vascular remodeling and neointimal formation. *Journal of Biomechanics*. 36: 681-688.

Wood, NB, Zhao, SZ, Zambanini, A, Jackson, M, et al. 2006. Curvature and tortuosity of the superficial femoral artery: a possible risk factor for peripheral arterial disease. *Journal of Applied Physiology*. 101: 1412-1418.

Zhao, S, Suciu, A, Ziegler, T, Moore, JE, et al. 1995. Synergistic Effects of Fluid Shear Stress and Cyclic Circumferential Stretch on Vascular Endothelial Cell Morphology and Cytoskeleton. *Arteriosclerosis, Thrombosis, and Vascular Biology*. 15: 1781-1786.

Chapter 8. Concluding Remarks and Future Perspective

Reports of high failure rates of peripheral stent devices, currently available in today's market are a continuous reminder that there is still a lot to be understood regarding the effect of stent placement in the femoropopliteal artery (Smouse et al., 2005, Scheinert et al., 2005). The femoropopliteal artery is a highly tortuous vessel with significant levels of arterial curvature and physiological loading from surrounding muscles. Stent fracture in the SFA was reported at a rate of up to 65% (Rits et al., 2008), with stent fractures linked to restenosis in 77 % of fracture cases. Although these figures have improved in recent years with some devices showing lower fracture rates, there are still fracture rates reported in the order of 58% (Endovascular Today, October 2011). Therefore stent fracture is a persistent problem, especially in long lesions of the SFA and is deemed an "unmet clinical need" in SFA intervention (Scheinert, 2012). This highlights a need for development of alternative approaches to the design of stents for the SFA, along with a comprehensive understanding of the femoropopliteal physiological environment and the behaviour of stents within it. Consequently, the suitability of a stent for use in the femoropopliteal artery may depend on its ability to shorten in a controlled manner without inducing strains which lead to fatigue fracture or cause excessive buckling of the artery in unstented regions of the vessel which may lead to damage in the vessel.

Whilst innovators and engineers work with clinicians to develop devices to achieve high vessel patency rates, it is important to take a step back and focus on developing the understanding of the key challenges to stenting in the femoropopliteal artery. These challenges relate to the environment in which the stent must exist and in turn directly relate to each other: the effect of a foreign body (i.e. stent) placed in the vessel and conversely, the effect of physiological loads placed on the stent. Studies have shown that stent failure can be a result of either the stent not withstanding the physiological loading environment of the artery and/or the body responding to the presence of the stent through cellular and biological processes. Therefore it is important to thoroughly understand both of these methods of failure

within the context of the target vessel, when endeavouring to make a successful femoropopliteal stent.

The main objective of this thesis was to advance the understanding of the loading conditions of the femoropopliteal artery along with the effect of this loading on stent vessel interaction of stents are placed in these arteries. Since this can only be fully understood by assessing both the mechanical and biological effects, and their interaction with each other, various experimental and computational investigations, directed towards distinct aspects of the challenges of stenting were undertaken. Specifically these included the identification of interactions between the stent and artery local to the stented region as a result of stent deployment and physiological loading; establishment of deformation characteristics of the artery as a result of knee bending; changes to deformation characteristics of the artery as a result of stent placement and the evaluation of stent-artery interactions in a cellular and biological context. As detailed discussions and conclusions of these investigations have been presented in Chapters 4, 5, 6 and 7, this chapter aims to highlight the primary findings of this thesis, their significance on the main thesis objectives and to provide recommendations for future experimental and computational studies that may arise from the results presented here.

Due to the complicated nature of computational models involving super-elastic Nitinol in contact with hyperelastic arterial tissue, an initial study of some computational modelling approaches for stent-artery interaction models was undertaken to investigate how different methods and assumptions of modelling stent-artery interactions can affect the accuracy of the results. This study is valuable in facilitating reduced computational times of self expanding stent-artery interactions models. The outcomes highlight where simplifications can be made to models of stent-artery interactions that have a particular focus on the effect of stent deployment on arterial stress concentrations and radial force levels imposed on the artery. without significantly affecting the accuracy of the results.

The results of this methodology investigation were then implemented in the development of a finite element model to simulate the deployment of a peripheral stent in the femoropopliteal artery in the presence of its associated physiological loading conditions. As it had been reported frequently in the literature that stents

must withstand high levels of loading *in vivo*, and that stent placement results in local stresses to the underlying vessel wall, it was the purpose of this model to assess the impact of the combination of stenting and physiological loads on the vessel tissue. The importance of investigations that focus on the effect of stent-artery interactions in combination with physiological loads were highlighted from this study, the results of which provide important consideration for stent design. Specifically, this investigation showed that stresses in the stented artery are dramatically increased in the presence of physiological loads, with a significant impact on stress concentrations at the end of the stented region of the vessel due to the stiffness mismatch between the stented and unstented artery segments. Design characteristics should account for this stiffness mismatch between the stented and non-stented portion of the vessel as it is at this ‘border’ that most vessel damage will occur. Whilst reducing the stiffness mismatch between these two regions would be favourable, it is a challenging aspect of device design due to the difference between the flexibility of the Nitinol stent and arterial tissue. The trade-off between stiffness and radial force is also a concern. Nevertheless, it is important for developers to understand the impact that this stiffness difference will have on the vessel in terms of increased vessel wall stresses, cellular damage, vascular injury, plaque rupture and inevitably restenosis.

While the model created for this investigation yields important conclusions regarding the consequences of stenting and the effects of stiffness mismatch on the tissue local to the stent, this ‘local’ model does not account for the affects of stiffening a portion of the vessel on the ‘global’ deformation of the artery. Altering the stiffness of parts of the vessel will impact entire vessel deformation patterns due to the physiological environment of bone, muscle and soft tissue that surround and restrain the artery.

To investigate such ‘global’ deformation effects, an anatomically accurate three dimensional finite element model of the femoropopliteal artery and its surrounding anatomy was created to simulate dynamic load levels and *in vivo* deformation characteristics of the femoropopliteal artery after knee flexion. This novel ‘global’ model once validated using deformation data determined from experimental angiographic images of the femoropopliteal artery, was then adapted

for the investigation of the effects of stenting on the entire arterial segment. It was shown in this investigation that the global deformation characteristics of the vessel along with stress and strain values are altered as a result of stented 'stiffened' portions of the vessel after dynamic loading by knee flexion. Results imply that changing stent length and location results in a corresponding change in the deformation characteristics of the vessel.

The major advantage of the novel approach of investigating stent/artery interactions presented in this model is that it allows correlation of vessel deformation characteristics with tissue stress and strain levels. This adds to the understanding of the effects of stent placement on the arterial tissue of the entire vessel, not just in the stented portion. Another main advantage of this complex model is that it allows for an in depth understanding of the physical loading environment faced by a stent in the femoropopliteal artery. Whilst devices available on the market have all been approved by regulatory bodies due to successful performance in fatigue bench tests, these devices do not show a corresponding clinical success rate. It is therefore thought that these tests are not a true representation of the complex loading of which the stent is subjected to *in vivo* and highlights a need for the development of improved approaches to the design of femoropopliteal stents and the testing of their fatigue life. Establishing values for the deformation and loading level of the unstented and stented SFA could aid greatly in device design, helping to combat fracture rates by determining design parameters such as the required shortening and flexion ranges of devices for this stent location. The use of the model for the quantification of length change, axial twist, curvature and radial compression reveals the main modes of loading on the stent, which are a vital design considerations for femoropopliteal devices. Results of such an analysis can be used as input design characteristics allowing the creation of a device that could comply with the movement and behaviour of the artery in its physiological environment whilst providing the required support to restore blood flow to a blocked vessel.

In addition, there are applications of a 'global' model such as that developed in this work in a clinical context as it could be adapted for patient specific cases to investigate the choices of multiple stent placements, a range of stent sizes and stiffness's. The model developed here allows for multiple viewing planes of the

deformed artery. The results have shown that deformation of the artery due to knee flexion occurs in three dimensions, and therefore multiple viewing planes must be assessed in order to fully determine deformation characteristics. This is not typically considered with angiographic images as it would be very time consuming. Verification of the stented models, by comparison to angiographic images of stented femoropopliteal arteries after knee flexion could be undertaken in future work. Also, as discussed in Chapter 6, the addition of hip flexion movements to the model will further strengthen its capabilities and results.

As a complete representation of the effect of stenting cannot be interpreted from these finite element models alone, an investigation of the effects of stenting and curvature on the cellular and biological environment of the vessel was investigated in an *in vitro* model. This investigation showed for the first time how curvature, in combination with stenting creates a pro-atherosclerotic environment in comparison to stenting in a straight vessel. As the outcomes verify that the response of the vascular endothelium is dependent on both curvature and stenting combined due to a change in flow conditions, the necessity for further *in vitro*, *in vivo* and computational examination of curvature in combination with stenting is highlighted. This will allow the effects on the endothelial layer of stenting in the tortuous femoropopliteal artery to be fully understood. In future work, the peripheral artery bioreactor could be further developed to incorporate the analysis of gene expression behavior of the model arteries. This would further define the nature of the response of stent placement in a biological context. The supplementary development of the complete inflammatory response through an *in vivo* model would further specify the biological response of the vessel to curvature and stenting combinations. Development of a fluid dynamic model to quantify flow levels of the model would also yield invaluable information about the effect of the change in flow conditions of a curved stented artery.

As mentioned, it is necessary, when attempting to understand the effects of stenting, to investigate the challenges related to the vessel environment through models that give conclusions on both the effect of the device placed in the vessel and conversely, the effect of physiological loads placed on the device. This was achieved by the models created for the investigations of Chapters 4, 5, 6 and 7 of this thesis

which each provide very different but equally important results. A ‘local’ model that only captures the effects of stent placement within the immediate vicinity of the stent is not sufficient in assessing the impact of stenting in the femoropopliteal artery alone since the effect of stenting on the deformation characteristics along the entire artery length is considerable. Additionally, a ‘global’ model that does not assess the interaction of stent geometry with vessel tissue is similarly not adequate at capturing all the effects of stenting. Furthermore, finite element models only capable of assessing mechanical effects of stent placement are not sufficient as the biomechanical effects of vascular injury and the change in flow conditions must also be considered. Fluid interactions should also be considered in future work. Therefore, the most significant outcome of this thesis is to highlight the necessity to incorporate multiple models when assessing the effects of stent deployment. The work presented here highlights the importance of taking both a ‘local’ and ‘global’ finite element model simultaneously, allowing a complete analysis of the consequences of stent placement in terms of the mechanical effect to vessel tissue to be realised.

For computational efficiency, stenting is simulated in the ‘global’ model using stiffened material properties in certain sections of the vessel. This then highlights the need for a ‘local’ model, which facilitates precise analysis of the interaction of a stent with arterial tissue. Local models provide a means of assessing the effects of stent design characteristics on the vessel tissue – in particular specific stent strut geometries and configurations which cannot be established from the global model. The ‘local’ model results, achieved by applying known values of physiological femoropopliteal artery loads to a stented artery segment, give insight into the effects of device placement proximate to the stented portion of the artery. The arterial stresses of the ‘local’ model replicate closely those of the stented portion of the ‘global’ model, validating the use of the physiological loads applied to the local model in this study.

In future work, models can be used in conjunction with each other by iteratively using the outputs of one model as the inputs to another, again developing the complexity of each model to expand the knowledge and improve the quality of the results provided by each individual study. Interactions of the models that have

not been considered in the work of this thesis, but that provide future work in this field include:

- The use of the results of the stented global model loading conditions (quantification of length change, axial twist, curvature) as inputs to a ‘local’ stent-artery interaction model to assess specific stent design traits.
- The use of deformed geometries of the stented ‘global’ model as input geometries for fluid interaction models to assess the change in flow characteristics in the stented vessel.
- The use of deformed geometries of the stented ‘global’ model as input geometries for *in vitro* models to assess the biological response due to the change in flow characteristics in the stented vessel.
- The association of the biological response of the *in vitro* model with the mechanical effect (stress/strain response) on vessel tissue from the local model.
- The association of the biological response of the *in vitro* model with quantified flow levels in fluid interaction models of a stented artery.

In conclusion, the simultaneous use of experimental and computational techniques presented in this thesis has yielded the development of two novel models – a ‘global’ finite element model of the lower limb and *in vitro* peripheral artery simulator. It has generated considerable understanding of the vascular mechanics in the field of peripheral stenting and has created the basis for future work for designing and validating new stents and for giving new research insights in this domain.

8.1 References

- Endovascular Today. October 2011. VIVA 2011: 3-Year VIBRANT results for bare stents and stent grafts in long SFA disease. Available at: <http://bmctoday.net/evtoday/2011/10/article.asp?f=viva-2011-3-year-vibrant-results-for-bare-stents-and-stent-grafts-in-long-sfa-disease>.
- Rits, J, van Herwaarden, JA, Jahrome, AK, Krievins, D and Moll, FL. 2008. The incidence of arterial stent fractures with exclusion of coronary, aortic, and non-arterial settings. *Journal of Vascular Surgery*. 36: 339-345.
- Scheinert, D, Scheinert, S, Sax, J, Piorkowski, C, et al. 2005. Prevalence and clinical impact of stent fractures after femoropopliteal stenting. *Journal of the American College of Cardiology*. 45: 312-315.
- Scheinert, D. 2012. Treatment paradigms for the superficial femoral artery. Are they a-changin? *Journal of the American College of Cardiology: Cardiovascular Interventions*. 5: 339-340.
- Smouse, B, Nikanorov, A, and LaFlash, D. 2005. Biomechanical forces in the femoropopliteal arterial segment. *Endovascular Today*. 4: 60-66.